DISSERTATION

SUBMITTED TO THE

COMBINED FACULTIES FOR THE NATURAL SCIENCES AND FOR MATHEMATICS

OF THE RUPERTO-CAROLA UNIVERSITY OF HEIDELBERG, GERMANY

FOR THE DEGREE OF

DOCTOR OF NATURAL SCIENCES

PRESENTED BY

DIPL.-PHYS. ANNA MOCKER

BORN IN MANNHEIM

ORAL EXAMINATION: 19. 1. 2011

Comparison of impact ionisation plasma with laser ionisation

Referees:
Prof. Dr. Eberhard Grün
Prof. Dr. Mario Trieloff

Abstract:

Impact ionisation is the basis for the method yielding the highest sensitivity for detection of dust particles in space. To cover a sufficiently big energy range for the investigation of dust particle impacts and the calibration of impact ionisation instruments, we attempted to supply the dust accelerator at the MPI for Nuclear Physics with laser ionisation. Therefore it is necessary to investigate the properties of both processes with respect to their comparability. For this, the characteristics of the emerging plasma, such as the velocity distribution of the ions, and the ion appearance in the *TOF* mass spectra are analysed and compared. The findings of this study show that, in general, laser ionisation plasma is not comparable to that generated by hypervelocity particle impacts. However, particular aspects of the the laser ionisation process can be used as a rough substitute for particle impacts, i.e. optimising and testing electronic components for impact ionisation instruments.
Furthermore, the dependence of the plasma properties on the impact parameters were studied. Here, the experimental results imply that the defining parameter of the impact process is either the impact velocity or the energy density.

Zusammenfassung:

Die effektivste Methode zum Nachweis von kosmischen Staubteilchen direkt im Weltall beruht auf dem Prozeß der Einschlagsionisation. Zur Kalibration der dabei verwendeten Instrumente muß einen genügend großen Energiebereich abgedeckt werden. Deshalb wird darüber nachgedacht, den Staubbeschleuniger am MPI für Kernphysik in Heidelberg mit einem Aufbau zur Laserionisation zu ergänzen. Nun ist es aber notwendig, die Vergleichbarkeit beider Prozesse zu untersuchen. Hierfür werden die Eigenschaften des beim Einschlag entstehenden Plasmas mit dem der Laserionisation verglichen. Dies sind z.B. die Geschwindigkeitsverteilung der Ionen oder die Häufigkeiten, mit für das Massenlinien in Flugzeitmassenspektren auftauchen. Hier zeigen die Experimente, die für beide Prozesse unter gleichen Bedingungen mit dem gleichen Aufbau durchgeführt wurden, daß im Allgemeinen nicht von einer Vergleichbarkeit ausgegangen werden kann. Jedoch kann Laserionisation zur Simulation von bestimmten Aspekten des Teilcheneinschlags genutzt werden. Zum Beispiel kann ein Laser zum Test und zur Kalibration von Einschlagsionisationsinstrumenten genutzt werden.
Darüber hinaus wurden untersucht, wie die Eigenschaften des Einschlagsplasmas von den Parametern des Teilcheneinschlags abhängen. Hier weisen die Experimente darauf hin, daß die bestimmenden Parameter des Einschlags die Geschwindigkeit des Teilchens und oder oder die Energiedichte sind.

Für Brigitte und Rolf.

Contents

1. Introduction

Dust plays an important role in may astrophysical processes. These tiny particles, often called "micro-meteorides", have sizes of few tenth nm up to 200 μm, can be divided into three groups: planetary, interplanetary and interstellar dust (Grün et al., 1994). Different origin and orbits are reflected in this categorisation.

Interstellar dust *Outside the solar system*, space is not empty: it is filled with rarefied but filthy, filthy gas (Hillier et al., 2010) and dust forms vast dark clouds, recognisable by the extinction of star light.

On one hand, the interstellar dust is an annoyance for astronomers, it is the dominant source of obscuration of starlight in galaxies. The true degree to which dust obscures was recognised by Trumpler (1930) while studying an open start cluster. The key to his realisation was that dust not only dims the light from distant stars , but also reddens is. This is accomplished in two ways. First, light is scattered out of the line of sight towards the observer. Second, dust absorbs photons, converting their energy into heat. This absorption of the light by dust constitutes an important source of energy in the interstellar medium and has the overall effect of making some galaxy emit their energy in the far infrared (at wavelengths $\lambda \approx 200\,\mu$m). Opposite to the surrounding gas, dust is able to emit continuous thermal radiation. Thus, it plays a major role during the cool-down of the interstellar medium and during the formation and development of stars in galaxies. This lesses the thermal pressure, and the cloud will continue to collapse.

On the other hand, interstellar dust is a major component to form starts and planetary systems and can be repeatedly recycled by the galactic evolution process (Dorschner and Henning, 1995).

The origin of interstellar dust is not yet completely clear, a possible process could be condensation in the cool atmospheres of red giants (Binney and Merrifield, 1998). Another major source are envelopes of novea and supernovea explosions and Wolf-Rayet stars (Amari and Lodders, 2007).

Currently, the Sun is flying through one of the warm clouds embedded in the hot medium of the local bubble called *Local Interstellar Cloud (LIC)* (Holzer, 1989). The cloud measures few parsecs in diameter and consists of dusty plasma with an electron density of about $0.1\,\mathrm{cm}^{-3}$ and a temperature of approximatly $10^4\,\mathrm{K}$. Recent measurements confirmed the relative velocity between the Sun and the LIC to be about 26 $\mathrm{km\,s}^{-1}$ (Witte et al., 1993). Although the existence of *interstellar dust within the solar system* was predicted theoretically since the mid-70th, (Levy and Jokipii, 1976; Gustafson and Misconi, 1979; Morfill and Grün, 1979), it was not before 1993, when the first unambiguous *in-situ* detection of interstellar dust grains was successfully achieved with the Ulysses dust instrument (Grün et al., 1993).

The dynamics of interstellar dust grains in the solar system are governed by solar gravity, radiation pressure, and the Lorentz force induced by the radically expanding solar wind magnetic field. These forces shape the trajectory of an individual grain and determine the ISD flux distribution at any given location in the solar system (Altobelli et al., 2006).

Figure 1.1.: Sombrero Galaxy (M104), one of the largest galaxies in the nearby Virgo Cluster of Galaxies. It has an diameter of $\sim$ 50,000 light years. The dark band of dust that obscures the mid-section of the Sombrero Galaxy in optical light as shown in the left picture taken by HST. Courtesy Hubble Heritage Team (AURA, STScI, NASA). The right image shows the infrared glow, recently recorded by the orbiting Spitzer Space Telescope, superposed in false-color on an existing image taken by NASA's Hubble Space Telescope in optical light. Courtesy R. Kennicutt et al. (Steward Observatory, SSC, JPL, Caltech, NASA).

Interplanetary dust particles move on orbits between planets around the sun.

There is a number of dust sources in the Solar System, i.e. collisions of bigger bodies in the asteroid or Edgeworth - Kuiper belt and impacts onto planetary moons and, infrequently, planets themselves (Hillier et al., 2007a). Dust can be also generated from sources within the giant planet systems; some moons have active volcanoes which eject material as gas and dust. If the emission speed of these grains is sufficient enough, the material is released into interplanetary space, moving on orbits around the sun.

In the inner Solar System, at heliocentric distances less then 2.5 AU, comets and asteroids are believed to be the dominant sources of interplanetary dust.

Dust played a key role in the formation process of the sun and the planets (Weidenschilling, 2000). During the formation process the dust grains are altered by the heat of the collapsing cloud and accretion shocks. The composition of the particles will change depending to their location within the disk and the consequential environment temperature. For example, volatile components are vaporised on grains closer to the protostar and recondensate later, representing the temperature profile of the accretions disk. Moreover, dust in the outer regions remains almost unaltered, reflecting the properties if interstellar dust.

Comets were formed from the solar nebular material during the formation phase of the solar system. Hence, they are believed to have preserved their original material composition.

As a comet approaches the Sun on a high elliptical orbit, the volatiles and the dust comprising the nucleus of a comet sublime due to solar heating. Two tails result from a coma cloud expanded radially around the nucleus, the dust tail and the plasma tail.

Planetary dust describes the population of dust grains bound by gravity to a central planet or its moons. It is well known by the formation of dust rings as in the Jovian or Saturnian system, as well at Uranus and Neptune. Despite the latter, planetary dust is present in dust clouds around small bodies and the active ice geysers on the surface of planetary moons like Enceladus (Fig. 1.3). Dust clouds around planetary moons were discovered by the dust detector onboard Galileo (Krüger et al., 1999; Krivov et al., 2003). The moon's surface is continuously

Figure 1.2.: Halley's comet on the Bayeux Tapestry, a medieval embroidery depicting the Norman Conquest of England in 1066. It is remarkable as a work of art and important as a source for 11th-century history and one of the most famous depictions of a comet in the history of art.

bombarded by particles originating from the ring background, interplanetary micrometeoroids and interstellar dust grains. They generate a faint shell above the surface filled with ejecta particles produced on the moons surface upon the primary dust impacts. This process is ongoing on all surfaces in the planetary system, which are not protected by an atmosphere.This includes asteroids, comets, the Earth's moon and all planetary moons, in the Jovian system extensively studied by Krivov et al. (2002) and Sremčević et al. (2005).

Another phenomenon of planetary dust, here defined by its origin within a planet's system, are the high-velocity dust streams of the jovian and saturnian system. These grains are extremely small, they have sizes between 5 and 50 nm. Thus, these particles, charged due to the environmental plasma and UV radiation, are expelled by electromagnetic acceleration in magnetic fields and can reach velocities up to a few $100\,\mathrm{km\,s^{-1}}$ (Horányi et al., 1993; Hamilton and Burns, 1993; Horányi, 2000; Kempf et al., 2005b).

Detection and characterisation of cosmic dust The existence of dust in the solar system is fairly well known since centuries. It was first recognised in its characteristic nature by trying to explain the phenomenon of the zodiacal light. This cone shaped illumination of the sky in the ecliptic plane accrues by reflection or dispersion of the sun light with interplanetary particles.

Due to the investigation of the dispersion and spectral properties of the light, it was possible to gain knowledge about the properties of the dispersing particle, such as sizes, temperatures and chemical composition of their surfaces (see Section 2.4.1).

Yet another important possibility to gain insight in the dynamical, physical and chemical properties of the dust in the solar system are *in-situ* measurements, meaning direct collection and analysis of the the particles by instruments on space probes. Several methods have been used to conduct in-situ experiments since the beginning of space age.

Dust compositional information may be obtained via either impact ionisation time of flight mass spectra or, in rare cases, direct sample return, meaning the investigation of surfaces in the laboratory which have been previously exposed in space.

Perhaps the most dominant method, determined from the analysis of samples on Earth-

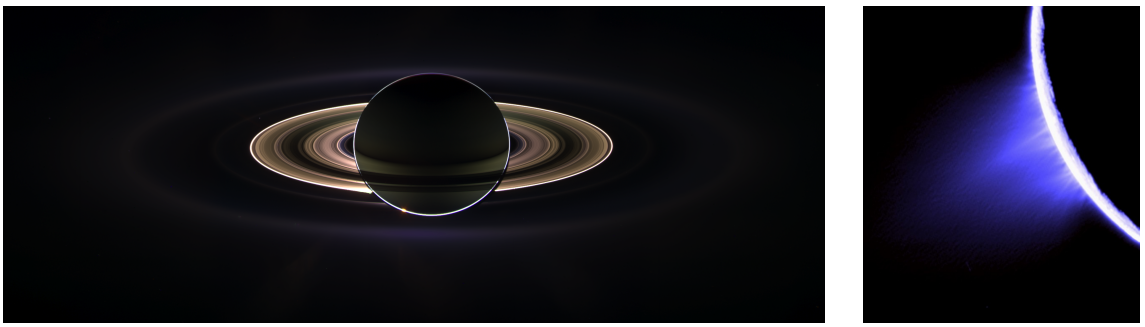

Figure 1.3.: Left: Saturns outer blueish E ring along the orbit of the moon Enceladus. Cassini acquired this global view during a Sun occultation of the planet. Right: Image of the dust plumes at the south pole of Enceladus. (NASA/JPL/SCI PIA08329 PIA08386)

whether delivered naturally and collected from sediment samples, ice cores and stratospheric collection techniques or collected in situ and returned to Earth.

There is a variety of methods for *in-situ* dust measurements. Each method described below, either alone or in combination, can reveal the particles' velocity, trajectory, mass and even chemical composition (Auer, 2001).

- **Thin-Foils penetration** A fast particle striking a thin foil (thickness of the foil $<$ particle diameter) causes compression and shock waves in the projectile as well as in the foil. This may then lead to deformation or even a rupture of the foil. There are two different detection methods using this effect:
  - One detector type registers an impact when the cell's gas pressure (monitored by a pressure switch) drops, because gas leaks into space through a penetration hole in the cell wall. One of the first dust detectors, yielding reliable near-Earth dust fluxes, was the thin-walled pressurised "beer-can" cell on the Explorer 16 satellite, flown in 1962 (Hastings, 1964). A decade later, a similar detector was put on the Pioneer 10 and 11 spacecraft to Jupiter and beyond (Meshejian et al., 1970).
  - For the other type, the striking particles cause a capacitor discharge or depolarisation due to local removal of polarised material in the foil volume. A typical sensor consists of a thin ($\geq 1.5\,\mu$m) foil of permanently polarised polyvinylidene fluoride (*PVDF*).
- **Impact flash detection** Hypervelocity particle impacts produce light. The light flash from impact on a solid target was used for dust impact detection by Berg and Meredith (1956) on a sounding rocket and by Kissel (1986) on the VeGa 1 & 2 and Giotto spacecraft to comet Halley. In the laboratory, this phenomenon and its dependence on the particle impact parameters were studied with photomultipliers, i.e. by Jean and Rollins (1970) and by Eichhorn (1972; 1974; 1975; 1976; 1978b; 1978a).
- **Inductive measurement of the particle charge** Cosmic dust particles are charged due to the environmental plasma and UV radiation(Whipple, 1981). Such particles, approximating a metal electrode, will induce a charge within the electrode. A number of electrodes, i.e. grids or wires, can be used to determine the particle charge and velocity and, depending on the geometrical alignment of the electrodes, even reveal the particles' trajectory and orbit (Shelton et al., 1960; Srama et al., 2004b).

- **Impact ionisation detectors** When a dust particle impacts onto a solid target, parts of the impactor and the target are vaporised and ionised by the energy released during the impact. This leads to the formation of an impact plasma, expanding rapidly into the surrounding vacuum. The constituents of the impact plasma are electrons, positive and negative ions, neutral atoms or molecules, and residual fragments of the impactor and target. The constituents of the plasma are separated due to an electrostatic field, afterwards, depending on their polarity, accelerated towards either an ion detector or the target plane, and amplified and recorded. Impact ionisation is the fundamental physical mechanism involved in the cosmic dust detection as discussed in this work. In the early 60s, the residual ionisation of a gas cloud generated upon impact of a high-velocity projectile onto a solid target was discussed theoretically by Raizer (1959). The first experimental verification of the theory succeeded as soon as facilities were built to accelerate micrometer-sized particles in vacuum to high speeds (some $\mathrm{km\,s^{-1}}$) (Friichtenicht and Slattery, 1963).Then, impact ionisation appeared to be the detection method yielding the highest sensitivity for the detection of dust particles in space. The first dust instrument based on the impact detection method was flown on the HEOS2 spacecraft in 1972. The descendants of the HEOS 2 dust instrument were launched in 1989 and 1990 on board of the Galileo and Ulysses spacecraft, respectively (Grün et al., 1992a,b). As the most recent instrument of this type, the Lunar Dust EXperiment (LDEX) onboard the LADEE space craft is supposed to map the spatial and temporal variability of the dust size and density distributions in the lunar environment (Horányi et al., 2009).

- **Time-of-flight mass (TOF) spectroscopy** The greatest sensitivity is provided by an impact ionisation detector combined with a *TOF* mass spectrometer. Here, the separated and accelerated ions are focused on an ion detector, registering the ions sequentially. Due to conservation of energy

$$\frac{1}{2}mv^2 = q \cdot U_{acc}$$

(with v being the ion speed, m its mass, q its charge, and U_{acc} the separating potential), the ion flight time can be assigned to a q/m and subsequently to an ion species. Thus, a mass spectrum can be obtained and the chemical composition of the particle can be revealed to some extent depending on the spectrometer's quality. The advantages of such detectors are the simplicity and the possibility of simultaneous measurements of the the dynamical properties of the particle and its chemical composition. The first, simple *TOF* mass spectrometer flown in space was the dust instrument on the Helios spacecraft in 1974 (Dietzel et al., 1973). The last upgrade of this type of dust instrumentation is the Cosmic Dust Analyser (CDA) onboard the Cassini spacecraft - currently investigating Saturn, its moons, and rings (Srama et al., 2004a). To obtain significantly higher mass resolutions an electrostatic ion reflector with a folded drift tube and a first-order energy focusing was used for the design of the dust instruments PIA and PUMA on the VeGa 1 & 2 and Giotto spacecrafts encountering the comet Halley in March 1986 (Sagdeev et al., 1987). The *CIDA* instrument onboard Stardust is a direct descendant of these mass spectrometers (Kissel et al., 2004, 2003). An instrument combining the advantages of both, the high mass resolution of a reflectron *TOF* mass spectrometer and the large target area of the *CDA*-type instrument, is the *Large Area Mass Analyser* (Sternovsky et al., 2007).

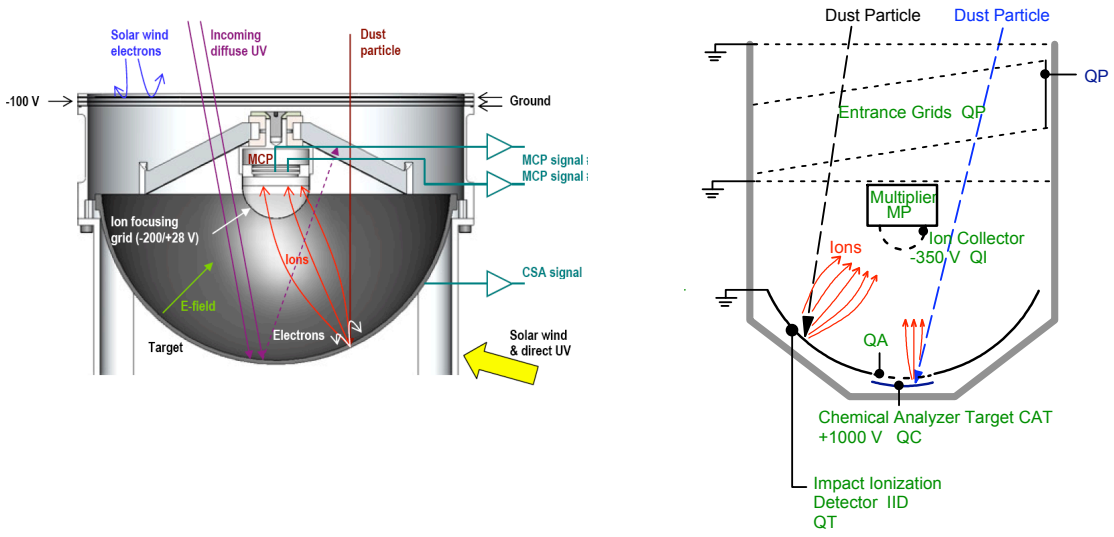

Figure 1.4.: Impact ionisation instruments for the detection and analysis of cosmic dust particles in space. Right: Schematical drawing of the LDEEX instrument, representing the simple impact ionisation instruments of the HEOS type(Horányi et al., 2009). Right: Schematics of the CDA mass spectrometer (Srama, 2010).

Simulation in the laboratory The accurate and reliable interpretation of collected spacecraft data requires a comprehensive program of terrestrial instrument calibration. This process involves accelerating suitable cosmic dust analogue particles to hypervelocity speeds in the laboratory. There are basically three types of accelerators in use for producing test particles at these high velocities. As shown in Figure 1.5 they provide different ranges of masses and velocities. The electrostatic dust accelerator covers the entire speed range needed for most of the applications except for i.e. extremely high velocities similar to those of the stream particles. For this study, the 2 MV Van-de-Graaff accelerator located in the Heidelberg dust laboratory was used, which accelerates charged micron and sub-micron sized dust particles to speeds in excess of $\sim$80 km s^{-1}. Due to its the working principle, as described by Friichtenicht (1965), the velocity of particles is related to their masses. This type of accelerator works only for small particles (0.01 $\cdots$ 3 μm). The plasma drag accelerator and the light gas gun produce projectiles, having sizes ranging from 10 μm to 100 μm, though achieving lower speeds. The velocity-mass ranges obtained with these different types of particle accelerators are shown in Figure 1.5. Besides the development, calibration, and testing of instruments dedicated to the investigation of dust particles in space, hypervelocity impact experiments provide the opportunity to gain a better understanding of the impact process itself and to study matter at extreme conditions, i.e. high pressures and temperatures.

But, although the dynamical properties particles match those of the main fraction dust particles in space, some cosmic dust populations like dust stream particles have speeds not accessible with particle accelerators in the lab (Kempf et al., 2005a) . For such conditions, calibration is not possible, leading to less reliable interpretation of impact signals recorded with the dust instrument in space.

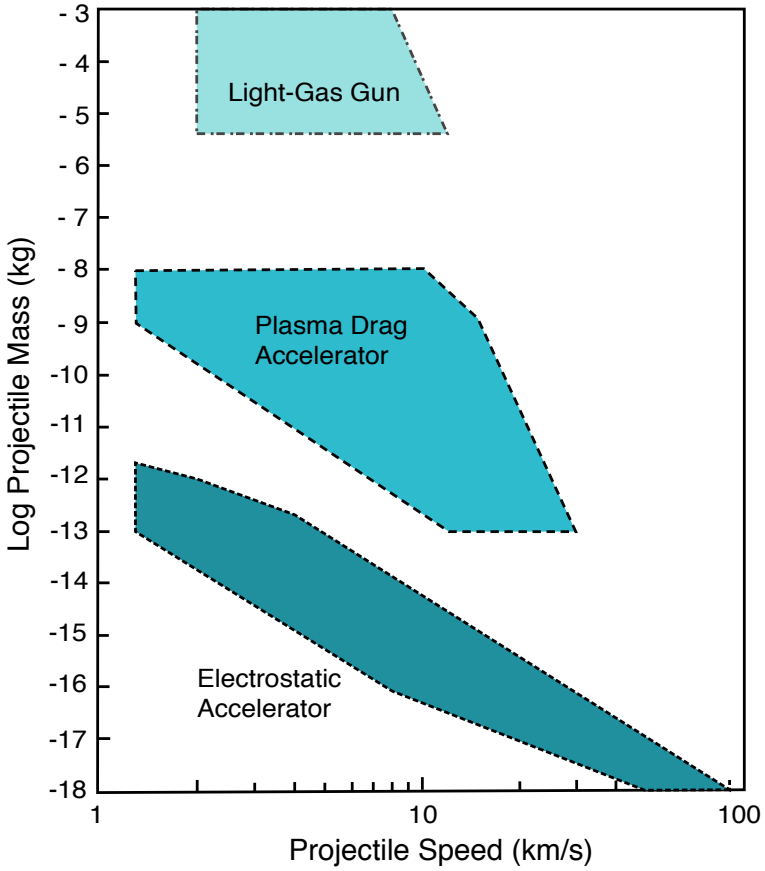

Figure 1.5.: The mass versus velocity ranges for the three common microparticle accelerators (Auer, 2001).

Soon after their introduction in 1962 (McClung and Hellwarth, 1962), high-powered pulsed lasers were to be recognised as a flexible and powerful tool for the studying the interaction of intense electromagnetic field with solid bodies (Ready, 1963; Friichtenicht, 1974). The formation of a hot plasma from the irradiated surface was found to be depending sensitively on laser parameters, such as energy density, pulse duration, wave length etc. as well as the properties of the irradiated material (Linlor, 1963; Mulser et al., 1973). In general, the resulting ablation plasmas or "plumes" have high ion and electron temperatures of the order of several thousand Kelvin and high degrees of ionisation. Due to this, laser set ups were designed to create plasma plumes in order to test and optimise time-of-flight mass spectrometer and other particle impact ionisation instruments or their components (Austin et al., 2002; Sternovsky et al., 2007).

Although there have been experimental and subsequent theoretical investigations of the similarity of both ion emitting processes, these studies, conducted mainly by Krueger (1982), Knabe and Krueger (1982), and Kissel and Krueger (1987), took place under specific experimental conditions and for a very particular choice of investigated materials.

Outline of this thesis Subject matter of this thesis is the investigation of the comparability of the impact ionisation process and the formation of a plasma cloud due to the irradiance if

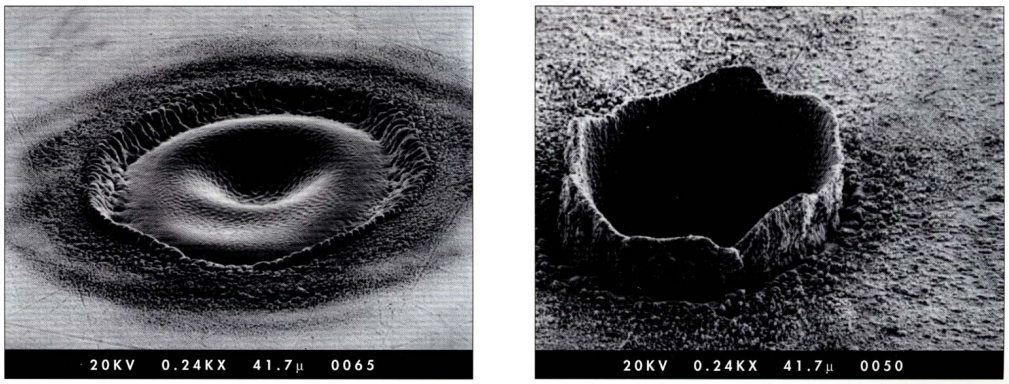

Figure 1.6.: Photographs of laser ablation "craters" in a copper surface generated with a 30 ps pulse from a Nd:YAG laser at wave lengths of $\lambda = 1064$ nm *(left)* and $\lambda = 266$ nm *(right)* (Russo, 1995).

a solid target. For this, one has to define what "comparability" exactly means in this context. Laser ionisation is regarded as a simple method to emit ions from a surface comparable to particle impact in a high repetition rate with much less effort and costs and in a wider energy range as with a micro-particle accelerator.

The guiding themes of this work were three questions concerning the processes of impact and laser ionisation:

- How reproducible are mass spectra produced by hypervelocity impacts and by laser ablation under similar physical conditions?
- Is laser ablation a useful analogue for the impact ionisation process?
- How deep is our understanding of the impact ionisation process?

For answering these questions, a program of hypervelocity impact and laser induced ionisation experiments was performed to investigate these themes.

These measurements were conducted with a time-of-flight mass spectrometer designed to provide as comparable as possible impact conditions and optimised to obtain direct information about the process, i.e. the velocity distribution of the generated ions. The results provide constraints for the comparability of the processes and for the possibility of simulating particle impacts with laser bombardment of solid surfaces. The laser used in this study is a Nd-YAG solid state laser with a wave length of 355 nm, pulse durations of about 5 ns and a pulse power of up to 200kW. For the laser ionisation measurements, the laser beam was focused to a focal spot of about 10 μm diameter on metal (iron and a copper/silver alloy) as well as silicate targets (gold coated olivine). These materials were chosen to be comparable to the particle impact experiments shots, which had been performed with iron particles as well as with orthopyroxene and olivine dust on metal targets.

In the following Sections 2.1 and 2.2 a brief overview of the involved processes will be given, followed by a discussion of the used method of investigation, namely time-of-flight-mass spectroscopy (see Section 2.3). Since the background of this study is the investigation

of physical and chemical properties of cosmic dust particles, the experiments have been conducted using analogous materials prepared to be accelerated. The general properties of these materials will be described in Section 2.4.

This is followed by an overview of the experimental set up in Section 3. The presentation and interpretation of the experimental results in Section 4 is focused on the the impact charge signals and the *TOF* mass spectra. The results are summarised in Section 5. In the appendix of this work, the resulting experimental data are listed and some of the used experimental methods and techniques are described.

The findings of this study show that, in general, plasma generated by laser ablation or desorption is not comparable to that created by hypervelocity particle impacts. However, particular aspects of the the laser induced ionisation process can be used as a rough substitute for hypervelocity particle impacts: once found and optimised, a particular laser set up can be used to produce many similar impact events at a high repetition rate, which can then be used for optimising and testing detectors, amplifiers and other electronic components for time-of-flight mass spectrometers developed for the investigation of impact ionisation plasmas.

Furthermore the experimental results imply that the defining parameter of the impact process is either the impact velocity or the impact energy density. Due to the the bias in the accelerated particles' velocities and masses introduced by the functional principle of the dust accelerator, the question, which parameter dominates, could not be answered. Further investigations over a wider range of kinetic energies of the particles are necessary in the future.

2. Basic Principles

The following section gives a short overview of the basic principles playing a role in the physical processes studied in this thesis. First the hypervelocity impact of micrometer sized particles onto solid surfaces and the consequential emitted plasma plume is described. Then an overview of the laser ionisation process is given, followed by a discussion of the chosen method of investigations, *TOF* mass spectroscopy. Finally, because the background of this study is the investigation of physical and chemical properties of cosmic dust particles, the experiments have been conducted using analogous materials prepared to be accelerated and shot at. The general properties of this materials will be described in Section 2.4 as well as the most important compounds of cosmic dust particles.

2.1. Shock wave ionisation of dust particles

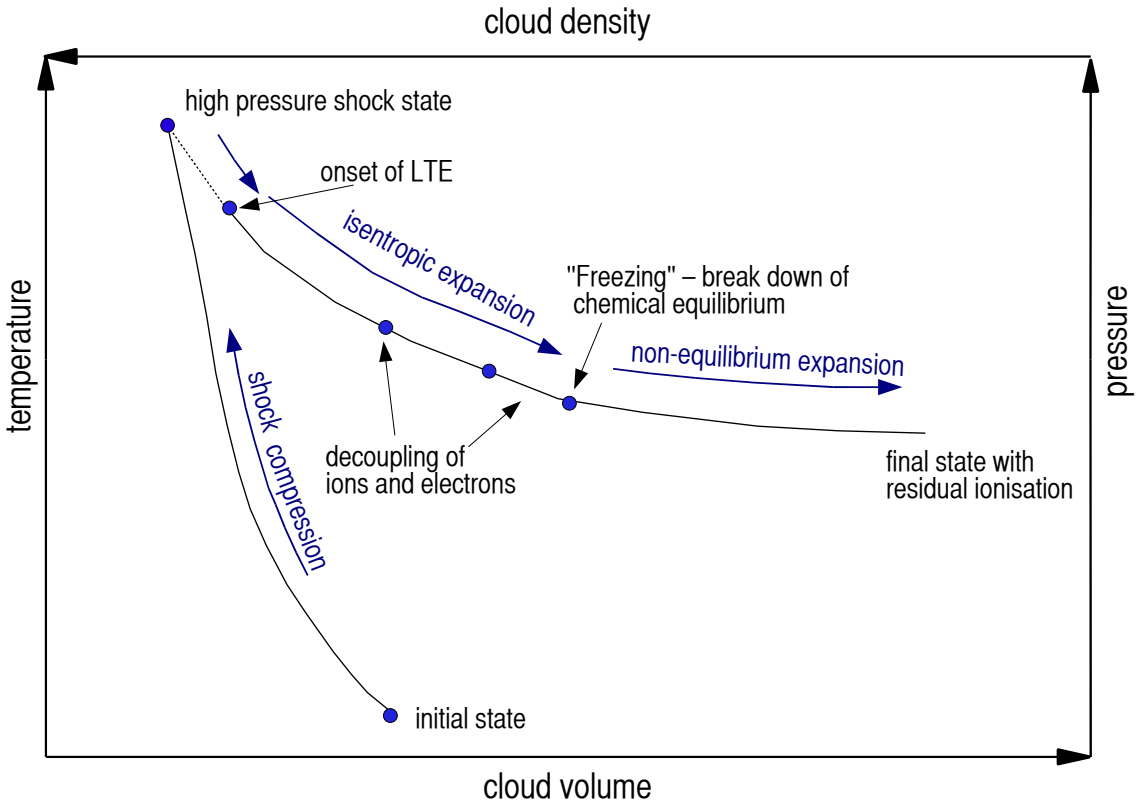

Figure 2.1.: Principle of the shock wave ionisation process (Hornung and Drapatz, 1979).

High velocity impacts of particles on a solid surface produce ions from the particle as well as from the target material. An attempt to explain this fact is the model of shock wave ionisation

developed by Drapatz and Michel (1974). As shown in Fig. 2.1, this model describes the impact process in sequent phases.

1. The particle is compressed by a strong shock to high pressures and temperatures. Dependent on the impact velocity and its mass, the particle will be partially or even completely evaporated. For sufficiently high temperatures molecules are considered to be dissociated and the atoms as strongly ionised. The corresponding timescale is of the order of the impact's duration. For a particle with the diameter of $1\,\mu$m and a velocity of $5\,\mathrm{km\,s^{-1}}$ this can be estimated to $\tau_{imp} = 1\,\mu\mathrm{m}/5\,\mathrm{km\,s^{-1}} = 0.2\,\mathrm{ns}$. The resulting gas cloud is assumed to be in thermodynamic equilibrium (Zel'dovich and Raizer, 2002).

2. When the shock wave within the dust particle reaches its outer boundary, rarefaction waves travel inward. This results in a release of the wave pressure into the gas phase, accelerating the material in all directions. This expansion is assumed to be isentropic (Hornung and Drapatz, 1979).

3. During the early state of the subsequent sudden expansion, at high densities and temperatures, all relaxation processes proceed rapidly and the gas remains in equilibrium. Characteristic state variables of the gas, e.g. the degrees of ionisation or dissociation, follow the expansion and cooling. Thus, the ionisation degree may be determined from Saha's equation

$$\frac{N_+}{N_0} n = \frac{Z_+}{Z_0} \cdot \frac{2\,(2\pi m_e kT)^{\frac{3}{2}}}{h^3} \cdot \frac{1}{N_e} e^{-\frac{I_0 - \Delta I}{kT}}, \tag{2.1}$$

   where Z_+ and Z_0 are the partition functions of the ions and atoms, N_+, N_0, and N_e are the numbers of ions, atoms, and electrons per unit volume, and I_0 is the ionisation potential (Kegel, 1998).

4. The equilibrium degrees of ionisation (*Saha-equilibrium*) and dissociation (*chemical equilibrium*) are established as a result of the mutual compensation of the direct and reverse process, the recombination of either ions and electrons to atoms or of atoms to molecules. The rates of ionisation and dissociation scale with temperature

$$R_{i/d} \sim e^{-\frac{I}{kT}}. \tag{2.2}$$

   as a consequence of the expansion the gas cools rapidly (Section 2.1.5)

$$T \sim \rho^{\gamma - 1} \to 0,$$

   with γ being the specific heat ratio. This implies that the exponential term in (2.1.5) drops rapidly with temperature and consequently with time. On the other hand, the rates of the revers recombination processes have only a power law dependence on density and temperature.Therefore, ionisation and dissociation will stop at a certain instant, after which the degrees of ionisation and dissociation will decrease with time following a power law, whereas the equilibrium values drop exponentially.

5. The recombination rates also decreases as a result of the expansion and may cease entirely. Therefore, the gas expands to infinity in the partially dissociated state with some residual ionisation. This phenomenon is called *"freezing"* of ionisation and of the atoms.

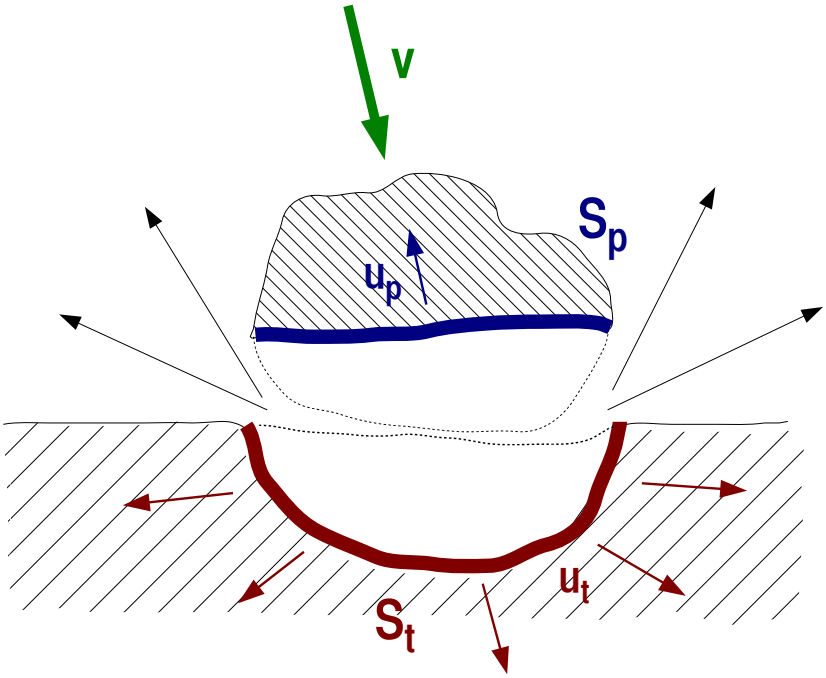

Figure 2.2.: Generation of shock waves moving through dust particle (S_p) and target (S_t). v terms the impact velocity, u_p and u_t the material velocities behind the shock front in either the dust particle and the target.

6. Further in the expansion process, gas-kinetic collisions in the gas also cease almost entirely. At this point the dynamics of the impact plasma cloud is not any longer governed by gas kinetics.

2.1.1. Shock dynamics

Upon hypervelocity impact of a dust particle on a solid surface, two shock waves are generated, one traveling into target, S_t, (Fig. 2.2) and one into the dust particle, S_d. For both, the target and the dust material, the shock dynamics shock is equivalent and can be described as follows.

Hugoniot curves of compressed media

The change of the state variables *mass*, *momentum*, and *energy* caused by a an one dimensional shock wave in a solid can be easily from the conservation laws. In the rest frame of the shock wave they are represented by

$$\rho_2 \cdot u_2 = \rho_1 \cdot u_1 \qquad \text{conservation of mass,} \tag{2.3}$$

$$p_2 + \rho_2 u_2^2 = p_1 + \rho_1 u_1^2 \qquad \text{conservation of momentum,} \tag{2.4}$$

$$\varepsilon_2 + \frac{p_2}{\rho_2} + \frac{u_2^2}{2} = \varepsilon_1 + \frac{p_1}{\rho_1} + \frac{u_1^2}{2} \qquad \text{conservation of energy,} \tag{2.5}$$

where ρ_1, u_1, p_1 are the density, material velocity and pressure before the shock wave and ρ_2, u_2, p_2 behind it. Since the density ρ_1 can be considered as a known quantity, this relation provides three equations for four unknowns, the density ρ, the pressure p, the velocity of the shock wave D and the velocity of the material behind the shock wave u. Thus, a fourth equation will be needed to completely describe the conditions behind the shock front. Even though any algebraic equation involving any two of the four unknowns would be sufficient, a relationship describing the thermodynamical properties of the material is required. This relationship is termed *equation of state* (*EOS*) (Gault and Heitowit, 1963).
The specific enthalpy $h = \varepsilon + p/\rho$ before and after the shock wave is

$$h_1 + \frac{u_2^2}{2} = h_0 + \frac{u_1^2}{2}. \tag{2.6}$$

After replacing density by the specific volume $V = 1/\rho$, and inserting Eq. 2.3 and Eq. 2.4 into Eq. 2.5 one yields

$$\varepsilon_2 - \varepsilon_1 = \frac{p_1}{\rho_1} + \frac{u_1^2}{2} - \frac{p_2}{\rho_2} - \frac{u_2^2}{2} = p_1 V_1 - p_2 V_2 + \frac{1}{2}(p_2 - p_1)(V_1 + V_2),$$

and thus,

$$\Delta\varepsilon = \frac{1}{2}(p_2 + p_1)(V_1 - V_2). \tag{2.7}$$

Equation 2.7 relates the initial and final pressures and volumes and is termed either shock adiabatic or *Rankine-Hugoniot relation* (Landau and Lifshitz, 1959).
The *Hugoniot curve* is represented by the function

$$p_2 = H(p_1, V_1, V_2),$$

which can be written in an explicit form, provided that the thermodynamic function $\varepsilon = \varepsilon(V, p)$ is sufficiently simple.
Whereas isentropes depend only on the entropy S, the Hugoniot curve is a function of two parameters, the initial pressure p_1 and Volume V_1.

Rest frame of the unshocked material: As shown in the previous section, the velocities u_1 and u_2 in Eq. 2.3 - Eq. 2.5 can be substituted by the shock front propagation velocity D and the jump in the particle velocity u. In laboratory coordinates, the velocity u is equal to the velocity of the material behind the shock front. Measurable parameters are the shock front velocity $u_s = u_2$ and the velocity of the material $u_p = u_2 - u_2$ in the frame of reference for the unshocked material (see Fig. 2.3 *right*). Thus, it is useful to rewrite the equations 2.3 and 2.4

$$\frac{\rho_2}{\rho_1} = \frac{V_1}{V_2} = \frac{u_1}{u_2} = \frac{D}{D-u}, \tag{2.8}$$

$$p_2 - p_1 = \frac{D-u}{V_1}, \tag{2.9}$$

$$\varepsilon_2 - \varepsilon_1 = \frac{1}{2}(p_2 - p_2)(V_1 - V_2). \tag{2.10}$$

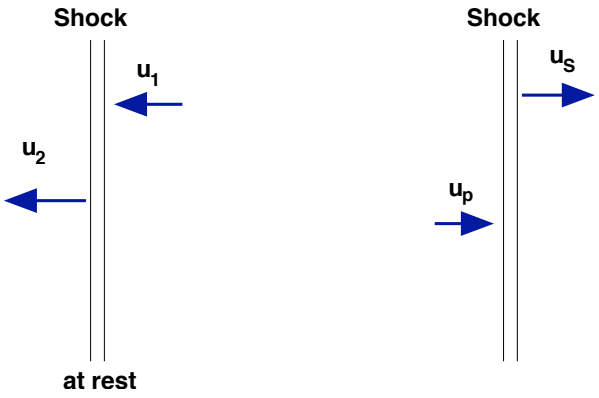

Figure 2.3.: Frames of references for the shock front within the impacting particle or the target. *left* Rest frame for shock front. *right:* Frame of reference for the unshocked material

Contrary to the representation in the rest frame of the shock wave (Eq. 2.3 to Eq. 2.5) there are now five parameters, ε, p, V, D and u. With three of the parameters constrained by the three equations above, this is leading to system with two degrees of freedom. Thus, Eq. 2.8 to Eq. 2.10 can be emphasised to describe the hydro- and thermodynamic characteristics of shock-compressed material, provided that any two of the five parameters ε, p, V, D and u are recorded (Fortov and Lomonosov, 2010).

The obtained internal energy is

$$\frac{\varepsilon_2 - \varepsilon_1}{\frac{1}{2}u^2} = \frac{p_2 + p_1}{p_2 - p_1} \tag{2.11}$$

(Michel and Wagner, 1971). For very strong shock waves, i.e. $p_2 \gg p_1$, this leads to

$$\Delta\varepsilon \geq \frac{1}{2}u^2. \tag{2.12}$$

It is to be noted that to the same degree of approximation, the total work done on the medium by the shock compression is $p(1/\rho_1 - 1/\rho_2)$. Thus equation indicates that the energy added by the shock process is equally partitioned in the compressed material between the specific kinetic energy $E_H = 1/2u^2$ and an increase in the specific internal energy $(\varepsilon_2 - \varepsilon_1)$ (Gault and Heitowit, 1963). This corresponds to the *Virial theorem*. For strong shocks, the *shock pressure* P_s is

$$P_s = p_2 = p_1 + \rho_1 Du \approx \rho_1 D \cdot u \tag{2.13}$$

(Hornung and Kissel, 1994). Laboratory measurements on solid state shock waves imply that the relation between the shock wave velocity D and the flow velocity u_p behind the shock wave is linear and can be represented by

$$D = A + Bu \tag{2.14}$$

(Michel and Wagner, 1971). This corresponds to a specific form of the Hugoniot curve, which relates the flow velocity to the pressure within the compressed material. In the case of no phase transition during compression, A corresponds to the speed of sound in the uncompressed material, whereas B is related to the *Grüneisen parameter* Γ (see next Section 2.1.1) via

$$\Gamma = 2(B - 1).$$

For strong shocks, the shock velocity is large compared to the speed of sound. Hence, the shock velocity is

$$D = \frac{1}{2}(\Gamma + 2)\, u. \tag{2.15}$$

Grüneisen parameter

Microscopically the Grüneisen parameter describes the volume dependence of the ith mode of vibration ω_i of the lattice of a solid body

$$\Gamma_i = -\frac{\partial ln\, \omega_i}{\partial ln V}$$

(Grüneisen, 1912). It has been shown, e.g by Barron (1957), that summation over all modes ω_i within the first Brillouin-zone leads to a macroscopic, i.e. thermodynamic, definition of the parameter

$$\Gamma = \frac{\alpha V k_T}{c_V}, \tag{2.16}$$

where α is the thermal expansion, V is the volume, k_T is the isothermal bulk modulus, and c_V is the heat capacitance at constant volume.
Integrating Equation 2.16 with respect to temperature leads to the Mie-Grüneisen expression

$$\Gamma = \frac{p_{th} V}{E_{th}}, \tag{2.17}$$

where p_{th} and E_{th} are the thermal pressure and the thermal energy respectively. Thus, the Grüneisen parameter describes the volume dependence of the thermal pressure and energy. It is an approximately constant dimensionless parameter varying slowly as a function of pressure and temperature (Vočadlo et al., 2000).

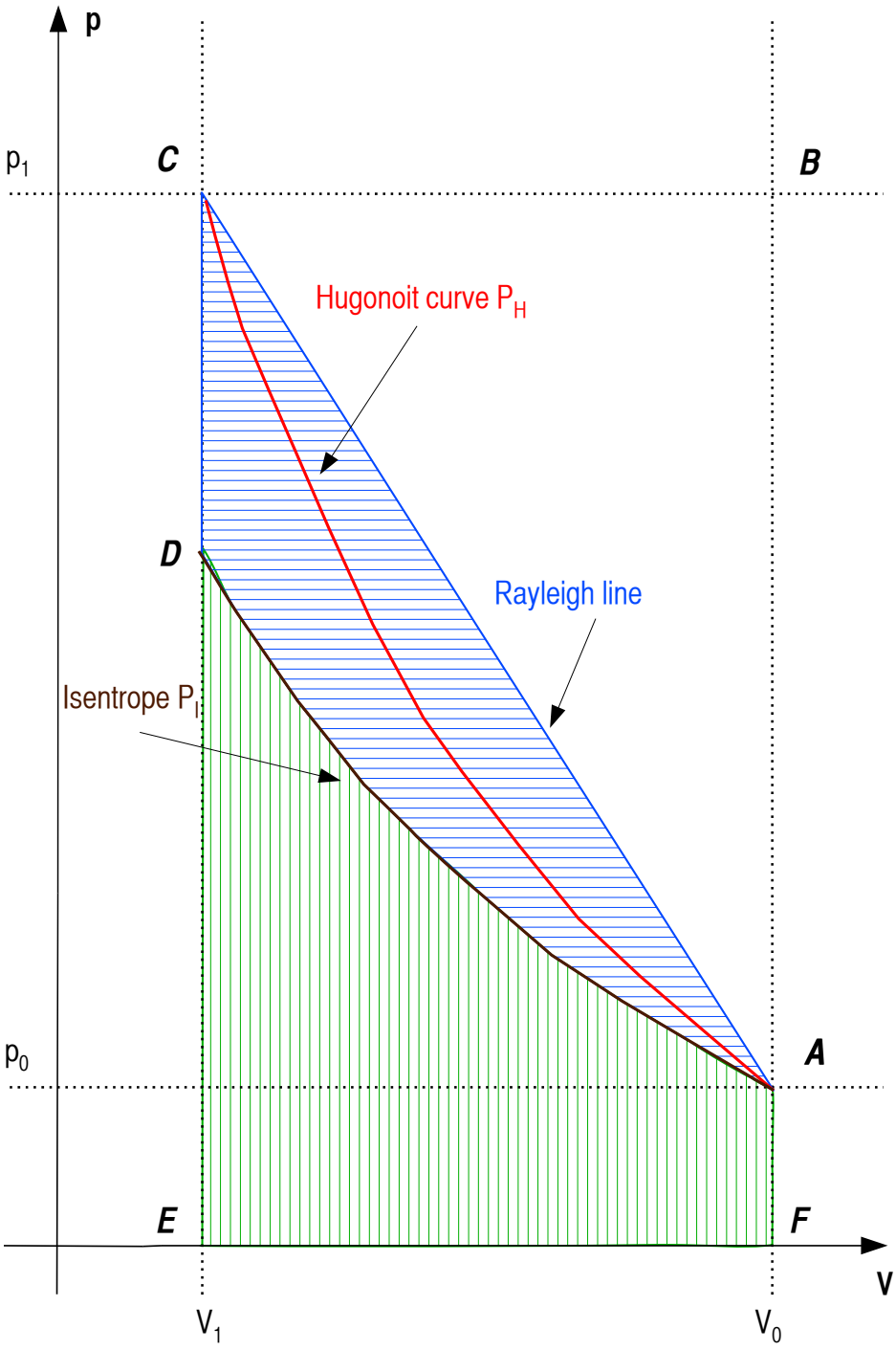

Figure 2.4.: *Hugoniot curve of a shock wave.* The line P_H connecings the points $A = (V_1, p_1)$ and $C = (V_2, p_2)$, is the *Hugoniot curve*, whereas the *isentrope* P_I originates in A and ends in D. The line between A and C is the *Rayleigh line*, which is characteristic for a specific propagation velocity. The rectangle *FBCE* corresponds to the total energy, the trapezoid *FACE* to the internal energy per mass unit. The area under the isentrope P_I matches the internal energy, which would be gained under isentropic compression to the same fine volume V_2. Thus, the horizontally hatched area determines the gain in entropy through the shock wave (Michel and Wagner, 1971).

2.1.2. Shock dynamics on a particle impact

To determine the impact conditions for the shock pressure P_s and the material velocity u, the Hugoniot curve for the impacting dust particle as well as the target is needed. The intersection of the curves then represents these impact conditions as shown in Figure 2.5. The particle's Hugoniot curve starts at impact velocity v towards slower speeds. The shock decelerates the dust material from the impact velocity down to *v-u* (Hornung et al., 1996).

Besides the conservation of mass, momentum and energy (Eq. 2.3 - Eq. 2.5) for the particle impact it is required, that the shock pressures P_i and material velocities u_i have to be equal on both sides of the contact surface:

$$\begin{aligned} v - u_d &= u_t, \\ P_d &= P_T, \\ \rho_d D_d u_d &= \rho_t D_t u_t \qquad \text{(from Eq 2.13).} \end{aligned} \tag{2.18}$$

From Eq. 2.15 follows that

$$u_d = \left(\sqrt{\frac{\rho_t \left(\Gamma_t + 2\right)}{\rho_d \left(\Gamma_d + 2\right)}} + 1 \right)^{-1} \cdot v \tag{2.19}$$

In the strong shock limit, the Grüneisen parameter is the same for all materials, implying

$$u_d \approx \left(\sqrt{\frac{\rho_d}{\rho_t}} + 1 \right)^{-1} \cdot v. \tag{2.20}$$

Thus, the total specific internal energy (Eq. 2.12) of a strong shock is approximated by

$$\Delta\varepsilon \approx \frac{1}{2} \left(\sqrt{\frac{\rho_d}{\rho_t}} + 1 \right)^{-2} \cdot v^2. \tag{2.21}$$

For lower impact speeds and masses typical for dust accelerators (Fig. **??**), experimental data for p and u_p is available. If there are no experimental data available for particular impact conditions, i.e. faster and more massive particles, the corresponding equations of state (*EOS*) $\varepsilon(\rho, T)$ and $p(\rho, T)$ have to be derived from theoretical models like the Thomas-Fermi model mentioned in Section 2.1.3, in order to solve Equations 2.9 to 2.12.

2.1.3. High pressure equation-of-state

The total internal energy in Eq. 2.12 and the pressure are sums of elastic and thermal contributions, whereas the thermal contribution can be broken up into two parts: one part representing the thermal motion of the nuclei and the other part the motion of the electrons (Appendix A and Zel'dovich and Raizer (2002)).

$$\begin{aligned} \Delta E &= \Delta E_c + \Delta E_T \\ &= -\int_{V_0}^{V} P_c \, dV + E_t \end{aligned} \tag{2.22}$$

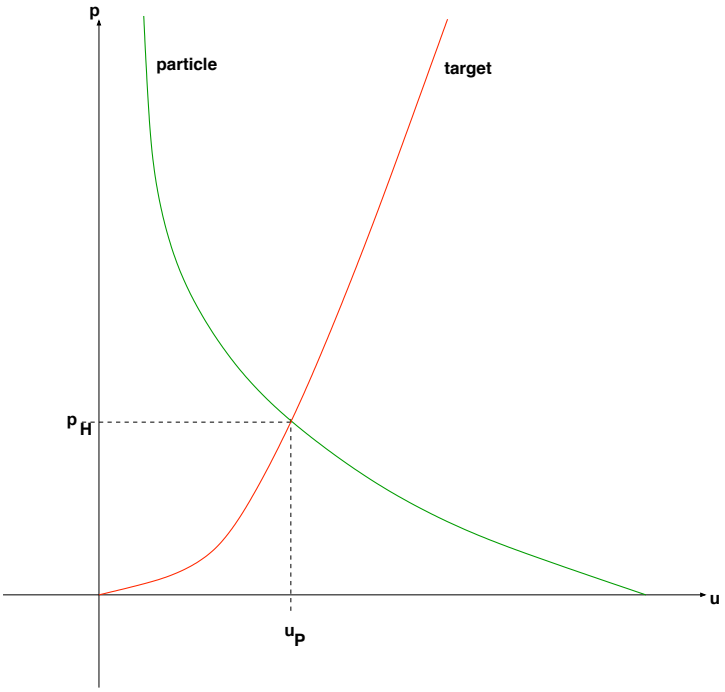

Figure 2.5.: Hugoniot curve (p, u diagram) for the impact of a dust particle on a target.

The total thermal energy $\varepsilon_{th} = (\varepsilon_t)_{atoms} + (\varepsilon_t)_{electrons}$ is the sum of the energy of the harmonically vibrating lattice $(\varepsilon_t)_{atoms}$ and the thermal energy of the electrons $(\varepsilon_t)_{electrons}$

$$(\varepsilon_t)_{atoms} = 3NkTD\left(\Theta(V)/T\right),$$
$$\frac{d\,ln\,\Theta(V)}{d\,lnV} = -\Gamma(V)$$

(Hornung and Michel, 1972), where $D\left(\Theta(V)/T\right)$ is the Debye function, Θ the Debye temperature, Γ the Grüneisen parameter, and N the number of atoms per unit weight.
For temperatures T ¡ 30,000 K, the thermal energy of the electrons is

$$(\varepsilon_t)_{electrons} \cong \frac{1}{2}\beta_0\sqrt{\frac{V}{V_0}}T^2, \tag{2.23}$$

with β_0 being the electronic specific heat constant.
Also the pressure is - analogous to the energy - a sum of three constituents

$$p = p_c + (p_t)_{atoms} + (p_t)_{electrons}\,. \tag{2.24}$$

The *thermal pressure of the atoms* is given by the Mie-Grüneisen *EOS* Eq. 2.17.
Furthermore, the *elastic pressure* is

$$\frac{dE_c}{dV} = -p_c, \tag{2.25}$$

while the *thermal pressure of the electrons* is

$$(p_t)_{electrons} \cong \frac{1}{2}\frac{(\varepsilon_t)_{electrons}}{V}. \tag{2.26}$$

To solve Eq. 2.8 to Eq. 2.10, one has to know the equation of state (*EOS*) for the compressed material.
The *EOS* describes fundamental thermodynamical properties of matter either in functional form like

$$f(x_1, \cdots) = 0, \tag{2.27}$$

where $x_1, \cdots$ are thermodynamical properties like volume or temperature, or in the form of graphs and tables (Fortov and Lomonosov, 2010). This information can be obtained using theoretical models or from fits to experimental data (Al'tshuler, 1965).

2.1.4. Experimental investigation of Hugoniot adiabatics

To derive the *EOS* of a material under high pressure experimentally, one has to measure two of the five parameters in Eq. 2.8 to Eq. 2.10. Depending on the method of the experiment listed in the following, the compression of the material, the pressure, shock wave velocity and the velocity of the shocked material can be measured. Shock wave data in a large range of conditions have been collected and put together to Hugoniot curves for a wide variety of materials (Al'tshuler et al., 1981; Fortov and Lomonosov, 2010; Ross, 1985).

Static methods

- Determination of the dependence *P(V, T=0)* by isothermal compression in diamond anvil cells. *(*$\sim$ Mbar*)*
- Measurements of the dependence *T(P)* with high pressure vessels or with melting experiments in laser heated diamond anvils
- Measurements of electrical and optical properties

Dynamic methods Shock wave experiments allow to study a large part of the phase diagram from the compressed solid to hot dense liquids, plasma, liquid vapour, and quasi-gas states. The experimental data on shock wave compression of solids and porous materials, as well as on isentropic expansion, cover by today nine orders of magnitudes in pressure and four ordersin magnitude in density.

- Explosive drivers ($p \sim 1\,\text{Mbar} - 10\,\text{Mbar}$)
- Spherical cumulative systems ($p < 100\,\text{Mbar}$)
- Underground nuclear explosions ($p < 100\,\text{Mbar}$)
- Laser driven shock waves ($p \sim 750\,\text{Mbar}$)
- Nuclear explosions ($p \sim 4000\,\text{Mbar}$)

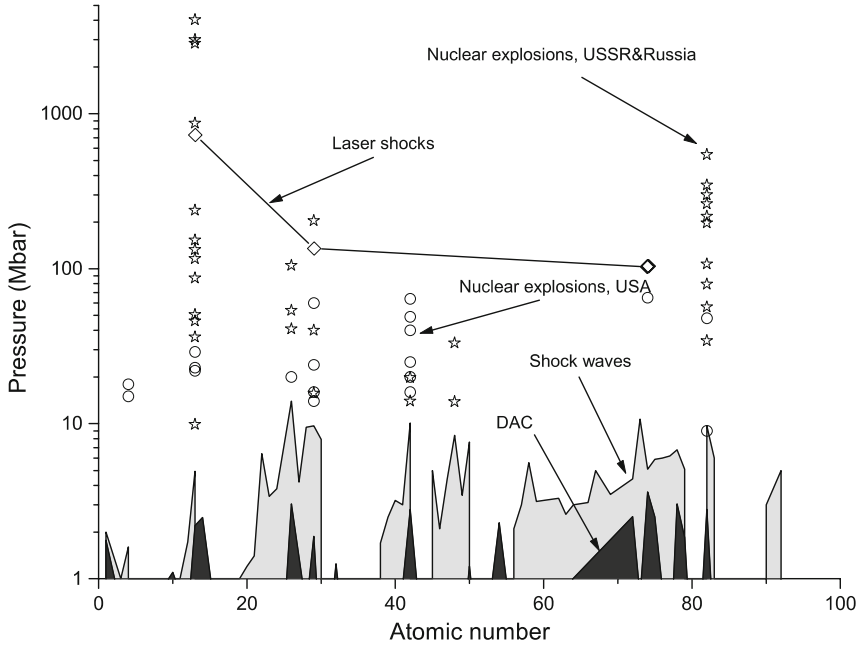

Figure 2.6.: Maximum pressures achieved by using traditional explosives (grey), lasers, static measurements with diamond cell anvils (black), and nuclear explosions (points) form. From Fortov and Lomonosov (2010).

Theoretical equation-of-state

There are several methods to solve the problem of a theoretical description of thermodynamical properties of matter at high pressures and high temperatures: classical and quantum mechanical methods (Gandel'man, 1966) , diagram techniques (Metropolis et al., 1953), Monte-Carlo simulations, and molecular dynamics methods. The disadvantage of these methods is that the applicability of each method is restricted to small regions in the phase diagram.

For particle impacts faster then 25 $\mathrm{km\,s^{-1}}$, a modification of the Thomas-Fermi-Model for very high high pressures and temperatures has been proven to to be useful (Metropolis and Feynman, 1949). In its original form, it is a semi-classical model, developed for approximate calculations of potential fields and charge densities in metals as a function of lattice spacing. The classical part assumes a Z-fold charged nucleus surrounded by a continuously distributed cloud of electrons with a radius of $R_0 = \sqrt[3]{3/4\pi n}$, where n is the atoms' number density (Thomas, 1927). The non-classical part describes the occupation of the continuous electron energy states by the Fermi-Dirac statistics.

At such conditions, the individual energy levels of electron shells of a solid broadens and shifts by collective interaction. Finally, they form a more or less continuous distribution of electronic states, populated according to the rules of Fermi statistics. This model had been modified for very high pressures and temperatures at which the pressure and energy distribution of the nuclei can be regarded as that of an ideal gas with only translational degrees of freedom. Further corrections for exchange and quantum effects are not required, because they are small for the conditions considered here (Hornung and Kissel, 1994).

Constructing Hugoniot curves for the whole range of impact conditions

To obtain Hugoniot curves for the whole parameter range relevant for dust particle impacts, i.e for velocities from 1 $\mathrm{km\,s^{-1}}$ to about 100 $\mathrm{km\,s^{-1}}$, experimental results must be combined with the theoretical calculations. The gap between the two ranges may be interpolated as shown in Fig. 2.7.

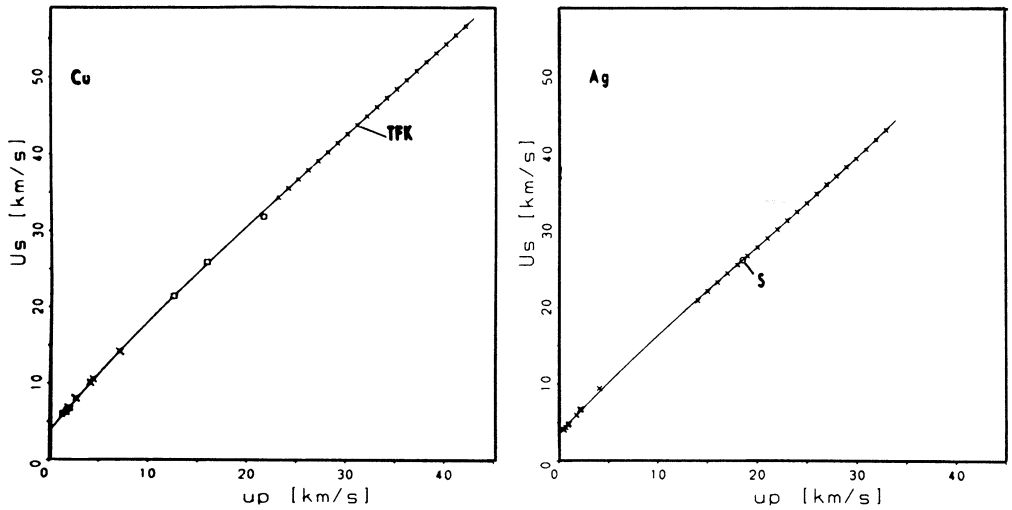

Figure 2.7.: Hugoniot curves constructed from experimental shock wave data and model calculations for copper *(left)* and silver *(right)* (Hornung and Kissel, 1994)

Thermodynamics

The thermal contribution $\Delta E_{T,i} + \Delta E_{T,el}$ to the internal energy is

$$\Delta E_T = \Delta E - \Delta E_c = \int_{T_0}^{T_S} \left(c_{v_{el}} + c_{v_i}\right)\, dT, \tag{2.28}$$

where $\mathbf{c_{v_{el}}}$ is the specific heat of the degenerated Fermi-system of electrons (given by the band model) and $\mathbf{c_{v_i}}$ is the specific heat heat of the ion core. This approach requires that the temperature is a meaningful quantity, i.e. the system is in local thermodynamic equilibrium (*LTE*). In this case, the corresponding entropy is

$$S = S_0 + \int_{T_0}^{T_S} \left(c_{v_{el}} + c_{v_i}\right)\, \frac{dT}{T}, \tag{2.29}$$

with S_0 being the entropy at standard conditions, i.e. $T_0 = 300\,\mathrm{K}$ and $p_0 = 1\,\mathrm{atm}$.

2.1.5. Isentropic expansion

After the impact, the compressed and heated gaseous material is assumed to be accelerated by the release of the pressure and to expand adiabatically into vacuum. The final state of the cloud is assumed to be given by an ideal gas

$$dE = -pdV = \frac{p}{n^2}\,dn, \tag{2.30}$$

where n is the number density of ions and neutral atoms. Thus, the state of the expanded gas can be determined by equating its entropy to the shock wave entropy

$$S_{gas}(n,i,T) = S_s \tag{2.31}$$

(Drapatz and Michel, 1974), where i is the ionisation degree and T the temperature, assumed to be equal for electrons and ions.
The gas entropy of the gas is the sum of entropies of its individual constituents, where each of which can be described by the ideal gas entropy

$$S_j(n,T) = k\left\{\frac{5}{2} - lnn_j + ln\left(\frac{2\pi m_j kT}{n^2}\right)^{\frac{3}{2}} + lnZ_j - T\frac{dlnZ_j}{dT}\right\} \tag{2.32}$$

(Hornung and Drapatz, 1979). Here,

$$Z_j = \sum_{E=0}^{I_0-\Delta I} g_i \cdot e^{\frac{E_i}{kT}} \tag{2.33}$$

is the partition partition function of ions or atoms, which can be computed from tabulated atomic level data.
I_0 is the ionisation energy and ΔI its lowering in a dense environment. The partition functions Z_j relate the entropy to the ionisation degree of the plasma for chemical equilibrium via Saha's equation (2.1).

2.1.6. Expansion time and expansion isentrope

If the expansion of the gas is approximated with a simple point explosion model, the expanding gas claud can be described as an sphere with a radius of the order $R = u \cdot t$ and the gas density decreases with

$$\rho = \frac{M}{4\pi R3/3} = \rho_0\left(\frac{t_0}{t}\right)^3 \tag{2.34}$$

(Zel'dovich and Raizer, 2002), where M is the mass of the gas sphere, ρ_0 is the initial density, R_0 is the initial radius of the sphere, and

$$t_0 \approx \left(\frac{M}{\rho_0 4\pi u^3/3}\right)^{\frac{1}{3}} = \frac{R_0}{0} \tag{2.35}$$

is the characteristic time scale.
The number density of atoms and ions tscales with time as

$$n(t) = \frac{3N_{tot}}{4\pi u_{exp}^3 \cdot t^3}. \tag{2.36}$$

Thus, the time scale of expansion can be expressed due to the number density as

$$t = (3N_{tot}/4\pi n u_{expt})^{1/3} \approx n^{-1/3}, \tag{2.37}$$

with $\{u_{exp} \sim \frac{1}{3} v_{impact}$ being the expansion velocity, which is of the same order of magnitude as the impact velocity (Arnaudeau et al., 1984).
Inserting Eq. 2.36 (n = n(t)) and Eq. 2.1 (i = i(n, T)) in Eq. 2.31 obtains the the equilibrium expansion isentrope.
Assuming the expanding sphere as an ideal gas with the same constant specific heat ratio γ the cooling can be described by

$$T = A(S) \cdot \rho^{\gamma-1} \sim t^{-3(\gamma-1)}, \tag{2.38}$$

where A(S) being a constant calculated from statistical mechanics and thermodynamics.

2.1.7. Relaxation times and freezing

In the expanding gas cloud, as described in Section 2.1.6, physical and chemical processes take place leading to exchange of translational energy, ionisation or chemical reactions. The characterisation of the extent of equilibrium in the system depends on the interplay of all these sub-processes and their relaxation times among each other and with the expansion time scale Eq. 2.37 (Hornung and Kissel, 1994). The partial processes are on one hand the ionisation and dissociation and their reverse processes, the recombination of ions and electrons, and respectively of atoms into molecules. On the other hand there is thermal contact, i.e. collisions between the constituents of the plasma: ions, electrons, and neutral atoms.

To determine the possible break-down of the equilibrium situation, one has to compare the relevant relaxation times τ_ν (Spitzer, 2006; Zel'dovich and Raizer, 2002) in comparison with the time scale t (Eq. 2.35). The instant of time at which a specific relaxing time starts to exceed the expansion timescale, i.e. $\tau_\nu \geq t$, is called *"freezing"* of the specific process.

Thermal relaxation due to collisions

- *Relaxation tine of exchange of translational energy between electrons and ions:*

$$\tau_{ei} = \frac{m_i}{m_e} \cdot \frac{(3kT)^{\frac{3}{2}} \sqrt{m_e}}{8\sqrt{2\pi}\, n X_e e^4 \ln\lambda}, \tag{2.39}$$

where m_i, m_e are mass of ions and electrons, T is the temperature, n the number density of ions plus atoms, X_e the degree of ionisation, i.e. number of electrons, and $\ln\lambda$ the Coulomb logarithm.

- *Relaxation of translational collision between electrons and electrons:*

$$\tau_{ee} = \frac{\sqrt{m_e}\,(3kT)^{1/3}}{8 \cdot 0.174\pi\, n X_e e^4 \ln\lambda} \tag{2.40}$$

- *Relaxation time for ion-ion collisions:*

$$\tau_{ii} = \frac{\sqrt{m_i}\,(3kT)^{3/2}}{8 \cdot 0.174\pi\, nX_e e^4\, \ln\lambda} \tag{2.41}$$

- *Relaxation time for ion-neutral and neutral neutral collisions ("two-body-collisions"):*

$$\tau_2 = \frac{1}{\sqrt{2} v_{th} n\sigma}, \tag{2.42}$$

with $v_{th} = \sqrt{\frac{8kT}{\pi m_i}}$ being the thermal energy and σ being the gas dynamic cross-section.

(2.43)

Disturbance of the ionisation equilibrium (*Saha-equilibrium*)

- *Characteristic life time of a free electron (recombination time):*

$$\tau_{rec} = \left| \frac{i}{\left(\frac{di}{dt}\right)_{rec}} \right|, \tag{2.44}$$

with i being the degree of ionisation

- *Characteristic time for the net change of i under Saha-equilibrium (ionisation minus recombination):*

$$\tau_{eq} = \left| \frac{i}{\left(\frac{di}{dt}\right)_{eq}} \right| \tag{2.45}$$

2.1.8. Non-equilibrium expansion and residual ionisation

The leading mechanism for the recombination in this stage is three body recombination (Kuznetsov and Raizer, 1965)

$$\left(\frac{di}{dt}\right) = \beta \cdot i^3 \cdot n^2, \tag{2.46}$$

with $\beta = 2.3 \cdot 10^{-8} \cdot T^{-9/2}$ being the recombination coefficient (Makin and Keck, 1963). Dielectric recombination is of minor importance, since the characteristic time for the stabilizing radiation is to long. Applying the principle of microscopic reversibility, ionisation and recombination rates are coupled by the equilibrium constant $\frac{N_+}{N_0} n$ in Eq. 2.1. Together with the energy conservation this leads to a set of differential equations to be solved numerically.

The point in time defined after which the degree of ionisation will not drop by more then $\approx 10\%$ to the asymptotical final value is called *"freezing point"*. Numerical calculation showed that this point occurs at $t < 10^{-9} s$, even for larger particles (Drapatz and Michel, 1974). Furthermore these calculations showed, that for velocities above $40\,\mathrm{km\,s^{-1}}$ the residual ionisation is independent of the size and mass of the particles. Whereas for impact velocities below $15\,\mathrm{km\,s^{-1}}$ the residual ionisation is not determined by the mass or volume of the target: At this velocities complete vaporisation takes not place and at least partially the impacted particle remains as a molten droplet: Thus, a different model will be necessary and will be described in the following section.

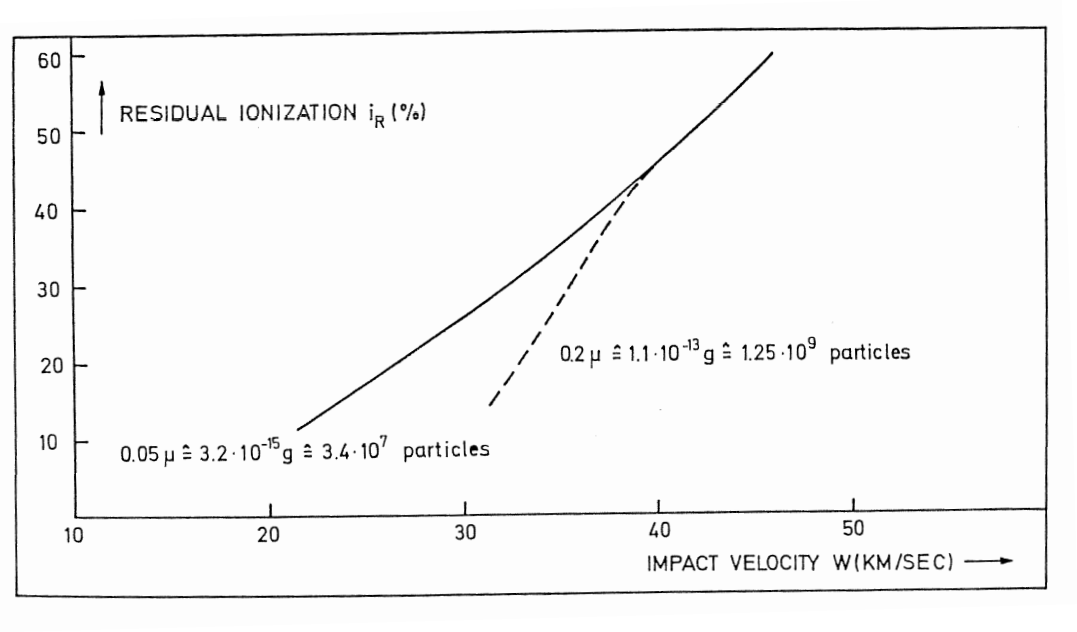

Figure 2.8.: Calculated residual ionisation as a function of impact velocity for iron particles of different mass (Drapatz and Michel, 1974)

2.1.9. Surface ionisation: A Model for low velocity impact

Drapatz and Michel (1974) proposed that at impacts speeds below $10\,\mathrm{km\,s^{-1}}$, the impact plasma results predominantly from ionisation of the surface. In this model, the dissipated specific energy is insufficient to vaporise the particle as such. As a consequence, the particle fragmentises. into little droplets with temperatures under 4000 K. During the cooling time $\tau \approx 10^{-7}s$, mainly impurities with low ionisation potentials, i.e. alkali metals, are expected to be ionised after diffusion through the liquid material to the surface from a depletion boundary layer as seen in figure Figure 2.9. The thickness of this layer is determined by

$$< x > = \sqrt{2D(T)\tau} \tag{2.47}$$

where $D = 5 \cdot e^{\frac{-5000}{T}}\ \mathrm{cm^2 s^{-1}}$ is the diffusion coefficient that has been achieved by experiments. Plasma ions are light species with low ionisation potentials. Thus in the case of Fe particles, one expects to observe primarily alkali contaminants instead of the bulk material. The mass ΔM of atoms of the main constituent of the particle, for example iron for laboratory experiments, evaporated during the cooling time τ depends on the vapour pressure p_s of this material and can be calculated with help of the Hertz-Knudsen-equation

$$\Delta M/\tau = 4\pi r^2 p_s \sqrt{m/2\pi kT} \tag{2.48}$$

The ionisation degree of the resulting cloudlet is given by the Saha-Langmuir-Equation

$$n_i/n_0 = g_i/g_0 \cdot exp\left(\frac{\Phi - I}{kT}\right) \tag{2.49}$$

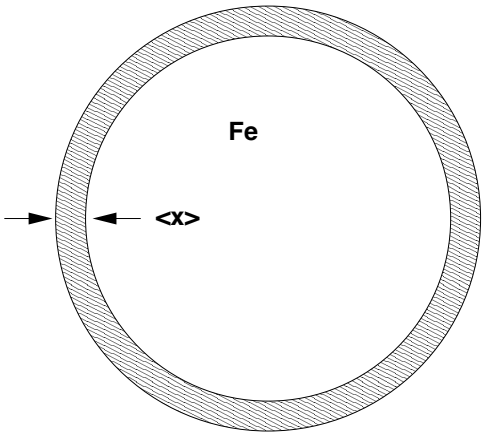

Figure 2.9.: Interphase $< x >$ of the molten droplet

where Φ is the work function of main constituent, I the ionisation potential, and g_0 and g_i are the statistical weights of atomic and ionic species.

(2.50)

With this model theoretical mass spectra can be calculated. Two examples of the calculated mass spectra by Drapatz and Michel (1974) are shown in Figure 2.10. For their calculations they assumed that the particle contains 3 atom percent of be alkali impurities. According to these calculations the main component Fe is not represented at all in the spectra for velocities under 7 km/s.

2.1.10. Target ionisation

In the target the situation as much more complicated: The shock wave expands to relatively large distances while it is fading to lower pressures. As a consequence all possible precesses take place - from volume ionisation at the very point of the impact to a relatively small disturbance of the solid surface at larger distances from the impact spot, which also may produce ions, as it is mentioned in Section 2.1.9 and other excitation methods (Krueger, 1983; Kissel and Krueger, 1987)

2.1.11. Other impact models

The predictions made by the shock wave ionisation model described above are contradicted by the results of measurements made both in the lab and by space instruments in various aspects like:

- Evaporation rates for slow impacts - for velocities $< 5\,\mathrm{km\,s^{-1}}$- predicted by the Hertz-Knudsen-Equation 2.2.2 are orders of magnitudes to low (Knabe and Krueger, 1982)
- Lines from the particle's bulk material occur at velocities slower than predicted by the model (Dalmann et al., 1977).
- Abundance of H^+, H_2^+ and H_3^+ lines in the spectra
- Occurrence of large molecules and clusters, which are contradicted by the high temperatures in an equilibrium plasma (Knabe, 1983)

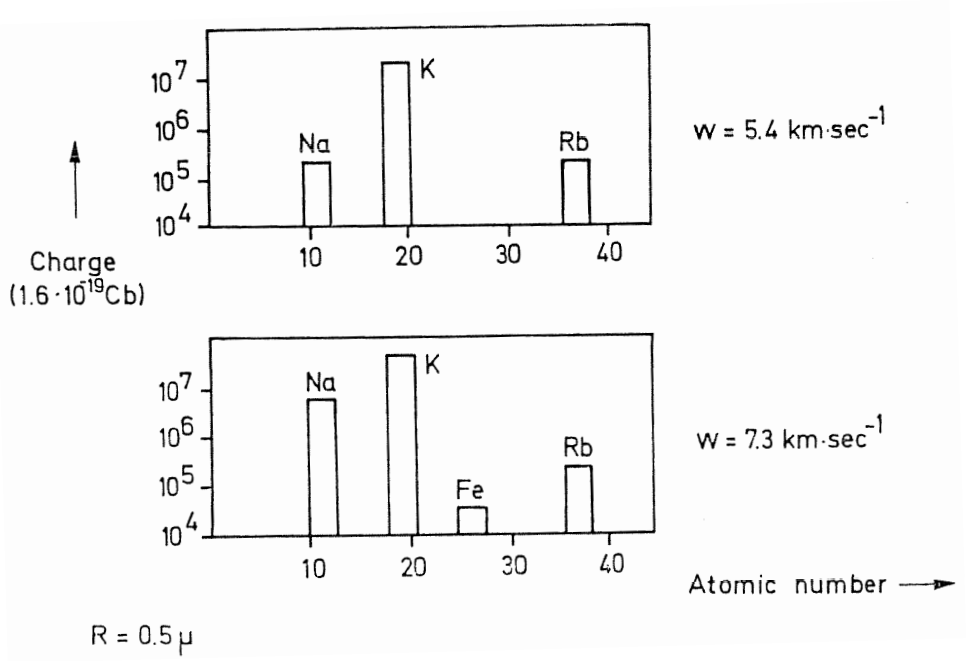

Figure 2.10.: Shots with iron particles on a tungsten target: Calculated mass spectrum of ions for an assumed alkali content of 3% (Drapatz and Michel, 1974)

Non-Equilibrium Desorption

There are several techniques of transient formation of ions and molecular ions from solid surfaces. These methods transfer energy either to the lattice or the electronic system of the solid body in various energy ranges. A semi-empirical model , which describes the release of preformed ions from the surface as a fast, far-from equilibrium dissipation of energy *on the surface* of a solid was developed by Knabe and Krueger (1982), Krueger (1982) and Krueger (1996). The starting point for this approach was the apparent similarity of some aspects time-of mass spectra of views obtained from dust impacts and non-equilibrium processes , such as laser desorption and ion bombardment (Fürstenau and Hillenkamp, 1981): For example the abundance of some ion species is nearly independent f the method of primary excitation. According to this model, the strength of the excitation determines only the yield of the ion formation but the composition of the mass spectra. The mass spectra therefore depend only on the chemical and physical conditions of the surfaces of target and particle. Thus, the variation of the excitation parameters change hardly the ion types but determine the quantity of ions released(Auer, 2001).

Effect of the particle's charge on the ionisation process

In this model the consequences of the positively charging of an impacting particle is considered by taking emission processes into account, which may occur in the gap between the approaching charged particle and a metal target (Sysoev et al., 1997):

When a positively charged particle is approaching the target surface a high-voltage electric field is formed. Without considerations of aberrations of the particle's shape from a perfect

sphere this field is given by

$$E = \frac{2q}{d^2} \tag{2.51}$$

where d is the distance between particle and target. The actual field will be amplified by the roughness of the particle's and and target's surfaces. This can be represented by a coefficient β, which may be equal to $\beta \sim 10 - 100$:

$$E^* = \beta \cdot E \tag{2.52}$$

This field can be approximate by numerical calculations. If this field exceeds the threshold for emissions electrons from the target begin to bombard a small area of the particles surface down to the depth of about $100\mathring{A}$. This bombardment will lead to desorption of atoms and heating of a small area of a near- surface area of the microparticle.At the distance of approximately $1\mu m$ the temperature of the hot spot will be about 500-800K, the most intensely heating takes at gap sizes from 08. to 0.4 μm place. There temperatures can reach 25000K, depending on the charge of the particle. Further on, both - the electric field intensity and the auto-emission current decrease due to the reduction of the particle's potential as the result of its decharging.

In this model, four mechanism there are four mechanism of ion production during the course of the impact

1. *Surface heating due to electron current*
   After the onset of heating but before the moment of vapour phase formation there is already some surface ionisation. This efficiency of this ionisation increases with the lowering of the potential barrier due to the electric field. The most part of ionised species during this phase will be alkali metal ions. Due to their low ionisation potential and low boiling point it is assumed that Na and K will be completely evaporated from the surface at this stage of the impact.

2. *Thermal ionisation after vapour formation (Surface Ionisation)*
   Further on the temperatures at hot spot will increase and exceed the boiling point of all of the particle's materials. At this conditions local thermodynamic equilibrium (*LTE*) is estimated and the ionisation degree can be calculated with the help of Saha's equation (Eq. 2.1).

3. *Ionisation by auto-emission electrons*

4. *Shock wave ionisation*
   After the event of the impact there will be shock evaporation as described in Section 2.1.1 to 2.1.10.

2.2. Laser ionisation

In this thesis ions produced by the incident of 5 ns laser pulses of 355 nm wave length were investigated with a linear time-of-flight mass spectrometer on targets with different chemical and physical properties and compared to measurements with hypervelocity dust particles impacting on metal targets. In the next section a short overview of the process of laser ionisation will be given: firstly the interaction of the laser light with a solid body, then the transformation of the light's energy into heat and subsequently the evaporation and eventual ionisation of the target material.

2.2.1. Interaction of light and matter

The interaction between laser light and matter depend on the parameters of the laser beam as well as on the physical and chemical properties of the material.The laser light is characterised by the wavelength, intensity, spatial and temporal coherence, its polarisation, the angle of incident and the pulse duration. The defining properties of the solid are its chemocal composition and the microstructure of the lattice and the topography of the surface. These parameters determine coupling of the laser energy into the solid body lattice and the type of the resulting elementary excitations of the atoms or molecules and the interactions between them.

Excitation mechanisms and their relaxation times

The primary interaction between light and matter are always non-thermal. In solids, this can result in different types of electronic excitation, i.e. inter- and intraband excitations, excitons, plasmons etc., excitation of phonons, polaritons or vibrational excitation. Furthermore there may be localised or non-localised electronic or vibrational states related to defects, impurities or the solid surface itself (Bäuerle, 1996).

At low and moderate light intensities electronic excitation is dominant. At higher intensities, thus at higher laser energies or shorter pulse durations the direct coupling of the energy into the lattice due to excitation of vibrations become more and more important and even shock waves can occur.

- **Inverse Bremsstrahlung:** In metals the dominant absorption process involves free-free transitions (Bloembergen, 1993): A electron in the conduction band increases its energy by the energy of a photon

$$E = \frac{c \cdot h}{\lambda}, \tag{2.53}$$

with c being the speed of light, and λ the wave length, while the moment balance is maintained by a simultaneous collision with another particle, i.e. the ion core.due to the absorption the temperature of the electron increases. By electron-phonon interaction the absorbed energy is coupled into the lattice. Typical transfer times between hot electron and the lattice are of the order of one picosecond for most materials. This short electronic relaxation time τ_e of the highly collisional electron plasma describes the reflectivity as well as the penetration depth of the transmitted light. Typical penetration depth for visible light are between $3\,\mu$m to $10\,\mu$m- in this thin layer the initial heat production takes place. Thermal conduction will carry this heat deeper into the material. This process will be described in the following paragraph

- **Collisions:** Ionisation is also produced by collisions of energetic ions with excited atomic and molecular species (Amoruso et al., 1996).

- **Multiphoton ionisation:** At sufficiently high laser intensities, multiphoton ionisation of ground-state neutral species as well as photoionisation of excited atoms and molecules occurs. These processes are dominant in insulating materials.

- **Avalanche ionisation** At sufficiently high laser-light intensities, the rate of electron excitation can overtake the rate of energy loss due to the generation of phonons. The electrons then become highly excited and attain sufficient energy to generate secondary electron-hole airs . because of the positive feed-back of this process, very high electron densities can be achieved. Under these conditions, even originally highly transparent materials can become strongly absorbing and, as a consequence, *optical breakdown* and *plasma formation* occur.

The various elementary excitation are coupled to each other via anharmonic or higher order dipolar interactions. The global effects of these excitation processes are rather similar for many materials: the resulting heating leads to melting, evaporation and plasma formations. These effects will be described in the following sections.

2.2.2. Thermalisation and heat transport

The excited electrons transfer their heat to the lattice within a few picoseconds within the optical absorption depth the degradation of the ordered and localised primary excitation energy into heat involves three steps (von Allmen, 1987):

1. Spatial and temporal randomisation of the morion of excited particles.

2. Collision time or momentum relaxation time, being extremely short

3. Energy equipartition, which involve a large number of elementary collisions and intermediate states.

Involved in this process are several energy transfer mechanisms, each with a characteristic time constant. For the description of the thermalisation the intricacies of elementary relaxation channels are ignored and the equipartition is characterised by an overall relaxation time τ_e.

The excited electrons transfer their energy to the lattice within a few picoseconds and heating begins within the optical absorption depth of the material $1/\alpha$, where α is the optical absorption coefficient. Thermal conduction carry heat deeper into the material. The thermal diffusion length is given by

$$l_T = 2\sqrt{D\tau_P}, \tag{2.54}$$

where D is the thermal diffusion constant and τ_P the pulse duration.

For pulse durations of about $\tau_P \approx 100\,\mathrm{ps}$ the diffusion length l_T is comparable to the absorption depth of the light in the material. If l_T becomes smaller than $1\frac{1}{\alpha}$, the material will be heated down to $1/\alpha$, independent of pulse duration. In ablation of multielemental targets, congruent evaporation can only be guaranteed if this condition is met, hence the use of fast UV-laser sources is favored.

2.2.3. Temperature distributions

The temperature distributions induced by the absorption of the laser radiation can be calculated on the basis of the *Heat Equation*. I the most general case, the temperature is a function f bot, the spatial coordinates **x** and the time t.With fixed laser parameters the distribution is defined by the optical absorption within the irradiated zone, on the transport of the heat, and , if relevant on the transforming of enthalpies for crystallisation, melting, vaporisation, and on chemical reaction enthalpies. in absence of heat transport due to convection or thermal radiation, the *Heat Equation* in the a coordinate system fixed with the laser beam is given by

$$Q(\mathbf{x},t) = \rho(T)c_P(T)\frac{\partial T(\mathbf{x},t)}{\partial t} - \nabla\left[\kappa(T)\nabla T(\mathbf{x},t)\right] + \rho(T)c_P(T)\mathbf{v_s}\nabla T(\mathbf{x},t), \tag{2.55}$$

where $\rho(T)$ is the mass density, $c_p(T)$ id the specific heat at constant pressure, $\mathbf{v_s}$ is the velocity of the substrate relative to the heat source Q(i.e. the scanning celocity of the laserbeam). If the substrate is uniform and isotrpic, the themal properties can be characterised by a single thermal conductivity κ and a single heat diffusivity D, which are related by

$$D = \frac{\kappa}{\rho c_P}. \tag{2.56}$$

The heat equation becomes linear if the material parameters are independent of the temperature.

2.2.4. Vaporisation

In order to remove an atom from a solid

When the laser power density is sufficient, the increase of the temperature leads lead to a melting or even vaporising of at least part of the irradiated material.

The resulting vapor consist of clusters, molecules, atoms, ions and electrons.

The energy required to remove an atom from the surface can be estimated by

$$\Delta H \approx \frac{\Delta H_V}{N_s},$$

where ΔH_V the the enthalpie of evaporation and N_s is the (atom) number density.

The species leaving the surface thermalise due to collisions within a few mean free paths, typically within a few microns from the surface. This region in called *Knudsen layer*. Beyond the Knudsen layer the cloud is in internal equilibrium with a temperature different from the surface. A strong forward direction of the motion of the ions is caused by strong temperature and pressure gradients in axial direction of the plume. The properties of the vapor follow from the conservation mass, momentum, and energy - in any case, the species leaving the surface generate a recoil pressure onto the substrate.

Similar to the impact ionisation plasma the expansion of the vapor cloud can be described as the simplest possible model by an adiabatically expanding gas.

The rate of the thermal conduction through the lattice defines the material removal from the surface, this means, according to Fick's law of diffusion, that the threshold fluence is proportional to $\sqrt{\tau}$.

Because of momentum conservation, the species evaporated from the surface cause a recoil pressure.

Table 2.1.: Enthalpies of evaporation and ionisation energies of the most important species investigated in this thesis. The values are given in kJ/mol, the values in brackets in $eV/atom$

	H	C	O	Na	Mg
H_V	0.5 (0.005)	715 (7.4)	3.14	98 (1)	128
I_1	1312 (13.6)	1087 (11.3)	1314	496 (5.1)	738
I_2	-	2353 (24.4)	3388	4562 (74)	1451

	Si	K	Fe	Cu	Ag	Au
H_V	359	77 (0.8)	34 7	300	255	330 (3.4)
I_1	787	419 (4.3)	763	746	731	890 (9.2)
I_2	1577	3052 (32)	1562	1958	2070	1980 (21)

2.2.5. Plasma formation

The plasma formation strongly depends on the properties of the emerging cloud (i.e. temperature and density) and the laser parameters, such as wave length or pulse duration, and can be described as a two-step process (Amoruso et al., 1996):

1. **Ionisation of the hot vapor:**
   Just as well as in the case of the impact process the degree of ionisation of the gas cloud emerging from the irradiation by the laser light is determined by the *Saha equation* (Eq. 2.1).

2. **Interaction of the plasma with the laser light:**
   In a partially ionised gas, the light is absorbed by thermally excited atoms *(bound-free absorption)* and ions *(bremsstrahlung absorption)*.This leads in the following to strong heating and further ionisation of the cloud in the vicinity of the target. With the onset of plasma formation, characterised by the threshold intensity $I_p = I_p(\lambda)$, the coupling between the laser light and the substrate becomes strongly nonlinear. Furthermore the absorbing plasma shield the substrate against the incident laser light.

With increasing irradiance temperature and enthalpy of the vapor increase. Also the absorption heats the the plume, leading to even more absorption. This positive feedback results to the evolving of a plasma even at light fluxes below the threshold for a breakdown in a cold gas (von Allmen, 1987), with typical irradiances for Nd-lasers of about $10^8 W/m^2$. Once, the plume is fully ionised, the absorption is dominated by *inverse bremsstrahlung*.

For laser set ups with pulse durations of several ns, the degree of ionisation of the plasma is for most materials close to unity (Willmott and Huber, 2000)

2.2.6. Pulsed-Laser Ablation

Material removal due to a short incident of an intense pulse of laser light is *termed pulsed-laser ablation*. Under these conditions the material removal takes place far from equilibrium

and permits to widely suppress the dissipation of the excitation energy beyond the during the pulse ablated volume. This requires that the thickness of the ablated layer per pulse, Δh is of the order of either the heat penetration depth $l_T \approx 2\sqrt{D\tau_l}$, or the optical penetration depth, $l_\alpha = 1/\alpha$:

$$\Delta h \approx max\left(l_T, l_\alpha\right),$$

which with many materials can be fulfilled reasonably well with UV-lasers and ns pulses

- **The threshold fluence Φ_{th}:** The threshold fluence above which a significant ablation will set on, decreases with increasing absorption coefficient and is in the order of 0.5 ro $2Jcm^{-1}$ for most inorganic insulators
- **Ablation rate:** The total layer thickness ablated per pulse depends on properties of the ablated material as well as on the laser parameters: the photon energy, the laser fluence, the size of the focal spot, the heat or optical penetration depth, enthalpies of vaporisation and so on.
- **Influence on the spot size:** The size of the illuminated spot $2r_0$ determines the expansion of the plasma plume. the transport of the ablated species as well as the attenuation of the incident laser light are thereby related to r_0.Also the ablation rate is, below a spot size of about 80 μm, higher for smaller spot sizes.

The velocities of the ablated species is of the order if 1 to 10 μm/ ns. Thus, for lasers with pulse duration below pico- or even femtoseconds almost no plasma plume can develop and plasma shielding would reduced or even avoided. With pulses as short as that , the ablation rate becomes independent from the size of the focal point.

2.2.7. Vapor and plasma properties

As already mentioned above, the properties of the resulting plume depend on the laser parameters as well as on the optical and chemical properties of the target. According to the laser power density the plume can be characterised as follows:

- 10^4 to 10^7 Wcm^{-2}: Vaporisation of the material without any significant ionisation
- $> 10^7$ Wcm^{-2}: Amount of ions is increasing, a plasma emerges. The temperature of the ions is about 10^4 K. The plasma velocity is below the speed of sound.
- $> 10^7$ Wcm^{-2}: The plasma becomes strongly ionised and the plasma frequency ω_p can exceed the laser -light frequency. Thus, the plasma becomes metall-like and absorbeds the light within a thin layer. Subsequently the temperatures can reach mor than 10^5K and explosive propagation of the plasma with supersonic waves is observed. These detonation waves move towards the laser beam and drives shock waves into bot the medium and the substrate (Bäuerle, 1996)

Plasma has a tendency towards electrical neutrality: The typical distance over which significant charge separation can occur is termed *Debye shielding distance* or *Debye length* and defined by (Spitzer, 2006)

$$r_D = \left(\frac{kT}{4\pi n_e e^2}\right)^{1/2} = 6.90\left(\frac{T}{n_e}\right)^{1/2}. \tag{2.57}$$

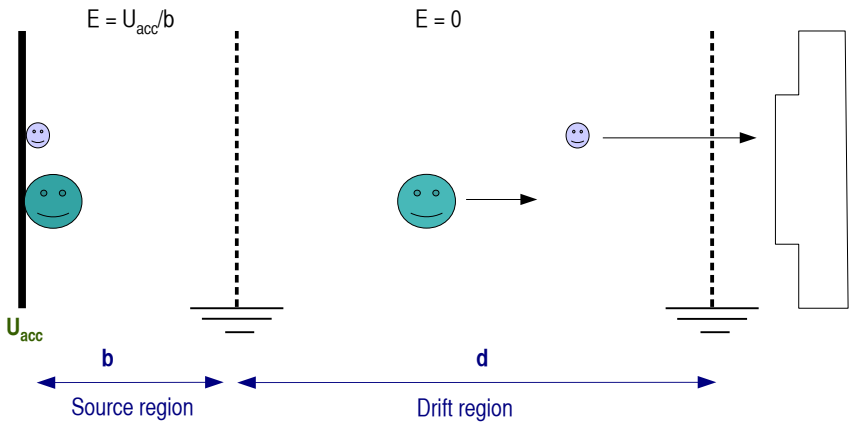

Figure 2.11.: Simplest time-of-flight mass spectrometer: An acceleration distance b between the source plate and a - in this case - grounded grid, a drift region d, which is defined by two grids, and an ion detector.

This measure plays also a role in the question, whether and how deep an electrostatic field can reach into the plasma in oder to separate and accelerate ions toward a detector. Thus, the debeye length and its linked valies will have an influence of the measured signals in an *TOF* mass spectrometer.

2.3. Time-of-flight mass spectroscopy

The basic idea underlying time-of-flight (*TOF*) mass spectroscopy is to analyse the composition of a substance by (Thomson, 1913)

1. *transforming* all or a part of the components of a sample to ions,
2. *accelerating* the ions in an electric field to a constant energy, and
3. *separating* the ions with different mass to charge ratios by means of their different times-of-flight over a field free drift distance.

Thus, a time-of-flight analyser consists in principle of a short source extraction region, usually of the size b of the order of a few centimeters, a drift region d and an ion detector as shown in Figure 2.11. The electrical field in the source region is defined by a potential difference between the source backing plate and a grid in front, and their separation distance b from each other. The voltage is either applied on the plate, then of the same polarity as the ions to be recorded, or on the grid with the opposite polarity. After being accelerated by the electric field $E = U_{acc}/b$ the charged particles cross a field free drift region d with velocities inversely proportional to the square root of their masses. Therefore lighter ions have higher velocities than heavier ones and reach the detector earlier. The detected output current, measured at the ion detector as a function of time can easily be converted into a mass spectrum.

A mass spectrum is a plot of relative intensity of the signal over the ratio m/q of mass to charge of the ions. This plot can be used to deduce the chemical structure on a compound.

In addition to this very basic setup, time-of-flight mass spectrometers may incorporate multiple acceleration regions, electrostatic energy analysers, reflectors or other energy-focussing devices to improve mass resolution.

2.3.1. Function principles

In the simplest case of ions emerging from the backing plate with zero initial energy, those ions are accelerated through the entire source region, reaching a uniform final energy (Cameron and Eggers, 1948)

$$\frac{1}{2}mv^2 = q \cdot U_{acc} \qquad \text{with,} \tag{2.58}$$

with U_{acc} being the accelerating potential, m the ion's mass and v the ion's final velocity. Thus, ions will cross the drift distance d with a constant velocity v and reach the detector in the time

$$t = \sqrt{\frac{d^2}{2qU_{acc}}} \cdot \sqrt{m} \tag{2.59}$$

which depends upon the square root of its mass. Regardless of the relative sizes of the acceleration or drift regions, or whether any other accelerating or decelerating regions like reflectors or Einzel lenses are utilised, the mass scale can be described as

$$t = \mathbf{b} + \mathbf{a} \cdot \sqrt{m}, \tag{2.60}$$

where the *stretch parameter a* is the proportionality constant, which is in principle determined by the physical set up of the instrument. The *shift parameter b* represents any time offsets between the triggering point and the start of the spectrum due to the production process of the ions, triggering or other electronic effects.

2.3.2. Calibration of time-of-flight mass spectra

To be able to convert the detector output current, which represents the relative intensity of the signal as a function of time, into a mass spectrum, one has to determine the two parameters a and b in equation 2.60. This can be done by various methods :

- *Approximating the parameters by fitting to two assigned lines:* By assigning two mass lines t_1 and t_2 to masses m_1 and m_2 one can derive the parameters a and b from Equation 2.60:
$$t_2 - t_1 = a\,(\sqrt{m_2} - \sqrt{m_1})$$
- *Approximating the parameters by fitting to n assigned lines:* If there are n assigned mass lines $t = \{t_1, t_2, \cdots, t_n\}$ corresponding to masses $m = \{m_1, m_2, \cdots, m_n\}$ Eq. 2.60 is overdetermined to the slope a of the function $t(m)b + a \cdot \sqrt{m}$ can be approximated with a least square fit (see Fig. 2.12).

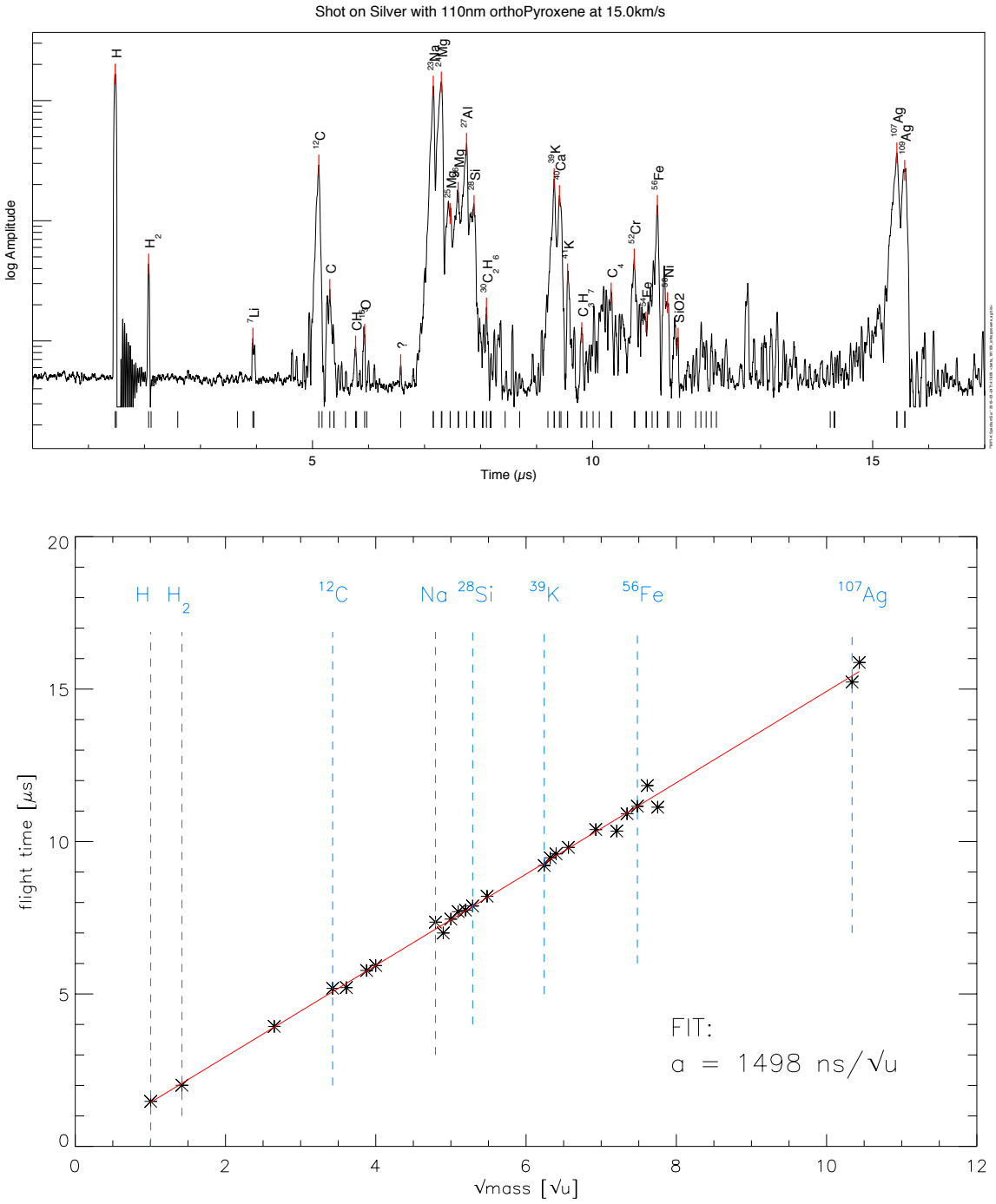

Figure 2.12.: Determination of the stretch factor a with a least square fit of the measured mass lines with their assigned masses. *Above:* The spectrum with the assigned lines. *Below:* Plot of the measured arrival times as a function of $\sqrt{\mathbf{m_i}}$ with the fitted slope *a*

Cross-Correlation with template spectra

Another possibility to calibrate time-of-flight mass spectra and assign masses to lines automatically is the cross correlate the measured signal with a theoretical template spectrum (Lavila, 2002).

This can be used for finding the shift parameter b or the stretch parameter a or both parameters. For this a theoretical spectrum is constructed by

1. Calculating the theoretical mass lines $\{t_{j,1}, t_{j,2}, \cdots, t_{j,n}\}$ for given parameters b_j and a_j with the equation
$$t_{j,1} = b_j + a_j\sqrt{m_i},$$
with $i = 1, 2, \cdots, n$, n being number of lines in the template spectrum and $j \in \mathbb{N}$.

2. Broadening the theoretical lines by a reasonable extent and distribution like for instance a gaussian distribution.

3. Weighting the lines by the likelihood of their abundance.

Then the cross correlation for these $t_{i,j}$ with the measured lines $\{t_{meas,1}, t_{meas,2}, \cdots, t_{meas,k}\}$ is been calculated by

$$(t_{meas} * t_j) \hat{=} \sum_{i=n}^{i=1} t_{meas,i} \cdot t_{j,i},$$

with $t_{i,j} = b_j + a_j\sqrt{m_1}$, $b = \{b_1, b_2, \cdots, b_l\}$, $a = \{a_1, a_2, \cdots, a_l\}$ and $l \in \mathbb{N}$.

The maximum of the $(t_{meas} * t_j)$ then represents the most likely combination of the stretch parameter a and the shift parameter b.

2.3.3. Mass resolution

In a mass spectrometer the mass resolution is defined as the ratio of the mass m of the ions of one specific species to the deviation in the mass Δm (Cotter, 1997).

$$\frac{m}{\Delta m} = \frac{t}{2\Delta t} \tag{2.61}$$

This resolution equation can be derived by a rearrangement of Equation 2.58 and its derivative

$$\begin{aligned} dm &= 2t\frac{2qU_{acc}}{d^2}dt \\ \Rightarrow \frac{m}{dm} &= \frac{t}{2dt} \end{aligned}$$

The resolution between ions of masses m_1 and m_2 will then be determined by the width of the mass peaks. This width depends on several aberration factors, which are caused by time, space and the initial energy distribution (Mamyrin, 2001).

Aberration due to the forming process of the plasma

1. Energy spread in the initial plasma cloud due to its formation process and finite thickness.
2. Broadening due to the angular spread in the ions' trajectories.
3. Effect of the initial velocities of the ions for example due to the expansion of the plasma cloud. So even if the ions form in the same source plane, they can have different directions in motion.
4. Differences in the times particular ions are affected by the accelerating field due to shielding within the plasma cloud.

Aberration due to the physical set up of the instrument

1. Deviation of the source, grids and detector planes from perpendicularity or parallelism to the instrument axis.
2. Effective depth of the ion detector, for example the mircrochannel plate (MCP).
3. Broadening of the detector output current pulses induced by electron avalanches in the MCP and in the course of the amplification by any other amplifiers.
4. Effect of stray fields in the field electrode grids.

The simple *TOF* instrument used for this thesis was designed and optimised in such a way that the peak shape and thus the resolution are primarily governed by the initial properties of the plasma cloud.

Besides the fact that the peak shape and its width can be used for investigating the properties of the initial plasma cloud (see Section 2.3.4), this implies that the resolution can be approximately be represented by

$$\frac{m}{\Delta m} = \frac{qUacc}{\Delta(qU_{acc})} = \frac{U_{acc}}{\Delta U_{acc}}, \tag{2.62}$$

with ΔU_{acc} being the stability of the acceleration potential. Thus, increasing the acceleration voltage for a given energy spread reduces naturally the effect of the latter on peak widths and increases the resolution of the instrument.

2.3.4. Peak Shapes and a model for the ion temperature

Molecular beams as an analogon for the situation in a TOF mass spectrometer

The set up of a molecular beam source can be regarded as an analogon for the situation of a linear time-of-flight mass spectrometer, because in both cases a beam of ions with a preferred direction of motion is produced.

In the case of time-of-flight mass spectrometers this is achieved by accelerating the ions using an electrostatic field (see Section 2.3.1). Whereas for molecular beams a simple selection of molecules or ions, which are effusing from a gas supply with a specific direction of motion, leads to a directed beam.

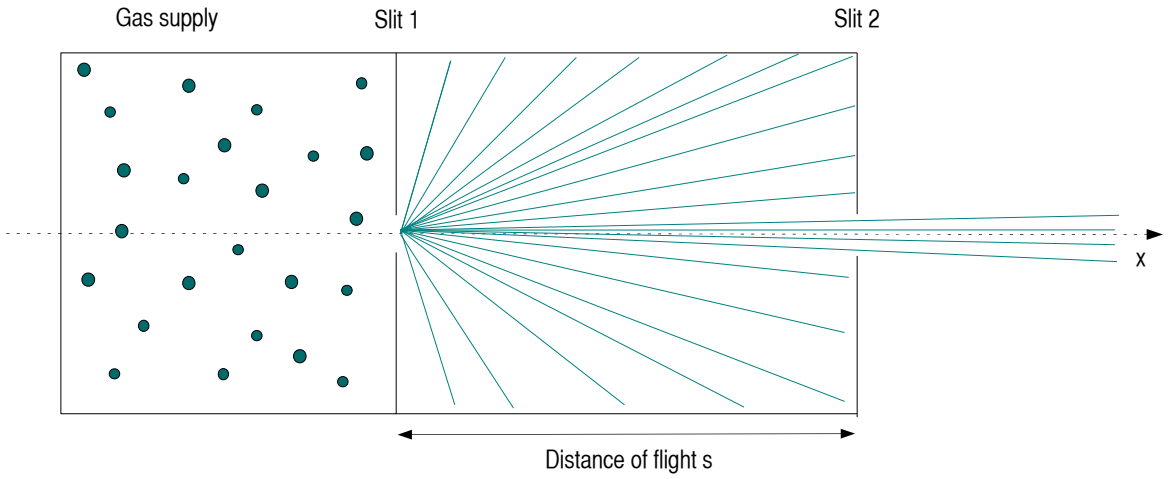

Figure 2.13.: Molecular beam source

For molecular sources theoretical models exist, which can be used to understand the formation of peaks in a time-of-flight mass spectrum and how their shapes relate to ion properties like energy.

Theoretical gain in intensity

Molecular beams are produced by effusion of gases through an orifice. The molecules are effusing from a vessel containing a gas into an evacuated space through an aperture in the wall. Since the molecules in the vessel have velocities in all directions, the effusing molecules will fill a solid angle of 2π (Esterman, 1946) as illustrated in Figure 2.13.

Assuming those molecules have a maxwellian distribution of velocities the fraction of molecules having a velocity v perpendicular to the slit (i.e. in the x-direction) in the range dv will be (Kantrowitz and Grey, 1951)

$$\frac{ve^{\frac{-mv^2}{2kT}}dv}{\int_0^\infty ve^{\frac{-mv^2}{2kT}}dv}. \tag{2.63}$$

When a screen with a second, collimating slit (Slit *2*, Fig. 2.13) is arranged coaxially to the direction of motion of the effusing molecules, it is possible to select those molecules whose velocity vectors lie in the solid angle determined by the widths of both slits and their separation distance. If u and w are the velocities in the plane of the first slit, the fraction of molecules effusing with the velocity v which reach the small area of the collimating slit will be

$$\frac{\int_{u_1}^{u_2} ue^{\frac{-mu^2}{2kT}}du \int_{w_1}^{w_2} we^{\frac{-mw^2}{2kT}}dw}{\int_{-\infty}^{\infty} ue^{\frac{-mu^2}{2kT}}du \int_{-\infty}^{\infty} we^{\frac{-mw^2}{2kT}}dw} \tag{2.64}$$

where $\frac{u_1}{v} = \frac{y_1}{s}$; $\frac{u_2}{v} = \frac{y_2}{s}$; $\frac{w_1}{v} = \frac{z_1}{s}$; $\frac{w_2}{v} = \frac{z_2}{s}$

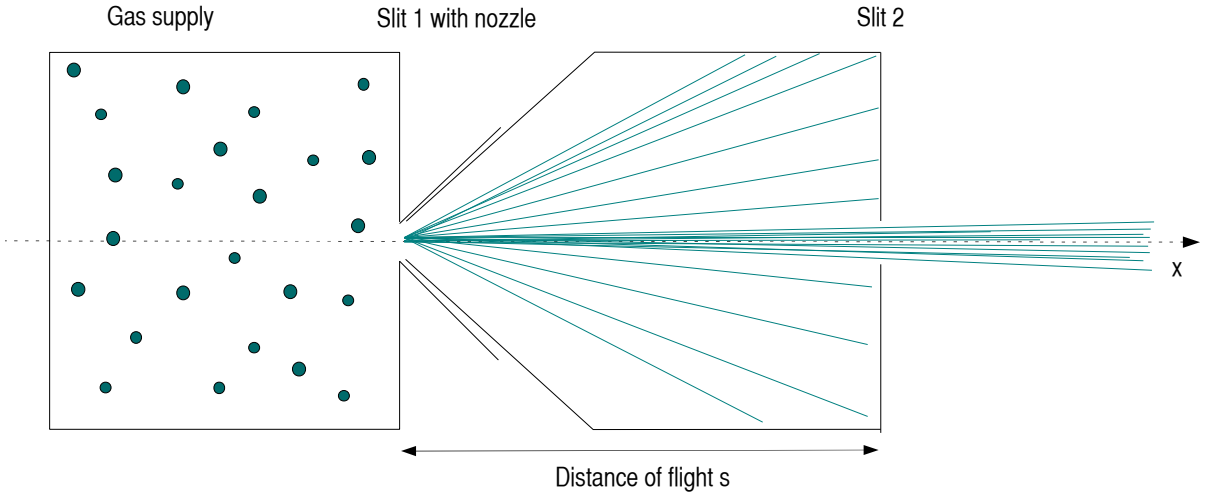

Figure 2.14.: High intensity molecular beam source

with $(y_2 - y_1)$, $(z_2 - z_1)$ being the slit boundaries and s the distance between the slits. If the dimensions of the collimating slit are very small compared to the distance between the slits then it can be assumed that

$$e^{-\frac{m}{2kT}u_1^2} \approx e^{-\frac{m}{2kT}u_2^2} \approx e^{-\frac{m}{2kT}w_1^2} \approx e^{-\frac{m}{2kT}w_2^2}$$

and thus the integration of Eq. 2.64 yields

$$(u_2 - u_1)(w_2 - w_1) \cdot \frac{\sqrt{\frac{m}{kT}}\sqrt{\frac{m}{kT}}}{\sqrt{\pi}\sqrt{\pi}} = \frac{mv^2 A}{2kT\pi s^2} \tag{2.65}$$

where A is the area of the collimating slit. In order to get the gain at the collimating slit it is necessary to integrate Eq. 2.65 over all velocities of molecules effusing out of the first slit

$$\frac{\int_0^\infty \frac{mv^2 A}{2kT\pi s^2} \cdot v \cdot e^{-\frac{mv^2}{2kT}} dv}{\int_0^\infty v \cdot e^{-\frac{mv^2}{2kT}} dv} = \frac{A}{\pi s^2} \tag{2.66}$$

Intensity gain and velocity distribution in a nozzle source In order to get a molecular beam source with a higher intensity gain, the first slit is placed in the flow from a miniature supersonic nozzle coaxial with the final beam as shown in figure 2.14. The nozzle will convert most of the translational an internal energy into a directed mass motion (Kantrowitz and Grey, 1951). The mass velocity or peak velocity v_p will then be considerably larger then the molecular velocity. Thus, the Mach number, which is in this case the ratio of the mass velocity v_p and the molecular velocity v_{th}

$$M = \frac{v_p}{v_{th}} \tag{2.67}$$

will be considerably greater than 1. The fraction of molecules passing through the collimating slit then becomes

$$\frac{mv_p^2}{2kT}\cdot\frac{A}{\pi s^2}=\frac{\gamma}{2}\cdot\frac{v_p^2}{v_{th}2}\cdot\frac{A}{\pi s^2}=\frac{\gamma}{2}\cdot M^2\cdot\frac{A}{\pi s^2} \tag{2.68}$$

$$\text{with}\qquad \frac{m}{kT}=\frac{c_p}{c_v}\cdot\frac{1}{v_{th}^2}=\frac{\gamma}{v_{th}^2}.$$

If then the influence of the random velocity v_{th} on the probability for a molecule to get through the second slit is neglected compared to the predominant effect of the mass flow, the velocity distribution will be given by

$$\frac{dI}{dv}\propto v_{th}^3\cdot e^{-\frac{m}{2kT}\left(v_{th}-v_p\right)^2} \tag{2.69}$$

Using equation 2.68 this distribution can be expressed in terms of the Mach number and γ (Anderson and Fenn, 1965):

$$\frac{dI}{dv}\propto\left(\frac{v_{th}}{v_p}\right)^3\cdot e^{-\frac{\gamma M^2}{2}\left(\frac{v_{th}}{v_p}-1\right)^2} \tag{2.70}$$

Determination of velocity distributions and ion temperature from experimental data

Experimentally determined curves of number density versus time-of-flight may be converted directly into velocity distributions. This distribution is given by (see **??**)

$$\frac{dI}{dv}=I_0\cdot f(v) \tag{2.71}$$

The number of ions reaching the detector in a time interval t_0 will be $N_0=I_0\cdot t_0$ and their velocity distribution will be analogous to 2.71

$$\frac{dN}{dv}=N_0\cdot f(v)=I_0t_0f(v) \tag{2.72}$$

A signal S of an ion detector like a MCP would be proportional to the number density D of impacting ions or molecules

$$S\propto D=\frac{dN}{dv}\cdot\frac{1}{t}=N_0f(v)\cdot\frac{1}{t}. \tag{2.73}$$

The predicted signal versus time-of-flight curve will then be (Anderson and Fenn, 1965)

$$\begin{aligned}S&\propto\frac{1}{t}f(v)=\frac{1}{t}\left(\frac{v_{th}}{v_p}\right)^3\cdot exp\left(-\frac{\gamma}{2}M^2\left[\frac{v_{th}}{v_p}-1\right]^2\right)\\&\propto\frac{1}{t^4}\cdot exp\left(-\frac{\gamma}{2}M^2\left[\frac{z_0}{tv_s}-1\right]^2\right)\end{aligned} \tag{2.74}$$

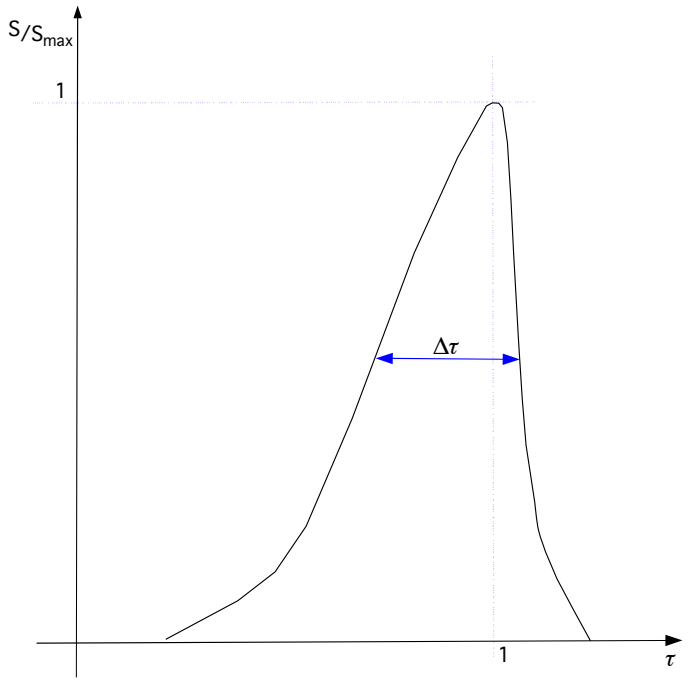

Figure 2.15.: Width of a peak in normalized time and height

with $t = z_0/v$. More convenient is the normalised equivalent of equation 2.74, introducing the normalised time-of-flight $\tau = t/t_p$

$$\frac{S}{S_{max}} = \frac{1}{\tau^4} \cdot \exp\left(-\frac{\gamma}{2} M^2 \left[\left(\frac{b}{\tau} - 1\right)^2 - (b-1)^2\right]\right), \tag{2.75}$$

where $b = 1/2 \cdot \left[1 + \sqrt{1 + 16/\gamma M^2}\right]$ is the relation between t_p and the time at peak maximum $t_{max} = \gamma/8 \cdot M^2 \cdot z_0/v_p \cdot \left[1 + \sqrt{1 + 16/\gamma M^2}\right]$.

(2.76)

For large Mach numbers, b approaches 1 and the time at peak maximum t_p approximates t_{max}. This relation allows to identify the time at peak maximum as the ion flight time, being fundamental for the assignment of mass lines to particular ion species in *TOF* mass spectra.

Figure 2.15 shows the normalised measured signal S/S_{max} in dependence on the normalised time-of-flight τ. The relative width of this peak $\Delta\tau = \tau_2 - \tau_1$ relates directly to the differences in the velocities for the ions of a particular species. Furthemore, on can assume this difference in velocities Δv being equivalent to the thermal velocity of the ions

$$v_{th} \approx \Delta v.$$

As a result, the relation between the mass flow or peak velocity v_p and the thermal velocity v_{th} (relative width in velocity Δv) is

$$\begin{aligned}\Delta v &= \frac{d}{t_p - \Delta t} - \frac{d}{t_p} \\ &= \frac{s}{t_p}\left(\frac{1}{1-\frac{\Delta t}{t_p}} - 1\right) = v_p\left(\frac{1-1+\frac{\Delta t}{t_p}}{1-\frac{\Delta t}{t_p}}\right)\end{aligned}$$

with s being distance-of-flight. This leads to the estimation of the nondirectional random velocity

$$\Rightarrow v_{th} \approx v_p\left(\frac{\frac{\Delta t}{t_p}}{1-\frac{\Delta t}{t_p}}\right).$$

The definition of the *Mach number* $M = v_p/v_{th}$ leads to the possibility of deriving the *Mach number* directly from the relative width of the measured peak:

$$\begin{aligned}M &= \frac{1-\frac{\Delta t}{t_p}}{\frac{\Delta t}{t_p}} = \frac{t_p}{\Delta t} - 1 \\ \Rightarrow M &\stackrel{!}{=} (\Delta\tau)^{-1} - 1\end{aligned} \tag{2.77}$$

with the relative flight time $\tau = t/t_p$. Inserting the actual ion velocity v_p for accelerated ions in a time-of-flight mass spectrometer $v_p = \sqrt{2U_{acc}q/m}$ and the thermal velocity $v_{th} = 2\cdot\sqrt{2kT/m\cdot\pi}$ yields the energy of the ions in eV under the assumptions of singly ionised ions and high *Mach numbers* ($M \gg 1$)

$$M = \frac{1}{2}\sqrt{U_{acc}\pi/kT} \qquad \Rightarrow \frac{kT}{[eV]} \approx (\Delta\tau)^2 \cdot U_{acc} \tag{2.78}$$

Example Figure 2.16 shows an example for a measured peak of iron ions for an accelerating potential of 500V. The absolute width of this peak is 0.75μs for a time-of-flight of 16 μs at the peak's maximum. This corresponds to a relative width of about 4.7% and to an energy of the ions of

$$\frac{kT}{[eV]} \approx 500V\,(0.047)^2 \approx 1.1eV.$$

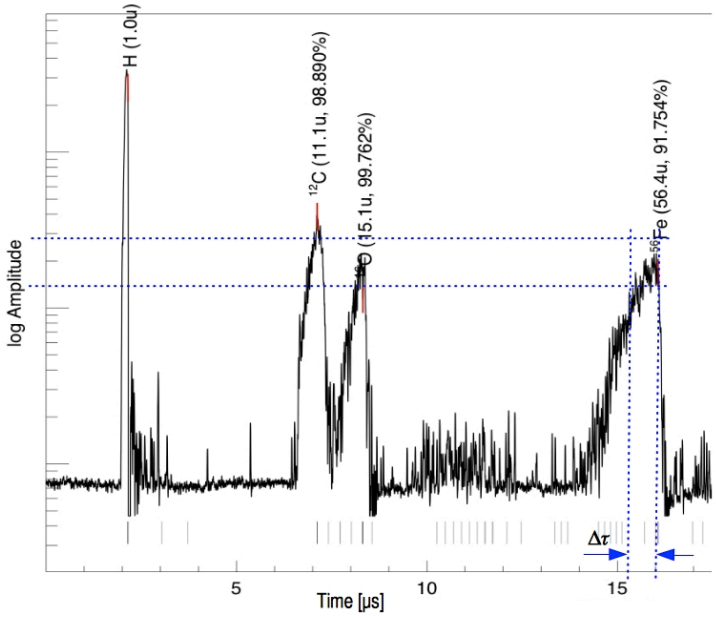

Figure 2.16.: Example: The peak of iron ions in a time-of-flight mass spectra of an iron dust particle impacting on a silver target with a velocity of 31 $\frac{km}{s}$ and an accelerating voltage of 500V.

2.4. Mineralogy

2.4.1. Constituents of cosmic dust

Generally, cosmic dust is comprised by interstellar and interplanetary dust and thus resembles a variety of sources. Interstellar dust (ISD) is generated mainly by AGB stars (Whittet, 1989)and, to a lesser extend, by novae, supernovae and Wolf-Rayet stars (Zhukovska et al., 2008) outside our solar system, whereas interplanetary dust (IDP) originates within our solar system. Comets, asteroids, atmosphere-less planetary satellites, Edgeworth-Kuiper Belt objects, the Jovian and Saturnian systems and mankind itself, in the perimeter of the Earth (e.g. rocket propellant residues), contribute to the formation of interplanetary dust particles. For detailed reviews of cosmic dust composition and sources see e.g. (Grün et al., 2009; Mann et al., 2006; Baggaley, 2004; Draine, 2003; Sekanina, 2001; Dorschner, 2001).

Composition of interstellar dust

Interstellar dust is a part of the interstellar medium (ISM), which is composed of gas and dust and makes a large fraction (about 20%) of the total mass of the galaxy(Binney and Merrifield, 1998) . ISD is being investigated using optical methods, e.g infrared spectroscopy(Dorschner, 2001), further in-situ analysis by spacecrafts or the investigation of samples returned by spacecrafts (Brownlee et al., 2006) and the investigation of ISD found in meteorites (Hoppe et al., 2001). ISD compositions include silicates (amorphous and crystalline), sulphides, metal oxides, silicon carbide, amorphous carbon, PAH's (polyaromatic hydrocarbons) and volatile species.

Composition of interplanetary dust

Since interplanetary dust is formed by the many different sources indicated above, this subsection will give short overviews over each source and the mechanisms that lead to dust formation in this specific environment.

1. **Cometary dust**

   Cometary dust, which is ejected by outgassing, was investigated via in-situ impact ionization mass spectroscopy (Kissel, 1986; Kissel et al., 2004; Dikov et al., 1989). , remote sensing techniques (Lisse et al., 2007) and the investigation of returned samples . It is mainly comprised by silicates and further by CHON particles, resembling carbonacous materials, metals, sulphides, carbonates and oxides (Sekanina, 2001; Flynn et al., 2006; Flynn, 2008).

2. **Asteroids, atmosphereless planetary satellites, planets, Edgeworth-Kuiper Belt objects**

   Dust derived by asteroids is a result of collision and dust impact ejection, atmosphereless planetary satellites and planets , as well as Edgeworth-Kuiper Belt objects may experience collisions, possibly outgassing or cryovolcanism and frequent dust impact ejection. The composition of the dust derived here should resemble the surface composition of the source body, or its bulk composition, if collisional events were catastrophic. Asteroids show silicates as the main constituent, with a lesser amount of metals, such as iron and

nickel, as well as sulphides and oxides, as seen in reflectance spectra or as investigated by direct analysis of the material (Mothé-Diniz et al., 2005) and terrestrial analysis of meteorites . Dust of larger planetary satellites or planets contain varying amounts of ices, organics, salts and silicates . The composition of the dust here depends on the particular source body and the region of the source from which the dust was ejected. E.g. in the case of Enceladus, the composition has been directly measured (Hillier et al., 2007b; Postberg et al., 2009b,a) 2008, 2009a).

3. **Stream particles**

   Stream particles have their source within their giant planetary system, e.g. Jupiter or Saturn. The particles will be charged and accelerated before they are ejected into the interplanetary space. Their composition resembles the composition of the source region within their planetary system. Stream particles of the Jovian system have their source in Io and the Io plasma torus (Graps et al., 2000)and are composed mainly of NaCl and KCl salts with traces of sulphur (Postberg et al., 2006). Saturnian stream particles have their sources in the A and E rings and are mainly composed of silicates and volatile species(Kempf et al., 2005b).

4. **Cosmic dust on Earth**

   The Earth and its atmosphere is heavily impinged by cosmic matter. Meteorites, being the main source of influx of extraterrestrial matter, range from 50 to 500 micrometers in diameter with an average density of 2.0 g/cm^3 and porosity about 40% (Love et al., 1994). The particles are mostly chondritic, comprised by anhydrous silicates, e.g. pyroxene and olivine and further phyllosilicates, silicates that bear an OH-group. Moreover, meteorites may contain non-chondritic particles, mainly composed of sulphides, olivine, pyroxene, metals (e.g. Fe/Ni), CAI's (calcium-aluminum-rich inclusion), carbonates and phosphates.

2.4.2. Silicates

Regardless of the source of a particular cosmic dust particle as describe above, there is a good probability that it will contain silicates. This chemical compound is the constituent of cosmic dust found most frequently in the solar system. Because of this, in this study two types of silicates, coated with different methods, were used as projectile material. This section describes the characteristics common to all silicates and gives a short overview of the these particular types, olivine and pyroxene.

Silicates are compound in which Si atoms are tetraedally surrounded by oxygen atoms. This SiO_4-Tetradhedra constitute the anionic part of the compound and can be linked to larger structures. Besides the anionic silicon-oxygen-group it contains cations like Mg^+ or Fe^+.

The basic element - the SiO_4-Tetrahedron

From the electronegativity of both elements, silicon (**1.9**) and oxygen(**3.44**) one can assume, that the Si-O-bond has both covalent and ionic fractions. For the covalent fraction the electron configuration of the silicon leads to a tetrahedral alignment of the oxygen atoms. For the ionic fraction of bonds this spatial alignment would also be expected, because the ratio of the atomic radii r_{Si} and r_O lies between the thresholds of 0.225 and 0.415, which are characteristic for this kind of alignment (Liebau, 1962).

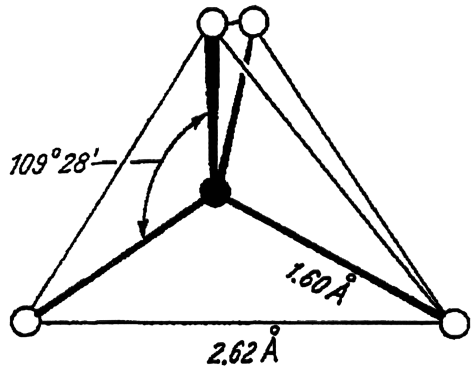

Figure 2.17.: Dimensions of the [SiO_4] tetrahedron

Structure of silicates

In almost every structure the bond of the between the silicon and the oxygen is stronger then the bond between the oxygen and the other cation. Therefor it is reasonable to use the [SiO_n] polyhedra and the way they are linked to each other to classify the silicate anions (Liebau, 1985):

- **Coordination number CN of silicon:**
  This is the number of oxygen atoms assigned to a silicon atom ([SiO_n]) In nature only [SiO_4] tetrahedra and [SiO_6] octahedra occur.

- **Linkedness L of [SiO_n] polyhedra:**
  This number L is defined as the number of oxygen atoms shared between two ([SiO_n]) polyhedra and can have the values (see Figure 2.18):

$$\mathbf{L} = 0,\ 1,\ 2,\ 3$$

- **Connectedness s of [SiO_n] polyhedra:**
  This is the number of other [SiO_n] polyhedra an individual [SiO_n] polyhedron is linked via common oxygen atoms. A [SiO_4] tetrahedron can share up to four oxygen atoms, a [SiO_6] octahedron up to six. This is symbolised by the number $\mathbf{Q^s}$.

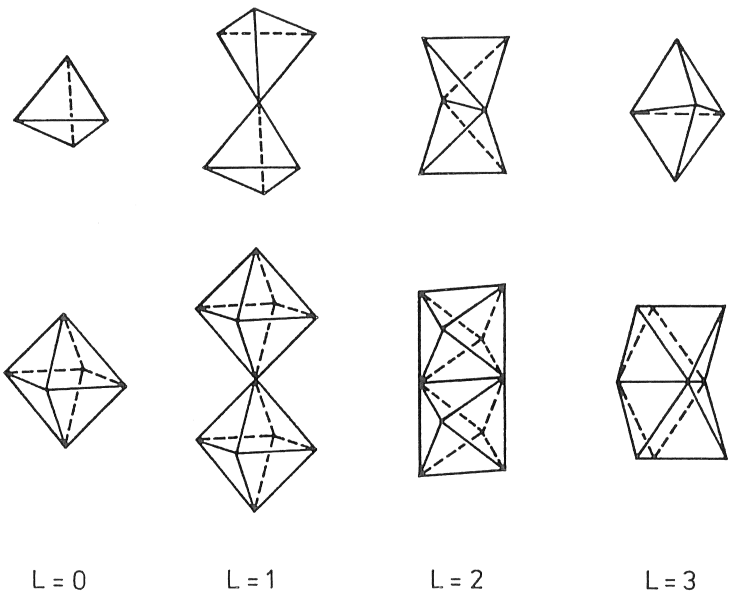

Figure 2.18.: Tetrahedra and octahedra with different linkedness **L**. **L** = 0 (isolated); **L** = 1 (corner-sharing); **L** = 2 (edge-sharing); **L** = 3 (face-sharing) (Liebau, 1985)

- **Branchedness of Silicate anions**
  The branchedness of a silicate is the property which describes whether the alignment of the anion in the crystal is unbranched, open-branched, loop-branched, mixed-branched or an hybrid alignment of anions.

- **Dimensionality of silicate anions:**
  This number describes he spatial dimensionality of the structure. Single polyhedra along with terminated structures like rings have the dimensionality **D = 0**, chains **D = 1**, layers **D = 2** and frameworks have **D = 3**

- **Multiplicity of silicate anions:**
  Limited numbers of individual polyhedra, single chains, rings or layers can be connected to each other in a way, that the resulting structure has the same dimensionality then the generating ones. The number of the connected structures is then called multiplicity **M**.

- **Periodicity of silicate anions:**
  In a crystalline silicate the structural motif of the structure repeats after several tetrahedra. The periodicity P is the number of polyhedra within one repeating unit of the

Silicate anions can now be filed into a hierarchical order of the categories introduced above

coordination number	**CN**	classes
linkedness	**L**	subclasses
branchedness	**B**	branches
multiplicity	**M**	orders
dimensionality	**D**	groups
rings or multiple polyhedra	**r** or **t**	subgroups
periodicity	**P**	families

	Multiplicity				
Dimensionality	1	2	3	4	···
0	Nesosilicates	Sorosilicates			
0	Cyclosilicates				
1	Inosilicates				
2	Phyllosilicates				
3	Tectosilicates				

Table 2.2.: Mineralogical nomenclature of silicates

Mineralogical nomenclature of silicates

Minerals are usually designated by trivial names, which are often related to some conspicuous property like morphology or color. Another possibility to name a mineral is after the locality here it has been discovered. To obtain some kind of systematic into the minerals' designations mineralogists use a nomenclature in which silicates are grouped due to their dimensionality and multiplicity as shown in Table 2.2.

- **Nesosilicates:** isolated [SiO_4] tetrahedra (*Olivines, Granates*)
- **Sorosilicates:** groups of two [SiO_4] tetrahedra, which are linked at one edge. (*Zoisite, Epidote*)
- **Inosilicate:** Chains in which the silicate anions are connected by two of their corners to two neighbouring tetrahedra. Two chains can be connected, thus the individual tetrahedra are linked to three other tetrahedra. (*Pyroxenes*)
- **Cyclosilicate:** rings, in which the silicate anions are connected by two of their corners to two neighbouring tetrahedra. (*Turmaline, Beryl*)
- **Phyllosillicate:** two dimensional structures, in which the silicate tetrahedra form parallel sheets (*Talc*).
- **Tectosilicate:** have a three-dimensional framework of silicate tetrahedra (*Quartz, Feldspat*).

2.4.3. Olivine

Olivine is a magnesium iron silicate with the general formula $(Mg_2Mn_2Fe_2)[SiO_4]$. There are three types of olivines (Markl, 2008):

Mg_2SiO_4:Forsterit
Fe_2SiO_4:Fayalite
Mn_2SiO_4:Tephroite

The mixture of those three types are usually called Olivine. It crystallises orthonormally with no connection of the individual [SiO_4] tetrahedra to each other. Thus olivines are Nesosilicates. Olivines incorporate only mir amounts of other elements then oxygen, silicon, manganese, magnesium and iron.

2.4.4. Pyroxene

Pyroxenes consist of single chains of silicate tetrahedra and thus belong to the group of Inosilicates. The general formula of Pyroxene is $XY[(Al_)Si_2O_6]$ where

X represents:Ca, Na, Fe^{2+}, Mg, Zn, Mn or Li

Y represents:Cr, Al, Fe^{3+}, Mg, Ti, Mn or Vn

To some extent the silicon atoms can be replaced by aluminium atoms. The crystallisation of Pyroxenes can lead to either orthorhombic or monoclinic systems and divides Pyroxenes into two groups:

orthoPyroxenes (Opx):

$Fe_2Si_2O_6$: Ferrosilite
$Mg_2Si_2O_6$: Enstatite

clinoPyroxenes:

$CaFeSi_2O_6$: Hedenbergite
$CaMgSi_2O_6$: Diopside
$NaAlSi_2O_6$: Jadeite
$NaFeSi_2O_6$: Aegerine
$CaAl_2SiO_6$: Ca-Tschermakit

3. Experimental Set Up

In this section gives an overview on the experimental set up used for this thesis. First there is a description of the linear *TOF* maß spectrometer. It was designed and build to compare the properties of the plasma generated by hypervelocity particle impacts as well as by laser ablation under similar conditions. This instrument was named *BERTA* for historical reasons and will be referred to with this name in the following. The results of the measurements done with the *BERTA* instrument have been compared with data obtained by two different reflectron *TOF* mass spectrometer. These two instruments, called *SUDA* and *LAMA*, will be also described in the next section (Section 3.1).

The following Section 3.3 gives an overview on the Heidelberg dust accelerator, the working principle of the Van-de-Graaf generator as well as the dust source will be described and the subsequent dynamical properties of the dust particle beam will be characterised. Then, in Section 3.4, the laser and the optical set up used for the laser ablation experiment is explained. This chapter closes with an overview of the studies target and dust materials and a summary of the performed measurements (Section 3.5).

3.1. Linear *TOF* mass spectrometer

3.1.1. General set up and geometry

The time-of-flight mass spectrometer used for the experiments in this thesis is linear with a total length from target to the detector of about 0.62 m. A scheme of the instrument is shown in figure 3.1.

The electrostatic field is generated between the target which has a variable potential of the order of several hundreds volts and the grounded grid.

To accelerate the ions in an electrostatic field as homogenous as possible the diameter of the target mounting and the grid is with 100 mm quite big and large in comparison with the distance of target and grid measuring 20 mm. A microchannel plate (*MCP*) is placed as an ion detector at the end of the following drift tube. The *MCP* can be operated with potentials between around 1500 V and 2000 V, the standard value used for this thesis is 1650 V (See Appendix B). To guarantee the electrostatic field in generated due to this potential to be homogeneous as well, a grounded grid is placed in front.

To guaranty identical conditions for either impact and laser ablation the set up is symmetrical for both processes: The beam hits in each of the two cases the target in an angle of 45° (see 3.2). this is possible because of the two entrance flanges in the vacuum chamber which contains the target and grid mounting as seen in picture 3.2.

The spectrometer consists in principle of two main parts as seen in Figure 3.3, a vacuum chamber of 30 cm diameter and about 40 cm height. On the bottom of the chamber is a turbo

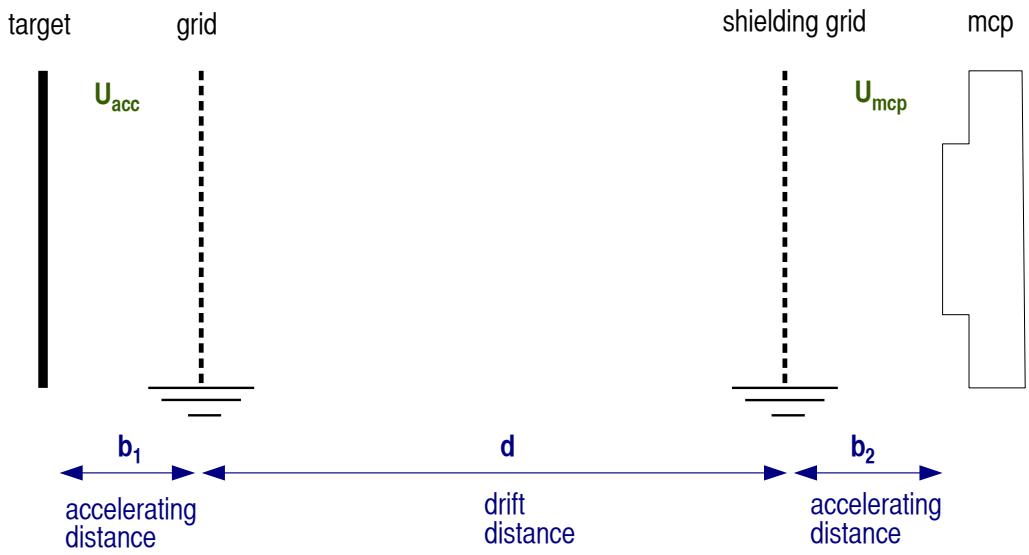

Figure 3.1.: Scheme of the *BERTA* time-of-flight mass spectrometer. In front of the target mounted on a plate with a diameter of 100 mm a grounded grid is placed. A positive potential applied on the target generates an almost homogeneous electrostatic field. Positive Ions released in the target's vicinity will be accelerated towards the *MCP* placed at the end of the drift tube. A grounded grid in front of the *MCP* guarantees the field generated by the potential applied on the*MCP* to be homogeneous as well.

pump which provides the vacuum necessary for the experiments of the order of $10^{-6} mbar$. The second part is a 1.2 m long low pressure tube with a diameter of 10 cm (flanges) in which the retarding field grid system lies and at its end the detector is.

To have not to adjust the laser's optical settings like lenses and polarizer all the time the spectrometer has moved even for little, the target chamber and the laser are fixed on the same mounting.

3.1.2. Theoretical performance of the spectrometer

Ions starting from a location on or near the target plane pass through three stages of the spectrometer on their way to the detector:

1. an accelerating field $E_1 = U_{target}/b_1$ between the target and the first grounded grid g_1,
2. a field free drift distance d,
3. a second accelerating field $E_2 = U_{mcp}/b_2$ between the second grounded grid b_2 and the MCP.

If and when a specific ion will hit the MCP and contribute to the recorded ion signal depends on the geometrical properties and potentials within the spectrometer and the initial conditions of the ion like the starting location x_0, the starting time t_0 and the initial velocity v_0.

Te initial location x_0 and time t_0 are defined bay the point at which the field E_1 reaches the ion and begins to accelerate it. The initial velocity v_0, i.e. the direction of motion of the ion as well as its initial energy E_0, on the other hand is determined by the forming process of the

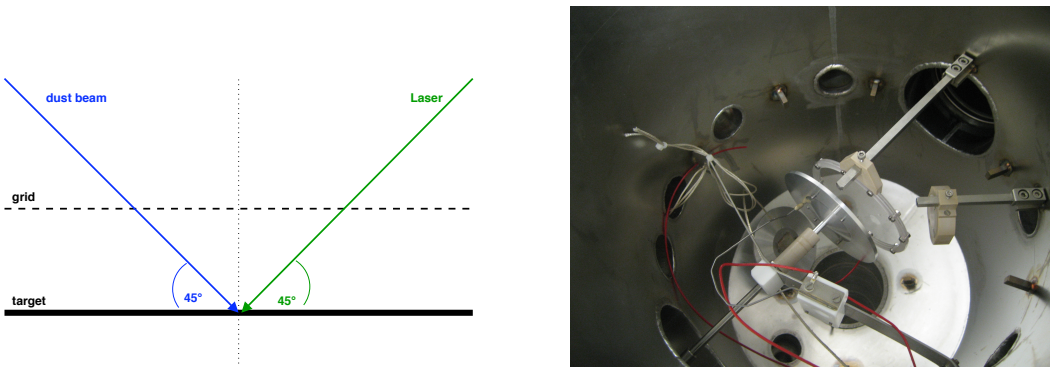

Figure 3.2.: (left) Geometry of impact for both particles and laser beam (45°) (right) Photograph of the target chamber's inner side, shown are the target, the grounded grid in front in the center of the chamber. On the right side there is the focusing lens for the laser beam, further right the entrance window for the beam. The large opening opposite to the target /grid system is the entrance of the drift tube with the ion detecting MCP at its end.

plasma. It is a combination of properties like the thermal velocity and the expansion of the plasma cloud at the moment the accelerating field E_1 is beginning to dominate the motion of the ions.

Due to the geometrical design of the spectrometer as shown in figure 3.1 the accelerating fields are approximately homogenous and the time and path of flight of an ion can be calculated as in the following section.

3.1.3. Time and path of flight

Pass through the accelerating field $\mathbf{E_1}$

In the moment the electrostatic field E_1 between the target and the grounded grid g_1 reaches in the plasma cloud, the ions are accelerated by an electrostatic force

$$\mathbf{F} = q \cdot E_1 = m \cdot \ddot{x} \tag{3.1}$$

Due to the geometric set up the field is almost homogeneous this the acceleration is directed in one (x-) direction:

$$\mathbf{E_1} = \frac{U_{acc}}{b_1} \begin{pmatrix} 1 \\ 0 \\ 0 \end{pmatrix} \tag{3.2}$$

The equation of motion for a specific ion will then be

$$\ddot{\mathbf{x}} = \left(\frac{q}{m} \cdot \frac{U_{acc}}{b_1}, \, 0 \, , \, 0 \right) \tag{3.3}$$

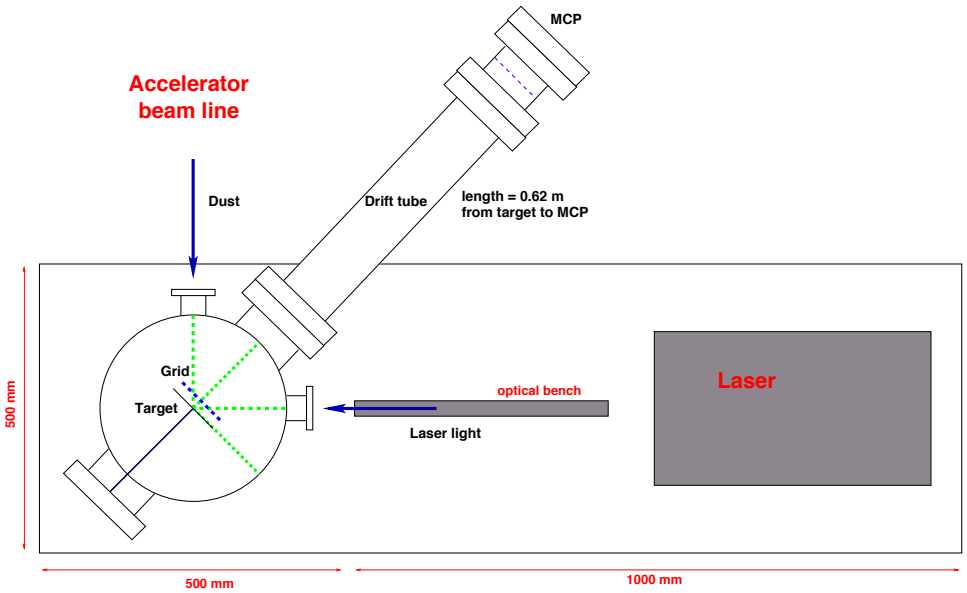

Figure 3.3.: Draft of the set up

Integration gives the velocity of the ion for a time t and then its location :

$$\dot{\mathbf{x}}(t) = \left(\frac{q}{m} \cdot \frac{U_{acc}}{b_1} \cdot t + v_{0x},\ v_{0y}\ ,\ v_{0y} \right) \tag{3.4}$$

with $\mathbf{v_0} = (v_{0x}\ ,\ v_{0y}\ ;\ v_{0z})$ is the initial velocity of the ion due to tho initial conditions in the plasma cloud. So the location of the ion at the moment t will be

$$\begin{aligned} x(t) &= \frac{1}{2}\frac{q}{m}\frac{U_{acc}}{b_1} \cdot t^2 + v_{0x}t + x_0 \\ y(t) &= v_{0y}t + y_0 \\ z(t) &= v_{0z}t + z_0 \end{aligned} \tag{3.5}$$

with $\mathbf{x_0} = (x_0\ ,\ y_0\ ,\ z_0)$ is the starting location of the ion.
The ion will pass the first grounded grid g_1 at the time t_{grid1} and the location $\mathbf{x}\left(t_{grid1}\right)$:

$$\mathbf{x}\left(t_{grid1}\right) = \left(b_1\ ,\ v_{0y} \cdot t_{grid1} + y_0\ ,\ v_{0z} \cdot t_{grid1} + z_0\ \right)$$

t_{grid1} is then defined by

$$\begin{aligned} b_1 &= \frac{1}{2}\frac{q}{m}\frac{U_{acc}}{b_1} \cdot t^2 + v_{0x}t + x_0 \\ 0 &= \frac{1}{2}\frac{q}{m}\frac{U_{acc}}{b_1} \cdot t^2 + v_{0x}t + x_0 - b_1 \end{aligned}$$

$$\Rightarrow t_{grid1} = \frac{-v_{0x} \pm \sqrt{v_{0x}^2 - 2\frac{q}{m}\frac{U_{acc}}{b_1}(x_0 - b_1)}}{\frac{q}{m}\frac{U_{acc}}{b_1}}$$

The constraints, that x_0 has to be between the target plane and the first grounded grid, ie. $0 \overset{!}{\leq} x_0 \overset{!}{\leq} b_1$ and $t_{grid1} \overset{!}{>} 0$ lead to

$$t_{grid1} = \frac{-v_{0x} + \sqrt{v_{0x}^2 - 2\frac{q}{m}\frac{U_{acc}}{b_1}(x_0 - b_1)}}{\frac{q}{m}\frac{U_{acc}}{b_1}} \tag{3.6}$$

Drift phase

After passing the first grounded grid $\mathbf{g_1}$ the ion enters the drift distance $\mathbf{d}$ at the location $\mathbf{x}\left(t_{grid1}\right)$ and travels through the drift distance with the constant velocity

$$\dot{\mathbf{x}}\left(t_{grid1}\right) = \left(\frac{q}{m} \cdot \frac{U_{acc}}{b_1} \cdot t_{grid1} + v_{0x},\ v_{0y}\ ,\ v_{0y}\right). \tag{3.7}$$

It will reach the second grid $\mathbf{g_2}$ after the time

$$t_{grid2} = \frac{d}{\dot{x}\left(t_{grid1}\right)} \tag{3.8}$$

and at the location

$$\begin{aligned} x\left(t_{grid2}\right) &= b_1 + d \\ y\left(t_{grid2}\right) &= v_{0y} \cdot \left(t_{grid1} + t_{grid2}\right) + y_0 \\ z\left(t_{grid2}\right) &= v_{0z} \cdot \left(t_{grid1} + t_{grid2}\right) + z_0 \end{aligned} \tag{3.9}$$

Passing through the accelerating field $\mathbf{E_2}$

After passing the second grid $\mathbf{g_2}$ the ion is accelerated again in the field $\mathbf{E_2}$ generated by the potential difference $\mathbf{U_{mcp}}$ between $\mathbf{g_2}$ and the MCP

$$\mathbf{F} = m\ddot{\mathbf{x}} = \left(q\frac{U_{mcp}}{b_2}\ ,\ 0\ ,\ 0\ \right)$$

After the time t_{mcp} the ion will hit the plane of the mcp at $x\left(t_{mcp}\right) = b_1 + d + b_2$. This time can be calculated similar to t_{grid1} in the section above.

$$\begin{aligned} b_1 + d + b_2 &= \frac{1}{2}\frac{q}{m}\frac{U_{mcp}}{b_2} \cdot t_{mcp}^2 + \dot{x}\left(t_{grid1}\right) t_{mcp} + d + b_1 \\ \Rightarrow 0 &= \frac{1}{2}\frac{q}{m}\frac{U_{mcp}}{b_2} \cdot t_{mcp}^2 + \dot{x}\left(t_{grid1}\right) t_{mcp} - b_2 \end{aligned}$$

$$\Rightarrow t_{mcp} = \frac{-\dot{x}\left(t_{grid1}\right) \pm \sqrt{\dot{x}^2\left(t_{grid1}\right) - 2\frac{q}{m}\frac{U_{mcp}}{b_2}(-b_2)}}{\frac{q}{m}\frac{U_{mcp}}{b_2}}$$

$$\Rightarrow t_{mcp} = \frac{-\dot{x}\left(t_{grid1}\right) + \sqrt{\dot{x}^2\left(t_{grid1}\right) - 2\frac{q}{m}U_{mcp}}}{\frac{q}{m}\frac{U_{mcp}}{b_2}} \tag{3.10}$$

The total time of travel and the spatial coordinates of the ion hitting the plane of the MCP will then be

$$t_{flight} = t_{grid1} + t_{grid2} + t_{mcp}$$

$$\begin{aligned} x\left(t_{flight}\right) &= b_1 + d + b_2 \\ y\left(t_{flight}\right) &= v_{0y} \cdot \left(t_{grid1} + t_{grid2} + t_{mcp}\right) + y_0 \\ z\left(t_{flight}\right) &= v_{0z} \cdot \left(t_{grid1} + t_{grid2} + t_{mcp}\right) + z_0 \end{aligned}$$

Time-of-flight for ions with the initial energy $\mathbf{E_0 = 0}$

For ions with the initial conditions

$$\begin{aligned} \mathbf{x_0} &= (0\ ,\ 0\ ,\ 0\ ) \\ \mathbf{v_0} &= (0\ ,\ 0\ ,\ 0\ ) \qquad \text{and} \\ E_0 &= 0 \end{aligned}$$

the representation of the time-of-flight is simplified as follows:

a) Acceleration in the field between target and the first grid

$$\begin{aligned} \text{From eq. (3.6)} \Rightarrow t\left(grid1\right) &= \frac{\sqrt{\frac{2q}{m} \cdot \frac{b_1}{b_1} \cdot U_{target}^2}}{\frac{q}{m}\frac{U_{target}}{b_1}} \\ &= \sqrt{\frac{2}{qU_{target}}} \cdot \sqrt{m} \cdot b_1 \end{aligned} \tag{3.11}$$

b) Drift phase

$$\begin{aligned} \text{From eq. (3.8)} \Rightarrow t\left(grid2\right) &= \frac{d}{\dot{x}\left(t_{grid1}\right)} \\ &= \sqrt{\frac{d^2}{2q \cdot U_{acc}}} \cdot \sqrt{m} \end{aligned} \tag{3.12}$$

c) Acceleration in the field between second and the MCP

$$\begin{aligned} \text{From eq. (3.10)} \Rightarrow t\left(mcp\right) &= \frac{-\dot{x}\left(t_{grid1}\right) + \sqrt{\dot{x}^2\left(t_{grid1}\right) - 2\frac{q}{m}U_{mcp}}}{\frac{q}{m}\frac{U_{mcp}}{b_2}} \\ &= \frac{-\sqrt{\frac{2q}{m}U_{acc}} + \sqrt{\frac{2q}{m}U_{acc} + \frac{2q}{m}U_{mcp}}}{\frac{q}{m}\frac{U_{mcp}}{b_2}} \\ &= \sqrt{\frac{2b_2^2}{q}} \cdot \frac{\sqrt{U_{acc} + U_{mcp}} - \sqrt{U_{acc}}}{U_{mcp}} \cdot \sqrt{m} \end{aligned} \tag{3.13}$$

d) Total flight time

$$
\begin{aligned}
t_{flight} &= t_{grid1} + t_{grid2} + t_{mcp} \\
&= \underbrace{\sqrt{\frac{2}{q}}\left(\frac{b_1}{\sqrt{U_{acc}}} + \frac{d}{2}\frac{1}{\sqrt{U_{acc}}} + b_2\frac{\sqrt{U_{acc}+U_{mcp}}-\sqrt{U_{acc}}}{U_{mcp}}\right)}_{\text{stretch factor } \mathbf{a}} \cdot\sqrt{m}
\end{aligned}
\tag{3.14}
$$

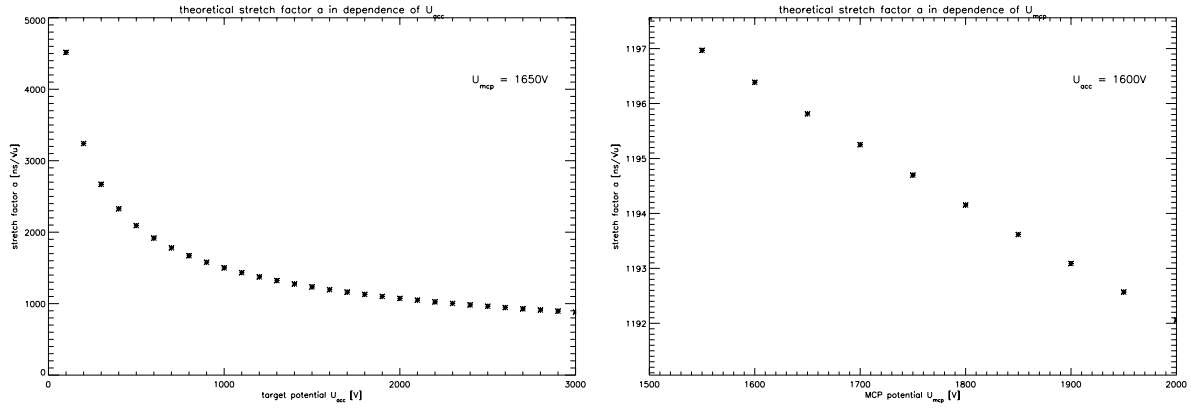

Figure 3.4.: Calculated stretch factor a as a function of the target potential U_{acc} for the in all measurements used MCP potential $U_{mcp} = 1650V$ *(left)* and as a function of the MCP potential U_{mcp} for a target potential $U_{mcp} = 1600V$ *(right)*

Instrument aperture

As shown in figure 3.1 the MCP lies on the axis of the spectrometer's tube. It is circular with a sensitive area of 40 mm diameter. An ion will hit this sensitive area when its spatial coordinates at the time of reaching the plane of the MCP at $x = b_1 + d + b_2$ fulfill the constraint

$$y^2(t_{end}) + z^2(t_{end}) = (0.02m)^2 \tag{3.15}$$

3.1.4. Measured values

For both processes two signals have been used to characterise the process of plasma formation and the resulting plasma.

- Total electron charge yield at the target.
- Time-of-flight mass spectrum at the MCP: When secondary electrons are emitted from the channel walls by input of particles or radiation, they are accelerated by an electric field generated by a voltage V applied across both sides of the MCP. They travel along parabolic trajectories to strike the opposite wall, thus producing more secondary electrons. This process repeats itself many times along the channel. The result is a large number of electrons released from the output side. The released electrons are collected onto a simple metal anode connected to an amplifier. The amplifier's output signal then is recorded by an oscilloscope. To obtain a larger dynamical range, the MCP signal is recorded by two channels with different amplification factors. The signals are later on combined during signal evaluation.
- Furthermore, for impacting particles, the particles speed and charge had to be recorded. For this, the charge induced by particle passing a conductive tube is amplified and recorded by the oscilloscope (see Section 3.3.3). From the duration of the signal and the known length of the particle speed can be calculated. The amplitude of the signal represents the particle charge.

Figure 3.5.: *(left)* Photograph of the target chamber with some nice peoples' heads for size comparison. *(right)* Target chamber on its mounting with the turbo pump on bottom. Lead bricks are attached to the set up to dampen vibrations caused by the pump.

3.1.5. Target chamber and target mounting

In this section - as the core part of the *BERTA* spectrometer - the vacuum chamber containing the target is described as shown in Figure 3.2. Besides the acclerating sytem for the ions, consistent of the target and a graunded grid in fron, the target chamber also contains the focusing lens for the laser light (Section 3.4.6). The chamber has a diameter of 400 mm and the cover on its top is sealed with an O-ring (Figure 3.5). Within the chamber a vacuum between 10^{-8} mbar and 10^{-8} mbar can be achieved for measurements. As also shown in Figure 3.5 a turbo pump is mounted directly under the chamber, causing vibrations. In the following an overview of detailed interior of the chamber will be given, the target mounting, the mechanical set up for its alignment and the electrical feedthroughs.

Feedthrough and target mounting

The target mounting consists of a round iron plate with a diameter of 100mm and a thickness of about 3 mm and a round rod at its backside. The mounting is connected mechanically via a piece of an insulator to the feedthrough into the vacuum chamber, so it is electrical insulated from the environment (see figure 3.7). The feedthrough is constructed in that way, that the target mounting can be rotated and moved in translational direction independently. This is necessary for the experiments with the laser because the focusing lens is mounted fixed in the chamber and the beam is focused by moving the target plane. So the focal point can be adjusted and afterwards the impact location be changed without defocusing the beam. The alteration of the impact location is realized by rotating the mounting and the fact that the axis of the mounting lies 1.5 cm out of the symmetry axis of the vacuum chamber and the impact location as can be seen in figure 3.6. Thus the impact location ambulates on a circle around the rotation

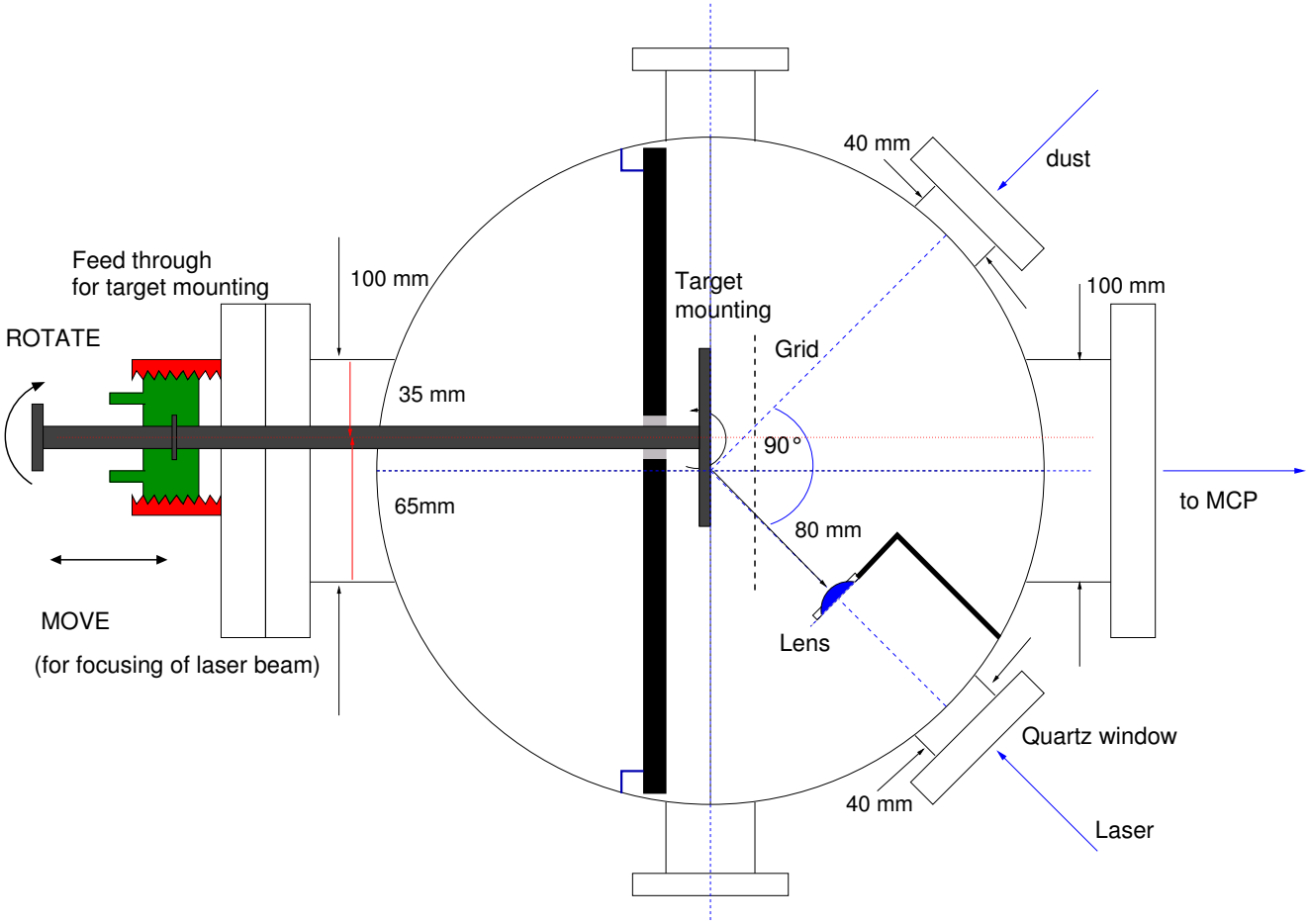

Figure 3.6.: Scheme of the target chamber

axis with a radius of 1.5 cm on the target.

Mounting for metal targets To guaranty an accelerating electrostatic field as homogenous as possible the metal target, which has a thickness os some tens of micrometers, is fixed on a plain iron plate. This plate is clamped with a clip into a matching cut-out in the plate (see figure 3.7)

Mounting for silicate targets The silicate targets are thicker and have much more irregular shapes then the metal ones. Thus the silicate pieces are fixed with two crossed wires on the target mounting as one can see in figure 3.7. Because of the resulting more complicated geometry of the target part one has to assume a field less homogenous.

3.2. Reflectron *TOF* mass spectrometer

The mass resolution obtained with the linear *BERTA* instrument has typical values of ∼10 to ∼80, depending on the acceleration potential and the properties of the particular ion mass line in question. As discussed above, in straight-tube time-of-flight mass spectrometers peak shape is directly related to the velocity distribution of the ions. To make up for that, reference data

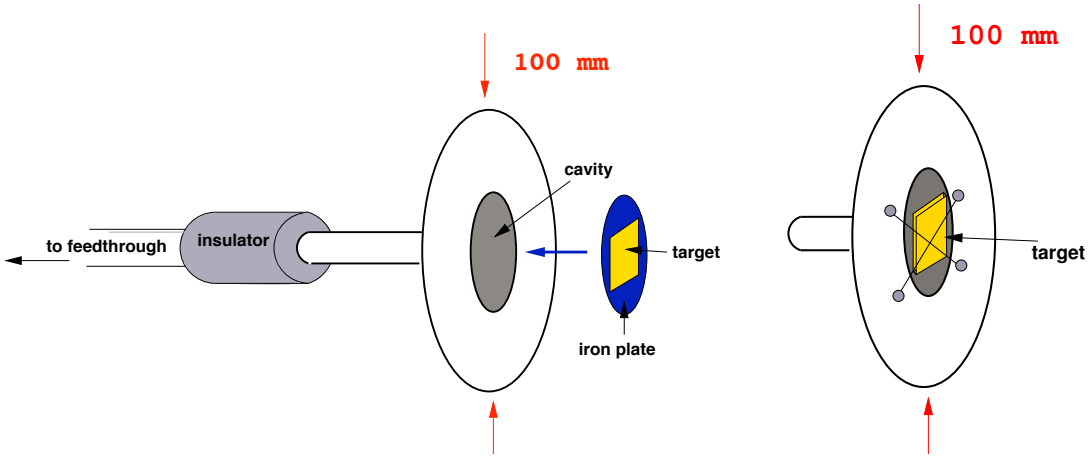

Figure 3.7.: Scheme of the target mountings for metal targets (left) and for silicate target (right)

with much higher mass resolution were recorded to obtain more reliable mass line assignments. for particle impacts with the same material combinations *TOF* mass spectra with two reflector type mass spectrometer, *LAMA* and *SUDA*, are recorded and compared to the *BERTA* spectra.

Reflectron mass spectrometer employ an ion reflector to compensate the spread in the ion initial energy. A retarding electrostatic field decelerates the ions and causes them to turn around. Thereby ions with higher initial energy will penetrate the reflectron more deeply then ions with lower kinetic energies. Consequently, faster ions spend more time within the retarding field. With the field strength and spatial configuration suitable chosen, ions with the same mass-to-charge ratio q/m will reach the detector at the same time (Mamyrin et al., 1973; Mauney and Adams, 1984; Moskovets, 1991; Bandura and Makarov, 1993).

Both mass spectrometers described in the following are components of a new developed type of instrumentation for in-situ investigation of cosmic dust particles in space, a so-called *dust telescope*. A dust telescope is a combination of a trajectory sensor and an analyser for the elemental composition of micrometeoroids or space debris. It was introduced by Grün et al. (2000) and its development and test is described in Srama et al. (2004b) and Srama et al. (2005). The trajectory sensor determines the dust particles' trajectories by the measurement of the electric signals that are induced when a charged grain passes through a position sensitive electrode system. The position sensitive system consists of four planes of wires where each wire is connected to a separate charge sensitive amplifier. Hence, the particle's velocity vector can be determined very accurately.

The elemental composition of particles is analysed by a time-of-flight system for the ions which are generated upon the particle impact. This mass spectrometer is represented by the *LAMA* instrument and for a modified, smaller version by the *SUDA* spectrometer.

3.2.1. LAMA

The Large-Area Mass Analyzer (*LAMA*) has a sensitive impact area of and a mass resolution of $m/\Delta m > 100$ (Srama et al., 2005). The instrument has a cylindrical symmetry and a ring-shaped impact target. There are different configurations were studied: LAMA1 has a short tube length in order to minimize the instrument size (Sternovsky et al., 2007), whereas LAMA2 is slightly larger due to an increased field free region between the acceleration grid and the ion reflector in order to incorporate a Trajectory Sensor (Figure 3.9). The impact detector consists

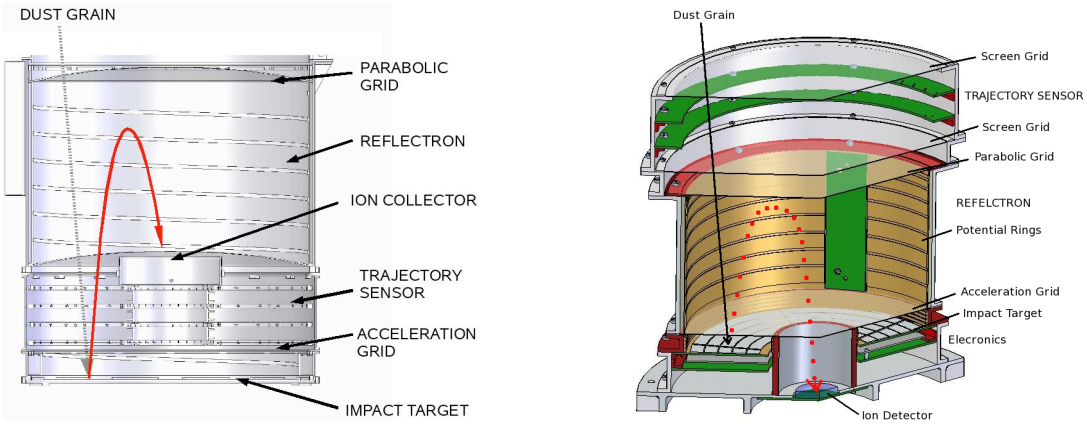

Figure 3.8.: Design studies of two different Dust Telescopes. Left: TS+*LAMA* with a target diameter of 60 cm (von Hoerner & Sulger). Right: *SUDA* with a target diameter of 20 cm (Schlemmer, 2008).

of a flat annular shaped impact target at +5 kV potential and a grounded acceleration grid mounted 50 mm in front of the target. Potential rings provide a smooth electric field close to the edges.

3.2.2. SUDA

The SUDA mass spectrometer is a scaled version of *LAMA* as described above. However, there are significant differences between the design of LAMA and SUDA, does not have a field-free drift region between the acceleration grid and the reflectron unit and employes a larger number of ring electrodes.

The impact target is a 220 cm^2 ring coated with a 20 μm gold layer. The target is attached to a *CSA* that measures the ion charge yield of the impact. Thus, the *SUDA* instrument can record the impact charge yield as well as the *TOF* mass spectrum. ions are accelerated to the energy $U_{acc} \cdot q$ by an electric field between the grounded target and the acceleration grid located 30 mm above the target. Four equally spaced ring electrodes between the target and the grid with voltages of 0.2Ue, 0.4Ue, 0.6Ue, and 0.8Ue en- sure a constant potential gradient inside the acceleration region. The deceleration region is between the acceleration grid and the lower shielding grid of the trajectory analyser and consists of the parabolically shaped reflectron grid and nine ring electrodes (Figure 3.9).

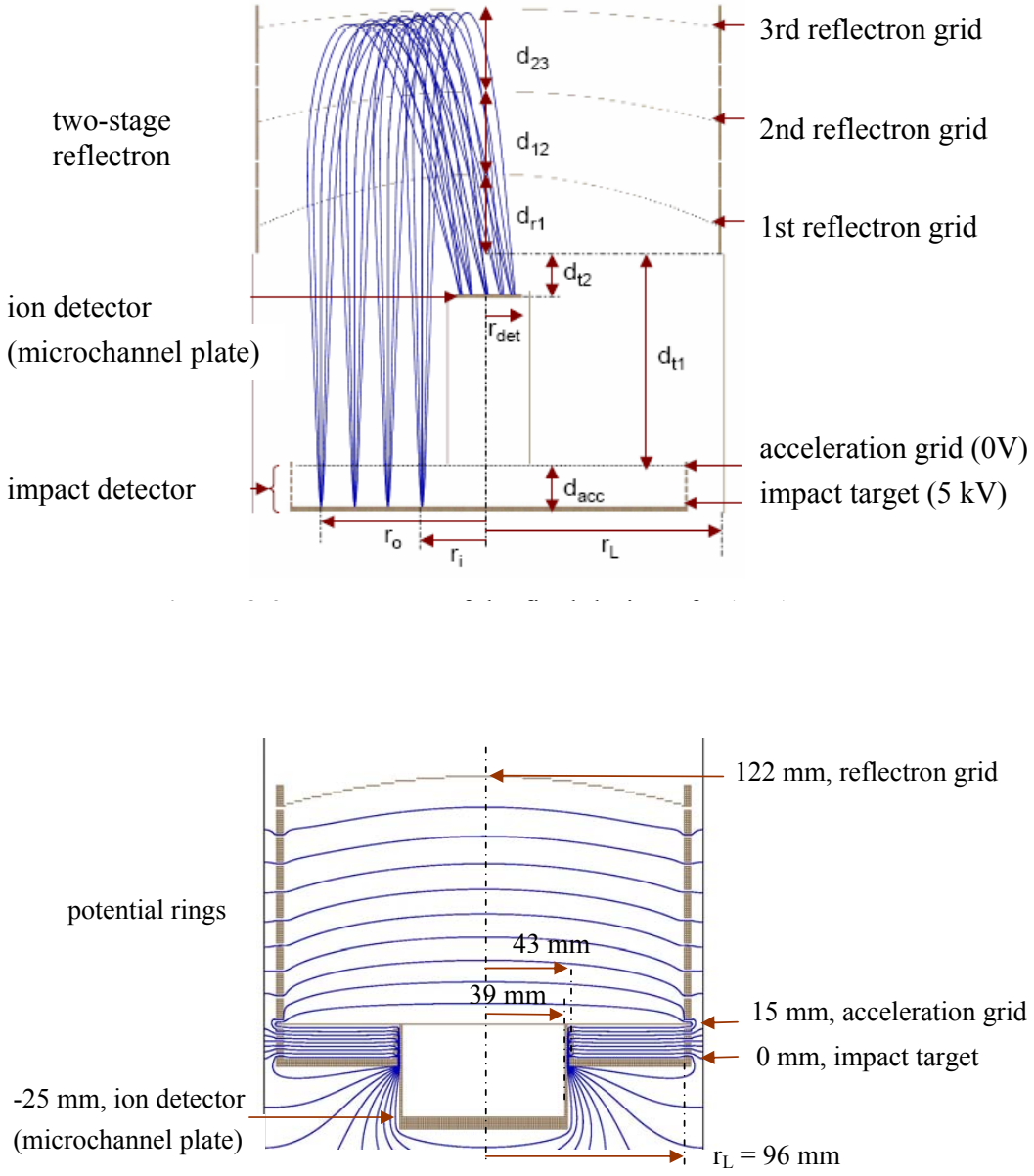

Figure 3.9.: Above: Schematics of *LAMA* and ion trajectories within the instrument. Bottom: Dimensions of *SUDA* including the potential lines shown in blue (Schlemmer, 2008).

3.3. Dust Accelerator

3.3.1. Generator

The dust accelerator is a modified Van De Graaff generator, able to reach a potential of 2 MV.

The generator uses a moving belt to accumulate very large amounts of charge on a hollow metal globe, the so-called *terminal*. On the bottom right side of the belt as shown in Figure 3.10 charge is sprayed onto a belt consisting of insulating Latex. The rotation of the belt then carries the charge to the high voltage terminal on the left side of the generator. There it is removed and collected on the terminal.

In order to obtain an electrostatically homogeneous electrical field, the gained potential of up to 2 MV decreases to ground over 60 potential rings, connected to each other by resistors of 1.2 GΩ. The potential is stabilised via corona discharge (Livingston and Blewett, 1962). To avoid discharging and sparking the generator is surrounded by a protective gas (SF_6 and CO_2) in a pressurised tank.

The dust source (see section 3.3.2) producing the dust beam is located in the high voltage terminal along with its associated electronic circuitry. After the positively charged dust particles leave the source they are accelerated in the electrostatic field which results from the decrease in the potential. They first pass the focusing cathode, in whose fields they are focused and afterwards two pairs of charged plates which are perpendicular to each other. With these so called *steerers* the beam can be deflected horizontally and vertically, and so be corrected if it is not perfectly axial.

The kinetic energies of the accelerated particles arise from the conservation of energy, where v the particle's velocity, q its charge and m the mass are linked by:

$$\frac{1}{2}mv^2 = q \cdot U_{pot} \qquad \text{with} \qquad U_{pot} = 2\ \text{MV} \tag{3.16}$$

From this equation and the measured charge and velocity the mass of the particle can be derived.

3.3.2. Dust sources and beam focusing

There are two types of dust sources used in the Heidelberg dust accelerator. One type is used for easily chargeable particles like iron, aluminium or carbon powder, developed by Shelton et al. (1960). The other type is a redesign of the original source optimised for the charging and acceleration of particles which are more complicated to charge, i.e. coated silicates or Latex particles (Stübig et al., 2001).

Common for both types is the so called *dust reservoir*, a cavity filled with the particles to be charged. This reservoir is charged in respect to the reference potential of 2 MV (acceleration potential). The resulting potential will be called the *electrode potential* in the following and is variable in a range from 0 to about 20 kV. The dust particles stored within the reservoir are then charged electrostatically by induction .

Old type dust source Figure 3.11 shows a schematic illustration of this type of dust source. The dust reservoir is a box-like cavity containing the particles to be charged. Several millimetres above the dust particles a small grid the so-called *tongue* is supported in a plane

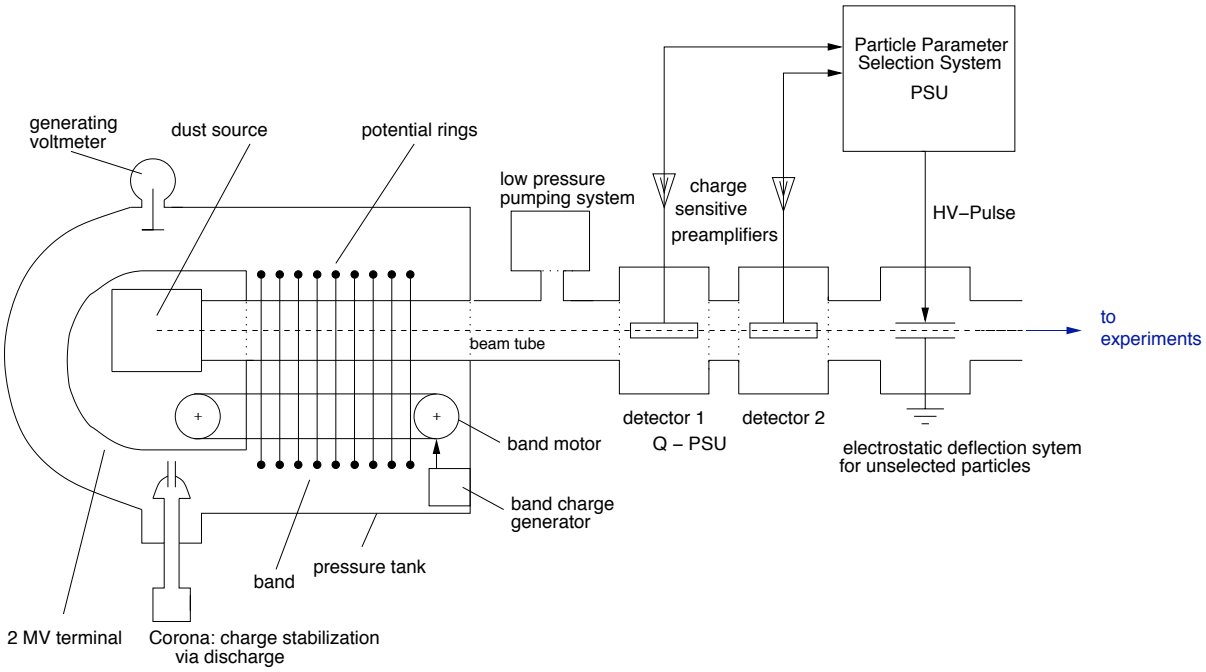

Figure 3.10.: 2 MV dust accelerator. The accelerating electrostatic field is provided by the potential difference of the *high voltage terminal* to ground. It is homogenous due to the decrease over 60 *equipotential rings* connected by resistors of 1.2 GΩ. The dust beam originates from the *dust source* within the *high voltage terminal*, after exiting the source, the dust particles are accelerated in the electrostatic field towards the experimental set-up located on the right side. Before reaching the target, the particles are registered, characterised, and eventually selected while passing the beam line detectors of the *Particle Selection Unit (PSU)*.

parallel to the powder's surface. The tongue is electrically insulated from the dust reservoir but normally maintained at the same potential. The potential of the tongue can be pulsed via the anode of a controlling tube (see Figure 3.11). An electric field is produced between the *tongue* and the particles, inducing a charge on the particles. If the electrical forces overcome the gravitational forces and the adhesion of the particles, some of the particles will be lifted from the surface (Friichtenicht, 1964). Hence the dust is dispersed in the reservoir and will behave similarly to molecules in a gas. Owing to collisions with the walls and other particles some dust will effuse out of the small hole shown in the upper left of the dust reservoir in Figure 3.11.They then enter the region between the outer wall of the reservoir and the *extraction plate* occupied by a *charging electrode* consisting of a little metal *tip* with a diameter of some μm supported by the outer wall of the reservoir and located in the accelerator axis. When a particle swirling around this region comes in contact with the *charging tip*, it acquires a much larger charge. Because of the small diameter of this tip - circa 50 μm, there is a very strong electrostatic field:

$$E = \frac{U_{electrode}}{r} = 4 \cdot 10^8 \frac{V}{m} \qquad \text{for} \qquad U_{electrode} = 20kV \tag{3.17}$$

Due to the shape of the grounded collimator plate located opposite, the electrical field in this region deflects the particle out of the source region in a trajectory relatively close to the accelerator's axis (beam line). Particles entering the accelerator tube are subsequently accelerated through the full potential difference of the accelerator.

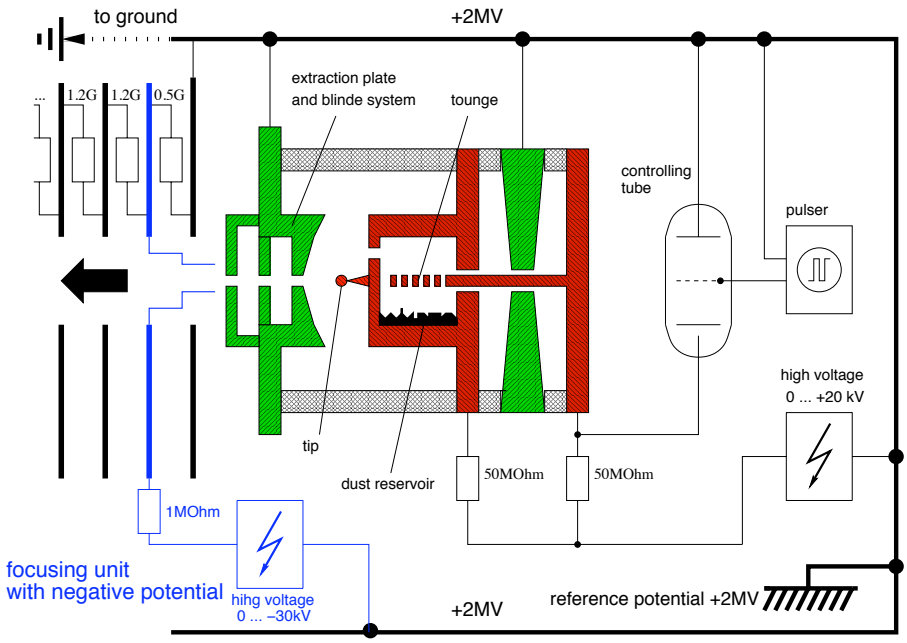

Figure 3.11.: Schematic of the old dust source with the associated electronic circuitry. The powder is charged due to the contact with the reservoir walls maintained with a tuneable potential of 0 to 20kV. The pulsed potential of the tongue located several mm above the powder leads to a random motion of particles within the reservoir. Particles effusing out of the hole in the reservoir wall slightly above the accelerator axis can come in contact with the charging electrode. Highly charged they are extracted by the field between the tip and the collimator plate and subsequently accelerated in the accelerator tube through the full potential difference towards the experiment.

New type dust source In order to maintain the opportunity to accelerate a bigger variety of dust materials, especially materials which are more difficult to charge, the dust source described above has been modified and redesigned. The shape of the reservoir has been altered to a cylindrical form of 10 mm diameter and 25 mm length.

The tongue has been replaced by a *tungsten needle* of 1 mm diameter, sharpened at the end to a few μm.The charging electrode outside the reservoir has been removed (see Figure 3.12).Additionally the hole through which the particles leave the reservoir has been moved just into the axis of the beam line. This leads to much more dust effusing out of the reservoir because the particles are directly injected into the beam line. An additional difference is the fact that unlike the old type dust source the potential of the reservoir is pulsed and not that of the needle. This is necessary because the projectiles will get their final charge at this needle and this has the corresponding function of both tongue and tip of the old type source.

Because of the pulsing of the electrode potential *(= potential of the reservoir)* the electrostatic charging of the dust fluctuates.

Beam focusing Charged particles are deflected by electrostatic and magnetic fields just like light in geometric optics. As in optics, such arrangements of fields are called lenses. This effect is used to focus the particle beam of the dust accelerator, in particular a electrostatic lens is applied (Demtröder, 2000a; Livingston and Blewett, 1962).

In the accelerator the lens system is realised by a particularly shaped aluminium cylinder

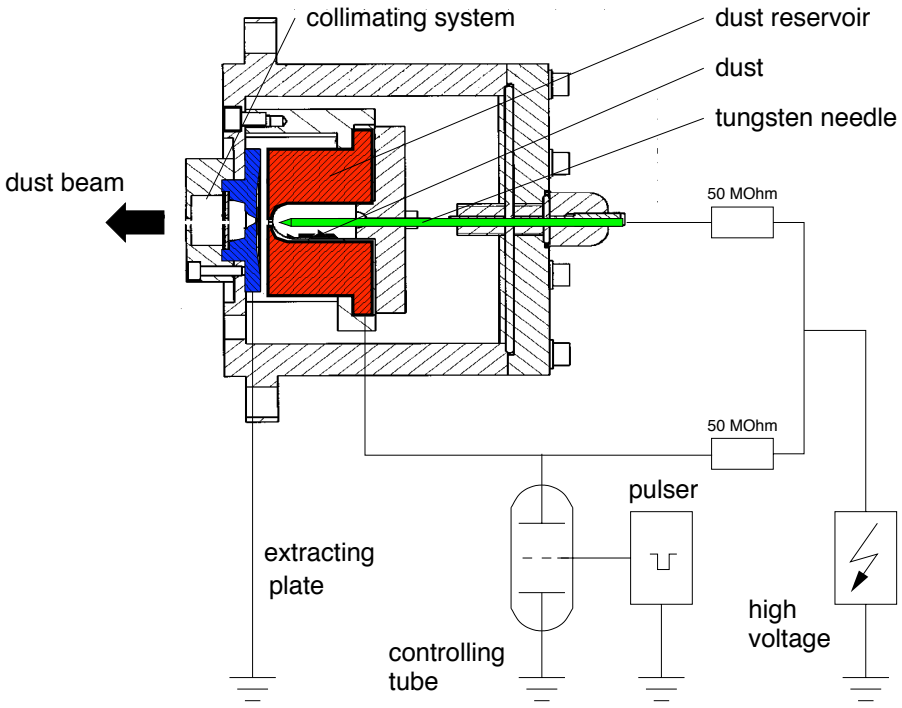

Figure 3.12.: Schematic of the new type dust source. The reservoir is re-shaped, the tongue is replaced by a tungsten needle, and the effusing orifice is placed in line with the beam line axis.

(*focusing cathode*), which lies in the beam tube directly behind the extraction plate closing the source. By varying the potential of the focusing cathode the potential difference between the two first equipotential rings can be varied as well. This leads to an alteration of the electrostatic field in this region and finally to a relocation of the focal point of the particle beam (Mocker, 2001).

Figure 3.13 shows the scheme of the focusing cathode and its location in the dust accelerator, together with a simulation of the field lines.

3.3.3. Particle Selection, velocity and charge measurement

After their acceleration the particles can be selected by their velocity, charge and mass according to the requirements of the specific experiment.

For this the individual particle's charge and velocity is acquired by a chain of detectors measuring the particle's primary surface charge using an induction tube and a charge-sensitive amplifier (*CSA*).

Charge and velocity measurement Passing into the induction tube of the detector, the charged particle induces electron movement in the metal tube. Electrons are attracted by the positive charge of the moving dust grain. If the electrode is connected to an electrical ground or a *CSA*, the positive charges move further away from the electrode. Now, the potential of the electrode is unbalanced by a negative charge of the same amount as the positive charge on the accelerated dust particle (Srama and S., 2008).

Due to a rising interest in measuring particles with very low primary charges a new low-noise

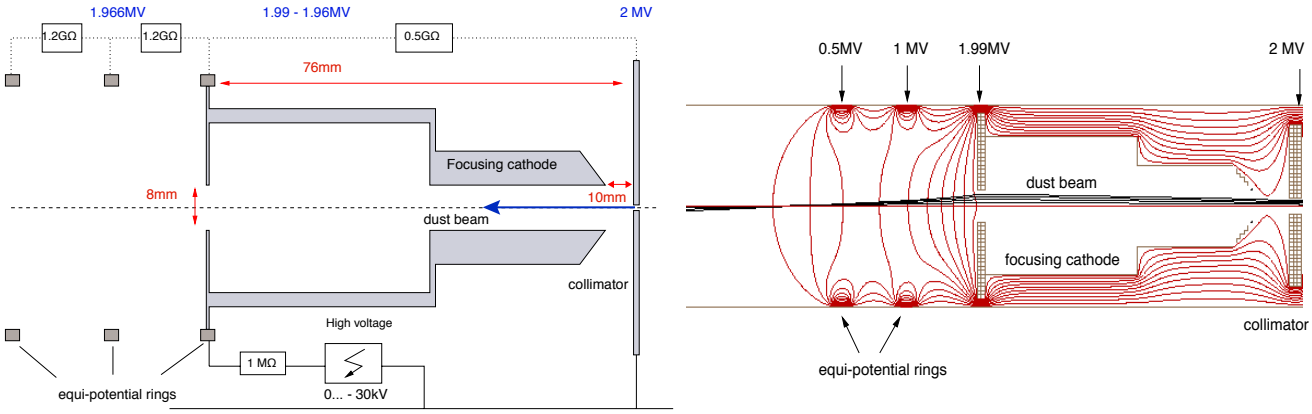

Figure 3.13.: Diagram of the focusing cathode *(left)*, electrostatic fields and dust beam within the focusing cathode. The potentials of the individual equipotential rings have been altered to better visualise the effect. *(right)*

detector has been developed for the beam line of the Heidelberg dust accelerator as shown in Fig. 3.14.

The velocity of the particle is determined by the flight time between two beam line detectors.

Particle Selection In its general functionality the Particle Selection Unit *PSU* has existed at the Heidelberg Dust Accelerator for decades (Rudolph, 1966). Over that time it has been modified and enhanced in many ways, with the most recent step being the implementation of the above described sensitive beam detectors and new control hardware and software.

For this the signals of three detectors are used: The first and the third give the trigger for the start and stop signals to calculate the particle speed, whereas the detector in between is used to determine the primary charge and therefore the mass of the particle.

Normally all particles are deflected away from the beam line by electrodes with a voltage of 4 kV. The user sets a speed and mass window within the control software to select dust grains with specific properties. The *PSU* compares the current particle speed and mass in real time and turns down the deflection voltage for a couple of microseconds if the dust grain lies within the set particle parameters (Rudolph 1966).

The main component of the new *PSU* is a *Field Programmable Gate Array (FPGA)*, capable of real time monitoring of the particle's speed and charge. The selection of particles by charge, speed and/or mass is possible.

The hardware consists of the FPGA and an embedded system running a hardened Linux variant hooked to an ethernet network (Helfert, 2010). On the Linux system, a small web server delivers the web client interface code to the *PSU* client computer. This client system can be placed anywhere, as long as there is connectivity to the institutional network. The *PSU* client runs on a web browser, and through an AJAX architecture (Asynchronous Javascript and XML) the data is sent from the *PSU* server. By this setup, the computing and network load on the *PSU* server is minimised. Only the actual measurement event values are transferred for an event. All data visualisation is done locally on the client system.

The error in the measured value of the particle mass consists of the errors in the measured acceleration potential U_{acc}, the charge of the particle and its velocity

$$\Delta m/m = \Delta U_{acc}/U_{acc} + \Delta q/q + 2\Delta v/v. \tag{3.18}$$

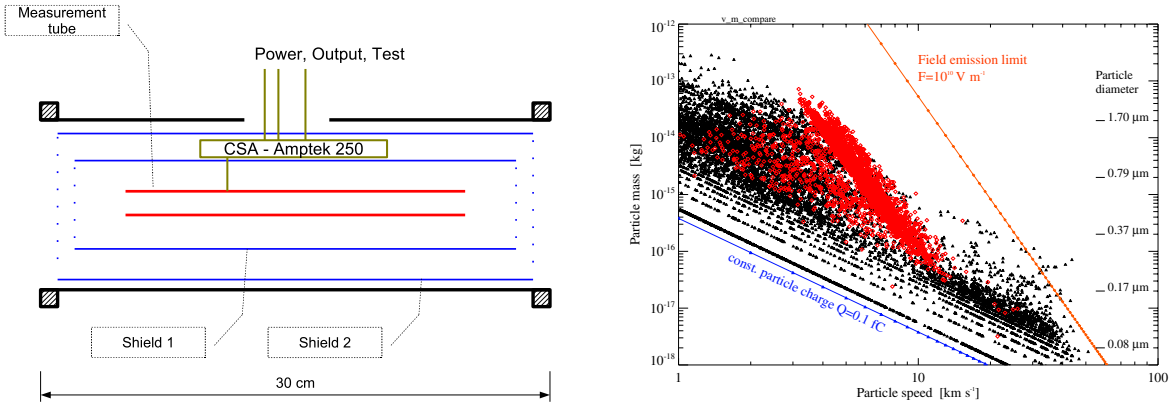

Figure 3.14.: Left: Charge detector developed with multiple electrical shields for the reduction of noise and thus lowering the threshold for particle detection. The inner cylinder acts as the charge detector only. The amplifier is located between the first and second shields. **Right:** Dust particle properties determined by the particle selection unit with the previous detector (red symbols) and the new beam detectors (black symbols) of the dust accelerator. The new detector monitors much smaller grains. The blue line at the bottom determines the detection threshold of 0.1 fC and indicates particles with a constant charge. The red line represents a field emission limit of the grains of 10^{10} V/m (grains with a constant field strength) (Srama and S., 2008).

The acceleration potential is determined very accurately, the error is about $\Delta U_{acc}/U_{acc} \approx 1\,\%$. The error in the velocity measurement is $\sim 5\,\%$. The uncertainty of the charge measurement due to the new set up improved from ~ 10 % to $\sim 3\,\%$.

Particle Parameters In order to reach high kinetic energies and subsequently high particle velocities, two requirements must be met. The accelerator potential as well as the charge-to-mass ratio (q/m) of the particles must be as high as possible. The accelerator potential is constrained by the generator and can be regarded as constant for a given facility. For this thesis the acceleration voltages ranged between 1.8 MV and 2.0 MV. The amount of charge which can be collected on a particles surface is restricted by the effect of field emission (Fechtig et al., 1978). Exceeding an electrical field strength at the particle's surface ($F \sim 10^{10}$ V/m), the repulsive force on the atoms forming the surface become sufficient to overcome the atomic binding energy. This leads to an emission of ions.

Electron Field emission from bulk metals was explained by quantum tunneling of electrons in the late 1920s by Fowler and Nordheim (1928). A family of approximate equations, *Fowler-Nordheim equations*, describing this process, is named after them (Čermák, 1994). Strictly, these equations apply only to field emission from bulk metals and (with suitable modification) to other bulk crystalline solids, but they are often used as a rough approximation to describe field emission from other materials.

Figure 3.15 shows speed and mass of iron and Opx particles monitored by the *PSU*. Both dust materials have been used for this thesis. The lower, blue, line indicates the detction threshold of 0.1 fC. The upper limit, drawn as a red line, is given by the maximum charge q a grain can contain on its surface. The threshold field emission limit for conductive material

equals surface potentials of up to 2000 V

$$\Phi = \frac{q}{4\pi\varepsilon_0 r} \tag{3.19}$$

(Srama and S., 2008). The potential Φ divided by the particle radius provides the electrical field strength $F = \Phi/r$ at the surface, limited depending on the grain shape and its surface properties. Assuming the maximum field strength is constant for all particle sizes for one particular material, broad fundamental relationships for the dynamical parameters of homogeneous spherical particles can be found. Knowing the particle's charge and velocity, its mass can be calculated using the conservation of energy Eq. 3.16. Estimating a spherical shape of the particle, its size can be calculated from the known mass and density.

$$m \propto r^3, \tag{3.20}$$

with m being the particle's mass and r its radius. A constant surface field leads consequently to a constant ration of charge per unit surface area

$$q \propto r^2. \tag{3.21}$$

Introducing this to Eq. 3.16 yields

$$r^3 v^2 \propto r^2 U_{acc}, \tag{3.22}$$

and subsequently

$$r \propto v^{-2},\ m \propto v^{-6},\ \text{and}\ q \propto v^{-4}. \tag{3.23}$$

Comparing this simple picture with empirical values, the assumption of a constant surface field strength F over the whole size range appears to be not correct. A better approximation is

$$F \propto r^{-1/2}, \tag{3.24}$$

(Fechtig et al., 1978), leading to

$$m \propto v^{-4},\ \text{and}\ q \propto v^{-2}. \tag{3.25}$$

Figure 3.16 illustrates the relation between the particle parameters, velocity v, radius r, mass m, kinetic energy $E_{kin} = 1/2mv^2$, and the energy density $D = E_{kin}/\pi\, r^2$, and their distributions for a large amount of iron particles.

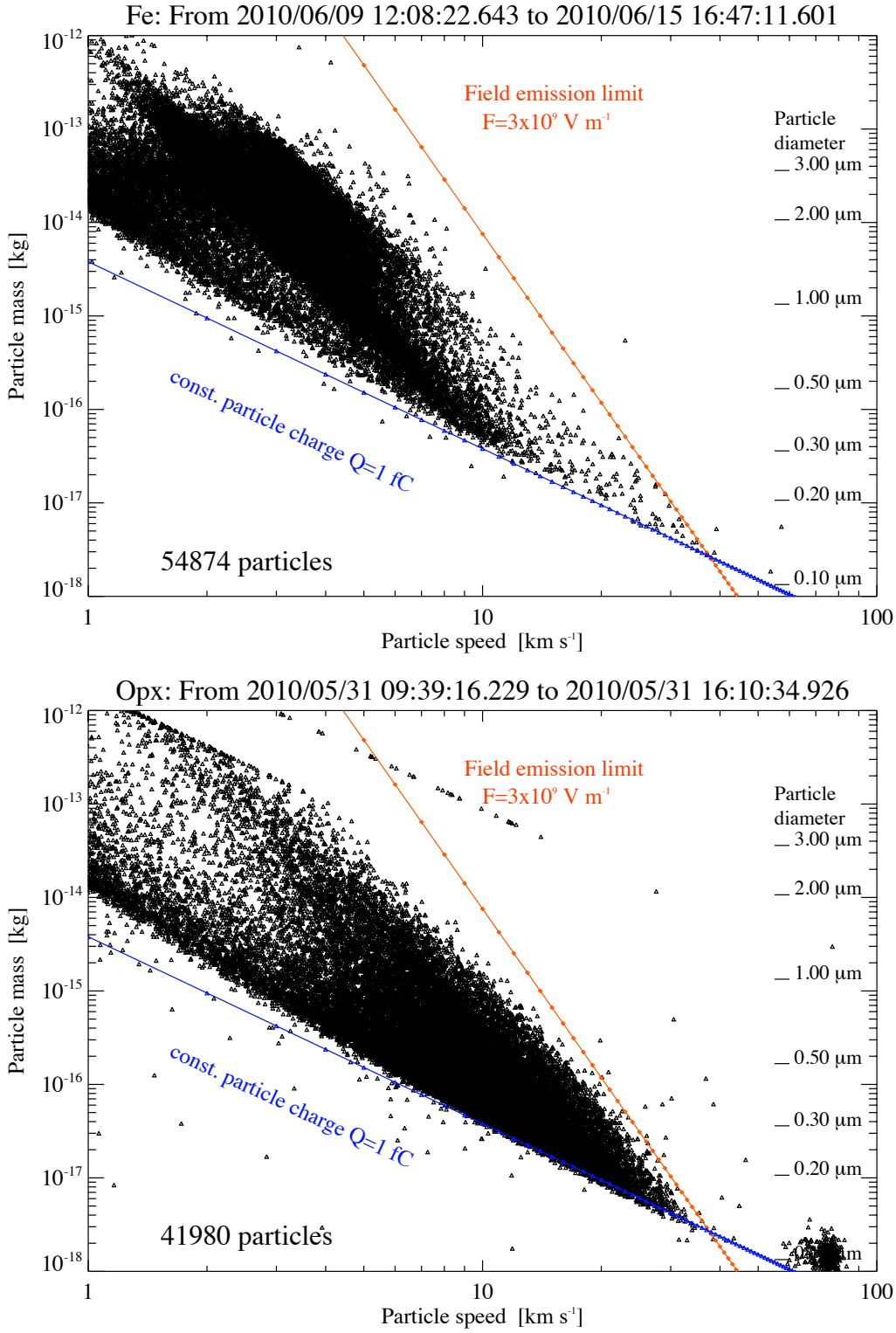

Figure 3.15.: Velocity mass distribution for iron *(above)* and orthopyroxene particles *(bottom)* As in Figure 3.14, the blue line at the bottom determines the detection threshold of 0.1 fC and indicates particles with a constant charge. The red line represents a field emission limit of the grains of 10^{10} V/m (grains with a constant field strength) (Srama and S., 2008).

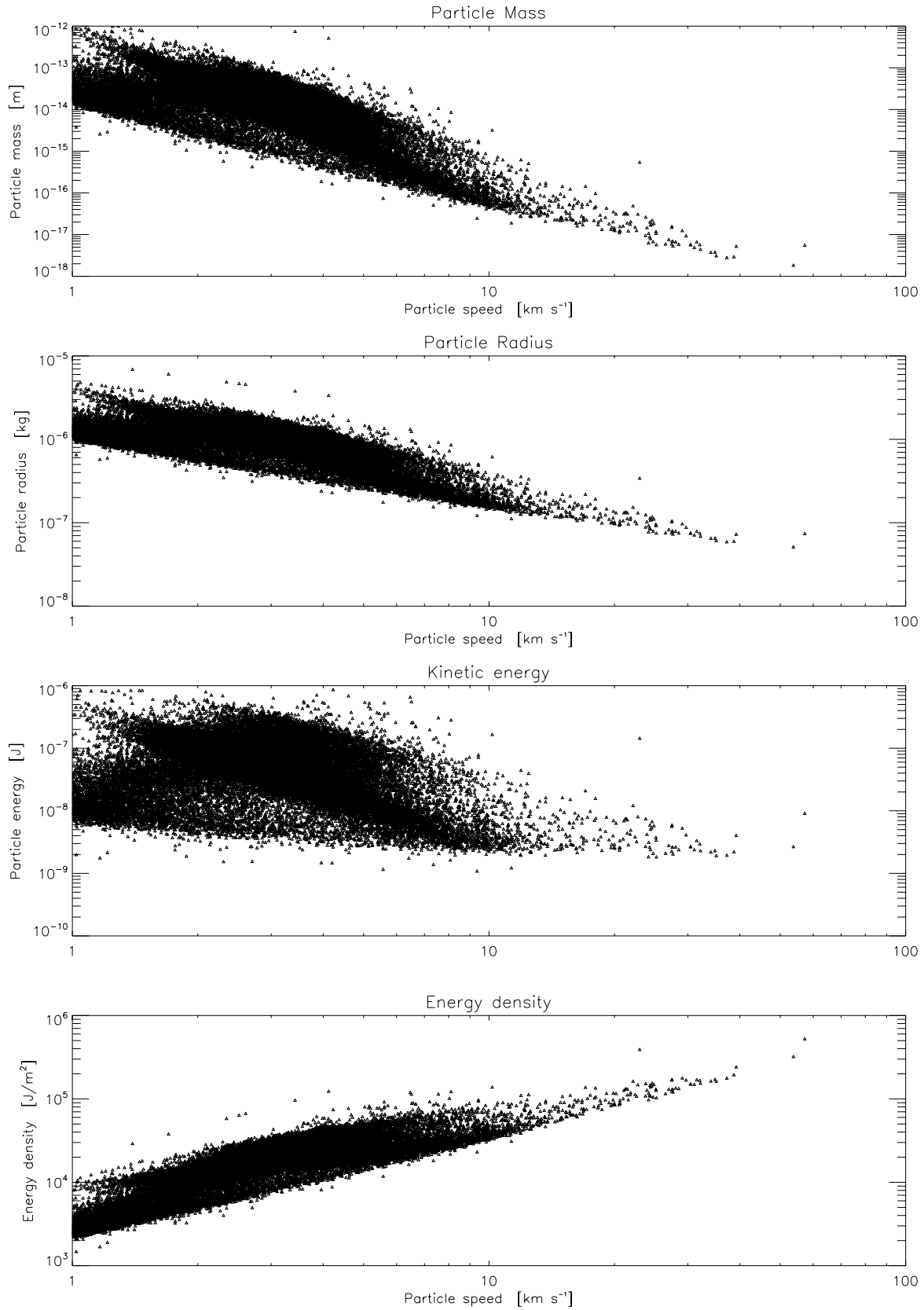

Figure 3.16.: Relation between characteristic particle parameters velocity v, radius r, mass m, kinetic energy $E_{kin} = 1/2mv^2$, and the energy density $D = E_{kin}/\pi\, r^2$ for iron dust particles.

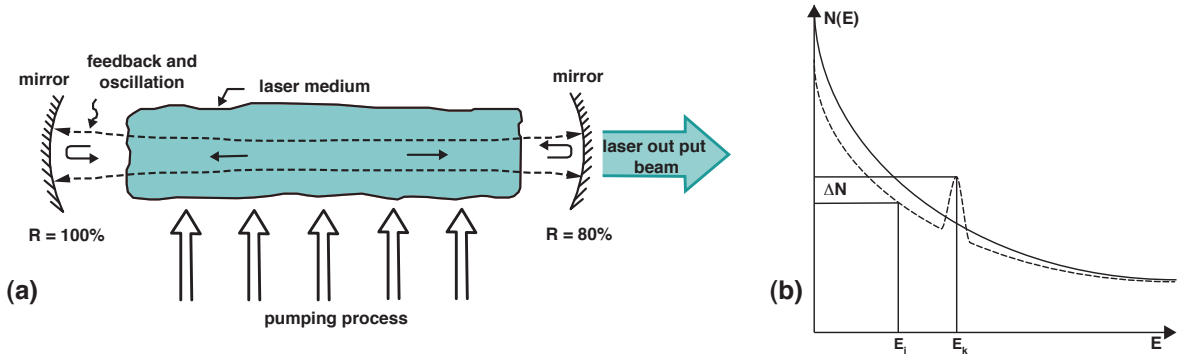

Figure 3.17.: (a) Elements of a typical laser oscillator. *(b)* Thermal population (solid line) and population inversion (dashed line)

3.4. Laser

In this section a short overview of the used laser set up is given. Firstly the overall working principle of lasers is described, followed by the technical and principle description of the used Nd:Yag. Then an overview of the optical beam line and the calibration of the laser set up is given.

Lasers are devices that generate or amplify radiation in the infrared, visible or ultraviolet regions of the electromagnetic spectrum (Siegman, 1986). ”Laser” is an artificial word, an acronym meaning *”**L**ight **A**mplification by **S**timulated **E**mission of **R**adiation”*, describing the underlying general principles of function. This principle was first invented at microwave frequencies by Gordon et al. (1955), termend ”maser”. The principle was extended to optical frequencies by Maiman (1960), inventing the first ruby laser.
There is a great variety of forms, used materials and resulting wave lengths for Lasers. But all have in common essential elements in their construction and a general principle in function.

- A *laser medium*, consisting of either a solid body, a liquid or gas,
- a *pumping process*, exciting the atoms or molecules of the medium into higher quantum-mechanical energy levels,
- an *optical feedback* that allows the beam of radiation either to pass through the laser medium (= *laser amplifier*) or bounce back an forth repeatedly through the laser medium (= *laser oscillator*).

The pumping process generates an occupation of one or more energy levels differing extremely from the occupation in thermic equilibrium. For high pumping powers for at least one energy level $|k\rangle$ with the energy E_k the occupation density N_k is exceeding the density N_i of an energetic lower level $|i\rangle$ connected with $|k\rangle$ by an *allowed transition* (Demtröder, 2000b). This state is termed *inversion*. Once population inversion is obtained, electromagnetic radiation passing through the laser medium can be coherently amplified within a certain band of frequencies. This means, the input signal will be reproduced by the out put signal, except for a substantial increase in amplitude.Carefully aligned mirrors at each end of the laser medium lead together with the coherent amplification lead to an oscillation, if the net amplification

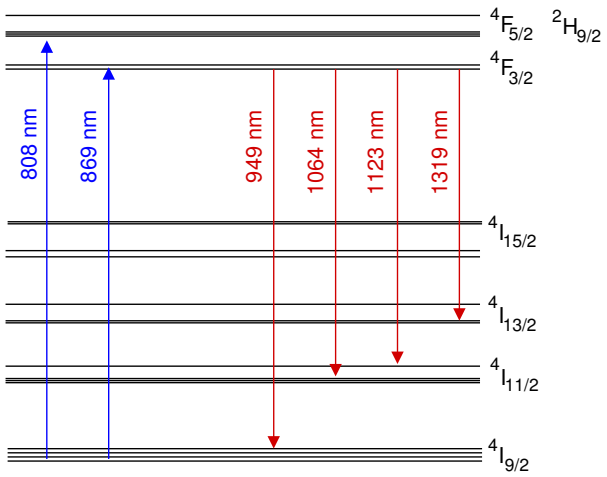

Figure 3.18.: Energy level structure and common pump and laser transitions of the trivalent neodymium ion in Nd^{3+}:YAG.

between the mirrors exceeds the losses due to scattering and absorption. Finally a highly directional and monochromatic out put beam can be coupled out of the laser, i.e. through a partially transparent mirror on one end of the laser medium. This out put is both, extremely bright and highly coherent.

3.4.1. Nd:YAG laser

For this work a solid-state laser with neodymium-doped yttrium aluminum garnet (Nd:$Y_3Al_5O_{12}$) as lasing material was used . The $Y_3Al_5O_{12}$ lattice is hard, stable, optically isotropic and accepts substantially trivalent ions of both the rare-earth and the iron group. Because of that it is easily doped with Nd^{3+}-ions, shown in laser operation for the first time at *Bell Laboratories* by Geusic et al. (1964).

The outcome is an four-level system, whose levels are splitting further more. It absorbs mostly in the bands from 730 nm to 760 nm and from 790 nm to 820 nm. Therefore, the laser can be pumped very efficiently at various wavelengths within this ranges.

The material typically emit light in the infrared at a wavelength of 1064 nm, besides there is also emittance near 940 nm, 1120 nm, 1320 nm, and 1440 nm (see Figure 3.18).

Nd:YAG is a four-level gain medium (except for the 946-nm transition), offering substantial laser gain even for moderate excitation levels and pump intensities. The gain bandwidth is relatively small, but this allows for a high gain efficiency and thus low threshold pump power (Koechner, 1976).

Nd:YAG lasers can be diode pumped or lamp pumped. Lamp pumping is possible due to the broadband pump absorption mainly in the 800-nm region and the four-level characteristics. They can be operated in continuous as well as in pulsed mode, depending on this the amount of the neodymium dopant in the material varies. For continuous wave output, the doping is significantly lower than for pulsed lasers.

The high-intensity pulses may be efficiently frequency doubled, tripled or quadrupled to generate laser light at higher harmonics, i.e. 532 nm, 355 nm, and 266 nm.

Table 3.1.: Manufacturer's specification for the laser used for this thesis

power of pulses:	$P_P \leq 200$ kW
wavelength:	$\lambda = 355$ nm (UV)
pulse length:	$T_P = 5$ ns to 20 ns
pulse frequency:	single pulse or $\nu \leq 200$ Hz
beam diameter:	0.4 mm
	after internal broadening: 2 mm
	after external broadening: 20 mm
broadening:	1.4 mrad ($TEM_{00}M^2 < 1.4$)
polarisation:	linear (100:1)

3.4.2. Functionality and Q-Switch

In general Nd:YAG solid state laser would work continuously. To obtain pulses of about 5 ns duration, a so called "Q-switch" is . Here, the letter Q stands for "quality" and describes the quality of the optical resonator of the laser.
A attenuator is placed inside the lasers's optical resonator. Initially the laser medium is pumped while the attenuator is set to prevent feedback of light into the gain medium. This results in a population inversion, but laser operation cannot yet occur since there is no feedback from the resonator.

The rate of stimulated emission is dependent on the amount of light entering the medium. Thus, the amount of energy stored in the gain medium increases as the medium is pumped. Due to losses from spontaneous emission and other processes, after a certain time the stored energy will reach some maximum level; the medium is said to be gain saturated. At this point, the Q-switch device is quickly changed from low to high quality, allowing feedback and the process of optical amplification by stimulated emission to begin. Because of the large amount of energy already stored in the gain medium, the intensity of light in the laser resonator builds up very quickly; this also causes the energy stored in the medium to be depleted almost as quickly. The net result is a short pulse of light output from the laser, which may have a very high peak intensity (Eichler and Eichler, 1998).

3.4.3. Technical Properties

In order to achieve a wavelength of 355nm (UV) the fundamental wavelength of the Nd:YAG-Laser is shortened by a frequency tripler (Franken et al., 1961). The pulse energy as well as the pulse duration depend on the supply current of the pumping diode. The beam widening attached on the exit window leads to an attenuation of the beam energy. The pulse frequency is to be varied an a range from 1 Hz to 200 Hz. Triggering the laser Q switch externally by a rectangular pulse of 5 V (TTL signal by a pulse generator) allows to operate in a single shot mode. The laser itself generates a out coming pulse, used for triggering the data recording by the oscilloscope. Besides the supply current of the diode, the output energy depends on the temperature of the gain medium (Geusic et al., 1964). Therefore it needs to be preheated for about 15 minutes before the measurements while shooting several hundred times.

Table 3.1 lists the technical properties of the laser used for this study.

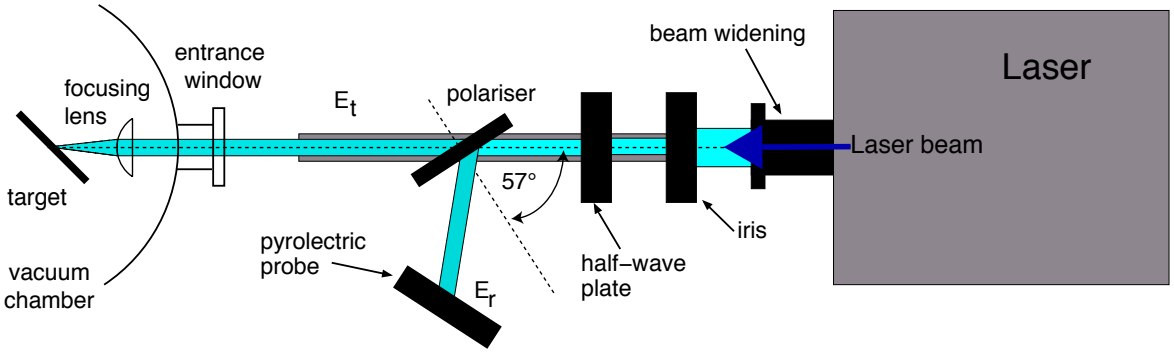

Figure 3.19.: Optical path: The path of the laser light form the laser device to the target is shown from right to left. First the beam is widened, then it is masked by an iris. After the polarisation state is rotated by a have-wave plate, the beam is splitted up into two perpendicular polarised beams, of which one is deflected outwards the beam line. The energy of the deflected part is measured for each pulse by a pyroelectric joulemeter. The transmitted beam part passes then the entrance window of the vacuum chamber and is afterwards focused onto the target by a plano-konvex lens.

3.4.4. Optical path and optical properties of the laser set up

Before the laser beam hits the target, it passes through a chain of subsequent devises, called *optical path*.

The optical path is designed to fulfill two main aims, to stabilise the laser energy out put and to measure and control the power density of the incident light. Besides the beam is guided and focused onto the target plane.

Beam widening The intensity profile of laser beam produced by the laser device described above is of Gaussian shape. After its generation it passes two stations of beam widening, expanding the diameter of the beam. In a first step still inside the device's casing it is expand to a diameter of 2 mm. In a second step it is broadened by an external lens system. Finally the beam diameter reaches a size of 20 mm.

Beam manipulation and laser energy control In order vary the laser energies for the experiments, the output energy of the laser has to be controllable. This can be done on the one hand by adjusting the diode's supply current. this method has disadvantages described later on due to the dependence of the stability of the out put energy on the pumping current (Section 3.4.7). As an alternative the laser beam can be manipulated to reduce and control the energy of the laser beam hitting the target. The following part of the *optical path* is dedicated to this purpose.

(a) Masking the extended beam with an iris. This reduces and stabilises the beam energy (see Section 3.4.7)

(b) Rotating the light's direction of polarisation with an *half-wave plate*, which retards the phase of by half a wavelength, or 180 degrees. Rotating the half wave plate causes the polarisation to rotate to twice the angle of the half wave plate's fast axis with the polarisation plane.

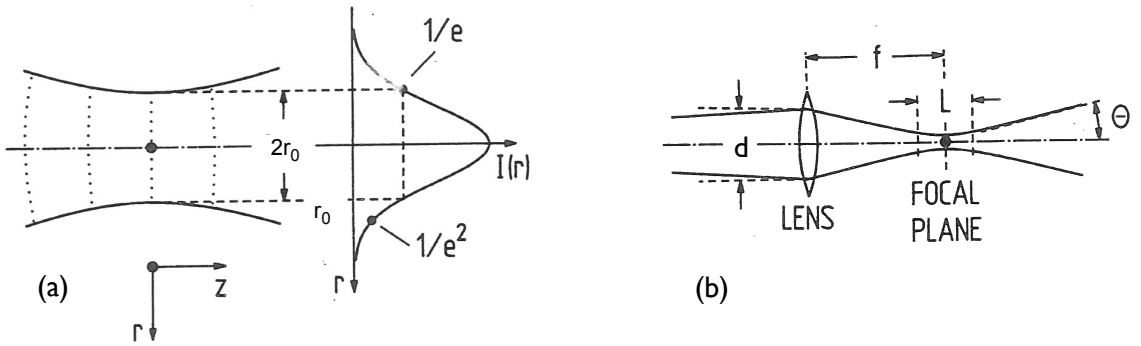

Figure 3.20.: (a) Intensity distribution and shape of a Gaussian beam near the focal plane. The dotted lines indicate the shape of the wave front. (b) Depth of sharpness *L*. $2r_0$ is the beam waist, *d* is the diameter of the beam in the middle of the focusing length, *f* is the focal length, and Θ the beam divergence angle. (Bäuerle, 1996)

(c) Partially deflection of the light outwards the beam line by a *polariser*. The linear polarised light incident under the *Brewster's angle* (57°) is partially deflected outward the beam line. The portion polarised parallel to the plane of incidence is transmitted, the part polarised perpendicular to it is deflected. Thus, rotating of the polarisation leads to varying the ratio of the energy of the reflected and transmitted beam.

Beam guidance Afterwards the beam is guided into the vacuum chamber, passing the entrance window. This window consists of fused quartz . Last plano-konvex quartz lens with a focal length of 80 mm focuses the beam onto the target.

3.4.5. Beam profile and focal point

The TEM_{00} mode used for this study is of Gaussian shape. Therefore the beam intensity within the focal plane has the form

$$I(r) = I_0 \cdot exp\left(-\frac{r^2}{r_0^2}\right), \tag{3.26}$$

where $\mathbf{r_0}$ is the radius of the laser focus defined by $I(r_0) = I_0/e$.
The total laser power is

$$P = 2\pi \int_0^\infty r \cdot I(r)\, dr. \tag{3.27}$$

The intensity distribution of a gaussian shaped beam profile is shown in the left of Figure 3.20.

Diameter of the focal point

The initial laser beam has a Gaussian profile and a diameter of 20 mm. Before it is splitted by the half-wave plate and the polariser, it is reduced in diameter by an iris to diameters of a few mm. After passing the have-wave plate, the polariser, and the entrance window of the

vacuum chamber, the beam is focused on the target by a lens with a focal length of 80 mm. The diameter of the focal point for a beam diameter of 2 mm for the incident beam is given by (Bäuerle, 1996)

$$r_0 \simeq \sqrt{2} \cdot \frac{f \cdot \lambda}{\pi \cdot d} = \sqrt{2} \cdot \frac{0.08m \cdot 355 \cdot 10^{-9}m}{\pi \cdot 0.002m} = 6.4\,\mu\text{m}, \tag{3.28}$$

with f being the focal length, λ the wave length, and d the diameter of the laser beam.
Since the laser beam incidents the target under an angle of 45°, the beam spot is an ellipse with a semi-minor axis of $2 \cdot r_0$ and the semi-major axis of $2 \cdot r_M = 2 \cdot r_0 / \cos 45° \approx 18.1\,\mu$m.

Depth of sharpness

The extent of the region in which the laser beam stays focused is determined by the depth of sharpness. This distance defines the necessary accuracy of the focussing the depth of sharpness. The depth of sharpness is determined by properties of bot the lens and the laser beam and is defined by

$$L = 2 \cdot z_R = \frac{4\pi r_0^2}{\lambda} = \frac{8 f^2 \lambda}{\pi d^2}, \tag{3.29}$$

where z_R is the *Rayleigh length*, the distance from the focal plane, over which the diameter of the beam changes by a factor of $\sqrt{2}$.
For a beam diameter of 2 mm and a focal length of 80 mm, the depth of sharpness is about 1.4 mm. This is large in comparison to the roughness of any surface used for this thesis.

3.4.6. Focusing

In order to focus the laser beam the target plane has to be moved because of the static nature of the lens mounting. As described in section 3.1.5 this can be done by manipulating the target mounting on the feedthrough its fixed on. Here the accuracy of the determination of the distance is more crucial to the quality of the focusing than the lead of the winding at the feedthrough's mechanism. Both uncertainties are small in respect to the depth of sharpness and because of that fair enough.
A direct control of the spot size and the focusing was not possible with the used set up. The focusing was done by optimising the resulting charge yield at the particular location on the target.
In the case of the gold coated olivine target an optical analysis of the irradiated sites was possible with an optical microscope. The laser obviously ablated the could coating leaving recognisable tracks on the target surface, able to be measured (Fig. 3.21). The width of the smallest features, identified as the size of the focal spot is about 10 to 15 μm. This matches the calculated spot size, justifying the performed process for finding the optimal focal settings.

Measurement of the laser energy

The energy of the laser beam is measured with an *pyrolectric probe* in combination with a joule meter. The probe translates the heat produced by the incident laser beam in a dielectric into the variation of the capacitance. The variation is then amplified and processed by the joule meter. In addition to the measurement of the energy of a single shot, the joule meter also provides the average energy over a set number of shots and the standard deviation.

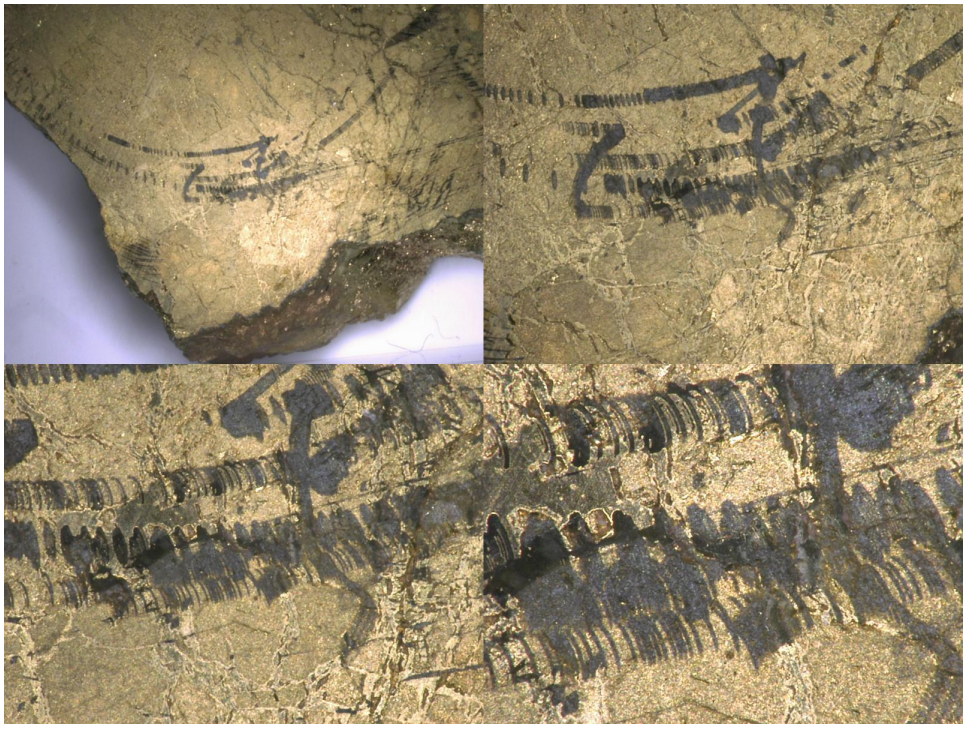

Figure 3.21.: Microscopic photographs of tracks generated by the laser on the surface of the gold coated olivine target. Shown is a series of photographs zooming in to the structures created by the laser beam ablating the gold coating. The smallest structures have a width of about 10 μm.

3.4.7. Calibration of the laser set up

This section describes the measurements performed to characterise and calibrate the laser set up. The stability of the laser out put and its dependency on laser parameters and the properties of the optical components and of the laser energy. For this, the statistical mode of the joule meter has been used, for each parameter setting the energy of 100 shots have been recorded, averaged and the standard deviation was calculated.

Dependence of the laser energy and the laser energy spread on the pumping current

The out put energy of a diode pumped solid state laser depends on the pump energy, thus, on the supply current of the pumping diode. The dependence of the out put energy on the diode current was measured with the pyrolectric probe placed directly after the beam widening (Fig. 3.22 (a)). Figure 3.23 shows the dependency of the measured laser energy in dependence on the set diode current, each data point is the average of 100 shots. The measurements was repeated four times, termed as *Run 1* to *Run 4*. The dependence of the output energy on the diode current is approximately linear for diode currents above about 50 A.
To measure the energy spread and characterise the stability of the laser energy output the standard deviation for each 100 shots was recorded with the joule meter for two of the four runs. From the dependence of the absolute spread as well as the relative spread on the diode current shown in the same Figure 3.23, one can see that the relative stability is increasing with

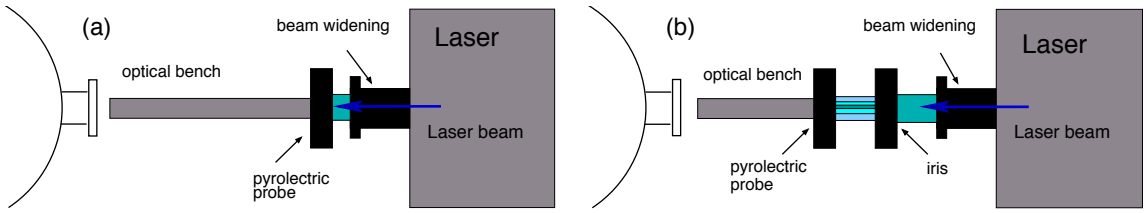

Figure 3.22.: Characterisation of the laser set up. (a) Measurement of the dependence of the laser energy put put and its stability on the diode current. The pyrolectric probe was placed directly after the beam widening. (b) Measurement of the energy and its spread in dependence of the iris' aperture.

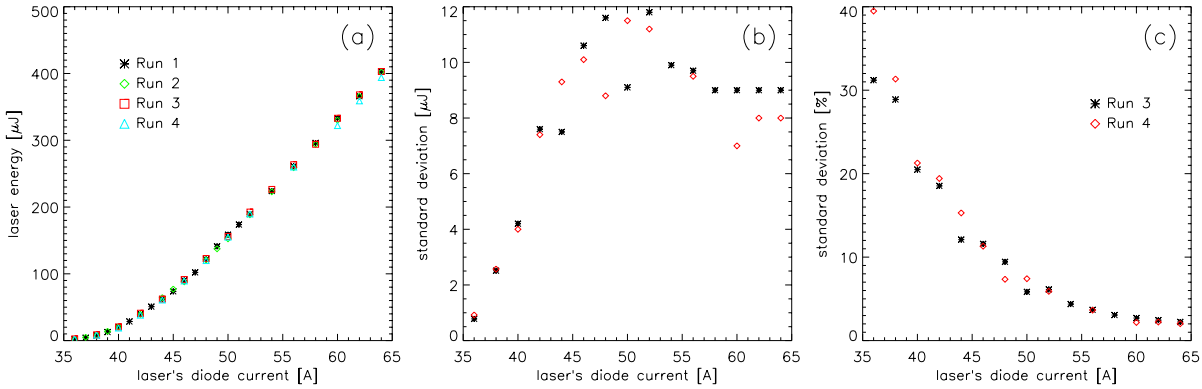

Figure 3.23.: Characterisation of the laser set up. (a) Dependence of the laser output energy on the pumping diode current. (b) Stability dependence on the diode current, shown is the absolute standard deviation of 100 shots for each setting of the supply current. (c) Relative spread of the laser energy as a function of the diode current.

increasing diode current.

Dependence of laser energy and laser energy spread on the iris' aperture

After the beam is extracted by the beam widening it is masked with a flexible iris to reduce the energy of the beam. In order to quantifiy this decrease in energy and to characterise also the dependence of the beam energy stability, the out put energy and its spread were measured directly behind the iris for apertures from 1 mm to 17 mm (Fig. 3.22 (b)). The accuracy of the aperture's setting is 0.1 mm.

Figure 3.24 shows the linear dependence of the laser out put energy on the iris aperture for diode currents from 40 A to 60 A, absolute energy spread, and the relative energy spread. The relative spread is constant for increasing apertures.

Consequential settings for the laser set up

The setting of the laser set put for the measurements have been chosen on the ground of an optimum for an wide energy range, the stability of the leaser energy out put, and the focusing

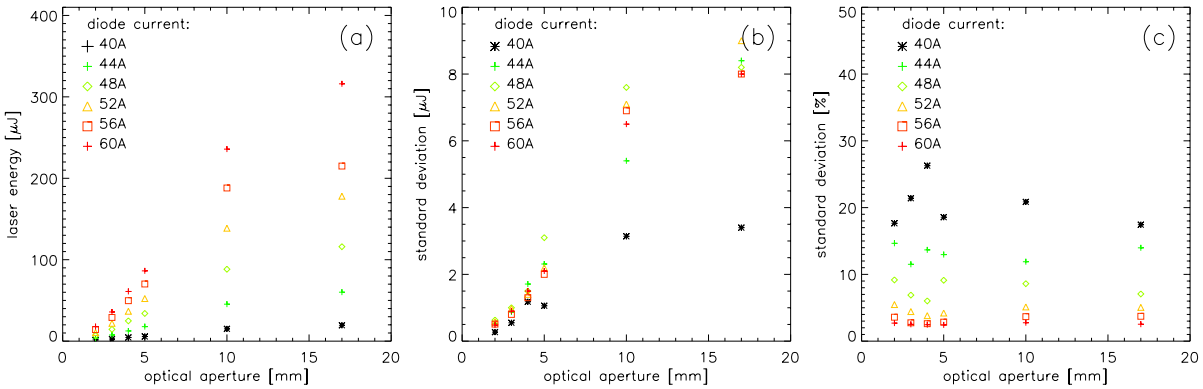

Figure 3.24.: Characterisation of the laser set up due to the iris aperture. (a) Dependence of the laser output energy on the iris aperture for different diode currents. (b) Stability dependence on the iris aperture, shown is the absolute standard deviation of 100 shots for each setting of the supply current. (c) Relative spread of the laser energy as a function of the iris aperture.

of the laser beam. onto the target. Thus, a high diode current of 58 A and an iris' aperture of 3 mm were set. The beam with a diameter of 3 mm can be the focused on a elliptical spot on the target with a theoretical semi-minor axis of $r_0 \approx 4.2\,\mu$m.

Attenuation of the laser beam by the optical path components

With each passing through one of the optical components chained up in the optical path a part of the laser energy is lost due to absorption and deflection. The material used for the entrance window and the focusing length have been chosen to obtain a suitable transmittance in the wave length range in question, i.e. 355 nm. Yet in order to get an estimation of the attenuation by the entrance window, the beam energy was recorded for 1000shots each in front and behind the window for a diode current of 56 A and an iris aperture of 3 mm. The averaged energy in front of the window was 21.9 μJ $\pm$0.6 μJ and after the passage through the glass 17.8 μJ $\pm$ 0.6 μJ. Thus the resulting attenuation is 18.7 % $\pm$ 0.04 %. In the following the attenuation will be not included into the given values of the laser energy.

3.4.8. Laser energy control

As described in section Section 3.4.4, the laser energy out put can be controlled by deflecting a variable portion of the laser beam outwards the beam line. The ratio of the transmitted to the reflected beam energy is determined by the orientation of the optical axis of the half-wave plate towards the spatial orientation of the laser light's polarisation. But neither the orientation of the half-wave plate nor the spatial orientation of the laser beam's field vector is known. Therefore, all specification of the angle of the half-wave plate are referring to an arbitrary position. The definition of the angle γ characterising the orientation of the halve-wave plane is illustrated in Fig. 3.25. Additionally the accuracy of the angle of the polariser towards the beam plays an important role. The mechanical tolerances and imprecisions of the mountings of both optical components, the half-wave plate's as well as the polariser's, lead to uncertainties in the determination of the ratio of transmitted as well as reflected energy and thus, requires a charac-

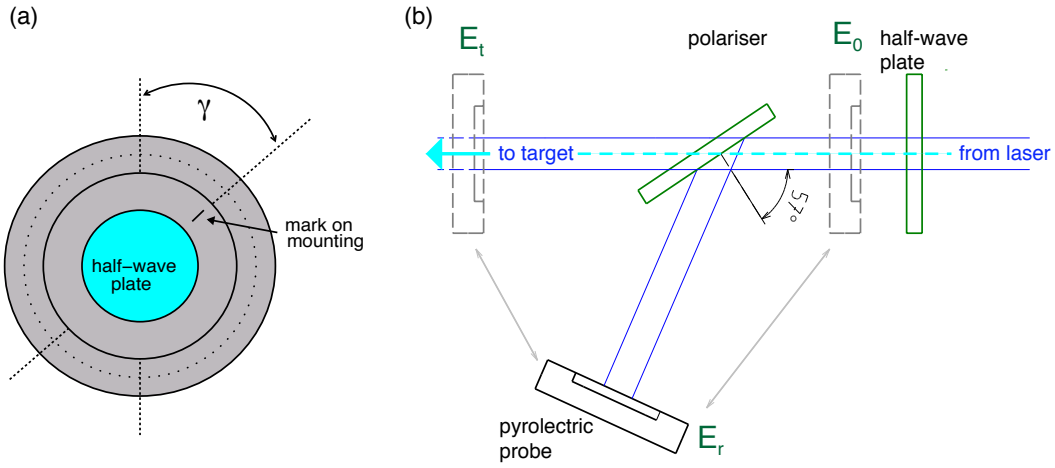

Figure 3.25.: Control of the laser energy. (a) Definition of the angle γ, which measures the rotation of the half-wave plate relative to an arbitrary orientation marked on the plate's mounting. (b) Set up for the calibration of the laser beam energy out put. The total energy E_0 is measured behind the half-wave plate well as the transmitted E_t and the reflected energy E_r behind the polariser.

terisation of the reflected and the transmitted beam after each interference with the mechanical set up of the optical beam line.

The pulse energies of the reflected and transmitted beam is measured for angles of the half-wave plate γ from 0° to 90° in steps of 2°. To this aim, for each angle set the probe is positioned alternating behind the half-wave plate and in the way of the reflected beam and for the two positions the averaged energy of 100 shots each is recorded aside with its standard deviation. The inaccuracy in setting up the angle γ is ± 2°. Figure 3.26 shoes the measured fraction for laser shots onto an iron target.

Relation between the reflected and the transmitted beam energy The total energy incident on the polariser is comprised of four constituents, the actual transmitted and reflected beam portions E_t and E_0 and losses in the transmitted part E_A and the reflected beam E_V (see Fig. 3.25 (b)):

$$E_0 = E_T + E_R + E_A + E_V \tag{3.30}$$

It can be assumed that the losses in energy of each fraction of the beam energy, the reflected and the transmitted beam part, is proportional to the beam energy without any losses.

$$E_A = A \cdot (E_T + E_A) = \frac{A}{1-A} \cdot E_T = B \cdot E_T$$
$$E_V = V \cdot (E_R + E_V) = \frac{V}{1-V} \cdot E_R = W \cdot E_E$$

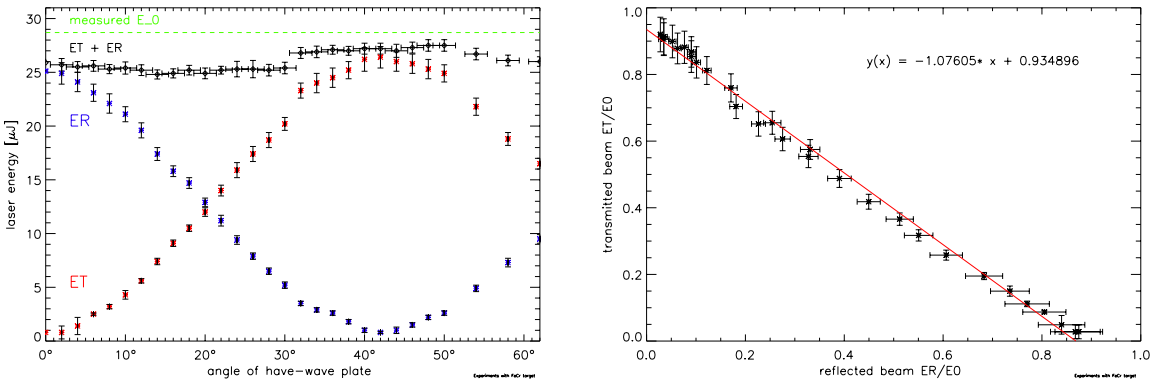

Figure 3.26.: Determination of the laser energy for laser shots onto an iron target. (a) Measured energies of the transmitted and reflected beam energy in dependence of the arbitrary orientation of the half-wave plate γ, E_0 is the total beam energy measured directly behind the half-wave plate. Each data point is the average of 100 shots, the error bars are the standard deviation.(b) Relation of E_t/E_0 and E_r/E_0.The resulting linear equation allows to determine the reflected energy for each shot by measuring the transmitted energy.

with 1-B=T being the *transmission coefficient* and 1-V = R the *reflection coefficient*. Replacing E_A and E_V in Eq. 3.30 and divided to the total beam energy E_0, measured directly behind the half-wave plate, leads to

$$\hat{E_T} = -(1-B+W)\cdot\hat{E_R} + (1-B) \tag{3.31}$$

with $\hat{E_X} = E_X/E_0$. Thus, the relation $\hat{E_0} = \hat{E_T}\left(\hat{E_R}\right)$ corresponds to a a straight line as shown in Figure 3.25 (a) for shots on an iron target. The parameters B and W can be derived from Eq. 3.31, leading tho the *transmission* and the *reflexion coefficient*.
The measurement of both the transmitted and the reflected beam for each of the used setting for the have-wave plate's orientation leads to the possibility of the determination of the parameters m and b of the straight line fitted with the measured data points

$$E_T = m\cdot E_R + b\cdot\bar{E_0}, \tag{3.32}$$

where $\bar{E_0}$ is the averaged energy incident on the polariser. The error of the fitted parameters is considered small compared with the of the the spread of $\bar{E_0}$ due to the spread in the laser out put for the following. The spread of the out put energy was to be found in the order of 2 % to 4 % as shown in Figure 3.24 (c). The error in the measured energy due the pyrolectric sensor is, according to manufacturer's specifications, about 2 %.

Hence, the determination of the fraction of transmitted light for each set of the half-wave plate's orientation offers an opportunity to control the incident energy on the rtarget by recording the reflected energy for each shot within the ranges of the uncertainty due to the variation of the laser output.

3.4.9. Photon number density

The density of photons Φ, the number of photons within a the illuminated spot, of a laser pulse is related to the energy density by

$$\Phi = \frac{\rho}{h \cdot f} = \frac{\rho \cdot \lambda}{h \cdot c} \tag{3.33}$$

with $\rho = E/(\pi r^2)$ being the laser energy density, h Planck's constant, and $f = c/\lambda$ the light's frequency. For a laser pulse of $5\,\mu$J energy and a size of the focus spot of $10\,\mu$m diameter this leads to a photon density of

$$\Phi = 1.24 \cdot 10^{41} \left[1/m^2\right].$$

3.5. Studied materials

In this study a variety of materials are used as projectile and target materials. This section gives an overview of their chemical and physical properties as well as a description of the preparations necessary to use a particular dust powder as a projectile in the dust accelerator or a metal or silicate plate as a target. There are two different categories of materials used, metal grains and fails and coated silicate powders and plates.

3.5.1. Targets

For impact ionisation experiments two different metal foils are used as targets, silver and an iron plus chromium alloy.

- **Silver** is the target material used for most the particle impact experiments. The heavy silver isotopes are located at masses $\sim$107 amu and $\sim$ 109 amu. In this region of the mass spectrum there are no lines of interest. Thus, the appearance of the target lines is not disturbing the detection and identification of lines representing the projectile material. Ag used as a target material provides two almost equally abundant isotopes, ^{107}Ag and ^{109}Ag, simplifying the mass scale assignment to spectra even for complex or unknown impactor materials. This on the other hand leads to a more reliable determination of the mass scale The foils used as target has a thickness of 0.025 mm and was manufactured by Goodfellow GmbH (product number *AG000260/14*).

- **Fe+Cr (Fecralloy):** This alloy consists of Fe (72.8 %) and Cr (22 %) with admixtures of Al (5 %), Y(0.1 %), and Zr (0.1 %). The foil is 0.05 mm thick and was also purchased from Goodfellow GmbH (product number *Fe080250/4*).

For studying laser ionisation, three different target materials are investigated, a relatively pure iron target, a copper + silver alloy and a gold coated olivine target.

- **Ag+Cu alloy:** This target foil consistent of 72 % silver and 28 % copper is 0.05 mm. It was, as all metal target foils, purchased from Goodfellow GmbH (product number *Ag060220/2*).

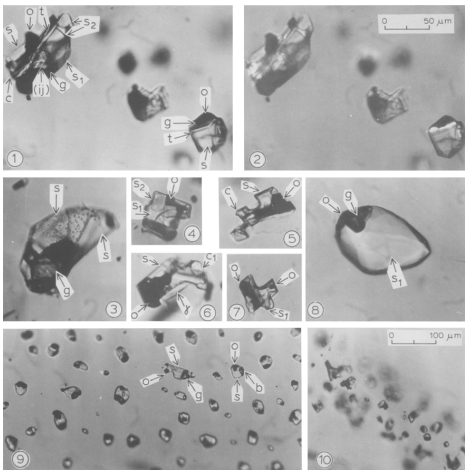

Figure 3.27.: Fluid inclusions in the olivine sample (Z-104) used as a target for laser ionisation measurements (Kurat et al., 1993).

- **Fe:** According to manufacturer's specifications (product number *FE000401*) this foils is 0.25 mm thick and contains 99.99 % of iron with trace quantities of B (2.2ppm), Ca (0.57ppm), Cl (1.1ppm), Co (19ppm), Cr (3.9ppm), Cu (1.7ppm), Ga (0.67ppm), Ge (2ppm), K (1.6ppm), Mn (0.6ppm), Na (0.96ppm), Ni (15ppm), Si (17ppm), andW (0.87ppm).

- **Gold coated olivine:** The olivine target used in the laser ionisation experiments is polished piece of the olivine sample z-104 found on Egyptian Zarbargad Island located in the Northern Red Sea (Kurat et al., 1993). This sample is a fluid inclusion-rich brown olivine (see Figure 3.27). Besides its main constituents it contains traces of chlorides, carbonates, sulfates and other minerals. This leads to a very inhomogeneous composition and topology of the surface, expected to be reflected in the measured *TOF* mass spectra. To obtain electrical conductivity on the surface and apply a potential on the target, the surface of the silicate plate was coated with several μm of gold.

In Table 2.1 the evaporation enthalpies and ionisation potentials of the most important elements consistent in these target materials are listed.

3.5.2. Composition of dust materials

In this section the dust materials used for this study are listed. For the electrostatic acceleration of dust grains to work as in Section 2.2.2, the particles must be capable of carrying charge. Hence the range of materials to be accelerated are restricted to those either consisting of wholly conductive materials or to dielectric particles coated with a conductive material. In this study, three different projectile materials were used, a mixture of iron and nickel, PPY-coated olivine dust and platinum doted orthopyroxene powder. Samples of the particle types used in this study were quantitatively analysed by Höfer (2010), the composition of both silicate powders are listed in Table 3.2.

- **Fe+Ni:** Iron is the material used most frequently as projectile material in the Heidelberg Dust Accelerator in the last four decades. This is due to the fact that iron is highly

Table 3.2.: Quantitative analysis of the silicate dust samples. Above the results for PPY-coated olivine dust, on bottom those for platinum-coated orthopyroxene are shown as ratios of the mass and ratio of numbers of atoms.

Olivine (*PPY*-coated)					
	Mg	Si	Fe	Ni	O
mass (%)	29.40 ± 0.29	19.66 ± 0.13	6.83 ± 0.52	0.31 ± 0.04	43.80 ± 0.04
atoms (%)	25.33 ± 0.25	14.66 ± 0.10	2.56 ± 0.19	0.11 ± 0.02	57.33 ± 0.05

Orthopyroxene (*Pt*-coated)				
	Mg	Al	Si	Ca
mass (%)	19.76 ± 0.07	2.05 ± 0.05	26.29 ± 0.06	0.41 ± 0.03
atoms (%)	16.84 ± 0.06	1.57 ± 0.04	19.39 ± 0.04	0.21 ± 0.02

	Cr	Fe	O
mass (%)	0.18 ± 0.03	4.88 ± 0.10	46.44 ± 0.01
atoms (%)	0.07 ± 0.01	1.81 ± 0.04	60.11 ± 0.02

conductive and thus, is easily charged. The dust sample used for this study is a mixture of 84 % iron Particles Fe/0.056.714 produced by BASF in 1970, 8 % iron powder of 200 nm small spheres produced by Goodfellow and 8 % nanometer sized nickel particles. Figure 3.28 shows a SEM-picture of the used BASF-particles.

- **Orthopyroxene (Opx):** The orthopyroxene used here, stem from a spinel peridotite originated from the Arabian peninsula. The sample was ground and afterwards coated with platinum to be accelerated in the dust accelerator. The coating process bonds metal to large areas of the surfaces of the silicate particles whilst the particles are in suspension. Agglomeration is reduced by frequent ultrasonic agitation of the particles (Hillier et al., 2009). The resulting layer has a thickness of ∼5 to ∼10nm (Höfer, 2010). The coating metal has a low cosmic abundance, this, it will not bias any results. Furthermore i it has high mass, providing an unambiguous calibration point for mass spectra and ensuring there are no spurious features in mineralogically relevant mass ranges. Figure 3.28 shows a backscatter-electron-picture of the Opx particles.

- **Olivine:** The olivine sample originates from San Carlos, Arizona. It was coated with Polypyrrole (*PPY*) (Burchell et al., 1999). Assuming a a uniform polypyrrole overlayer, the coating thickness is estimated to be approximately 7.4 nm (Fielding and Armes, 2009). Figure 3.28 shows a backscatter-electron-picture of the olivine particles.

3.5.3. Measurements for various combinations of materials

In the following, an overview of the measurements conducted for this study is given. For particle impacts a wide variety of material combinations and different acceleration voltages were

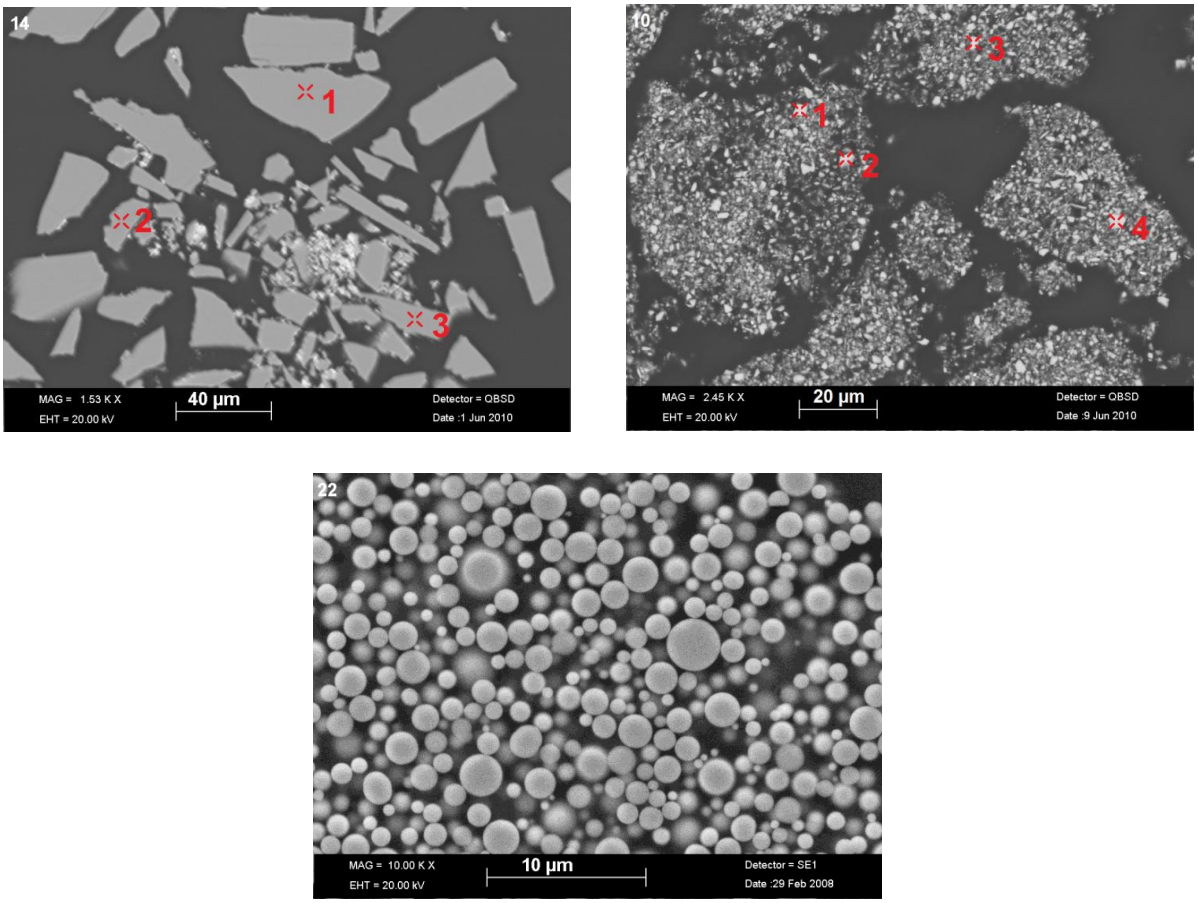

Figure 3.28.: **(above)** Backscattered electron picture of the used Opx (left) and olivine dust (right). **(bottom)** SEM-picture of the used iron dust 714 produced by BASF AG (Ludwigshafen a.Rh.) (Höfer, 2010).

used. Furthermore, experiments were conducted with three different instruments (seeTable 3.4). For each material combination, the dynamic properties of the particles were recorded as shown in Figure D.1 to D.6.

Table 3.3 shows the measurements performed with the laser and different target materials.

Table 3.3.: Overview of the measurements for laser ionisation

No.	acc. voltage (V)	Material	Laser intensity (μJ)	Number	Date
1	1000	Fe	0.70 - 6.97	55	03 May 2010
2	1600	Fe	0.37 - 27.96	337	03 May 2010
3	1000	Ag+Cu	12.24 - 25.38	73	03 Feb 2010
4	1600	Olivine (Loc1)	1.65 - 14.40	86	11 Mar 2010
5	1600	Olivine (Loc2)	0.91 - 19.45	151	11 Mar 2010

Instrument	No.	acc. voltage (V)	Material	impact speed ($km s^{-1}$)	Radius (nm)	number [a]	Date	Reference
BERTA	1	300	Fe+Ni → Ag	4.97 - 52.63	42 - 625	76 / 44 / 40	23 Nov 2009	Figure D.1
	2	500	Fe+Ni → Ag	5.50 - 53.97	39 - 872	78 / 46 / 34	23 Nov 2009	
	3	600	Fe+Ni → Ag	4.91 - 57.38	42 - 1081	86 / 62 / 48	23 Nov 2009	
	4	700	Fe+Ni → Ag	4.77 - 48.75	50 - 794	65 / 41 / 22	23 Nov 2009	
	5	800	Fe+Ni → Ag	4.85 - 47.42	44 - 674	68 / 62 / 32	23 Nov 2009	
	6	900	Fe+Ni → Ag	4.72 - 48.34	46 - 902	74 / 48 / 35	23 Nov 2009	
	7	1000	Fe+Ni → Ag	6.12 - 50.91	40 - 638	59 / 53 / 44	23 Nov 2009	
	Sum	–	Fe+Ni → Ag	4.72 - 57.38	40 - 1018	506/356/255	19 Nov 2009	
LAMA	8	–	Fe+Ni → Ag	3.19 - 38.83	48 - 1341	82 / 82 / 82	19 Jan 2007	Figure D.2
BERTA	9	1000	Opx → Ag	2.89 - 32.98	72 - 1271	131/118/112	18 Dec 2009	Figure D.3
SUDA	10	–	Opx → Ag	1.06 - 28.56	64 - 2535	231/219/149	31 May 2010	Figure D.4
BERTA	11	400	Olivine → Ag	20.14 - 46.57	38 - 139	62 / 43 / 8	18 Dec 2009	Figure D.5
	12	600	Olivine → Ag	18.97 - 64.81	28 - 143	59 / 44 / 13	18 Dec 2009	
	13	800	Olivine → Ag	18.87 - 67.87	30 - 146	61 / 31 / 25	18 Dec 2009	
	14	1000	Olivine → Ag	20.04 - 59.00	23 - 108	69 / 69 / 15	18 Dec 2009	
	15	1500	Olivine → Ag	18.70 - 58.51	31 - 122	88 / 78 / 65	18 Dec 2009	
	16	2000	Olivine → Ag	19.00 - 51.79	22 - 129	82 / 41 / 39	18 Dec 2009	
	17	2500	Olivine → Ag	18.77 - 60.02	31 - 154	62 / 59 / 53	18 Dec 2009	
	18	3000	Olivine → Ag	18.95 - 73.13	25 - 125	84 / 81 / 22	18 Dec 2009	
	Sum	–	Olivine → Ag	18.70 - 73.13	22 - 154	567/446/240	18 Dec 2009	
BERTA	19	1000	Olivine → Fe+Cr	18.76 - 73.08	27 - 140	87 / 85 / 85	18 Dec 2009	Figure D.6

[a] shots / spectra / resolved spectra

Table 3.4.: Overview of the measurements for particle impacts

4. Results

4.1. Impact charge signal

This section deals with the total ion and electron charges produced by particle impacts as well as by laser irradiance. Due to the positive potential applied on the target, positive ions are repelled from the target and accelerated, in the field between the target and the grounded grid in front, towards the ion detector. The electrons and negatively charged ions are collected on the target. A charge sensitive amplifier (*CSA*) attached to the target records the signals, representing the total charge produced in the process as well as the temporal evolution of the plasma.

4.1.1. Signal form

Figure 4.1 shows four example charge yield signals for iron particles impacting on silver with impact velocities of $7.3\,\mathrm{km\,s^{-1}}$, $11\,\mathrm{km\,s^{-1}}$, $24.7\,\mathrm{km\,s^{-1}}$, and $50.9\,\mathrm{km\,s^{-1}}$. The amplifiers used for this study invert the charge signal. Thus, the negative signal recorded on the target plate appears positive in the figures.
The four signals shown were selected as they are typical of target responses for impacts at similar velocities, regardless of the projectile and target material combinations, as presented in this thesis.

- **Slow particles (up to $\sim 8\,\mathrm{km\,s^{-1}}$):**
  Ahead of the impact the approaching charged particle produces an induced charge on the target, appearing as a fall on the charge amplifier channel some tenth of a $\mathrm{m\,s^{-1}}$ before the impact. Due to the high charges carried on large, slow particles, this effect is apparent mainly for slow particle impacts. The fall of the signal stops with the impact of the particle, followed by a very steep rise of several 100 ns duration. After this rise the slope of the signal flattens, in many cases even preceded by a slight drop in the signal. This gradual rise in signal continues for several μs (Auer and Sitte, 1968).

- **Particles with velocities of about 10 - 15 $\mathrm{km\,s^{-1}}$:** With increasing impact velocity, the induced part of the signal becomes weaker and a greater fraction of the signals begin to exhibit step features. The first, steep rise is almost constant, this phase is much faster then the other steps, having typical timescales of several μs. The remaining signals show, most of the time, a dominant, steep rise at the beginning and one or two changes in slope later, with shallower rises.

- **Fast particles (15 - 30 $\mathrm{km\,s^{-1}}$):** With further increases in impact velocity, the first step becomes more and more dominant, with the height of the following steps diminishing.

- **Very fast and small particles (above 35 $\mathrm{km\,s^{-1}}$):** For very fast particles only the first steep rise remains.

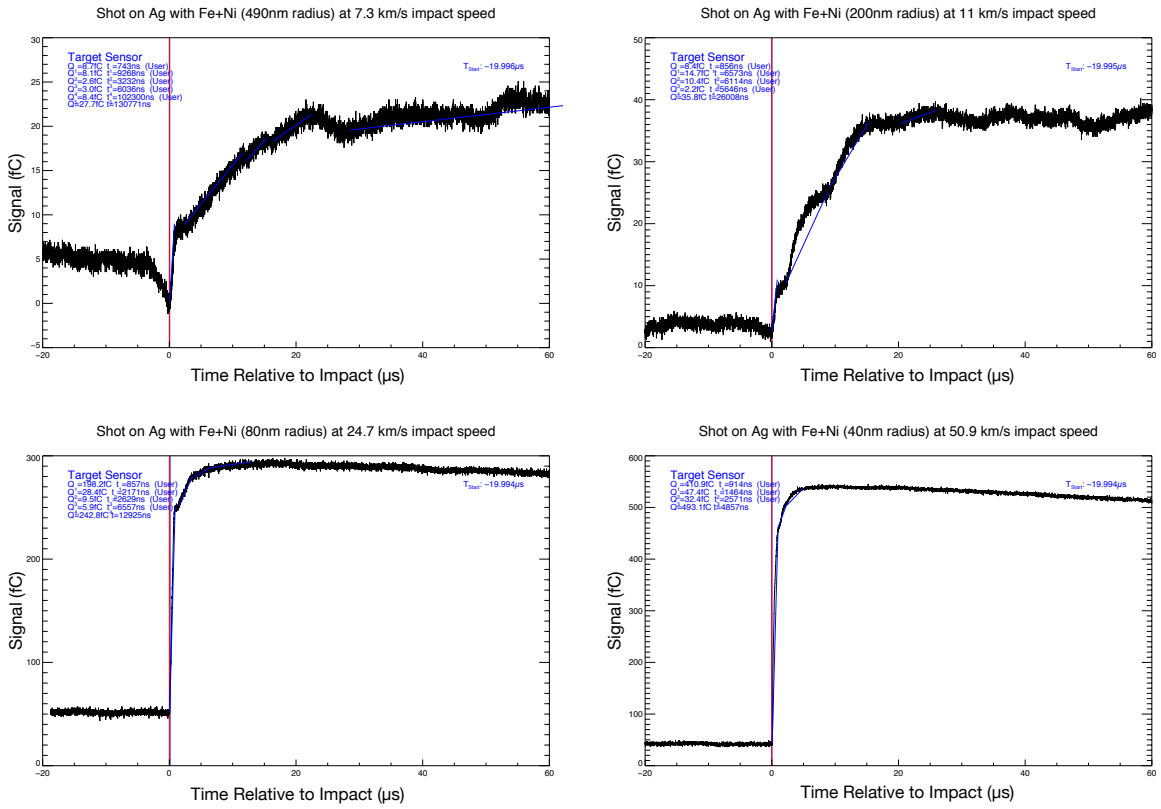

Figure 4.1.: Four typical impact charge signals for shots with Fe+Ni particles on a silver target at impact velocities of $7.3\,\mathrm{km\,s^{-1}}$, $11\,\mathrm{km\,s^{-1}}$, $24.7\,\mathrm{km\,s^{-1}}$, and $50.9\,\mathrm{km\,s^{-1}}$.

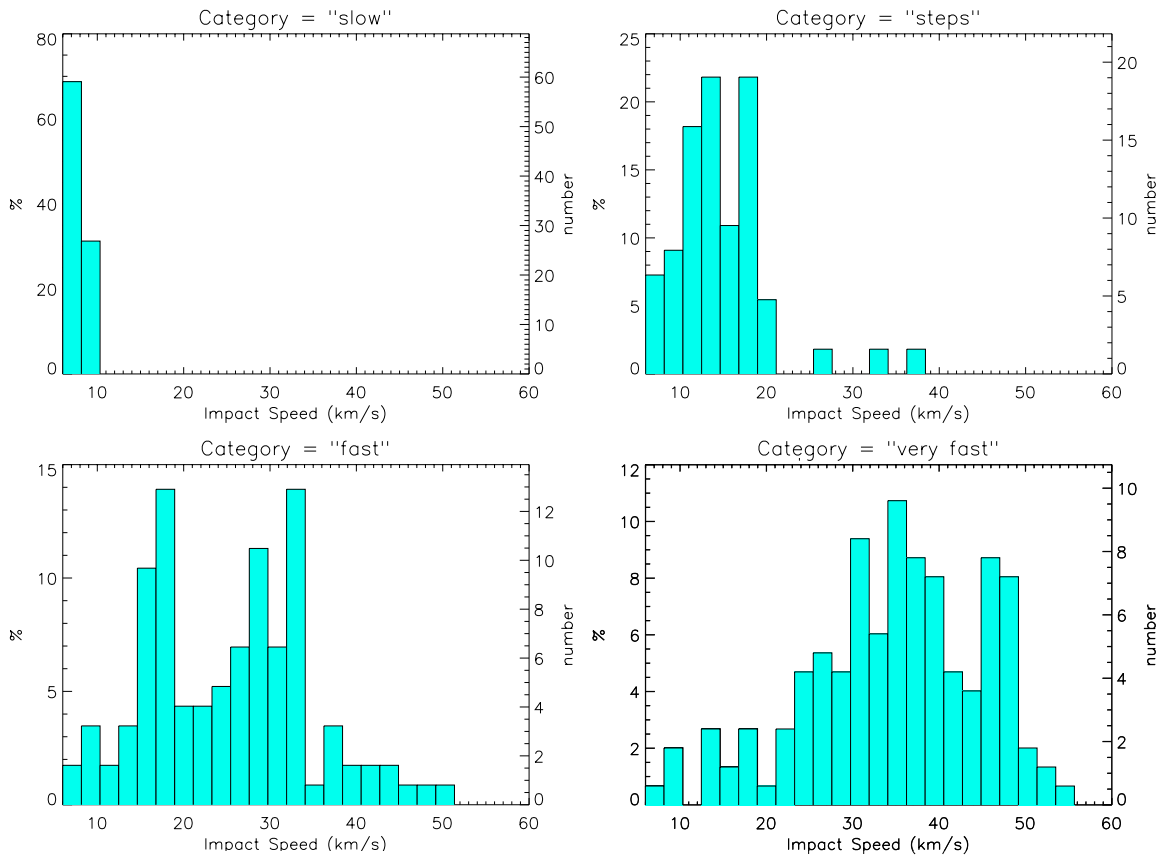

Figure 4.2.: Velocity distribution of particles assigned to the four charge yield signal categories for shots with iron and nickel particles on a silver target.

The velocity distribution for particles assigned to one of the four categories is shown in Figure 4.2 for shots with iron and nickel particles on silver.

Comparable with particle impacts, the charge yields for laser ablation also show a change in shape with increasing laser energy. This result contrasts with an earlier study conducted by Müller (2004) with the same laser but a different experimental set up. Figure 4.3 shows that, for laser shots with low beam energies, the charge yield rises rapidly within several ns. With increasing energies the slope becomes less steep, and even in some cases the charge yield rises in two to three steps. For very high laser energies the rise becomes very slow. For different energy ranges different charge amplifiers have been used. *(Thus, the different character of the charge yield signals can be attributed to differences between the applied amplifiers, such as their response times.)*

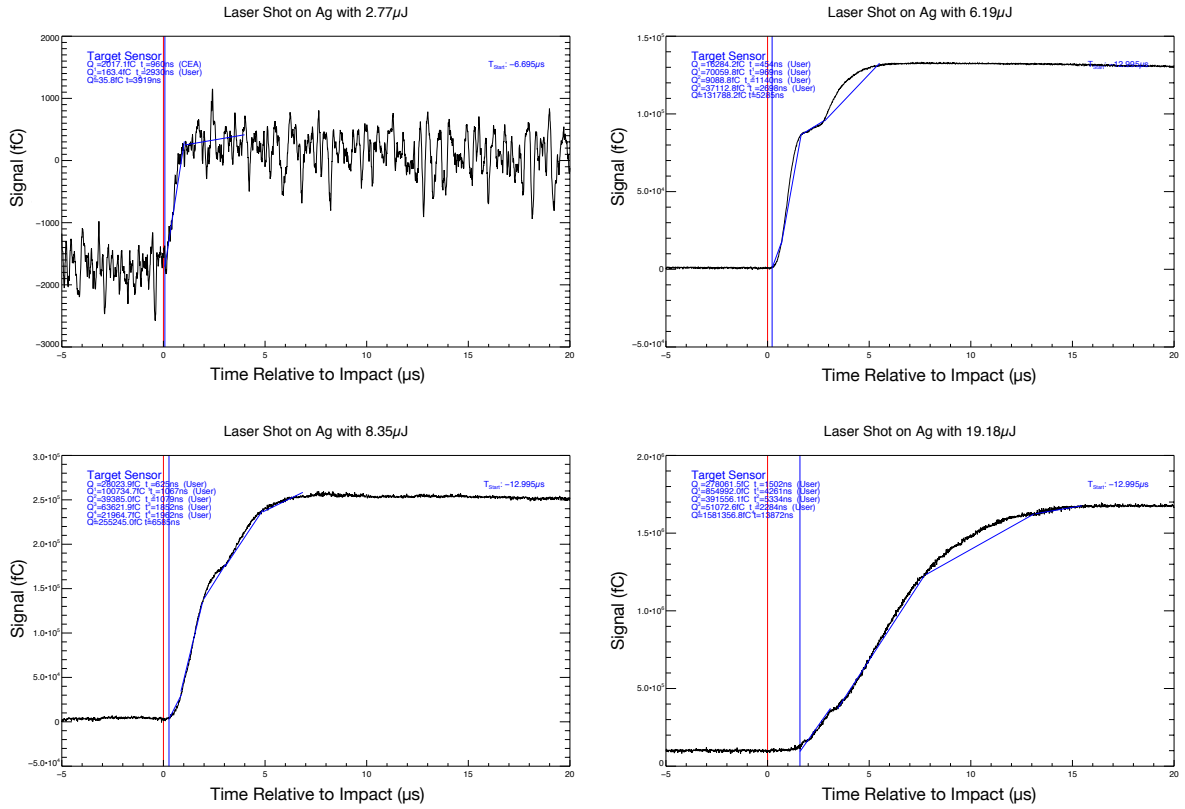

Figure 4.3.: Four typical charge signals from the target, for laser shots on iron at various laser energies.

4.1.2. Charge yields from particle impacts

The amount of charge emitted due to a particle impact and its evolution with time is a very sensitive measure of the impact ionisation process. The charge yield and its rise time are related to properties of the impinging particle and the target (Auer, 2001). Therefore, measurements of the impact charge yield alone, or in combination with other techniques, has been used by dust instruments on spacecraft since the early 1970s to investigate the properties of cosmic dust particles (Dietzel et al., 1973; Göller and Grün, 1989; Srama et al., 2004a). Even though there have been several attempts to determine the charge yield quantitatively (Drapatz and Michel, 1972; Hornung and Drapatz, 1979; Kissel and Krueger, 1987), a complete description of all measured quantities and their relation to the impact parameters is still not available. Hence, calibration and experimental measurements were and are still essential, providing a large amount of impact data. Because of this fact, for this thesis, as well as the obtained *TOF* spectra, the impact charge data have also been recorded for the four combinations of dust and target materials listed in Table 3.4, and analysed in an attempt to relate them to parameters of the impacting particle.

Figure 4.6 shows the amount of emitted charge as a function of the impact velocity. Apart from in the case of orthopyroxene particles impacting onto silver, there seems to be a relation between the charge yield and the speed of the particles. However, the spread of the charge yield within a certain impact velocity range is very large – from about 50% to 100% as can be seen in Table D.1 and Table D.2.

Since the first experiments to characterise the impact ionisation plasma by Friichtenicht (1964) and succeeding works (Auer and Sitte, 1968; Adams and Smith, 1971) it has been known that the charge generated during an impact is a function of both particle mass and speed - describable by a power law:

$$Q = K \cdot m^{\alpha} \cdot v^{\beta}. \tag{4.1}$$

Most authors report the mass exponent α in to be about 1.0. Common to these works is the hemispherical shape of the target used in the experimental set up (Dietzel et al., 1973; Göller and Grün, 1989) as shown in Figure 4.12.

Figure 4.8 shows the dependence of the impact generated Q/m ratio for the four material combinations studied for this thesis. The velocity exponent β varies from 3.45 ± 0.12 for shots with orthopyroxene particles on a silver target to 5.50 ± 0.07 for olivine particles fired onto a silver target.

Contrary to dust impact measurements with cosmic dust particles in space, laboratory particle impacts are biased due to the restricted kinetic energy regime of the grains. This results from the acceleration process and the relation between the particle mass and velocity due to Eq. 3.16. To filter out this biasing, the mass exponent can determined for a number of very narrow velocity ranges (Göller, 1988). Because of the wide spread in the charge yield, the sample, i.e. the amount of data recorded, should be large enough to guarantee the statistical significance of the results. To obtain this, for two dust and target material combinations, the data sets for all ion acceleration voltages have been combined in order to study the charge yield properties. This can be done because the variation of the acceleration voltage on the target has no significant effect on the total charge yield (Auer and Sitte, 1968). The resulting mass exponents for all velocity ranges are listed in Table D.1 (for Fe+Ni onto Ag) and Table D.2 (for olivine powder on silver). The mass exponents α are then averaged under the assumption that the mass exponent is constant for the whole investigated velocity range. The number of particle impacts for each velocity range is about 10-40. This is far fewer than in earlier works like

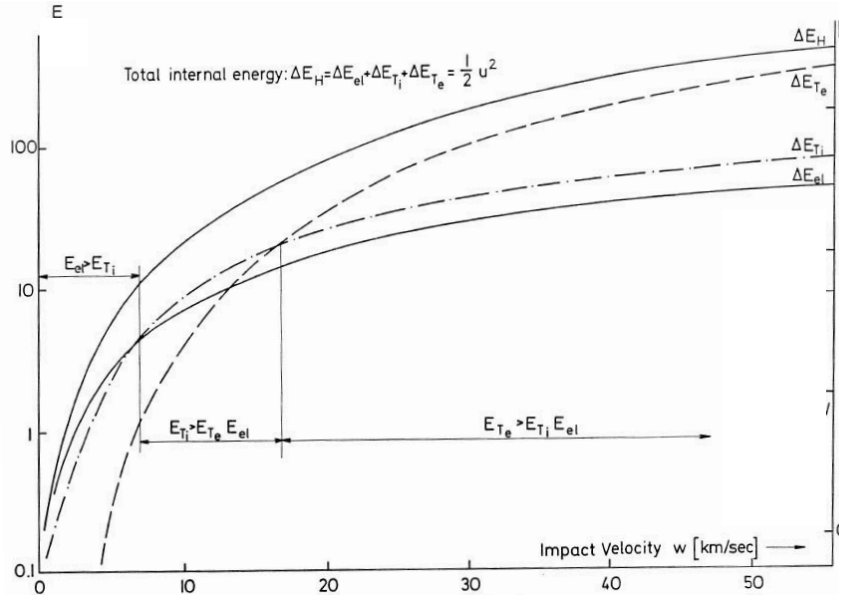

Figure 4.4.: The different contributions of the specific energy ΔE_H behind a shock wave through Fe upon impact onto a tungsten target in dependence on the impact velocity w. ΔE_{el} is the elastic contribution, ΔE_{Ti} the thermal energy of the nuclei , and ΔE_{Te} of the electrons (Drapatz and Michel, 1974).

Göller and Grün (1989) and Srama (2000) leading to less reliable conclusions.

Figure 4.7 shows the velocity dependence of Q/m^{α} for both material combinations. The resulting exponents and their errors are listed in Table 4.1.

Shots with iron and nickel particles onto a silver target The measurements for shots with Fe+Ni powder onto a silver target constitute the data set with the greatest number of impact events and the widest velocity range. Plots for this data set indicate a variation of the dependence of the charge yield on the impact parameters for increasing impact velocities. Because of the focus of this thesis, this aspect has not been investigated as such that enough data were acquired to study this effect in detail and quantitatively.

Nevertheless, the impact ionisation model by Drapatz and Michel (1974) predicts the existence of two different ionisation processes depending only on the impact velocity (Section 2.1). According to this the heating of the material of both, the particle and the target, and subsequently the properties of the resulting plasma cloud, are determined by specific internal energy in the shocked materials

$$\Delta E_H = \frac{1}{2}u^2 = \frac{1}{2}\left(\frac{v}{\sqrt{\rho_p/\rho_t}+1}\right)^2,$$

where u is the reduced shock velocity, v the impact velocity, ρ_p the particle's density and ρ_t the density of the target material. This dissipated specific internal energy is a sum of elastic and thermal contributions $\Delta E_H = \Delta E_{el} + \Delta E_{th}$. It is the thermal contribution which causes the heating of the material and subsequently leads to the emittance of charge due to ionisation. Besides the increase of the specific internal energy ΔE_H in total with increasing impact velocity,

also the fraction of the thermal contribution is growing as shown in Figure 4.4.

For *slow velocities* the added internal energy is not sufficient to vaporise the entire particle. Thus, the particle material remains as a melted liquid droplet, ionisation occurs mainly by diffusion through the surface. Being a pure surface phenomenon, the ionisation would be expected to be determined by the surface of the particle and a narrow ring area around the impact area on the targets surface. This leads to charge yields for the particle material $Q_p \propto r_p^2 \propto m_p^{2/3}$ and for the target material $Q_t \propto r_p \propto m_p^{1/3}$ (Kissel and Krueger, 1987).
For *high impact velocities* the vaporisation is expected to be total. Thus, the charge yield for the projectile would be determined by the volume of the particle. The charge emitted from the target depends on the area of impact. For these velocities the charge yield of the particle will be $Q_p \propto r_p^3 \propto m_p^1$ and the charge emitted by the target $Q_t \propto r_p^2 \propto m_p^{2/3}$.

Hence, an increase of the slope of the relation between the emitted charge yield and the impact parameters may be expected, as the mass exponent of the value $\alpha = 1$ represents the limit of a strong shock as defined in Section 2.1.2.

Shots with silicate particles The averaged mass exponent $\bar{\alpha}$ for PPY-coated olivine particles impacting a silver surface is 0.93 $\pm$0.20 as shown in Table D.2. For impacts of the same particles on a Fe+Cr alloy, the was not determined because of the small size of the studied data set. To obtain an averaged mass exponent, data sets recorded with two mass spectrometers where combined. The measurements made with the *BERTA* and the *SUDA* instruments lead to $\bar{\alpha} = 0.87 \pm 0.23$ (Table D.3).

Velocity exponents in the strong shock limit (α =1) As mentioned above, the value of the mass exponent α =1 may be regarded as a representation of particle impacts in the limit of strong shocks. Impacts at velocities above about $20\,\mathrm{km\,s^{-1}}$ lead to a complete vaporisation of the particle material. Figure 4.8 the dependence of Q/m for four material combinations is plotted in dependence on the velocity. The resulting velocity exponents show a hierarchical sequence from β = 3.34 $\pm$ 0.12 (Opx on Ag) over β = 4.43 $\pm$ 0.05 (Fe on Ag) and β = 4.48 $\pm$ 0.36 (Olivine on Fe+Cr) to β = 5.50 $\pm$ 0.07 (Olivine on Ag).

In the limit of a strong shock, the reduced shock velocity u (left) and the specific internal energy behind the shock E_H can be estimated for the various target and impactor material combinations used for this study. In the case of strong shocks, meaning $v > 20\,\mathrm{km\,s^{-1}}$, the reduced shock velocity corresponds to the material velocity behind the shock and depends on the impact velocity v and the ratio of the densities of the particle and the target material as one can see in Eq. 2.21.

Figure 4.5 shows, that the specific internal energy is higher for impacts of silicate particles on silver then for the denser iron particles. This is consistent with the observation in Figure 4.6 of Olivine impacts producing a higher charge yield then the denser iron particles. Furthermore, the increase of internal energy itself is higher for less dens materials hitting the same target or for the same material impacting onto a denser material. One may assume that this effect is reflected in the observed hierarchy of velocity exponents, describing the dependence of the increase in charge yield on the impact velocity.

Only the findings for Opx particles impacting a silver target do not correspond with this considerations. The charge yield of these measurements are in the same or even in a lower range then for iron particles hitting a silver target. Also the increase in the yield as a function

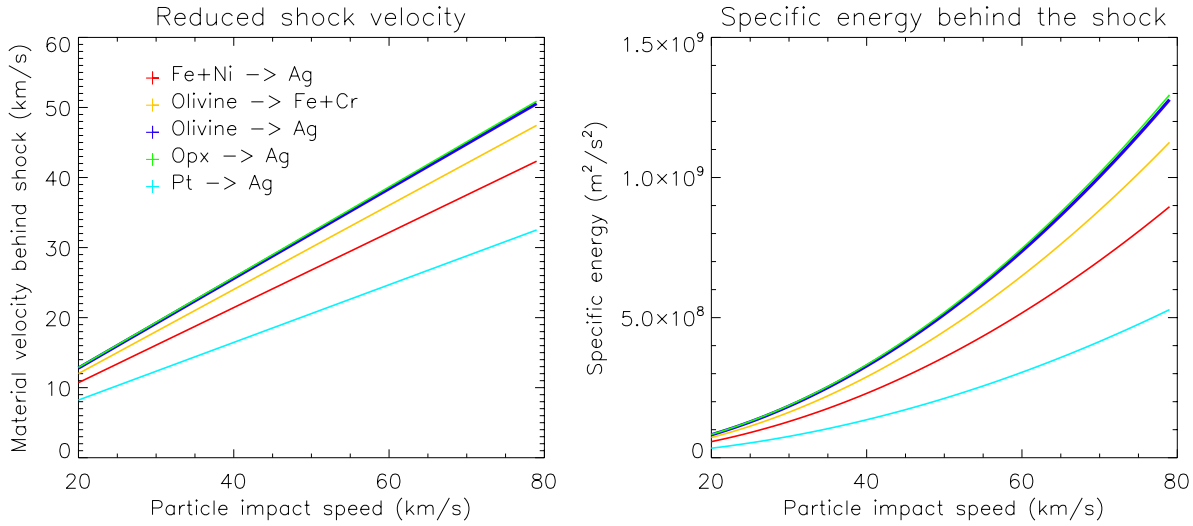

Figure 4.5.: The reduced shock velocity u (left) and the specific internal energy behind the shock E_H (right) for five target and impactor material combinations. In the case of strong shocks, meaning $v > 20\,\mathrm{km\,s^{-1}}$, the reduced shock velocity corresponds to the material velocity behind the shock and depends on the impact velocity v and the ratio of the densities of the particle and the target material as one can see in Eq. 2.21. The specific internal energy can be derived from $E_H = 1/2u^2$. The materials have densities of $\rho_{Olivine}$= 3.32 and ρ_{Opx} = 3.2, ρ_{Fe} = 7.84, and rho_{Ag} =10.49. The density of the Fe+Cr alloy used as a target was assumed as the average of both material's density ρ_{Fe+Cr} = 7.55. To obtain better understanding of the behaviour of the platinum coated Opx particles, the reduced shock velocity and the specific internal energy of platinum grains with a density of ρ_{Pt} = 21.48 impacting a silver target was estimated as well.

of the impact velocity is smaller as one would expect from Figure 4.5. This may be caused by the platinum coating of the Opx particles. The platinum coating layer is quite thick and may for smaller particle even dominate the overall properties of the particle. To obtain better understanding of the behaviour of the platinum coated Opx particles, the reduced shock velocity and the specific internal energy of platinum grains with a density of ρ_{Pt} = 21.48 impacting a silver target was estimated as well in Figure 4.5. It results in the smallest and least increasing internal energy of all studies material combinations. Ab combination of the properties of a pure Opx particle and platinum grains may lead to the observed behaviour

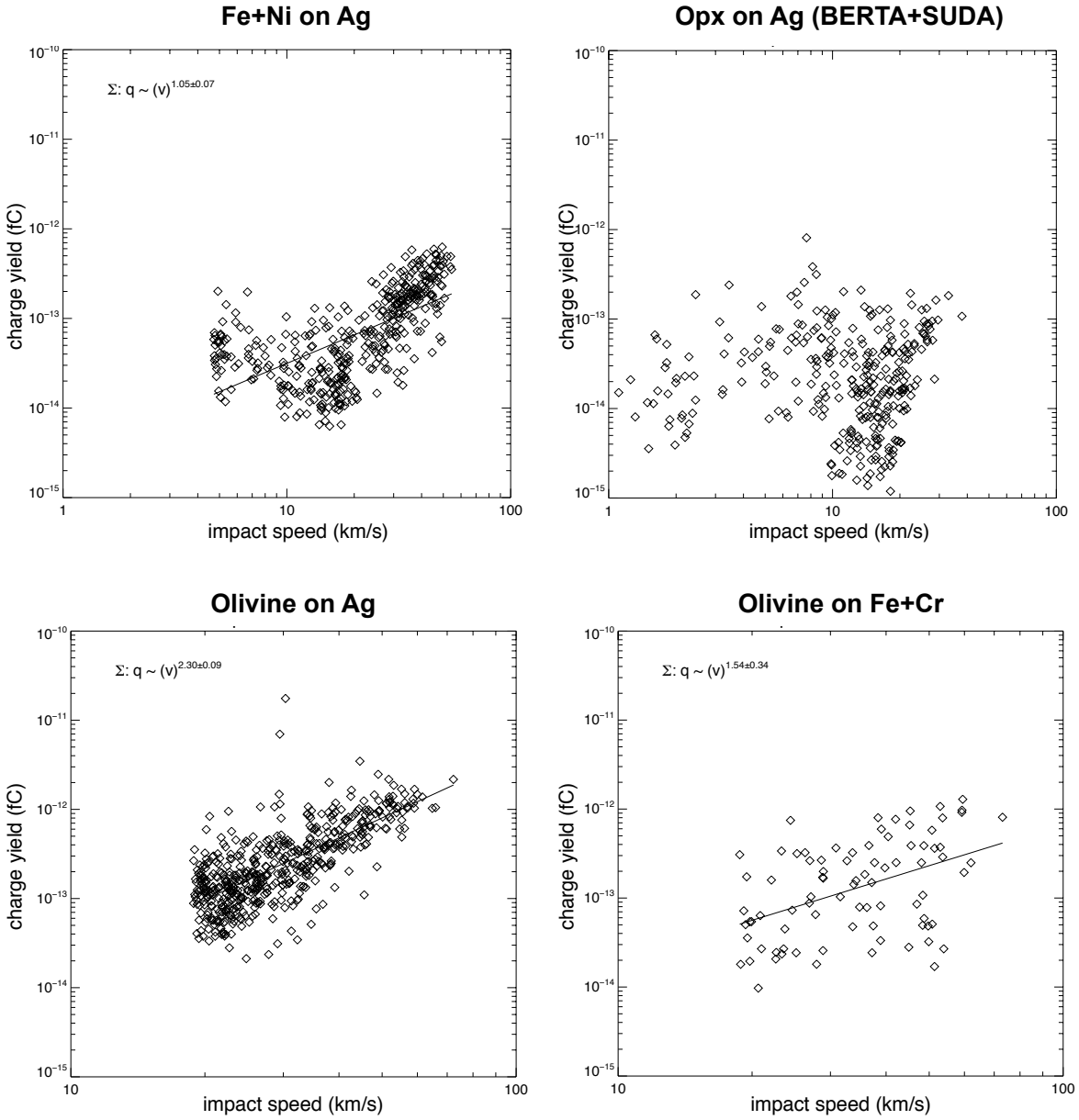

Figure 4.6.: Impact ionisation: Charge yield at the target as a function of the impact velocity for various dust and target material combinations.

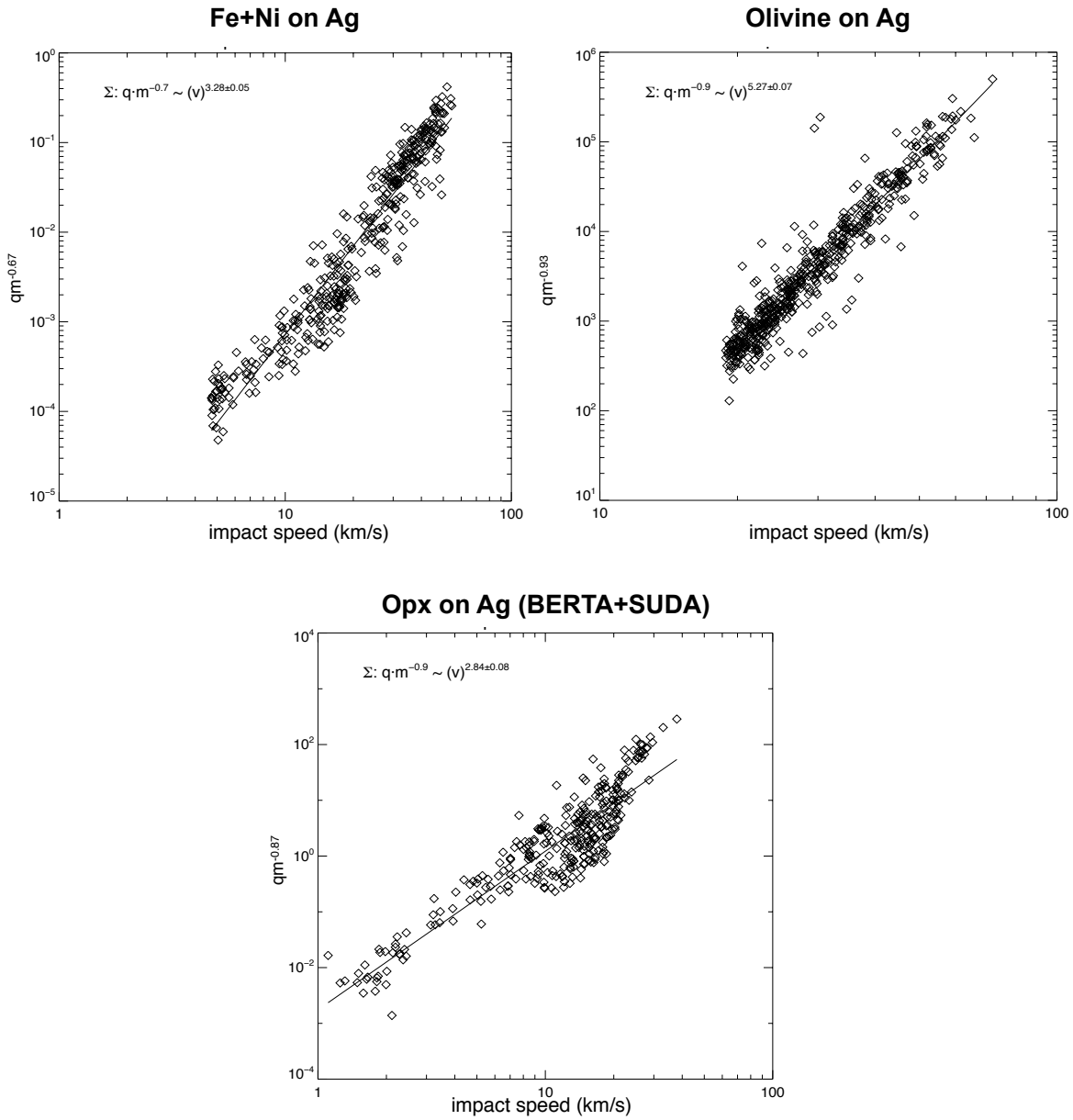

Figure 4.7.: Impact ionisation: Dependence of Q/m^{α} on the impact velocity for various dust and target material combinations.

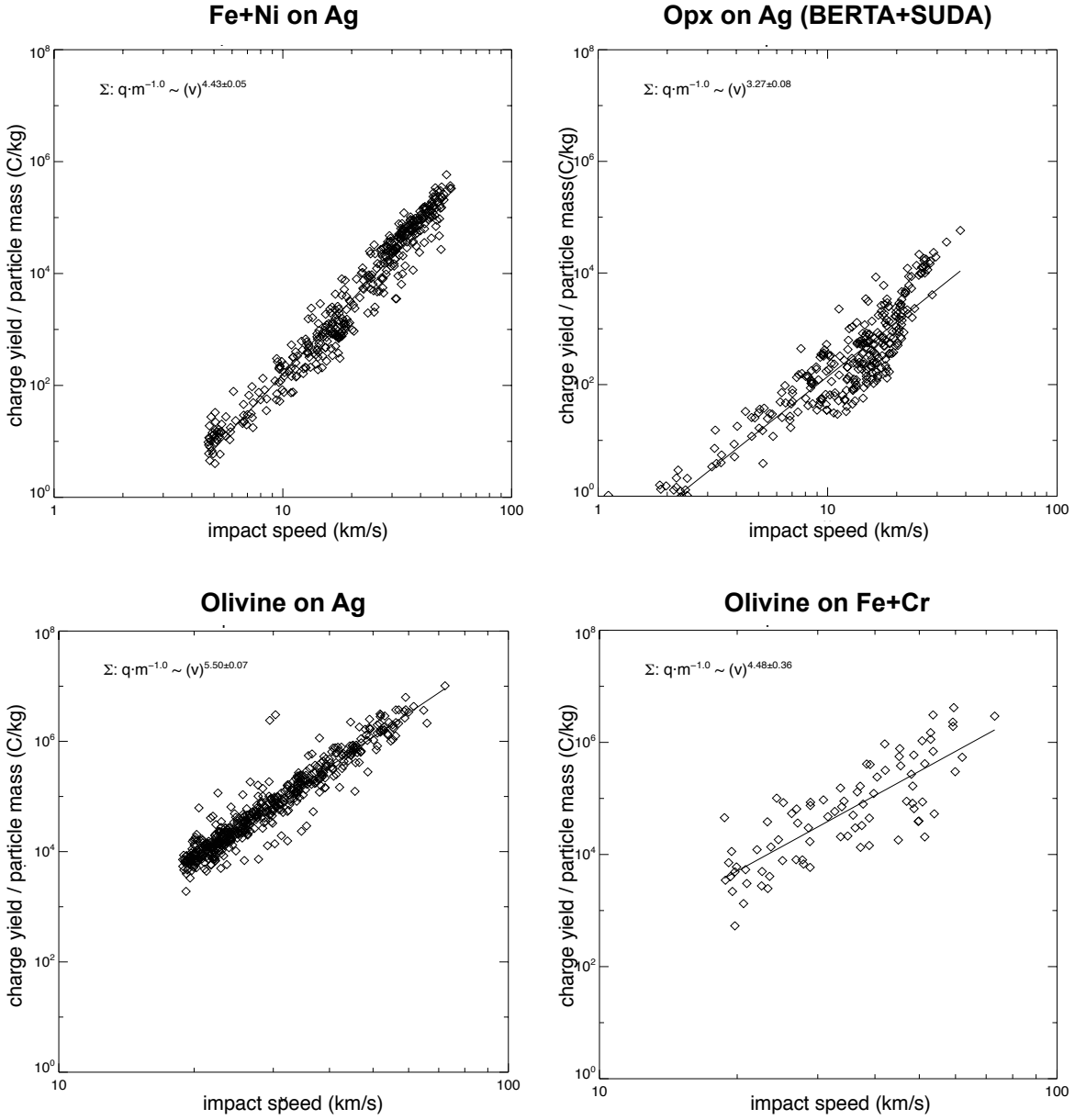

Figure 4.8.: Impact ionisation: Dependence of Q/m on the impact velocity for various dust and target material combinations.

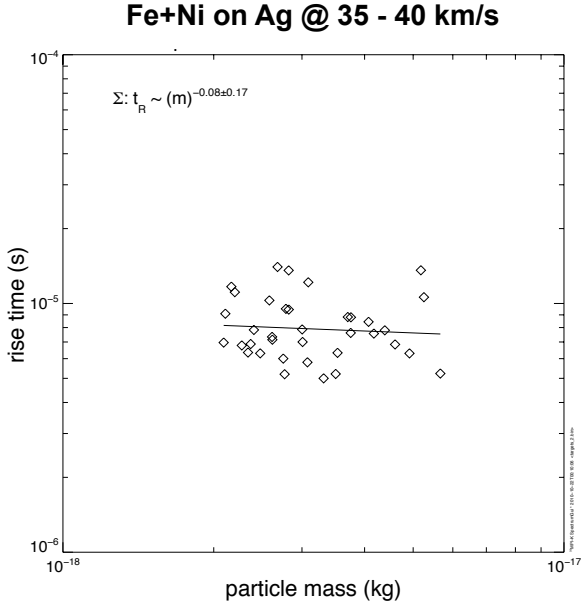

Figure 4.9.: The rise time of the charge yield signal as a function of the particle mass. The example shows impacts of Fe+Ni grains on a silver target at impact velocities of between $35\,\mathrm{km\,s^{-1}}$ amd $40\,\mathrm{km\,s^{-1}}$.

4.1.3. Temporal evolution of the impact plasma

In this section the rise times of the charge yield and their relation to the impact parameters is studied. The rise time is defined as the time from the moment of impact until the time at which the charge signal reaches a maximum.The error of this measure is determined by the uncertainties in establishing exactly the times of impact and of the maximum of the signal.

The moment of impact can be determined quite accurately because of the very steep rise in the beginning of the plasma evolution. The maximum of the charge yield signal on the other hand is quite flat (see Figure 4.1). Thus, even small disturbances, such as noise in the charge sensitive amplifier, can lead to a large shift of the maximum and subsequently to a quite wide spread in the rise times measured for a set of impact events. The error of the measured rise time $\Delta t_r/t_r$ is dominated by the reading error of the point of maximum and estimated as about 5-10 % depending on the impact velocity and noise characteristics of the individual charge yield signal.

Earlier works have investigated the charge signal dependence upon the impact parameters (Hoffmann, 1971; Knabe, 1980; Göller, 1988) - the particle's mass and the impact speed, in much greater detail than was possible for this thesis due to smaller sizes of the data sets recorded for individual sets of experiment parameters.

Dependence of the rise time on the particle mass

Making the assumption that the rise time is independent of the acceleration voltage U_{acc} applied on the target, as found in Hoffmann (1971) Obviously, data sets of rise times recorded at similar speeds should only depend on the impactors' masses. Figure 4.9 shows rise times plotted as a function of the masses of iron particles impacting a silver target at impact speeds of between

$35\,\mathrm{km\,s^{-1}}$ and $40\,\mathrm{km\,s^{-1}}$. Empirically, the rise time scales with the mass like

$$t_r \propto m^{\sigma}.$$

Table D.1 lists the mass exponents σ dirived for Fe+Ni impacts at speeds between $4\,\mathrm{km\,s^{-1}}$ and $50\,\mathrm{km\,s^{-1}}$, while Table D.2 lists the exponents derived for olivine on Ag at speeds between $18\,\mathrm{km\,s^{-1}}$ and $45\,\mathrm{km\,s^{-1}}$. Figure 4.10 (b) shows the dependence of the mass exponents σ on the impact velocity. For both studied material combinations there are no significant velocity dependencies. The values of σ oscillate around their average value (zero) within the boundaries of error corresponding the standard deviation. This is consistent with the results of the aforementioned works which find the rise time independent of the particle mass.

Dependence of the rise time on the acceleration voltage U_{acc}

The dependence of the rise time on the acceleration potential applied on the target can be studied by making the assumption that the rise time is independent of the particle's mass. To this aim, the velocity dependence of the rise time:

$$t_r \propto v^{\delta},$$

was studied for a variety of acceleration potentials as listed in Table D.4.Figure 4.10 (a) shows the velocity exponent δ as a function of the acceleration potential, U_{acc}, applied on the target for two studied material combinations, Fe+Ni on Ag and Olivine on Ag. Within the boundaries of the standard deviation the velocity exponent can be regarded as constant. Again, this finding is compatible with the results of Hoffmann (1971) and Göller (1988).

Dependence of the rise time on impact velocity

In Figure 4.11 the rise times are plotted as a function of the impact speed again for shots with iron particles, orthopyroxene and olivine on a silver target as well as for shots with olivine powder on an iron-tungsten alloy. Again, the data sets obtained in measurements with various acceleration potentials are combined as can be seen on the left of the figure. The rise time of the charge yield signal decreases with increasing impact velocity. The slope of the decrease is steeper for impacts of iron grains than for shots with olivine powder. The exponent is the same for olivine particles hitting a silver target as well as for impacts on a iron-tungsten alloy. The most shallow progression is obtained for the impacts of Opx particles on silver. As mentioned above the relation can be described by a power law $t_r \propto v^{\delta}$, the exponents are listed in Table 4.2.

Phases of the plasma evolution for impacts of iron particles on a silver target:

The appearance of distinct phases in the evolution of the impact plasma may be explained by charge emitted from secondary or tertiary impacts (Auer, 2001). These impacts occur due to ejecta particles, originating from the primary particle breaking apart while hitting the target surface (Eichhorn, 1978b). For impacts in the target normal, more then 98 % of the ejecta mass displaced with velocities sufficiently high to produce secondary impact ionisation is ejected in an angular range between 35° and 75° (Nagel et al., 1975). For shallower impact angles, i.e. for 45° as applied in this study, the production of secondary ejecta is more effiecient (Iglseder, 1986). The ejecta have velocities up to 5 times the impact velocity (Eichhorn, 1976).

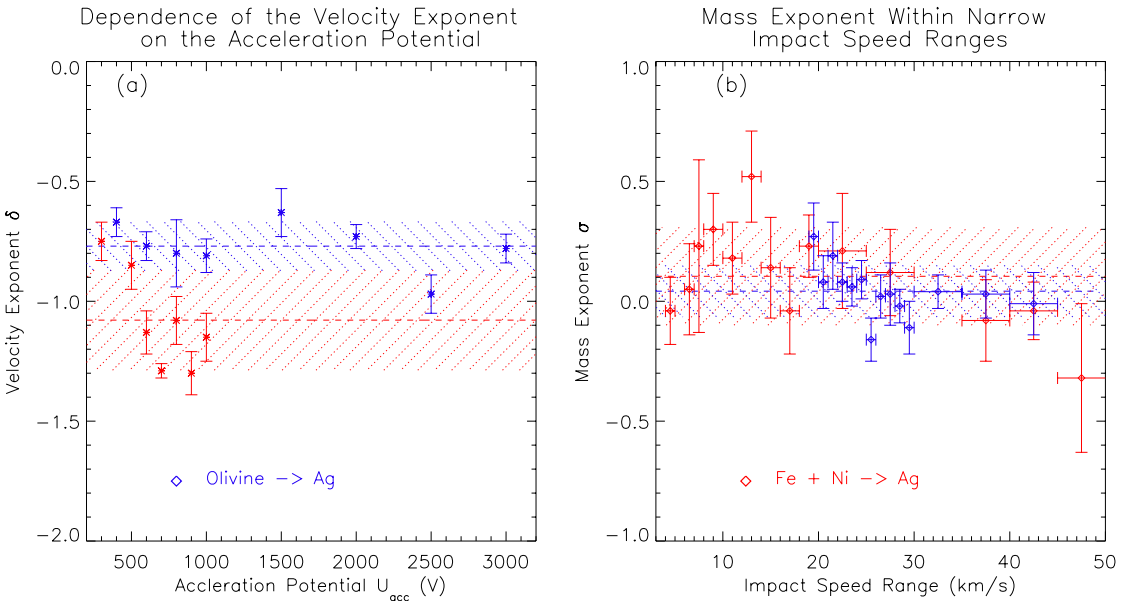

Figure 4.10.: ***(a)*** Dependence of the velocity exponent δ on the acceleration potential U_{acc} for shots with iron - nickel particles *(red)* and *PPY*-coated olivine particles *(blue)* onto a silver target. The dotted lines show the average value, the hatched regions the boundaries of the error determined by the standard deviation. Within these boundaries the velocity exponent is almost constant, consistent with δ being independent on the acceleration potential. ***(b)*** The mass exponent σ within narrow ranges of the impact velocity as a function of the impact velocity. Again, the dotted lines show the averaged value of the mass exponent, the hatched regions the boundaries of the error. The mass exponent σ is constant within these boundaries and about zero. Thus, the rise times are not dependent on the particles' masses.

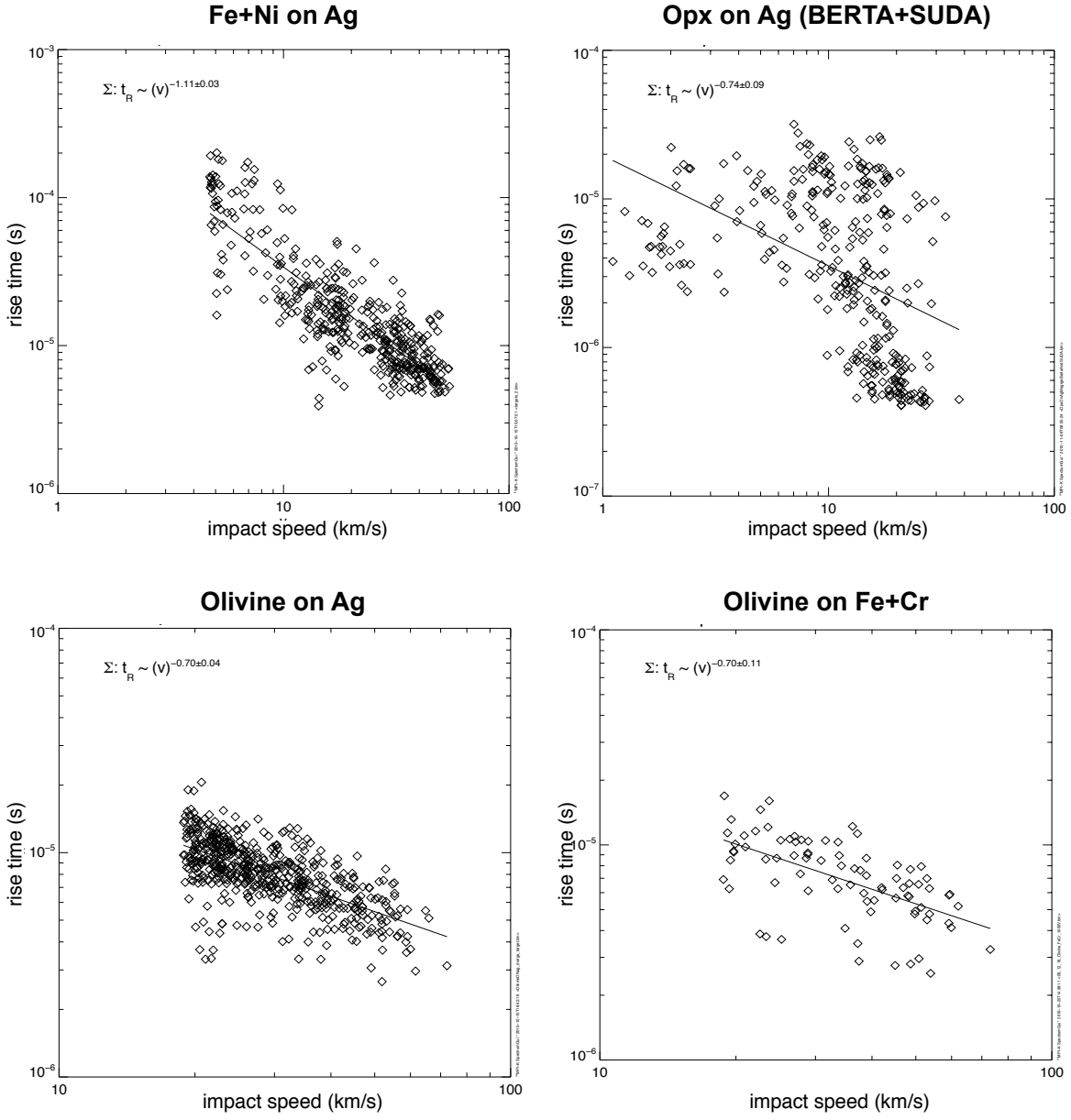

Figure 4.11.: Dependence of the rise time on the impact speed for four combinations of dust and target materials. The relation can be described by a power law $t_r \propto v^{\delta}$. The velocity exponents δ are summarised in Table 4.2.

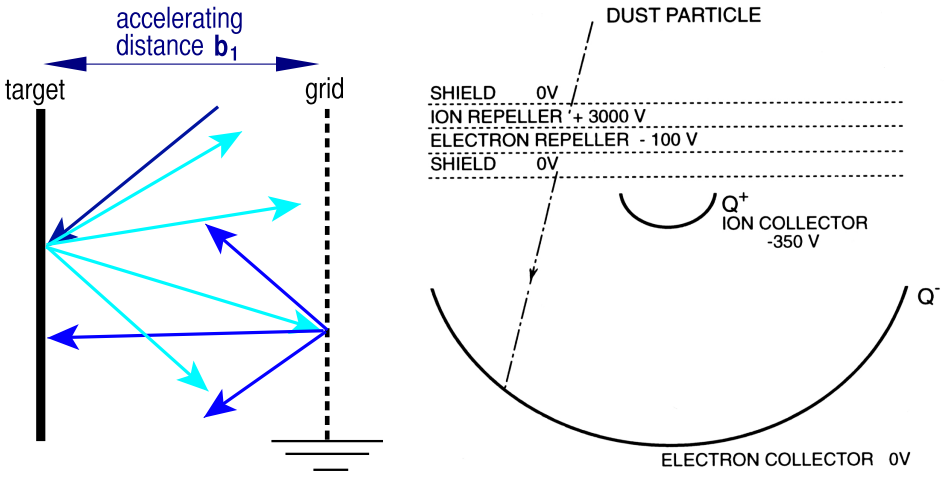

Figure 4.12.: *(left)* Geometry of the linear *BERTA* mass spectrometer and possible flight paths for ejecta production.*(right)* Geometry of iHEOS2 dust instrument.

Depending on the instrument geometry and the incident angle, ejecta formation is dominant in the velocity range from $5\,\mathrm{km\,s^{-1}}$ to $15\,\mathrm{km\,s^{-1}}$ (Göller, 1988). This range is not congruent with the velocity range in which the stepped charge yield signals occur most abundant. Considering the geometrical set up of the extraction region as shown in Figure 4.12, i.e. with a distance beteween the target and the grid of 20 mm, the timescale for the production of secondary ejecta impacts is $20\,\mu$s for $1\,\mathrm{km\,s^{-1}}$ ejecta velocity and $0.65\,\mu$s for $30\,\mathrm{km\,s^{-1}}$. This is indeed in the time range of the phases in the charge yield signals. But to generate more then two steps in in the charge yield evolution due to secondary ejecta impacts, one would have to assume a forth and back bouncing of ejecta between the target ad the grid. This scenario cannot be excluded, it seems to be unlikely on the other hand.

Another reason for the steps in the charge yield signals might be an effect within the recording electronics, i.e. in the charge sensitive amplifier. Apart from these possible explanations the cause of this effect is unclear. To get a better understanding of this phenomenon, the dependence of the height of individual steps, mainly the first steep rise and the number of steps on the total charge yield produced in the impact was studied (Figure 4.15) for the most complete data set obtained with iron and nickel particles impacting a silver target. The ratio of the first phase's height to the total charge increases with increase of the total charge, as well as with increasing impact velocity.

Analogously to the total charge yield, the height and duration of the individual evolution phases can be related to the impact parameters, the particle's mass and impact speed. The relation can also be described by power laws as shown in Figure 4.13 and Figure 4.16. For the heights of the steps each of resulting exponents is decreasing with the order of the phase (Tab. D.5). Also for the duration of the exponent describing the velocity dependence is decreasing with faster impact velocities. One exception is the first, fast evolution phase, being constant at about $1\,\mu$s as also shown in Figure 4.15. This first phase is the charge of the electrons produced instantaneously in moment of the impact. The following phases are generated by the charges of the electrons and negatively charged ions of contained in the evolving plasma cloud. Theoretical models, i.e. by Hornung and Kissel (1994), correlate the the time scale of the charge yield with the expansion time of the plasma cloud and possibly with an additional

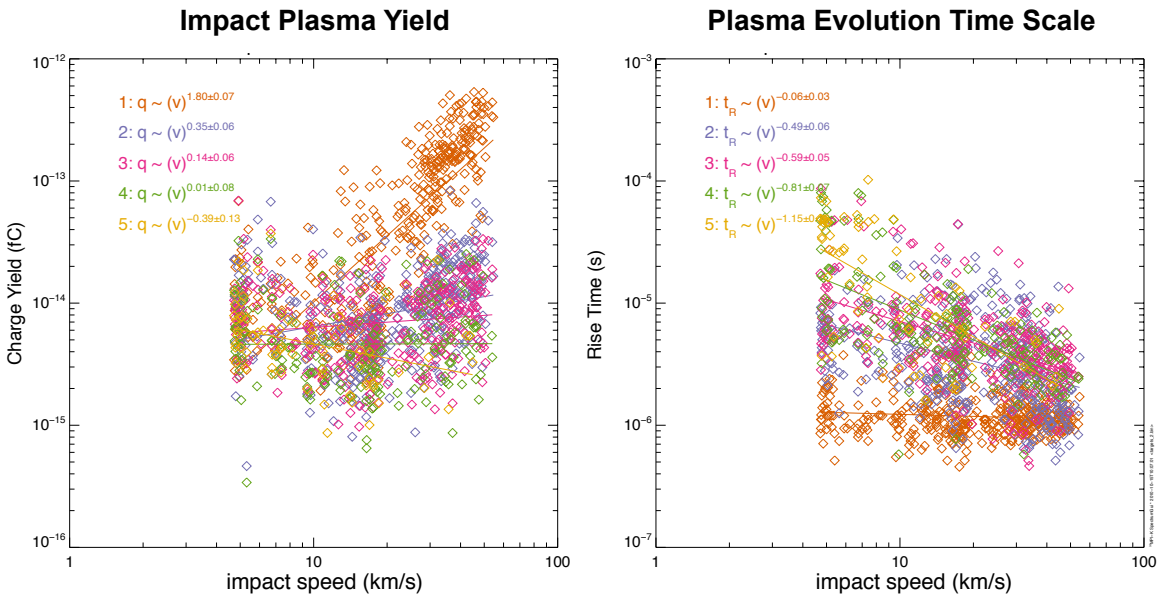

Figure 4.13.: Dependence of the charge yield of individual plasma evolution phase and of the evolution time scale on the impact velocity for shots with iron particles on silver.

bulk velocity of the evolving plume. Thus, according to this considerations the measured timescales as shown in Figure 4.16 give some hints about the expansion time of the plasma cloud.

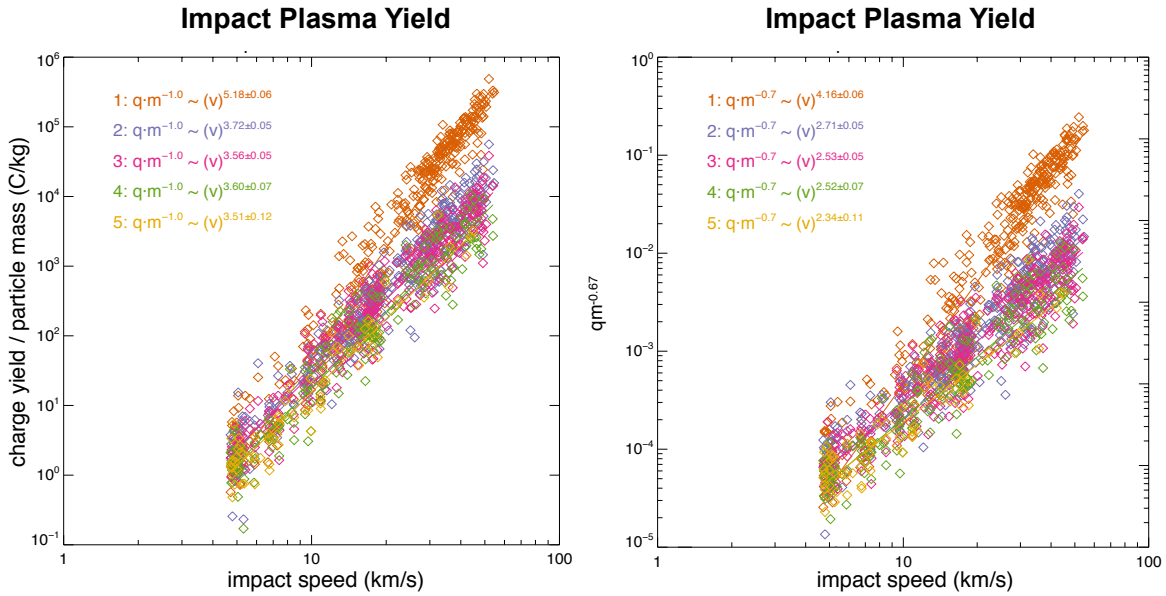

Figure 4.14.: Dependence of the charge yields normalised to m and to $m^{\alpha} = m^{0.68}$ of individual plasma evolution phases and of the evolution time scale on the impact velocity for shots with iron particles on silver.

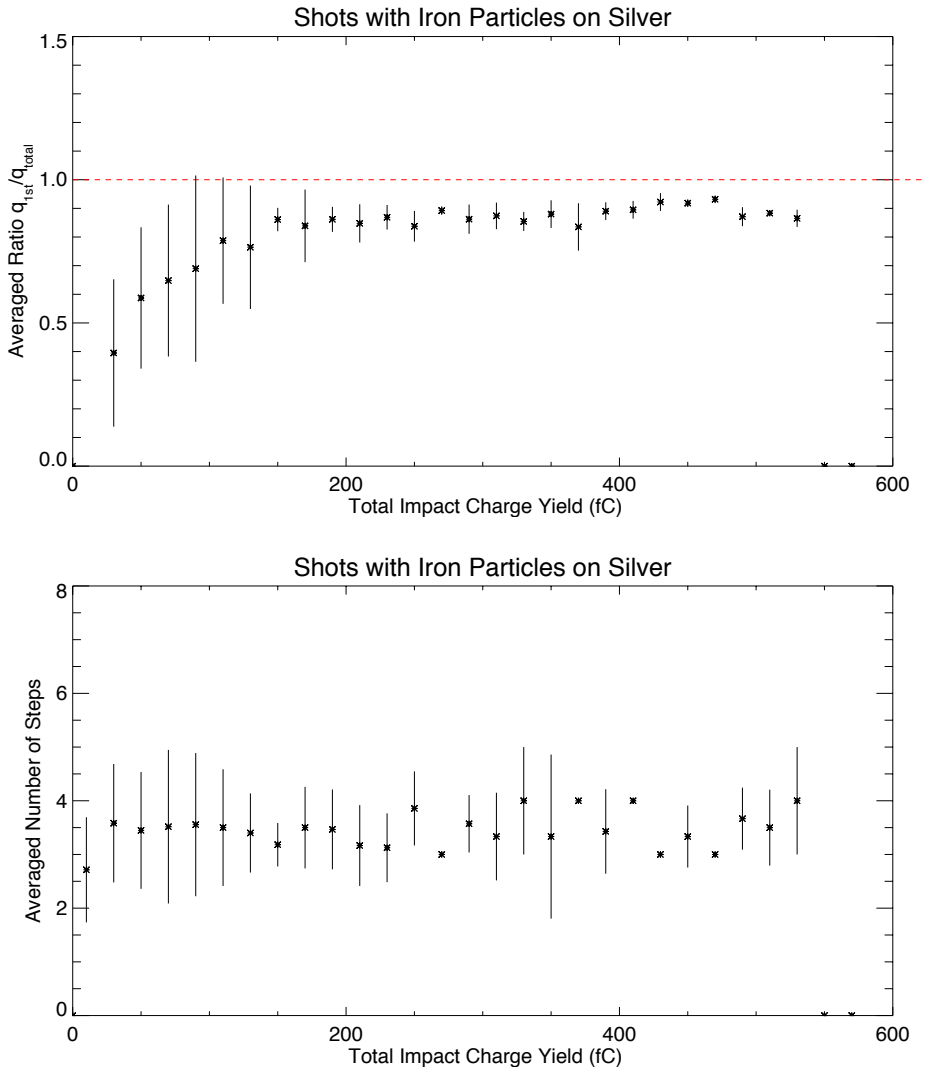

Figure 4.15.: Dependence of the plasma evolution phases on the total charge produced in the particle impact. ***(above)*** Ratio of the height of the first phase to the total charge yield in dependence on the total charge yield. With increasing charge the first, steep rise becomes more and more dominant. Its value approaches the height of the total charge signal, drawn as the red dashed line. ***(bottom)*** The number of phases is not related to the total charge yield.

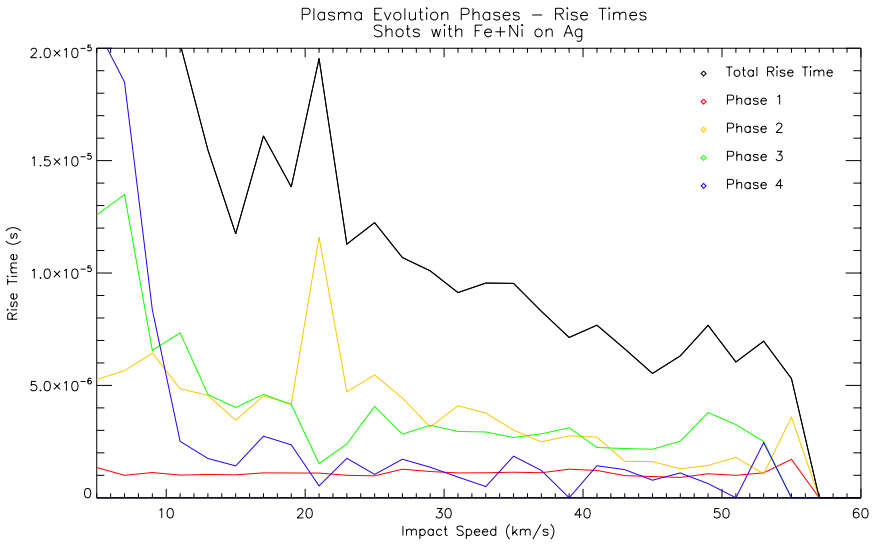

Figure 4.16.: Rise times of the four phases of impact plasma evolution. Except for the first evolution phase, the duration of the phases decreases with increasing impact velocity. The first step is of constant duration of about 1 μs.

4.1.4. Variability of the total charge yield for Laser ablation

The measure used to evaluate this reproducibility and variability is firstly the deviation of the total charge yield across a narrow range of a particular experiment parameter, for example a narrow range of laser energy or particle impact velocity, for fixed experimental conditions. To this end the average of the total charge yield and the standard deviation were calculated. To compare two or more sets of experimental conditions, the averaged charge yield and the standard deviation for the same range of a parameter can be compared. Furthermore the dependency of the charge yield on a experiment parameter can be evaluated and also compared to the behaviour of the resulting yield of another data set.

Variability due to the impact location

Laser experiments showed a strong dependency on the incident location of the beam: even with exactly the same laser parameters for shots on various spots on the same target the resulting signal differed widely. To evaluate and quantify this behaviour, measurements for two different locations on the same gold coated olivine target, whilst varying the laser energy, have been made. The procedure was the same for both data sets and all other laser experiments: After cleaning and preparing the surface with about 1000 high energy shots the measurements were performed, with variation of the laser energy by turning the half-wave plate as described in Section 3.4.8. The two plots on the bottom line of Figure 4.17 show the total charge yield as a function of the laser energy for both locations, Table D.6 lists the averaged charge yields and their standard deviations for laser energies from $6\,\mu$J to $12\,\mu$J in ranges of $1\,\mu$J. For the two locations the variation in yield differs by a factor of two for the energy range between $11\,\mu$J to $12\,\mu$J, up to about one order of magnitude for the energy range from $6\,\mu$J to $7\,\mu$J. Thus, the slope of the the fitted function to describe the energy dependency of the charge yield varies strongly. The spread of the charge yield within an energy range is large, from about 60% to 260%. There is also a difference between the two locations, as seen for the averaged yields.

4.1.5. Charge yields of laser ionisation

By analogy to the dependence of the total charge yield on the parameters of a particle impact, attempts can be made to link the charge yield to the only controllable laser parameter, the incident beam energy:

$$q \propto E^{\gamma}, \tag{4.2}$$

with E being the laser energy. The charge yield increases proportionally with increases in the laser power as shown Figure 4.17 for all investigated data sets. The energy exponent for is listed in Table 4.1.

On set of ion formation: The energy necessary to incur ion formation is a characteristic measure for the process of laser ablation . For this study a variety of charge sensitive amplifiers have been used, each with a distinct amplification factor and other potentially influential properties, primarily the bias potential which can be applied. Due to the fact that the amplifier capable of voltages higher than 1000 V was designed for higher charges, the set-up for higher acceleration potential was subsequently less sensitive. Thus, for these measurements, the lowest charge to be measured was higher than the charge produced at the onset point of ion formation. Here, the onset of ion formation is determined by the onset of the formation of an

evaluable *TOF* mass spectrum. For the iron and the gold coated olivine target, the onset of ion formation takes place at about 1 μJ, whereas for the copper-silver alloy it is at 12.45 μJ.

The wide variation in the the exponent γ for the two illuminated locations on one and the same gold coated olivine target is remarkable, as it is the large spread within the values for the two metal targets. There seems to be no significant difference between the onset of ion formation and the resulting charge yields due to the electrical properties of the target materials. Even though the absorption process is different for metal surfaces as for the absorption of the laser light due to a dielectric material (Stuart et al., 1995) , the gold coating of the Olivine target seems to lead to similar ion formation.

4.1.6. Rise time of the charge yield for laser ablation

In Figure 4.18 the rise time of the charge yield signal is shown as a function of the incident laser beam energy for three different target materials, iron, a silver-copper alloy and gold coated olivine. For the olivine target measurements at two distinct locations have been conducted.

The evolution time scale increases with increasing energy for three of the two data sets. For shots on one location on the olivine target, the rise time seems to decline with increasing laser energy. On the other hand the spread in the rise time for this data set is larger than for the others. The increase can also be described with a power law

$$t_r \propto E^{\varepsilon},$$

with E being the laser energy. The resulting values of the exponent can be found in Table 4.2. As mentioned in Section 4.1.1 the slope of the charge yield progression gets shallower with increasing laser energy. In particular the beginning of the rise is less distinct and sharp than for particle impacts. Also the point of maximum is more difficult to determine. Thus, the uncertainty of the rise time measurement is larger than for particle impacts. It is estimated as 10 % up to even 20 % for high energy measurements.

4.1.7. Summary and comparison

In this section the results of the investigations described in the sections above are summarised and compared with each other. The plasma emerging after either an impact of a dust particle or the impact of a laser beam on a solid target is described by its total charge yield and the time scale of its evolution. Table 4.1 and Table 4.2 list the exponents of the power laws describing the properties of the evolving impact plasmas as functions of the impact parameters for both processes. Additionally in order to compare the resulting charge yield and its rise time, the charge yields for all data sets studied in this theses are plotted as functions of the particle velocity or the laser energy respectively in one graph (Fig. 4.19) as well as the rise times (Fig. 4.20).

- **Total charge yield** The total charge is increasing with increasing impact velocities as well as for growing laser energies. The lowest impact charge yields measured are about 1 fC, whereas for the laser ablation the smallest charge yields where measured for laser shots onto a Ag+Cu all with charges $<$1 fC. The maximal charge yields differ very strongly due to the fact, that the laser energy can be increases far more extent the a increase in the impact parameters is possible due to the dust accelerator's functionality

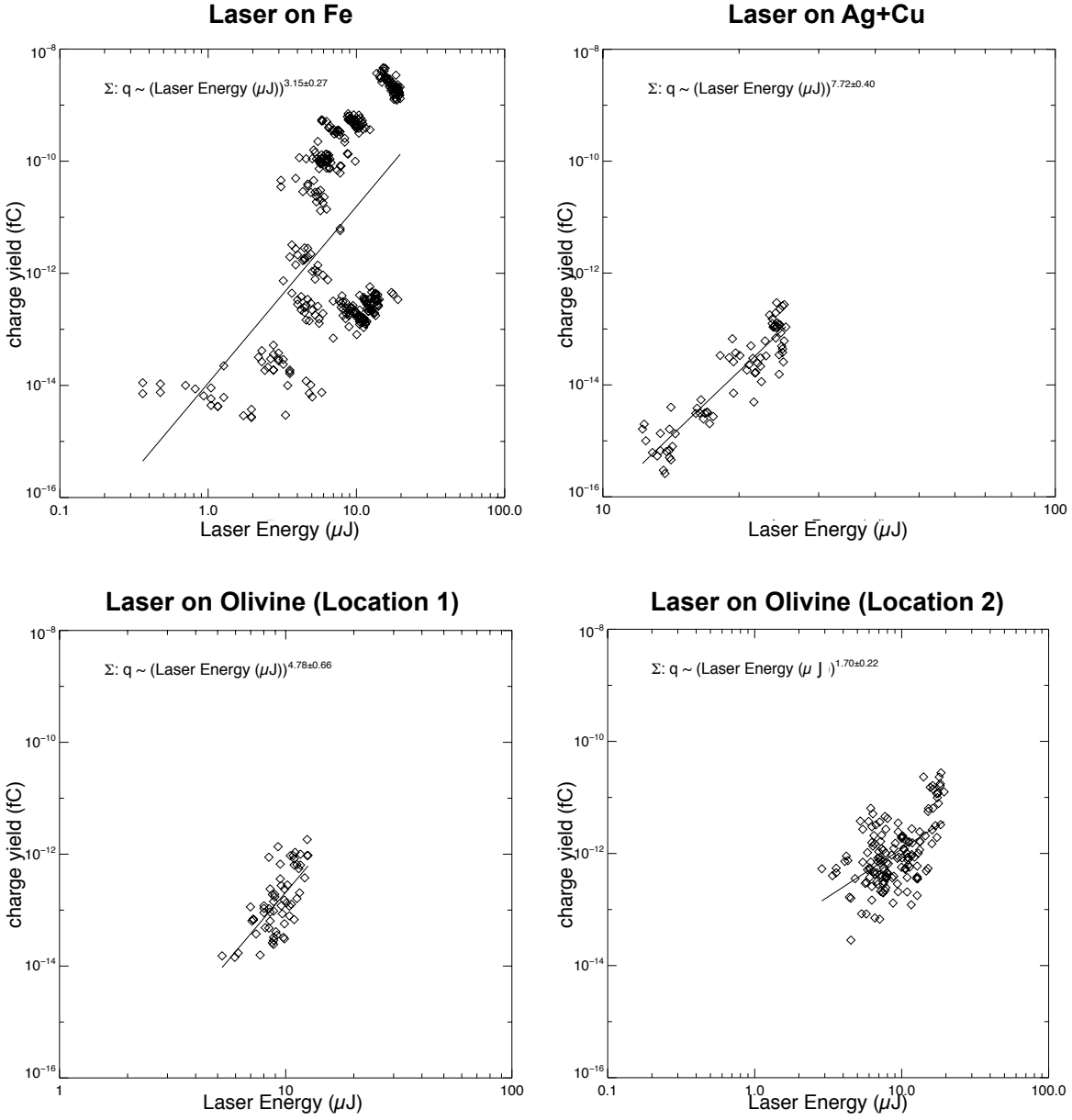

Figure 4.17.: Laser Shots: Charge yield at the target for various target materials. The top row laser shots on metal targets, the bottom row the charge yields for laser shots on two locations on a gold coated olivine target.

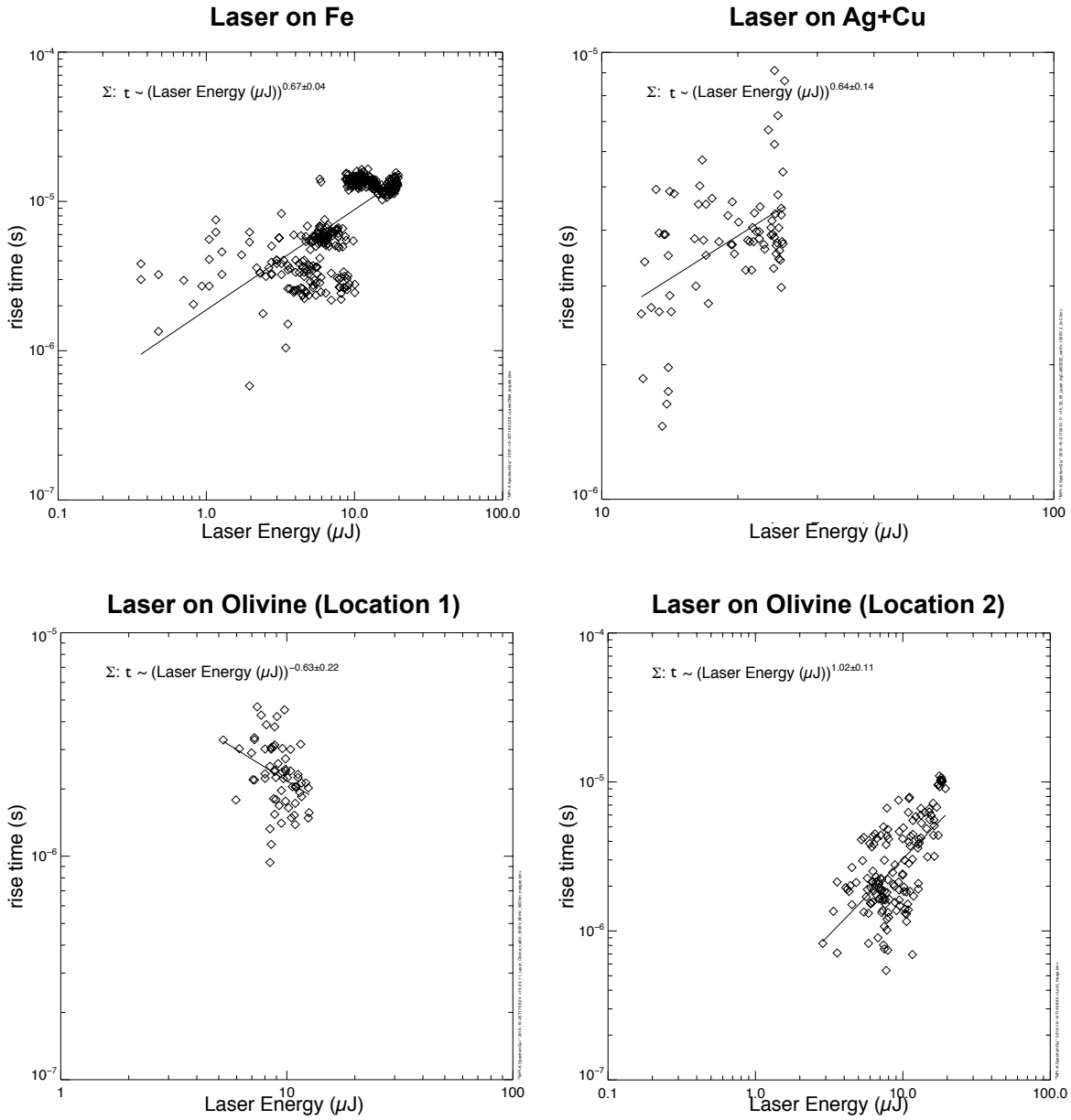

Figure 4.18.: Dependence of the rise time on the laser energy.

Table 4.1.: Summary of the derived relations of the total charge yield on the impact parameters for particle impacts and laser ablation. v is the impact velocity in $\mathrm{km\,s^{-1}}$, m the particle mass in kg and E the laser energy in μJ.

Relation	Experiment	Parameter α	Parameter β	Parameter γ
$q \propto v^{\beta}$	Fe → Ag		1.05±0.07	
	Opx → Ag		-0.23±0.16	
	Olivine → Ag		2.30±0.09	
	Olivine → Fe+Cr		1.54±0.34	
$q \propto m^{-1} v^{\beta}$	Fe → Ag		4.43±0.05	
	Opx → Ag		3.43±0.12	
	Olivine → Ag		5.50±0.07	
	Olivine → Fe+Cr		4.48±0.36	
$q \propto m^{\alpha} v^{\beta}$	Fe → Ag	0.67±0.08	3.28±0.05	
	Olivine → Ag	0.93±0.06	5.27±0.07	
$q \propto E^{\gamma}$	Laser → Fe			3.20±0.28
	Laser → Ag+Cu			7.90±0.41
	Laser → Olivine (Loc1)			5.14±0.68
	Laser → Olivine (Loc 2)			1.70±0.22

principles. For impact ionisation the largest charges measured are about $5 \cdot 10^3$ fC for olivine particles impacting an Ag target. The maximal charges recorded for laser ablation are about 10^7 fC.

- **Plasma evolution time scale:** The rise time decreases for increasing impact velocities of dust particles impacting a target. For laser ionisation on the other hand, the rise time gets longer with increasing laser energy. The plasma evolution time scale for impact ionisation is about one order of magnitude larger than for the laser ablation case.

Table 4.2.: Summary of the derived dependences of rise time t_r on the impact parameters for particle impacts and laser ablation. v is the impact velocity in $\mathrm{km\,s^{-1}}$, and E the laser energy in μJ.

Relation	Experiment	Parameter δ	Parameter ε
$t_r \propto v^{\delta}$	Fe → Ag	-1.11±0.03	
	Opx → Ag	-0.41±0.10	
	Olivine → Ag	-0.70±0.04	
	Olivine → Fe+Cr	-0.70±0.10	
$t_r \propto E^{\varepsilon}$	Laser → Fe		0.67±0.04
	Laser → Ag+Cu		0.64±0.14
	Laser → Olivine (Loc1)		0.63±0.22
	Laser → Olivine (Loc 2)		1.02±0.11

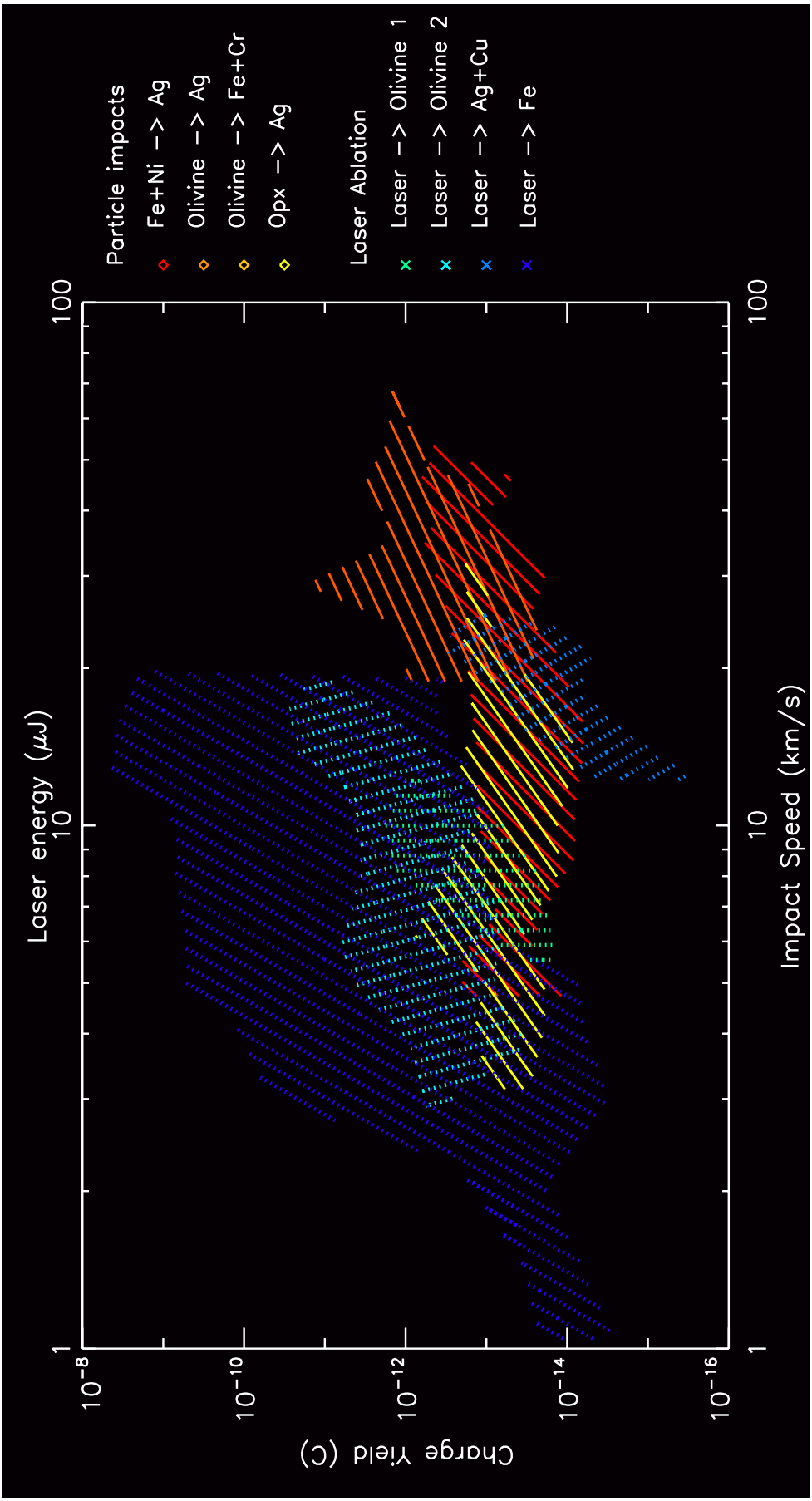

Figure 4.19.: Overview of the charge yields obtained with particle impact and laser ablation.

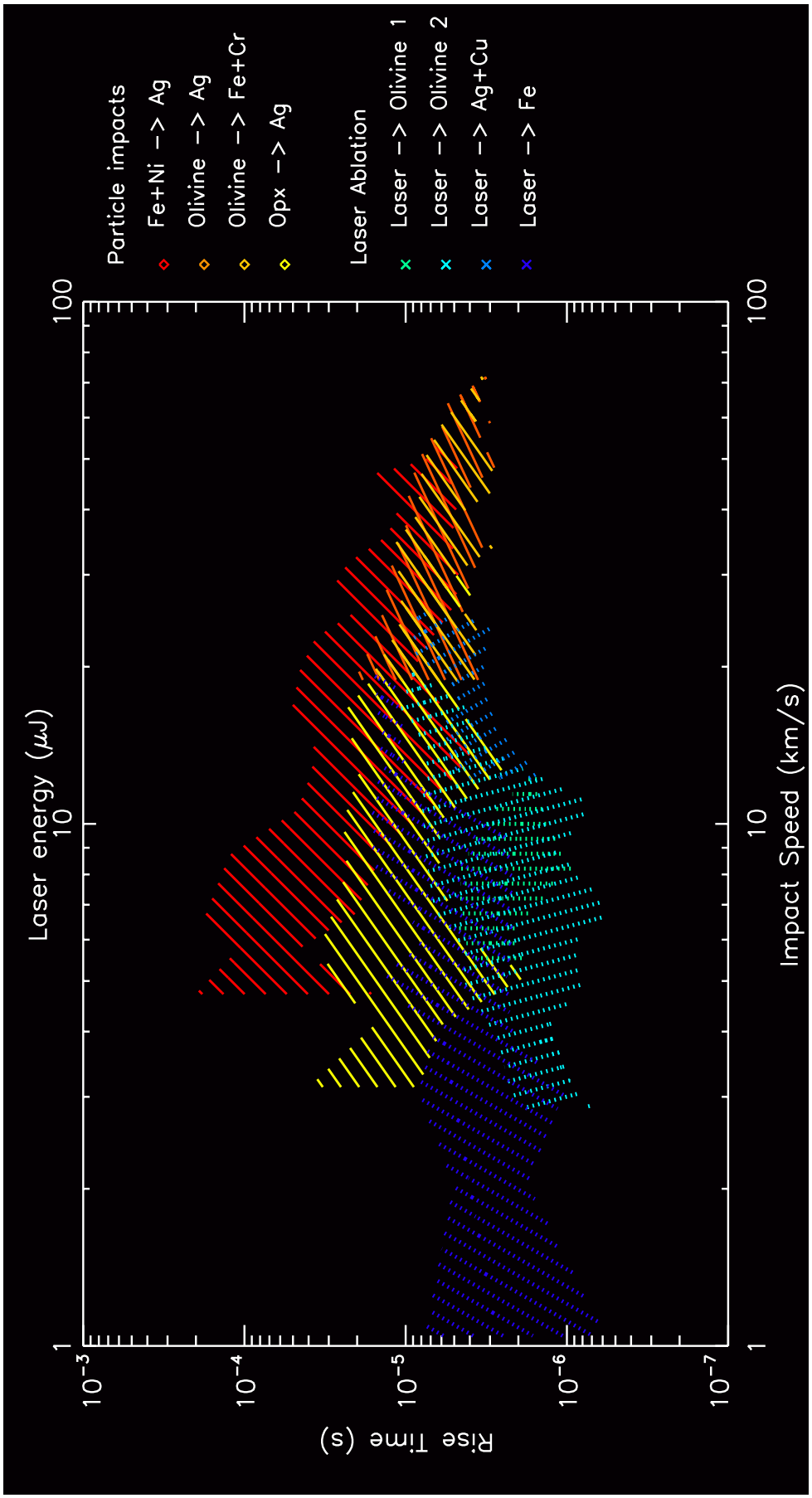

Figure 4.20.: Overview of the rise times obtained with particle impact and laser ablation.

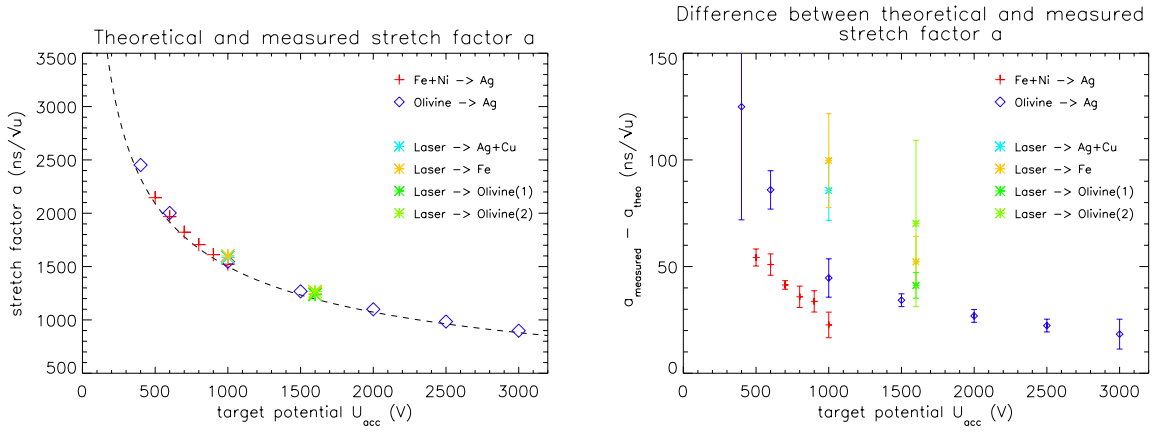

Figure 4.21.: *(Left)* The calculated stretch factor *a (dashed line)* in dependence on the acceleration voltage U_{acc} applied on the target and the stretch factors determined due to hypervelocity impacts with Fe+Ni *(red crosses)* and Olivine *(blue diamonds)* particles on a Ag target. The stretch factors for laser ablation on various targets are plotted with variedly coloured asterisks. Olivine(1) and Olivine(2) designate laser shots on one and the same gold coated Olivine target at two different locations. *(Right)* Difference between the theoretical and measured values in dependence on U_{acc}. In contrary to the left figure the error bars are visible here.

4.2. Resulting *TOF* mass spectra

This - and the following sections - deal with the resulting *TOF* mass spectra for both, hypervelocity impacts and laser ablation. The resulting spectra are characterised and compared with theoretical considerations conducted in Section 3.1.2. Furthermore the performance of the instrument, i.e. the *stretch factor a* (Section 2.3.1) and the mass resolution $m/\Delta m$ (Section 2.3.3), is discussed.

4.2.1. Theoretical and empirical determined stretch factor a

The plasma generated by either the hypervelocity impact of a particle on solid surface or the irradiation with laser light can be separated by an electrostatic field in its negative and positive components. In the case of a positive acceleration field, as given in the instruments used for this thesis, the negative component consisting of electrons and negatively charged ions is attracted to the target. The positive ions are accelerated towards an ion detector, i.e. a mcp, and generate a *TOF* mass spectrum.

A mass spectrum is a plot of relative intensity of the signal over the ratio m/q of mass to charge of the ions. In this plot, there are intensity peaks appearing due to specific values of the ratio m/q representing individual species of ions. To identify the ion species, mass scale can be assigned due to

$$t = b + a \cdot \sqrt{m},$$

where the *shift parameter b* represents any time offsets between the triggering point and the start of the spectrum due to the production process of the ions, triggering or other electronic effects. The *stretch parameter a* is the proportionality constant, which is in principle determined

by the physical set up of the instrument. In Section 3.1.2 the stretch factor has been calculated due to the properties of the *TOF* mass spectrometer for a variety of acceleration potentials U_{acc} applied on the target.

Figure 4.21 shows this theoretical stretch factor in comparison with empirical values derived from measurements of hypervelocity impacts of iron and nickel particle as well as Olivine grains on Ag targets. On the left side the measured data point and the theoretical function are plotted in dependence of the acceleration voltage. The error in the potential applied on the target is about 0.5 V. For hypervelocity particle impacts the spread in the measured stretch factors varies from $3\,\mathrm{ns}\,\sqrt{\mathrm{u}}^{-1}$ to about $10\,\mathrm{ns}\,\sqrt{\mathrm{u}}^{-1}$, corresponding with relative variations in the order of of 0.2 % to 0.6 %. Whereas for laser ionisation, the spread in the measured stretch factors a is about the factor 2 larger, it varies from 0.88 % to 3.08 %. On the right side the difference of the theoretical value and the measured stretch factors a is plotted as a function of the acceleration voltage U_{acc}.

The divergence between the theoretical value and the empirical determined stretch factors ranges from 1.51 % to 2.59 % for iron and nickel dust and from 2.09 % to 5.37 % for olivine grains hitting a Ag target. For laser ablation the difference ranges from 3.44 % to 6.64 %, resulting an a difference about the factor 2 to 3 larger then for impact ionisation. Thus, the empirical determined stretch factor is significantly larger than the theoretical values resulting from the geometrical and electrical properties of the *BERTA TOF* mass spectrometer.

One reason for this difference could be that there is an uncertainty in the geometrical set up of the spectrometer, i.e. the distance between the target and the first grounded grid. Especially for the laser ablation measurements this distance is probably less accurate, because the laser focussing is achieved by varying the distance between the target and the plane of the focusing lens (Section 3.4.6), leading also to a shift between the target plane and the fixed mounted grounded grid (Section 3.1.5). Nevertheless, for one studied data set the focusing was constant, therefore, this does not explain the wider spread of the empirical determined stretch factors for laser ablation in comparison with particle impacts.

In addition, the difference of the theoretical and the actual stretch factor decreases with increasing acceleration potential. In the theoretical considerations the electrostatic field was assumed to effect all the ions right from the starting point in time and indecently from the location of the individual ion. This means, that no shielding effects were taken into account. Besides on the accuracy of the determination of the flight time, the stretch factor a (Eq. 3.14) as a function of the measured flight time depends on the distances in the geometrical set up of the spectrometer and on the electrostatic field generated by the acceleration potentials between the target. For one data set the distances as well as the potentials are constant. This leads to two possible explanations for the difference between the calculated stretch factors to the measured values, its dependency on the acceleration potential and the slightly different properties of laser ablation and impact ionisation. The determination of the flight time of one individual line is achieved by the time of the peak maximum. Line broadening due to a wider velocity distribution of the ions constituting the line would lead to a uncertainty in the determination of the maximum as well as possibly to a shift of the time of the maximum. An increase in the stretch factor a translates into larger time differences between the individual lines (Lavila, 2002). That in turn suggests that the ions are not exposed to the accelerating electrostatic field during the complete distance the field is applied, implying shielding effects as discussed in Section 4.1.3. Again the fact that this effect is larger for laser ablation experiments leads to the conclusion, that the plasma cloud produced by laser ablation is of larger size then for impact ionisation.

Of course the most probable reason for a systematic aberration is the uncertainty of the theoretical stretch factor's determination. Here the uncertainties are on one hand the instabilities and uncertainties in setting up the electrostatic potentials, The manufacturer's specifications state these uncertainties in the order of magnitude 0.1 %. On the other hand there are the inaccuracies in the geometrical set up, mainly the distances and alignments of the target and the grounded grids. These inaccuracies will lead to aberration in the strength and homogeneity of the accelerating electrostatic fields. Here the uncertainty is estimated as smaller then 1 mm leading to errors in the order of 1.25 % to 5 %, matching the size of the observed effect.

4.2.2. Aperture and angular focusing

As described in Section 2.3 for a linear *TOF* mass spectrometer, the velocity and angular distribution of the ions translate in the broadening of the lines (Mamyrin, 2001). The shape of a peak is determined by both distributions, complicating the investigation of the underlying processes leading to the form of the line.

To study the the distribution of the ion velocities in direction of the spectrometer axis, the *BERTA* mass spectrometer is designed to filter out the angle distribution of the moving ions. This is obtained by the geometrical set up. The length of the ions' flight path (0.657 m) and the diameter of the *MCP* ($\varnothing$= 40 mm) lead to an aperture angle of 1.74°, translating into a space angle $d\Omega \approx 2.90 \cdot 10^{-3}$ sr . The motion of an individual ion constitutes of its initial velocity, representing an initial kinetic energy, and the accelerated motion within the electrostatic field provided by the target potential. Thus its total velocity has a component in the direction of the spectrometer axis and a perpendicular one. A stronger accelerating field will lead to a larger velocity and subsequently, to a shorter time of flight, in which the ion will additionally move according in perpendicular direction. Thus a higher accelerating potential is focussing the ions toward the ion detector. Figure 4.22 shows the angular focusing of ^{56}Fe ions due to the acceleration potential U_{acc} applied on the target. The opening angles of the path of flights of the ions in dependence to their initial kinetic energy perpendicular to the spectrometer axis are plotted for various acceleration potentials form 400 V up to 3000 V. The aperture angle of the instrument determines range of a perpendicular motion a individual ion can execute and still hit the ion detector at the end of the drift tube. Thus, the crossing point of one individual line with the line representing the aperture determines the maximum of the kinetic energy component directed perpendicular to the spectrometer axis for ions to reach the detector. For instance, ions with energies above 2 eV (perpendicular component) do not reach the detector for acceleration voltages below 2500 V.

Of course the filtering leads to a decrease of the number of ions contributing to the signal at the *MCP*. One can try to estimate the amount of this losses by considerations of the actual angular distribution of the ion motion.

For laser ablation the angular distribution has been investigated for a large variety of target materials as well as laser properties, i.e. laser energy, pulse lengths and focal spot sizes. Under conditions quite similar to those applied for this theses, the findings are much more consistent and profound then in the impact ionisation case (Dinger, 1980). The experimental results indicate that ablated ions are highly directional and moving normal to the irradiated surface. Often the the empirical data of the angular distribution is fitted by function of $\cos^n$ or Gaussian distribution peaking at the target normal (Rohr and Srivastava, 2005) It was observed by Müller et al. (2003) by that the angular distributions of the emitted ions had mainly three characteristics. For a given laser energy and a given target element, the angular distribution

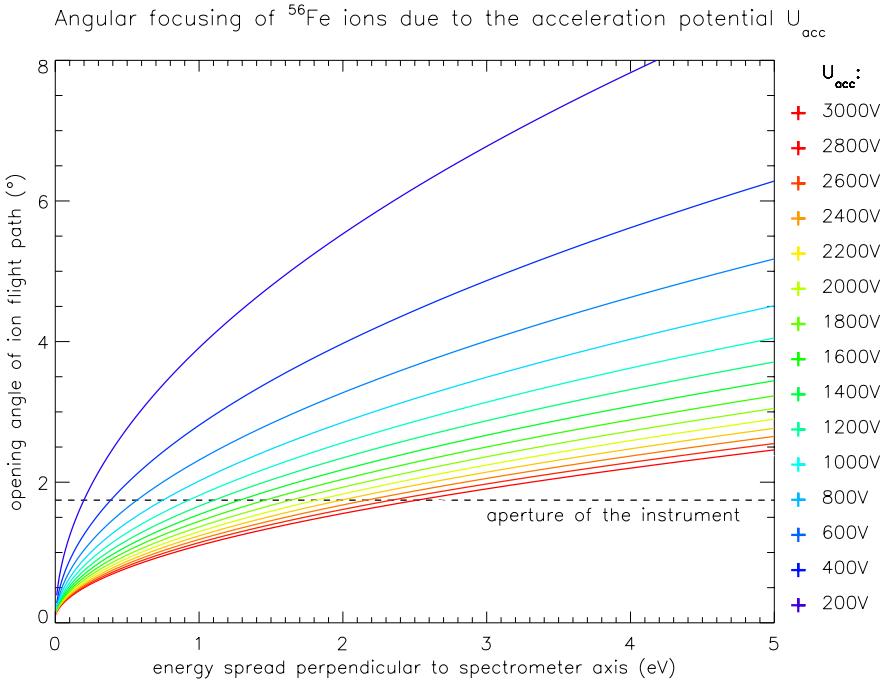

Figure 4.22.: The angular focusing of ^{56}Fe ions due to the acceleration potential U_{acc} applied on the target. The opening angles of the path of flights of the ions in dependence to their initial kinetic energy perpendicular to the spectrometer axis are plotted for various acceleration potentials form 400 V up to 3000 V. The dashed line represents the aperture angle of the instrument determined by the distance between the target plane and the ion detector and the size of the detector area ($\varnothing$ = 40 mm) . Thus, the crossing point of one individual line determines the maximum of the kinetic energy component directed perpendicular to the spectrometer axis for ions to reach the detector. I.e. ions with energies above 2 eV (perpendicular component) do not reach the detector for acceleration voltages below 2500 V.

showed more preferential focusing toward the target normal as the value of the focal spot size B increased. Second, for a given laser energy and a given focal spot size, the focusing was more pronounced toward the target normal as the atomic mass number of the target materials increased. Third, for a given energy, a given focal spot size and a given element, the particles with higher ionisation states were much more focused toward the target normal (Láska et al., 2002). Furthermore, the collimating of the ion beam is also dependent on the target material (Bleiner et al., 2007).

In the case of impact ionisation, empirical data of the angular distribution of ion velocities are very rare, partially contradicting each other and coincidently cover very specific, non-overlapping impact parameters. Sternovsky et al. (2007) report the measurement of the angular and velocity ions emitted due to impacts of Al particles on a Ta target at impact velocities of 1 km s^{-1} to 11 km s^{-1} by Abramov et al. (1991). In this range of slow impact velocities the evaporation of the particle remains incomplete. The resident droplet shields the the line of sight normal to the target plane leading to a angular distribution being hollow close to the spectrometers axis. In contrast a study by Øren (2001) resulted in a narrow distribution close to the target normal. Here, the properties only of the lines of alkali metal contamination ^{23}Na

and ^{39}K were investigated. These lines represent a very distinct group of species, emitted by different processes then the main constituents of the ion spectrum as discussed in Section 4.6. Ratcliff and Allahdadi (1996) discussed the energy and angular distribution of positive ions emitted in an impact a 70 nm boron carbide particle on a Ag -doped aluminium target at a velocity of $94\,\mathrm{km\,s^{-1}}$. The observed line profiles of the *TOF* mass spectrum were tried to reproduce as accurate as possible using a various angular and energy distribution in a computer simulation. For each individual line, the angular distribution had been assessed besides the assumption of an isotropic distribution, (with?) a variety of possible functions, like $\cos$, $\cos^3$, and $\cos^3$ measured relative to the target normal. The authors concluded their findings that the ion trajectories are focussed in the direction of the target normal, independently on the incident angle of the the dust grain. For example, the line profile of the H^+-ion was reproduced best under the assumption of an angular distribution described by $\cos^3$.

Modelling of CDA mass spectra by Hillier et al. (2006) on the other hand resulted in the necessity of assuming broader functions for the ion emission distribution to fit the studied lines.

A quite narrow angular distribution and subsequently a certain directionality of the ions motion toward the target normal match particular aspects of models for the hypervelocity impact. It is quite obvious that the directory of the emitted material depends on the formation of the crater due to the particle impacts (Rudolph, 1969; Nagel and Fechtig, 1980). First the direction of the ion motion is constraint by the geometrical boundaries of the crater. The mechanics of the impact cratering however go through several phases during the process of the impact leading to various directionalities and velocities of the emitted material as shown in Figure 4.23 . In the beginning shock wave run through the particle as well as the target. In this early state, the compressed material is limited to a a small lens-shaped region directly below the art of the penetration. As the particle penetrates more deeply into the target, the shock waves engulf an ever increasing mass of the target and the projectile. The geometry of the shock wave system, is heavily influenced by the presence of free surfaces on the surface of the target and the sides of the impacting particle. There are rarefaction waves running across the target surface and along the sides of the projectile. This leads a hydrodynamic ejection of mass at very high velocities, the so-called *"jetting"*. When the shock wave reaches the backside, it will be reflected and scattered back into the particle. the geometry of this waves is exceedingly complex, with the flow pattern dominated by a spherically expanding shell of compressed target and projectile material (Gault et al., 1974). Numerical calculation have been carried out on the dynamics of the cratering for example by Anisimov et al. (1984). The simulation of an impact of a particle with the density of $1\,\mathrm{g\,cm^{-3}}$ and a mass of $6\cdot10^{-7}\,\mathrm{g}$ on a Al target with a velocity of $80\,\mathrm{km\,s^{-1}}$ resulted in a flow field of the shocked matter also directed towards the normal of the target plane.

Furthermore, crater formation deforms and transforms surface considerably. Subsequently, the effect due to the impact angle can be neglected. The stopping shock is determined by the total impact velocity, justifying the considerations of Section 2.1

Secondly, there will be an additional velocity component perpendicular to the target normal due to momentum transfer from the target surface. According to numerical simulations, the value of this so-called bulk velocity is about 1/3 of the impact velocity (Hornung, 2010). A recoils pressure on the target is as well present in the case of laser ionisation (Bäuerle, 1996).

In summary, the small number of available empirical data and the fact that the existing data sets do not match in their range of parameters, make it difficult or even impossible to predict the ration of ions produced on the target to reach the MCP. Putting aside the possibility of

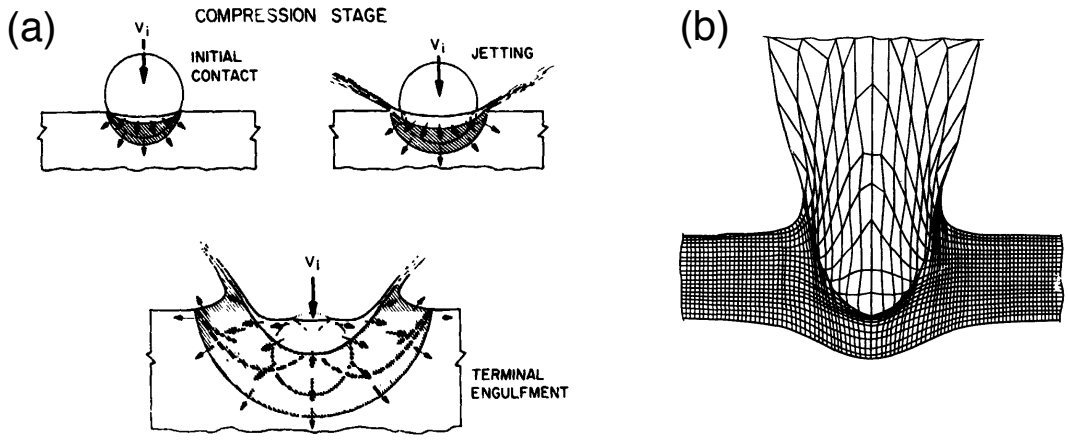

Figure 4.23.: ***(a)*** Schematic representation of the formation of an impact crater. In the first stage, the compressed material is limited to a a small lens-shaped region directly below the art of the penetration. As the particle engulfs further into the target are rarefaction waves running across the target surface and along the sides of the projectile, leading to *"jetting"*. The terminal phase represents a state with a stress wave geometry exceedingly complex. (Gault et al., 1974) ***(b)*** Numerically calculated flow field caused by an impact of a particle with the density of $1\,\mathrm{g\,cm^{-3}}$ and a mass of $6\cdot10^{-7}\,\mathrm{g}$ on a Al target with a velocity of $80\,\mathrm{km\,s^{-1}}$ (Anisimov et al., 1984).

a collimated ion beam along the direction of the impact as proposed by Hornung and Kissel (1994) for extreme ratios of densities for particle and target, the minimal ratio can be estimated by assuming an isotropic velocity distribution and neglecting any focusing due to the accelerating potentials. In this case, the ratio of the ions reaching the MCP to the total number of ions produced will be the same as the space angle of the instrument's aperture compared to this of a complete sphere

$$\frac{dN}{N} \geq \frac{d\Omega}{\Omega} = \frac{2\pi\,(1-\cos 1.74^\circ)}{2\pi} \approx 2.31\cdot10^{-4} = 0.231‰$$

As explained in the following, to reach a more reliable assignment of the lines to ion species, the spectra recorded with two reflectron *TOF* mass spectrometer, *LAMA* and *SUDA*, are compared to the *BERTA* mass spectra. Contrary to the linear mass spectrometer, both high resolution instruments, have been designed to optimise the spatial and timely focusing of the ion trajectories(Sternovsky et al., 2007; Kempf et al., 2010). This leads, besides to a larger mass resolution, to a more efficient ion collection and thusly to a higher sensitivity (Srama, 2010).

4.2.3. Mass resolution and line assignment

As mentioned in the section, above the line shape and width is determined by the velocity distribution of the the ions relative to the axis of the *BERTA TOF* mass spectrometer. The upper parts of Figure 4.24 and Figure 4.25 show *TOF* mass spectra recorded with the *BERTA* instrument for impacts of *Fe+Ni* particles and *Opx* dust on a Ag target.

As it will be discussed in Section 4.6, the width of lines recorded with a linear *TOF* mass spectrometer depends on the impact velocity and the impact energy density. The lines broaden

Table 4.3.: Mass resolution on the *BERTA TOF* mass spectrometer. *(above)* Values of $\Delta m/m$ for the most important lines in mass spectra obtained with hypervelocity impacts of Fe+Ni onto a Ag target for acceleration potentials U_{acc} from 500 V to 1000 V. *(bottom)* Values of $\Delta m/m$ for the most important lines in mass spectra obtained with hypervelocity impacts of Fe+Ni onto a Ag target for acceleration potentials U_{acc} from 400 V to 3000 V. The impacts occurred at velocities from 18 km s^{-1} to 22 km s^{-1}.

Shots with Fe+Ni on Ag

U_{acc}	^{1}H	^{12}C	^{23}Na	^{39}K	^{56}Fe
1000 V	42 ± 23	43 ± 50	107 ± 29	114 ± 44	23 ± 13
900 V	29 ± 20	38 ± 27	102 ± 38	163 ± 80	18 ± 5
800 V	14 ± 11	20 ± 14	142 ± 40	142 ± 40	24 ± 39
700 V	21 ± 17	24 ± 18	–	–	14 ± 4
600 V	21 ± 15	16 ± 12	–	–	10 ± 1
500 V	17 ± 11	12 ± 6	–	–	9 ± 3

Shots with Olivine on Ag

U_{acc}	^{1}H	^{12}C	^{23}Na	^{24}Mg	^{28}Si	^{39}K	^{56}Fe
3000	55 ± 7	79 ± 10	124 ± 19	48 ± 33	89 ± 11	163 ± 45	246 ± 135
2500	57 ± 6	51 ± 27	91 ± 40	43 ± 23	64 ± 21	200 ± 47	–
2000	64 ± 14	56 ± 41	117 ± 44	87 ± 41	150 ± 89	175 ± 101	88 ± 45
1500	62 ± 12	69 ± 43	115 ± 48	77 ± 33	64 ± 22	173 ± 49	90 ± 53

with an increase of the impact speed. Thus, the mass resolution is expected to decrease with growing impact speeds. On the other hand, the mass resolution $m/\Delta m = t/2\Delta t$ is increasing with an increasing acceleration potential U_{acc} as shown in Section 2.3.3. The upper half of Table 4.3 shows the mass resolution $m/\Delta m$ for the most important lines in spectra obtained by *Fe+Ni* particles impacting a Ag target. The mass resolutions of all lines except for those of the alkali contaminants Na and K are increasing with increasing acceleration potential. The values for the $m/\Delta m$ range from 9 for the iron lines recorded with and acceleration potential to up to 163 for the ^{39}K-line and an acceleration potential of 900 V. The lines of the alkali contamination are very narrow and lead to $m/\Delta m > 100$, assumed to be the effect of a different formation process for those ions in comparison to ions of the bulk material of impactor and target. This will be discussed further on in Section 4.6. Thus, the lines of the surface contaminants ^{23}Na and ^{39}K will be left out for further considerations of the mass resolution and its implications. The bottom part of Table 4.3 lists the mass resolutions for the main constituent lines of spectra obtained with *PPY*-coated *Olivine* grains onto a Ag target. Here, the acceleration potentials selected for this comparison were much higher and ranged from 1500 V to 3000 V, leading to mass resolutions between 50 and 90.

The low mass resolution of the *BERTA* mass spectrometer complicates the assignment of a mass scale as described in Section 2.3.2. It is difficult to identify the time at peak maximum for broad lines.Therefore, additional information is needed to get a more reliable assignment of the measured peaks in the ion intensity to lines.

- For laboratory experiments the chemical composition of both, the target and the impacting particle is known. Thus the probability of the abundance of a particular line and even its expected relative intensity can be can be estimated. This can be used to decide how likely if a particular mass peak represents a species of ions(see Section 3.5).
- The appearances of elements with distinct isotopic abundances are good markers to identify lines, because the recorded line pattern has to match the isotopic abundances of the assumed specie. For instance, Ag used as a target material provides two almost equally abundant isotopes, ^{107}Ag and ^{109}Ag, simplifying the mass scale assignment to spectra even for complex or unknown impactor materials. This on the other hand leads to a more reliable determination of the mass scale, optimising the determination of the stretch factor a. Table 4.4 lists prominent lines of the materials used in this study. Given are the naturally occurring isotopes, their atomic masses and their naturally abundances.
- The comparison with spectra obtained with the same materials and under similar conditions with reflectron *TOF* mass spectrometers helps to identify lines unambiguously. A reflectron is a magnet-free *TOF* spectrometer with the capacity to achieve second order time focusing with regard to variation of ion energies and angles of divergence of their departure from the source. To this aim, I used spectra of Fe+Ni grains impacts onto Ag recorded with the *LAMA* spectrometer and spectra of Opx grains onto Ag recorded with the *SUDA* spectrometer (see Section 3.2).

4.2.4. Characterisation of spectra

The analysis of exemplary spectra as shown in Figure 4.24 and 4.25 leads to the following conclusions:

- *BERTA* spectra are much noisier then spectra recorded with *LAMA* and *SUDA*, the ringing of the MCP (see Appendix B) is much more prominent. Saturation occurs for less intense signals. This is due to a lower degree of optimisation of the implemented MCP and its electronic circuitry. But as shown in Figure 4.25 this effect can also occur for the *SUDA* and *LAMA* instrument.
- Because the angular distribution is filtered out due to the small aperture of the spectrometer, line broadening is mainly due to the velocity distribution of the ions. Thus, all following considerations relate to the velocity distribution.
- The upper panel of Figure 4.24 whose lines are grouped in 5 bunches. A comparison with a corresponding high resolution spectrum reveals that the ”line forrest” between around 50 amu and 62 amu is formed by the lines of the isotopes ^{54}Fe, ^{56}Fe, ^{58}Ni, ^{60}Ni, and ^{62}Ni. Indeed the relative isotopic abundances are represented in the *BERTA* spectra as good as in the high resolution spectra. The is also the case for ^{107}Ag and ^{109}Ag lines , with the limitation that the ratio of the abundances is not apparent correctly due to the overlapping of the two lines. The linear *TOF* spectrometer shows the $^{1}H^{+}$line and its cluster ions H, H_2, H_3, and the ^{12}C and ^{16}C lines. Between 20 amu and 40 amu, the BERTA spectrum differs from the LAMA spectrum. Whereas the *LAMA* spectrum shows lines due to the surface contaminants ^{23}Na and ^{39}K and some other distinct lines, disintegrate those peaks on a BERTA spectrum into a bunch of individual spikes (see Section 4.6.5).

Table 4.4.: Overview of important elements contained in the materials studied for this thesis. Listed are the naturally occurring isotopes, their atomic masses and their naturally abundances.

Magnesium			*Silicon*		
Isotope	mass	abundance	Isotope	mass	abundance
^{24}Mg	23.99 amu	78.99 %	^{28}Si	27.98 amu	92.22 %
^{25}Mg	24.99 amu	10.00 %	^{29}Si	28.98 amu	4.68 %
^{26}Mg	25.98 amu	11.01 %	^{30}Si	29.97 amu	3.05 %
Iron			*Nickel*		
Isotope	mass	abundance	Isotope	mass	abundance
^{54}Fe	53.94 amu	5.85 %	^{58}Ni	57.94 amu	68.08 %
^{56}Fe	55.94 amu	91.75 %	^{60}Ni	59.93 amu	26.22 %
^{57}Fe	56.94 amu	2.12 %	^{61}Ni	60.93 amu	1.14 %
^{58}Fe	57.93 amu	0.28 %	^{62}Ni	61.93 amu	3.64 %
			^{64}Ni	63.93 amu	0.93 %
Copper			*Ag*		
Isotope	mass	abundance	Isotope	mass	abundance
^{63}Cu	62.93 amu	69.17 %	^{107}Ag	106.91 amu	51.84 %
^{65}Cu	64.93 amu	30.83 %	^{109}Ag	108.91 amu	48.16 %

- *BERTA* spectra of OPX onto Ag (Figure 4.25) show nicely the three main magnesium isotopes (^{24}Mg, ^{25}Mg, and ^{26}Mg) according to their relative abundances in both types of spectra (see Table 4.4). Furthermore, the lines of the potassium isotopes, ^{39}K and ^{41}K,together with the ^{40}Ca-line are resolved.

4.3. Variability of *TOF* mass spectra

The resulting signals of both, laser ablation and impact ionisation are known to show a large variability: To valuate, interpret and compare the signals quantitative measures have to be found to do so.

For both processes two signals have been used to characterise the process of plasma formation and the resulting plasma, the *total charge yield* at the target, recorded by a charge-sensitive amplifier and the *time-of-flight mass spectrum*, showing the relative intensities of the different ion species and their velocity distribution.

Since the size focal point of the laser beam and the pulse duration have been approximately constant over at least on period of measurements, there are constant relations between the laser energy, the energy density and the laser power density. Thus, the laser energy, which was the

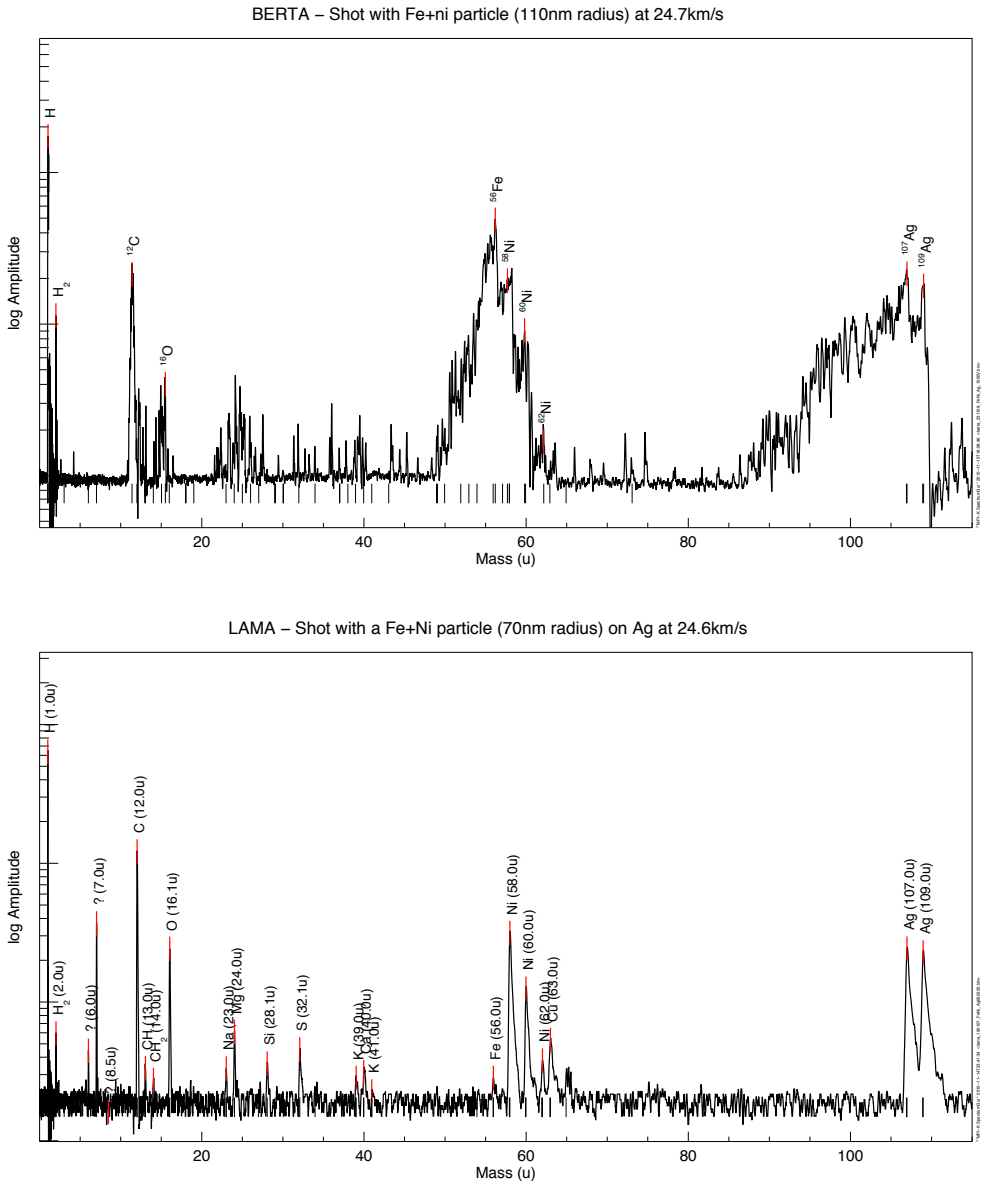

Figure 4.24.: *(above)* A TOF mass spectrum recorded with the *BERTA* instrument after an impact of a *Fe+Ni* particle with 110 nm radius at an impact velocity of 24.7 km s^{-1}. *(bottom)* In comparison a mass spectrum taken with the high resolution *LAMA* instrument for an impact of a *Fe+Ni* particle with 70 nm radius and an impact velocity of 24.6 km s^{-1}.

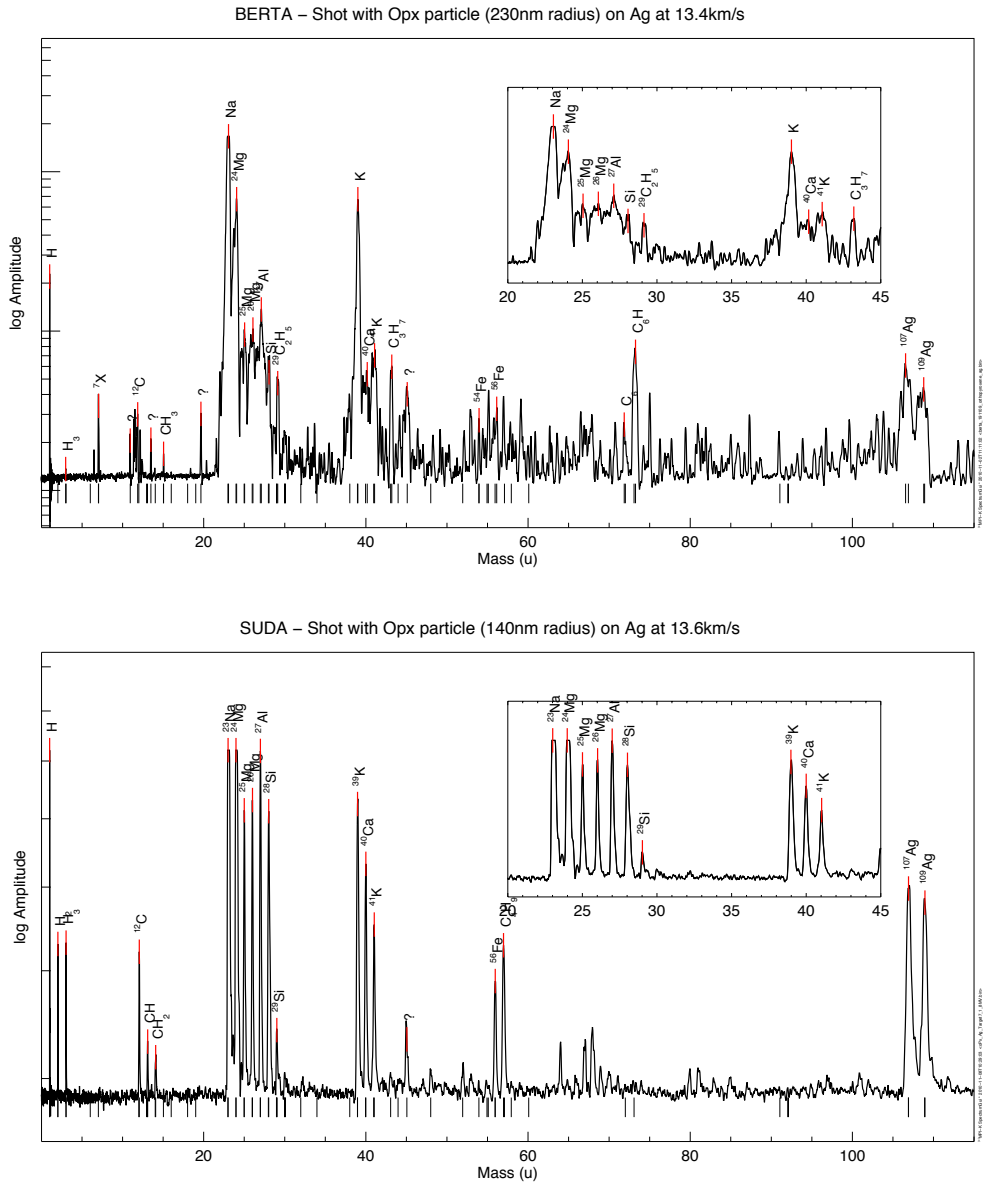

Figure 4.25.: *(above)* A TOF mass spectrum recorded with the *BERTA* instrument after an impact of a *Opx* particle with 230 nm radius at an impact velocity of 13.4 km s^{-1}. *(bottom)* In comparison a mass spectrum taken with the high resolution *SUDA* instrument for an impact of a *Opx* particle with 140 nm radius and an impact velocity of 13.6 km s^{-1}.

only actively controlled parameter for the laser, will be considered as the defining parameter for laser ionisation in the following.

For particle impacts on the other side, there are three parameters in question: the particle impact velocity, the particle 's kinetic energy and the impact energy density. Thus, for the consideration of the reproducibility and variability particle impacts and their outcomes one has to discuss, the variability of the resulting signals in dependence of all three of these parameters.

4.3.1. Variability of spectra data sets

To assess the variability of mass spectra produced under similar conditions such as narrow impact speed or impact energy ranges one needs to introduce an mathematical measure. There is no canonical way to define such a "variability number", the choice needs to based on quantities relevant for the goals of the study. Here, we are primarily interested in the fact how often in a data set certain lines appear and how strongly the lines' amplitude fluctuates around a mean value. Probably the most natural way to obtain such a measure is to compare the amplitudes a_i of selected lines of a data set with the amplitudes s_i of a reference spectrum, which is given by the normalised sum spectrum of the data set in question.

Suppose that the reference spectrum $\{s_1,\ldots,s_n\}$ consists of n lines with relative amplitudes s_i. Empirically, the variability E_i an the i-th spectrum of the data set can be characterised by the expression

$$E_i = \sum_j^n \left| \frac{a_j - s_j}{s_j} \right| w_j / E_{norm}, \tag{4.3}$$

where the weight

$$w_j = \frac{s_j}{\sum_j^n s_j} \tag{4.4}$$

describes the relevance of the j-th reference line for the appearance of the spectrum. Then, the total variability V of the data set with respect to the reference spectrum $\{s_1,\ldots,s_n\}$ is given by the average value of $\{E_1,\ldots E_m\}$. It remains the question for the normalisation E_{norm} of E_i, because the value of E_i obviously depends on the choice of the reference spectrum.

The values of variabilities depend aside from the actual fluctuations within the data set, also on parameters like the number of chosen characteristic lines and their weight in the sum spectrum. In order to develop an better understanding of the actual meaning of variabilities derived from the experimental data and to be able to compare the values of individual data sets of measurements made under different experimental conditions, the empiric values can be compared with values derived from theoretical models representing specific conditions:

1. **Variability of completely randomised spectra:** The variability is calculated for a large set of spectra composed by the characteristic lines with completely random line intensities. Since this model represents the maximum amount of variability possible in the data set, the resulting value can be used as a normative correction for the variability derived from the measured data. Correcting the measured values with this factor, a direct comparison of individual data sets, even with very different experiment parameters, becomes possible.

2. **Random variation of all lines in the spectra except for the two maximum lines:** This model represents the assumption, that the spectrum, for specific impact parameters, or

Table 4.5.: Empirical variability of spectra in narrow ranges of the impact velocity. Variabilities for combinations of dust and target materials, for shots with Fe+Ni and Opx particles on Ag targets, are compared for *TOF* mass spectra with high and low mass resolutions. The mass spectra obtained with high mass resolution were recorded with either the *SUDA* or the *LAMA TOF* mass spectrometer, low resolution spectra were obtained with the *BERTA* instrument.

Experiment	Instrument	Velocity range	Number	Norm	V	V (normalised)
Fe on Ag	BERTA	5-10 $km\,s^{-1}$	11	2.15	0.33 $\pm$0.11	0.15 $\pm$0.05
	BERTA	15-20 $km\,s^{-1}$	6	4.82	0.23 $\pm$0.00	0.05 $\pm$0.00
	BERTA	30-35 $km\,s^{-1}$	10	4.53	0.26 $\pm$0.01	0.06 $\pm$0.00
	BERTA	35-50 $km\,s^{-1}$	6	2.76	0.29 $\pm$0.02	0.10 $\pm$0.01
	LAMA	5-10 $km\,s^{-1}$	3	3.41	0.55 $\pm$0.03	0.16 $\pm$0.01
	LAMA	15-20 $km\,s^{-1}$	11	5.36	0.27 $\pm$0.04	0.05 $\pm$0.01
	LAMA	30-35 $km\,s^{-1}$	8	6.46	0.32 $\pm$0.05	0.05 $\pm$0.01
	LAMA	35-50 $km\,s^{-1}$	17	6.53	0.19 $\pm$0.01	0.05 $\pm$0.00
Opx on Ag	BERTA	3-4 $km\,s^{-1}$	8	1.61	0.14 $\pm$0.01	0.08 $\pm$0.01
	BERTA	9-11 $km\,s^{-1}$	14	3.49	0.16 $\pm$0.01	0.05 $\pm$0.00
	BERTA	18-20 $km\,s^{-1}$	7	5.26	0.29 $\pm$0.06	0.06 $\pm$0.01
	SUDA	3-4 $km\,s^{-1}$	3	0.99	0.06 $\pm$0.00	0.06 $\pm$0.00
	SUDA	9-11 $km\,s^{-1}$	8	3.04	0.47 $\pm$0.04	0.15 $\pm$0.05
	SUDA	18-20 $km\,s^{-1}$	19	1.94	0.63 $\pm$0.04	0.32 $\pm$0.02

sometimes in general, are dominated by the lines of the alkali contamination sodium and potassium. Thus, the intensity of these lines are independent on the experimental parameters and the chemical information of impacting particle and target is contained in the remaining, weaker lines.

3. **Random variation of the two maximum lines:** In comparison with the above mentioned model, here all lines are kept constant except for the varied two maximum lines. This model shall give a some indication of the values expected for the assumption that only the variation of the dominant lines contributes to the overall variation behaviour of an data set.

4. **Spectra generated by adding white noise to the sum spectrum:** Here the fluctuations in the spectra are assumed to originate only from normal distributed noise in the experimental apparatus and independent from the process itself.

The results of these various models are listed in Table D.7 - D.11.

Here, we normalise E_i with respect to the mean variability of a data set composed of random spectra, because such a data sets is expected to show the largest possible variability at all. With this choice, E_i takes values between 0, i.e. no variability at all, and 1, i.e. completely random.

Table 4.6.: Empirical variability of spectra in narrow ranges of the impact energy. Variabilities for combinations of dust and target materials, for shots with Fe+Ni and Opx particles on Ag targets, are compared for *TOF* mass spectra with high *(SUDA / LAMA)* and low *(BERTA)* mass resolutions.

Experiment	Instrument	Energy range	Number	Norm	V	V (normalised)
Fe on Ag	BERTA	1.5 -2.0 nJ	11	3.65	0.41 ±0.09	0.11 ±0.02
	BERTA	2.0 -2.5 nJ	15	4.08	0.28 ±0.05	0.07 ±0.01
	LAMA	1.5 -2.0 nJ	22	6.96	0.26 ±0.03	0.03 ±0.00
	LAMA	2.0 -2.5 nJ	11	6.40	0.21 ±0.01	0.03 ±0.00
	LAMA	3.0 -3.5 nJ	4	3.46	0.30 ±0.02	0.08 ±0.01
Opx on Ag	BERTA	2.65-2.85 nJ	6	3.35	0.38 ±0.08	0.11 ±0.02
	BERTA	4.5 -5.0 nJ	10	3.85	0.34 ±0.03	0.09 ±0.01
	SUDA	2.65-2.85 nJ	13	1.93	0.59 ±0.06	0.30 ±0.03
	SUDA	4.5 -5.0 nJ	8	1.86	0.41 ±0.16	0.22 ±0.09

Table 4.7.: Empirical variability of spectra in narrow ranges of the energy density. Variabilities for combinations of dust and target materials, for shots with Fe+Ni and Opx particles on Ag targets, are compared for *TOF* mass spectra with high *(SUDA / LAMA)* and low *(BERTA)* mass resolutions.

Experiment	Instrument	Energy density range	Number	Norm	V	V (normalised)
Fe on Ag	BERTA	10-15 kJm^{-2}	13	2.32	0.37 ±0.04	0.16 ±0.02
	BERTA	15-20 kJm^{-2}	8	5.32	0.26 ±0.01	0.05 ±0.00
	BERTA	20-25 kJm^{-2}	5	3.67	0.44 ±0.03	0.12 ±0.08
	LAMA	10-15 kJm^{-2}	7	6.25	0.74 ±0.11	0.11 ±0.02
	LAMA	15-20 kJm^{-2}	15	5.65	0.63 ±0.38	0.11 ±0.07
	LAMA	20-25 kJm^{-2}	15	6.29	0.24 ±0.04	0.04 ±0.01
Opx on Ag	BERTA	5-7 kJm^{-2}	11	2.64	0.11 ±0.01	0.04 ±0.00
	BERTA	9-11 kJm^{-2}	14	3.92	0.18 ±0.01	0.05 ±0.00
	BERTA	19-21 kJm^{-2}	7	3.03	0.36 ±0.01	0.12 ±0.00
	SUDA	5-7 kJm^{-2}	11	1.98	0.87 ±0.01	0.44 ±0.05
	SUDA	9-11 kJm^{-2}	12	3.17	0.51 ±0.01	0.16 ±0.00
	SUDA	19-21 kJm^{-2}	20	1.48	0.52 ±0.02	0.35 ±0.01

Table 4.8.: Empirical variability of spectra in narrow ranges of the laser energy. Laser ablation measurements have been performed only with the BERTA *TOF* mass spectrometer. Thus, only spectra with low mass resolution have been obtained.

Target material	Laser energy range	Number	Norm	V	V (normalised)
Olivine (Spot 1)	4.5 - 5.0 μJ	4	3.45	1.00 $\pm$0.72	0.29 $\pm$0.21
	6.0 - 6.5 μJ	7	3.95	0.87 $\pm$0.60	0.22 $\pm$0.15
	7.5 - 8.0 μJ	8	3.74	0.82 $\pm$0.50	0.22 $\pm$0.13
	9.0 - 9.5 μJ	3	1.31	0.37 $\pm$0.03	0.28 $\pm$0.02
Olivine (Spot 2)	4.5 - 5.0 μJ	9	4.05	0.26 $\pm$0.01	0.06 $\pm$0.00
	6.0 - 6.5 μJ	9	0.71	0.27 $\pm$0.08	0.38 $\pm$0.11
	7.5 - 8.0 μJ	18	0.86	0.27 $\pm$0.07	0.32 $\pm$0.08
	9.0 - 9.5 μJ	6	0.72	0.32 $\pm$0.12	0.45 $\pm$0.16
Iron	1.0 - 1.5 μJ	6	1.47	0.02 $\pm$0.00	0.01 $\pm$0.00
	2.0 - 2.5 μJ	4	2.70	0.03 $\pm$0.01	0.01 $\pm$0.00
	3.5 - 4.0 μJ	4	2.86	0.02 $\pm$0.01	0.01 $\pm$0.00
	8.0 - 8.5 μJ	4	1.07	0.03 $\pm$0.01	0.03 $\pm$0.01
Ag+Cu	12.0 - 13.0 μJ	4	2.65	0.72 $\pm$0.32	0.27 $\pm$0.12
	14.0 - 14.5 μJ	7	2.71	0.71 $\pm$0.33	0.26 $\pm$0.12
	16.0 - 16.5 μJ	4	2.93	0.76 $\pm$0.38	0.26 $\pm$0.13
	19.0 - 19.5 μJ	4	1.09	0.17 $\pm$0.01	0.16 $\pm$0.01
	21.5 - 22.0 μJ	4	2.23	0.98 $\pm$0.41	0.44 $\pm$0.18
	23.5 - 24.0 μJ	6	0.46	0.35 $\pm$0.03	0.76 $\pm$0.07
	24.5 - 25.0 μJ	11	0.82	0.30 $\pm$0.03	0.37 $\pm$0.04

Table 4.9.: Empirical variability of spectra in narrow ranges of the total charge yield. The variability of spectra of impact and laser ablation events producing charge yields within a narrow range is compared. Due to the lack of high resolution mass spectra for laser ablation measurements, a comparison between high and low resolution spectra could not me made.

Experiment	Charge yield range	Number	Norm	V	V (normalised)
Laser on Olivine (Spot 1)	10 - 20 fC	4	2.86	0.30 ±0.05	0.11 ±0.02
	60 - 70 fC	6	1.65	1.04 ±0.07	0.63 ±0.04
	100 - 120 fC	6	1.12	0.22 ±0.02	0.19 ±0.02
Olivine on Ag	100 - 120 fC	5	3.18	0.35 ±0.10	0.11 ±0.03
Laser on Fe	1 - 10 fC	19	2.28	0.39 ±0.09	0.17 ±0.04
	10 - 20 fC	9	1.88	0.24 ±0.04	0.13 ±0.02
	20 - 30 fC	7	1.58	0.09 ±0.00	0.06 ±0.00
Fe on Ag	1 - 10 fC	3	1.75	0.54 ±0.14	0.31 ±0.08
	10 - 20 fC	4	2.36	0.46 ±0.18	0.19 ±0.08
	20 - 30 fC	9	1.62	0.44 ±0.03	0.27 ±0.02

Impact velocity

The empirical variabilities are listed in Table 4.5 for particle impacts within narrow velocity ranges. The normalised variability is small (0.05 to 0.3). There seems to be a slight dependence on the impact velocity, at least for impact of *Fe+Ni* particles on a Ag target. The variability is smaller for higher impact velocities, implying a more stable and constant process. This finding is consistent with the model of impact ionisation by Drapatz and Michel (1972) postulating two different impact velocity regimes. The evolution of plasmas produced by impacts in excess of $20\,\mathrm{km\,s^{-1}}$ (volume ionisation) is more defined and stable then the ionisation caused by slow particle impacts.

The variability is slightly smaller for spectra recorded by the *LAMA* instrument then for those of *BERTA*, and it is smaller for impacts of Fe+Ni particles then for impacts of OPX grains.. This means, the spread of the *Opx* spectra is wider, being consistent with the properties of the used Opx powder. As described in Section 3.5 the Opx grains were obtained by grinding and coating a natural mineral. Thus, the chemical composition Opx is less defined than the one of iron dust. The wider variation of the spectra obtained with the *SUDA* instrument may originate in a not yet optimal set up of the applied potentials (Schlemmer, 2008).

Impact energy and energy density

The variability of spectra produced at similar impact energies is listed in Table 4.6, the results for narrow while Table 4.7 gives the variability of spectra generated at similar energy densities.

The variabilities are small but show a stronger fluctuation then for those in dependence on

the impact speed and range from 0.03 to 0.35

Here again show high resolution mass spectra a lower variability. For the determination of the variability the relative intensities of the ion peaks are compared. A reflectron mass spectrometer filters the speed distribution to some extent out. Thus, in reflectron spectra is the line height a good measure for the number density of the corresponding ion, while in case of a linear spectrometer the ion density corresponds to the line integral. This implies, that the variability of *BERTA* spectra may be prone to small systematic errors.

Laser

Table 4.8 lists the variabilities of spectra obtained by laser bombardment of a variety of target materials with different laser energies. For the Olivine and the copper-Ag alloy target, the variabilities are about the factor 2 to 5 higher then for the impact ionisation experiments. Furthermore, there seems to be no correlation between the laser energy and the variabilities. Also the spread of the variability is wider then for particle impacts. An exception is the data set obtained with a pure iron target. Here, the results are even more stable then with compared process of hypervelocity impacts. This may lead to the conclusion, that for the laser ablation the properties of the target are more determinant then the laser energy. Due to the experimental set up properties there had been no measurements with laser irradiation of a high resolution mass spectrometer.

Laser and Impact spectra with similar charge yield

Table 4.9 list the variability of laser and dust impacts sorted with respect to the charge yield. The spread ranges from 0.11 to 0.63 and is therefore larger then the spread of data sets arranged with respect to speed, energy, or energy density. This suggests, that the charge yield at the target is an rather unsuitable measure to describe and compare the process of ion formation due to hypervelocity impacts and laser irradiance.

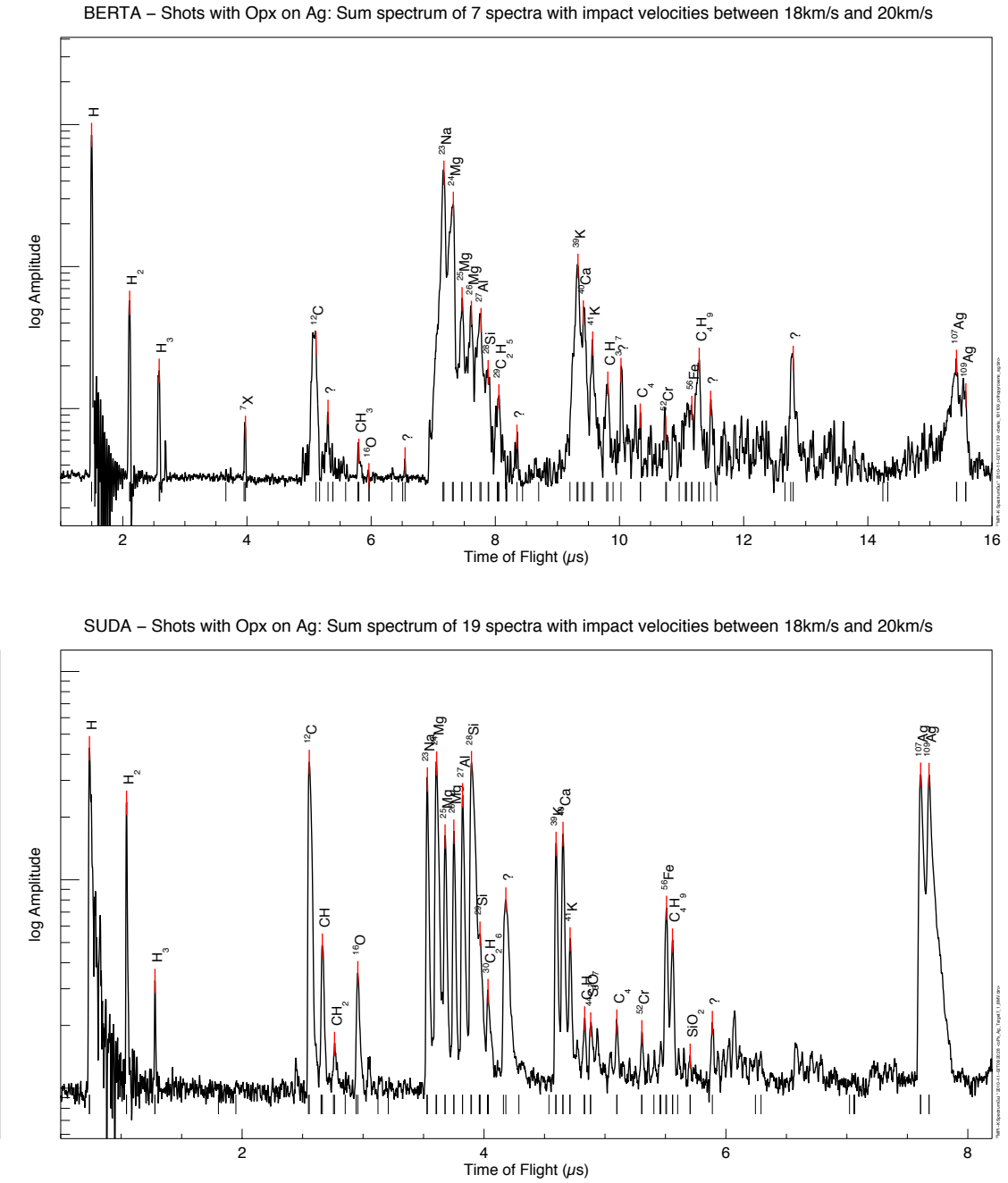

Figure 4.26.: Sum spectra of spectra obtained with Opx particle impacts on a Ag target at impact velocities between 18 km s^{-1} and 20 km s^{-1}. The low resolution spectra above were recorded with the *BERTA TOF* mass spectrometer the high resolution spectra on the bottom with the *SUDA* instrument.

4.4. Ion plasma composition for impact ionisation

In this section the dependence of a spectra's apparent ion composition on its impact parameters is studied.

Using *TOF* mass spectroscopy to determine the chemical composition of an impacting particle or of laser irradiated solid surface, means to evaluate the ion populations contained in the hot, expanding and evolving vapour plume. Ion formation in a hot, initially dense and expanding plasma is not least affected by the conditions within the cloud. The rates of ionisation and the antagonistically working process, recombination, as well as chemical processes such as cluster formation, are determined by properties of the plasma like temperature, densities, collision rates and the expansion velocity (Hornung and Drapatz, 1979; Hornung, 1982; Drapatz and Michel, 1972). This has of course to be taken into account when it comes to the interpretation of *TOF* mass spectra. On the other hand this relation can be used to gain insights and a deeper understanding of the processes in question. The abundance of lines in the spectra and their relative intensities reflect the conditions in the plasma plume and depends on the parameters determining these conditions (Friichtenicht et al., 1971). To do so, the appearance and disappearance of lines are evaluated in respect to the impact parameters, impact velocity, energy, energy density, and - in the following section for laser ionisation - in respect to laser energy. For this, a wide range of the data sets for shots with the mixture of nickel and iron powder on a Ag target and with Opx particle on also a Ag target have been studied. Figure 4.27 shows exemplary the dependence of the line appearance of the target material ^{107}Ag for *Opx* particle impacts onto Ag in dependence on the impact speed, the kinetic impact energy and the energy density. To get more reliable data, the results of measurements with the *BERTA* spectra are compared to those obtained with the *SUDA* instrument.

For both data set, the impacts of Fe+Ni particles as well of Opx dust onto Ag the line frequencies for the most important lines have been investigated as described exemplary above for. The resulting plots Figure D.7 to Figure D.30 can be found the Appendix D.4. For both investigated material combinations, the lines can be divided into groups according the origin and chemical properties of the particular species.

4.4.1. Defining impact parameters for the appearance of lines

In the first instance the dependence of the relative line appearance were considered for the individual line abundant in the *TOF* mass spectra.

- **Atomic ions of impactor and target material:** Both data sets were obtained with measurements with the same target material, Ag. Considered was only the lighter isotope, ^{107}Ag. For the Fe+Ni particles as the particle material line, the most abundant isotope if iron ^{56}Fe had been studied. In the *TOF* mass spectra gained in hypervelocity impacts of Opx grains, the bulk material is represented by both, the O and Si-ions originated from the SiO_4-tetrahedra constituting the anionic part of the silicate. and the metal cation ^{24}Mg, ^{27}Al, and ^{56}Fe. The appearance of the bulk material lines showed all a strong dependence on the impact velocity and a slightly weaker dependence on the density of the kinetic energy, whereas there was no significant dependence apparent on the kinetic energy itself.

- **Molecular and cluster ions:** The appearance of cluster ions was already described in detail, i.e. by Knabe (1983) and Knabe and Krueger (1982). There are two possible

reasons for the abundance of cluster ions in the impact ionisation spectra: either the molecules or clusters stem from the original material and survive the impact or they are formed in the expanding plasma. Each of the two possibilities lead to distinct, different conditions for the plasma cloud measured by the mass spectrometer. First one has to distinguish between homo-nuclear and hetero-nuclear cluster ions. The first are formed from the same type of atoms by homo-nuclear bonds(Kissel and Krueger, 1987). For Fe+Ni impacts on Ag as well as for Opx grains hitting a Ag target, the cluster ions of the target material Ag_2 and Ag_3 are apparent according to their isotopic abundance. Sometimes carbon cluster ions C_n are observed. These lines often are quite weak. Thus, their abundance is not frequently enough to study the behaviour and the dependencies of these types of ions systematically. The most common hetero-nuclear cluster ions are cluster ions of the target and the impactor material. For Fe+Ni impacts this is the AgFe-cluster ion. This line is easy to recognise, because parted into two equally distributed main isotopic lines, ^{163}AgFe and ^{165}AgFe, due to the also equally intense ^{107}Ag and ^{109}Ag isotopes. The same kind of clustering of target and dust particle material is observed for Opx grains impacting a Ag target. Here, the cluster ions ^{131}AgMg and ^{133}AgMg are very frequently apparent in both, the *BERTA* as well as the *SUDA* spectra. In contrast to the homo-nuclear cluster ions, the target and impactor material cluster ions originate from combination of the constituent atoms within the expanding plasma cloud and cannot be residual molecules from the material before the impact. The number and quality of the spectra obtained in this thesis only allow a qualitative description. A more accurate and systematic investigation would allow to compare the relative abundance of the target and impactor material cluster ions with other apparent species, especially it atomic components, in dependence on the impact parameters and material combinations used. This may provide further insights into the conditions in the plasma cloud generated in the impact (Wojciechowski, 2004). Common for all cluster ions is the dependence on the impact velocity as well as on the energy density. Again, there is no significant correlation with the impact energy.

- **Contaminants:** For the Fe+Ni particle impact, there are two types of contaminants, C and O. Similar to the bulk material lines, both lines show a strong dependence on the impact speed and the density, while no dependence on the energy became obvious. In the case of Opx particle hitting a Ag target, the O is a important constituent of the crystal's lattice (see Section 2.4.2). For this data set the C and the hydro-carbon CH, CH_2, and CH_3 lines were investigated. Except for the CH_3 line, which is often overlapped by the O line at higher impact velocities, there is also a dependence of the line abundance on the impact velocity and energy density. Also, there are C_2H_n and C_3H_n-ions observed in small amounts.These species are fragments from larger hydrocarbons originating most likely from residues from rom lubricant oil originating from the vacuum pumps.

- **Atomic and molecular hydrogen:** Hydrogen appears in the spectra as atomic H and as H_2 and H_3. The lines show a strong dependence on the impact speed for both data sets. With increasing impact velocity as well as with increasing energy density, the relative abundance is growing. For very high velocities, the abundances of molecular H_2 and H_3 are decreasing. This is probably an effect of the broaden H line and even more of its increasing ringing. This leads to an overlapping of the hydrogen lines and makes it impossible to identify the very close lines of H, H_2 and, H_3. The increase of the hydrogen

appearance with increasing impact velocity may suggests that the hydrogen originates from inside the solid body lattices of the particle and the target (Postberg et al., 2009a).

- **Alkali contaminants:** For both data sets of the alkali contamination, Na and K showed the same dependence on the impact velocity This is in contrast to the properties of the bulk material's lines. After being dominant for slow velocities, the relative appearance of these lines is decreasing with faster impact speeds. This is consistent with the idea of the alkali species being a surface contamination.The model of surface ionisation suggests that at slow impact velocities the specific irreversible internal energy is not sufficient to vapourise the whole volume of the impacting particle. In this case a molten droplet forms with a defined surface, leading to surface ionisation of the contaminants located on the surface atom as described by Drapatz and Michel (1974). Furthermore, this is congruent with the model taking emission processes into account, which may occur in the gap between the approaching charged particle and a metal target by Sysoev et al. (1997). At least for laboratory measurements where slow particle velocities translate into higher masses and larger sizes, leading to higher charges, this model is consistent with the observation of the alkali lines as dominant. Also the low ionisation potentials lead to the legitimate assumption, that for slow velocities the alkali contaminations are the dominant contributions to the mass spectra(Auer and Sitte, 1968).

4.4.2. Velocity and energy density thresholds

Since the earliest mass spectrometric investigation of impact ionisation plasmas it has been recognised that the appearance of mass lines in a spectrum depends on the impact velocity (Hansen, 1968; Friichtenicht et al., 1971; Dalmann et al., 1977). Shock wave ionisation models by Gault and Heitowit (1963) and Drapatz and Michel (1974) predict alkali contaminants to be dominant at low velocities and target and projectile ions to appear only at higher speeds, where vaporisation and ionisation of the bulk material occurs. Besides these 1D thermodynamical model there are numerical simulations to derive results with a more accurate geometrical setting (Ratcliff et al., 1997), leading also to velocity thresholds for the appearance of specific ion species.

Thus, the velocity dependence of the line is a promising tool to determine the velocity of an impacting particle due to the apparent lines in the *TOF* mass spectrum.

As shown in Figure 4.27, the dependences on the impact speed and the energy density can be fitted with an empirical *Fermi* distribution type (Kempf, 2010). The results show no significant dependence on the impact energy whatsoever. The error bars represent the *Poisson* distribution of the measurement and depend therefore on the number of data points obtained in a specific range of the impact parameter in question (Gardiner, 1996). The resulting threshold velocities and energy densities for Fe+Ni particles impacts on an Ag target and for shots with Opx grains onto Ag are listed in Table D.12 - D.14. The threshold velocity is defined by the speed above which 10 % of the recorded spectra show the line in question.

In this study, I determined the threshold velocities for the appearance of particular lines in the *BERTA* berta of Fe+Ni on Ag and *SUDA* spectra of Opx impacts on Ag. As listed in Table 4.10, the target material line ^{107}Ag shows up at very slow impact velocities. Hence, Ag lines are not usable as a marker for the determination of the particle speed.

- For Fe+Ni impacts, the projectile material line ^{56}Fe starts to appear at velocities $\sim 3.6\,\mathrm{km\,s^{-1}}$. This implies that ^{56}Fe is not useful for the speed determination. Furthermore this thresh-

Table 4.10.: Threshold velocities or the appearance of lines in mass spectra recorded with Fe+Ni particle impacting on Ag (*BERTA*) and Opx shots onto Ag (*SUDA*).

	Velocity thresholds ($km\,s^{-1}$)												
	H	H_2	^{12}C	^{16}O	^{24}Mg	^{28}Si	^{44}SiO	^{56}Fe	^{107}Ag	AgMg	AgFe	Ag_2	Ag_3
Fe+Ni	3.8	–	5.5	12.1	–	–	–	3.6	1.8	–	12.3	15.8	19.3
Opx	3.9	5.4	3.7	12.8	2.3	2.7	8.6	3.2	0.8	5.4	–	5.3	4.0

old velocity is much smaller then the 7.3 km/s predicted by model calculations by (Drapatz and Michel, 1974) and hydrocode simulations ($8\,km\,s^{-1}$) by Ratcliff et al. (1997). Also the ^{12}C lines has its first appearance at velocities of $5.5\,km\,s^{-1}$, whereas ^{16}O with its velocity threshold of $12.1\,km\,s^{-1}$ is a good marker for particle velocities. Also the cluster ions AgFe, Ag_2, and Ag_3 provide useful constraints for the impact speed.

- The projectile material lines ^{24}Mg ($2.3\,km\,s^{-1}$), ^{28}Si ($2.7\,km\,s^{-1}$), and ^{56}Fe ($3.2\,km\,s^{-1}$) and the cluster target material cluster ions MgFe ($5.4\,km\,s^{-1}$), Ag_2 ($5.3\,km\,s^{-1}$), and Ag_3 ($4.0\,km\,s^{-1}$) show up at low velocities and thus, provide no useful no constraints for the particle speed. For this projectile material, the SiO ($8.6\,km\,s^{-1}$) and again the ^{16}O lines are good markers for the particle velocity.

These results prove that an in-depth investigation of the speed-dependent line appearance is one of the most promising approaches to develop a more accurate method for determining the impact speed than the rise time method (Göller and Grün, 1989).

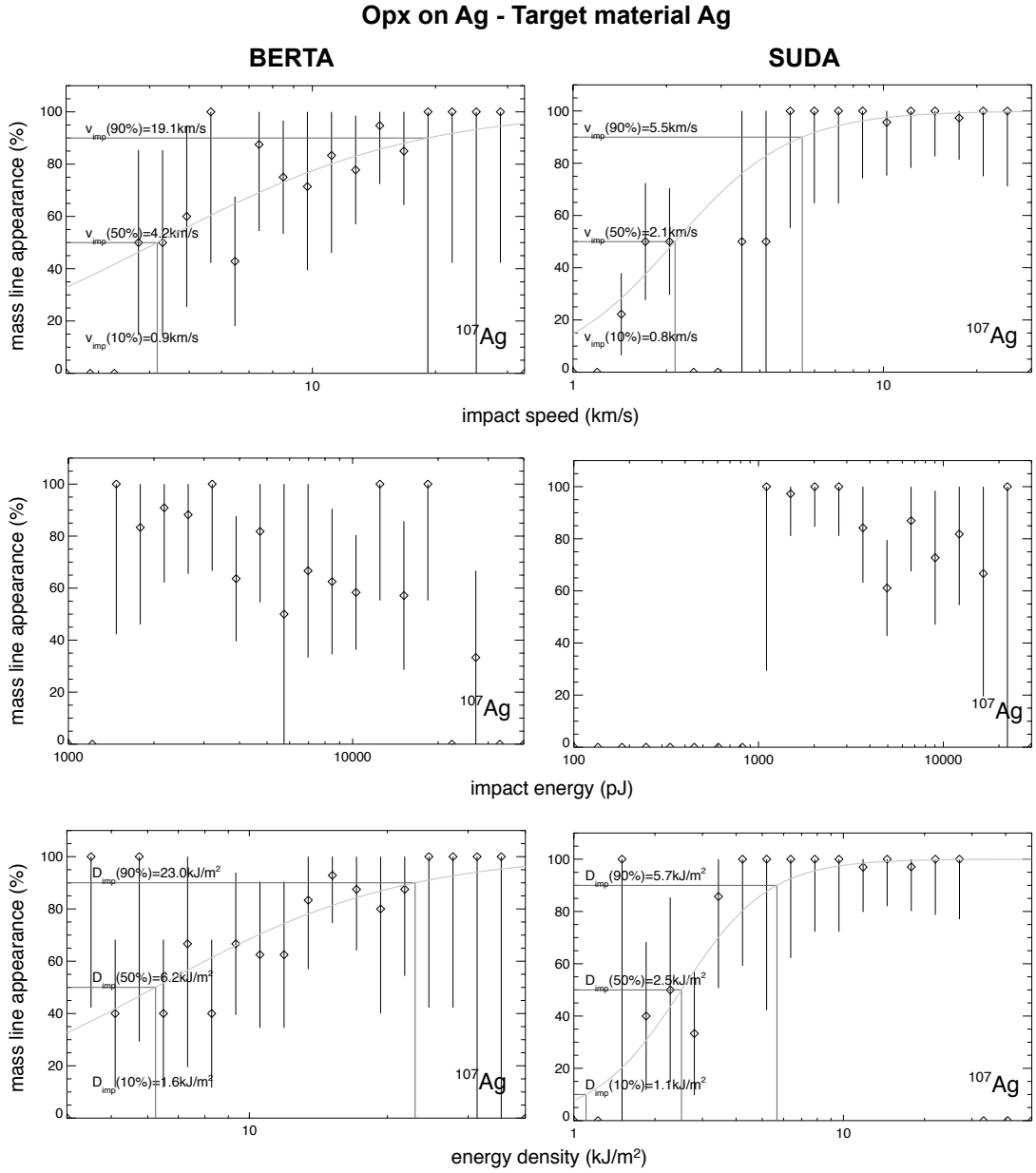

Figure 4.27.: Line frequencies for the target material line ^{107}Ag for Opx particle impacts onto Ag in dependence on the impact speed, the kinetic impact energy and the energy density. The results of measurements with the *BERTA* mass spectrometer are compared to those obtained with the *SUDA* instrument. For the dependency on the impact speed and the energy density the data points could be fitted with a *Fermi* distribution. The result show no significant dependence on the impact energy whatsoever. The error bars represent the *Poisson* distribution of the measurement and depends therefore on the number of data points obtained in a specific range of the impact parameter in question.

4.5. Time-of-flight (TOF) mass spectra for laser ablation

4.5.1. Dependency of the line shapes and width on the laser energy

In this section the dependence of the resulting spectra characteristics on the increasing laser energy is described.

Ahead of each measurement, the target spot to be investigated was prepared by cleaning the surface with about 1000 shots with a high laser energy in order to guarantee an optimum of comparability for the contamination and surface properties. After that, the measurement was performed starting with the lowest energy set up producing an ion signal at the target or and spectrum. This particular condition for the laser energy setting will be termed as *on-set of ion formation* in the sections to follow. With increasing laser energy the characteristics of the spectra undergo strong alterations (Figure 4.28 and 4.29).

- Starting with *on-set of ion formation* the spectra show a steady number of lines representing mostly the chemical constituents of the target bulk material. The lines are very narrow and symmetric. For the metal targets the alkali contaminants are weak or even absent. There are cluster ions and even twofoldly charged ions abundant in small amounts.

- Increasing the laser energy, the spectra remain unchanged in their characteristical properties over a certain range of laser energy with. There occurs only slight broadening of the lines.

- Exceeding a certain laser energy threshold, the line shapes change rapidly. They become broader and almost instantaneously saturated. Thus, the line width cannot be characterised any longer. Furthermore, the assignment of line and subsequently the calibration of the spectra is complicated or even impossible. This effect is partial caused to a further interaction between the evolving plasma cloud and the laser light.due to the pulse length of 5 ns.

- The character of the spectra changes over the further course of increasing laser energy for several times, each alteration is rapid and erratic: Lines appear and disappear, move to flight times larger or smaller determined by the equation of the *TOF* Eq. 2.60.

To compare the properties of the laser ablation plume with impact ionisation plasma, the resulting spectra have to be comparable: it has to be possible to use the same methods and measures to describe the signal, i.e. by evaluating line widths or the appearances of particular lines. Thus, in the following laser energy ranges will be studied, in which the *TOF* spectra were not entirely saturated or showed some other erratic behaviour like line drifts (Table 4.11). The chosen energy ranges vary strongly for the various target materials also slightly for different focal spot location on one and the same target.

Table 4.11.: Energy ranges used to compare impact ionisation with laser ablation.

Target	Acc. potential	Entire energy range	Selected energy range
Iron	1000 V	0 μJ-20 μJ	0 μJ-6 μJ
Iron	1600 V	0 μJ-10 μJ	0 μJ-8 μJ
Ag+Cu	1000 V	12 μJ-26 μJ	12 μJ-17 μJ
Olivine (spot1)	1600 V	2 μJ-12 μJ	2 μJ-6 μJ
Olivine (spot2)	1600 V	3 μJ-20 μJ	3 μJ-6 μJ

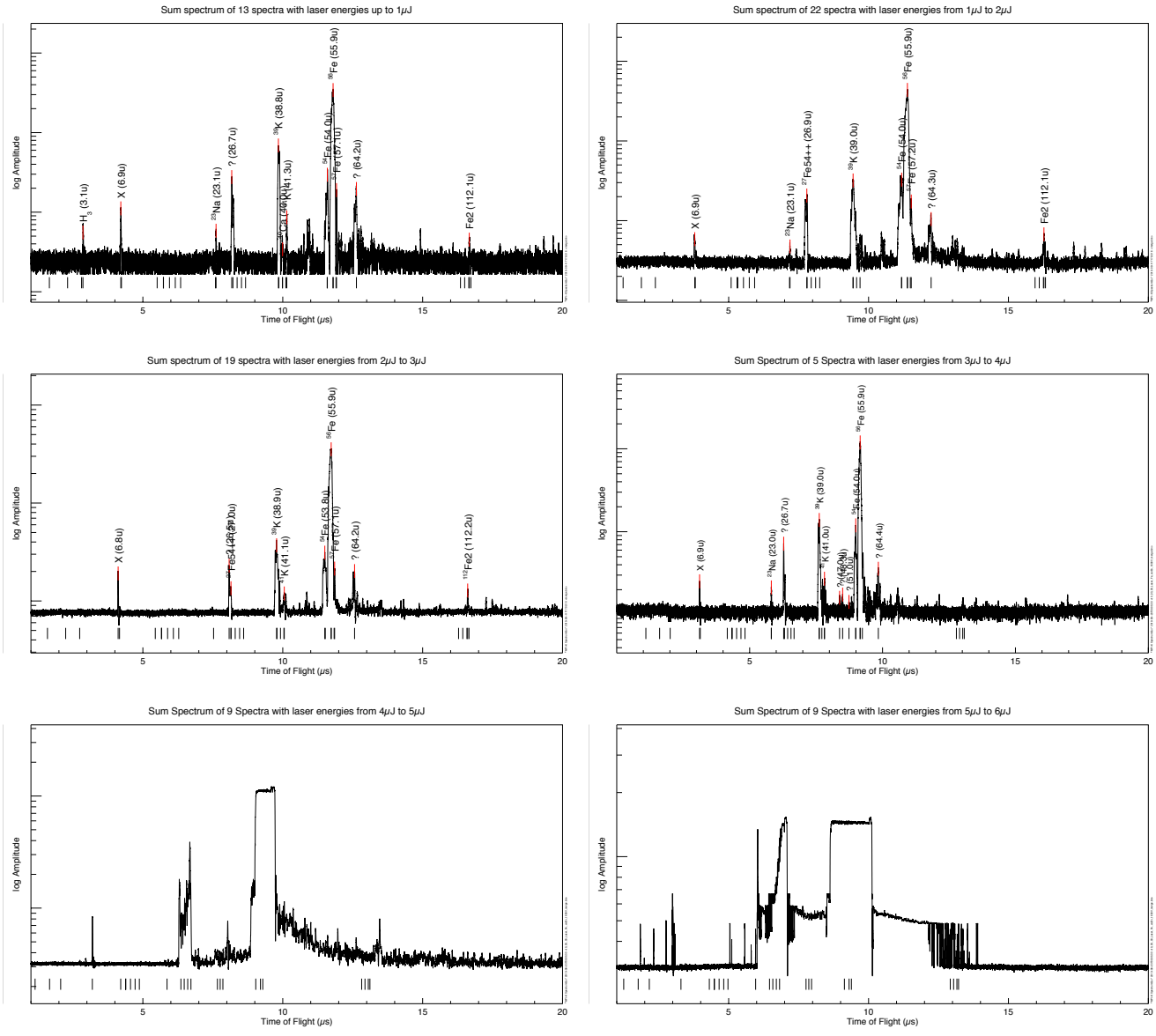

Figure 4.28.: Change of *TOF* spectra characteristics with increasing laser energy, expamplarily shown for laser shots on an iron target. Laser energy range from 8 μJ to 19 μJ from 0 μJ to 6 μJ

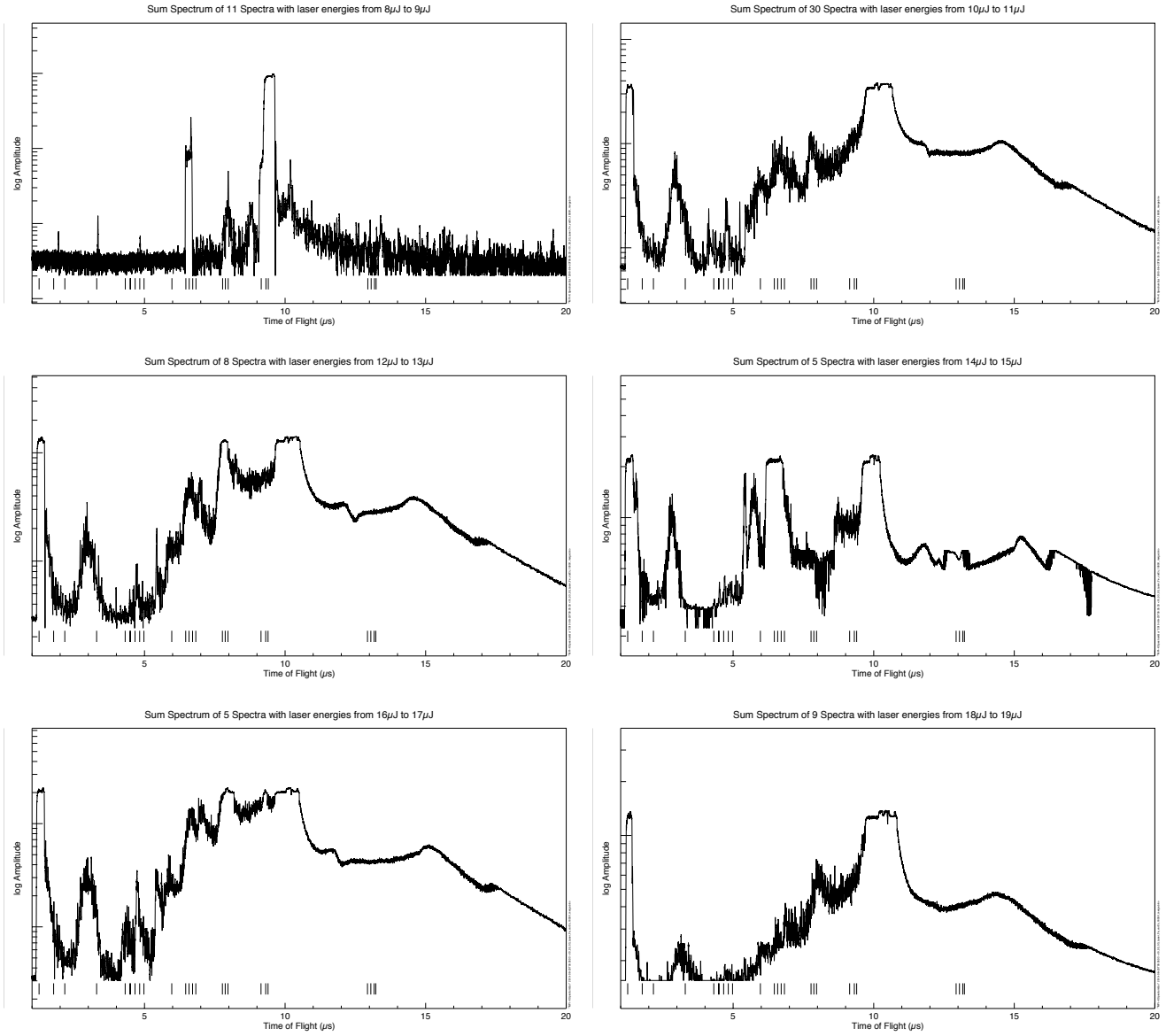

Figure 4.29.: Change of *TOF* spectra characteristics with increasing laser energy expamplary shown for laser shots on an iron target. Laser energy range from $8\,\mu$J to $19\,\mu$J

4.5.2. Ion plasma composition for laser ionisation

Similar to the line frequency considerations for the impact ionisation experiments in Section 4.4, the dependence of the relative appearance of the lines was studied for three different target material, two metal targets, iron and a copper + Ag alloy, and a gold coated olivine target.

- **Iron:** For laser irradiance of an iron target, the strongest lines apparent in the spectra are the alkali contaminants and the main isotope ^{56}Fe. Figure 4.30 shows the line frequencies for the target material line ^{56}Fe and for the alkali contamination lines ^{23}Na and ^{39}K for laser bombardment of an iron target in dependence on the laser energy. The disappearance of the lines due to the increase of the laser energy is caused by the increasing difficulties of identifying the lines due to the broadening and saturation of the peaks.The result show no significant dependence on the laser energy whatsoever.

- **Copper + Ag:** For laser shots onto a Cu+Ag-alloy, the strongest lines are the two copper isotopes, the Cu_2 cluster ions and the ^{39}K-contamination line. Astonishingly, the other main target constituent, Ag appears only as double ionised ions ,Ag^{++}. As for the shots on the iron target, there is no significant dependence on the laser energy apparent (Figure D.30).

- **Gold coated Olivine:** For this target material, three groups of ions exist. There are target bulk material lines, ^{24}Mg and ^{56}Fe and the alkali contaminates ^{23}Na and ^{39}K. Furthermore, there is the the coating material-ion ^{196}Au, and the cluster ions AuMg (Figure D.31).

Summarising, there is no significant dependence of the line abundance of lines on the laser energy. In contrast to the impact ionisation experiments, the hydrogen line becomes apparent in the spectra only at very high laser energies, far outside the range defined in Section 4.5.1 as comparable to impact ionisation spectra.

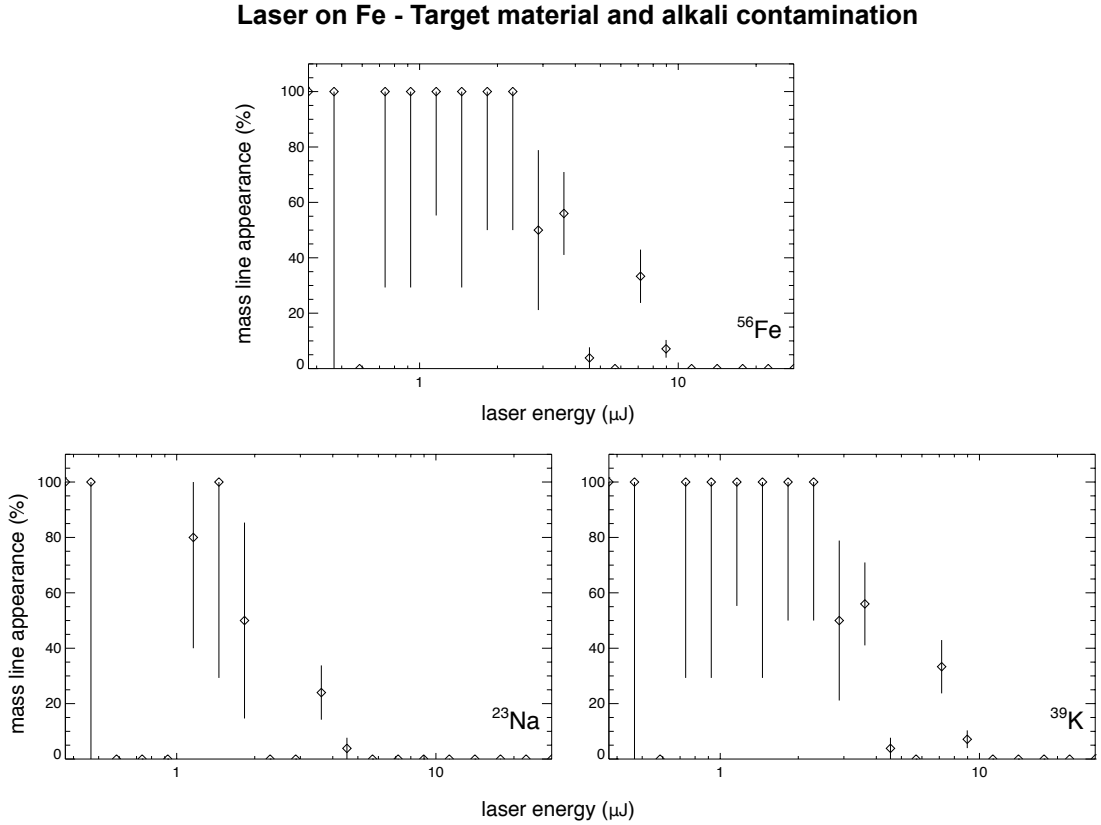

Figure 4.30.: line frequencies for the target material line ^{56}Fe and for the alkali contamination lines ^{23}Na and ^{39}Kfor *Opx* laser bombardment of an iron target in dependence on the laser energy. The disappearance of the lines due to the increase of the laser energy is caused by the increasing difficulties of identifying the lines due to the broadening and saturation of the peaks.The result show no significant dependence on the laser energy whatsoever.

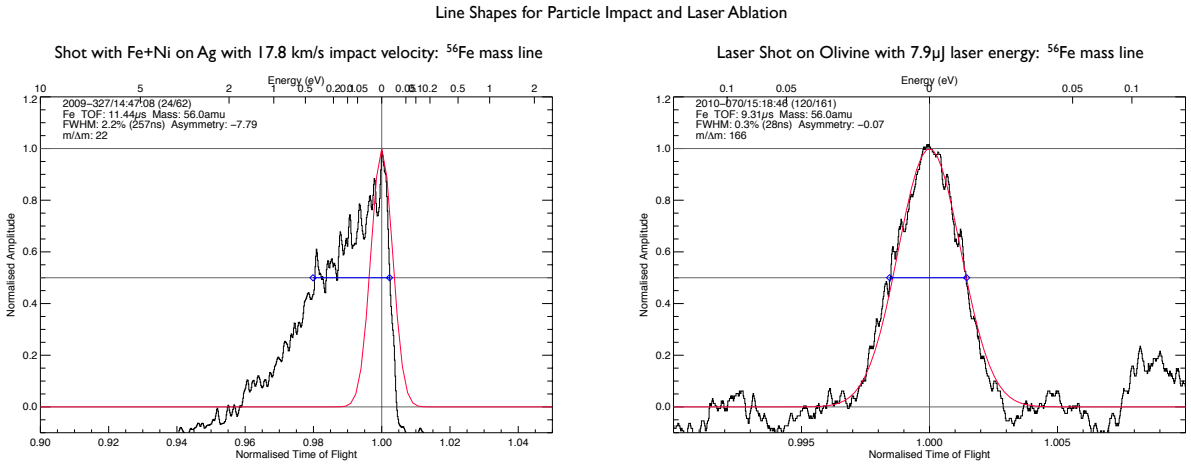

Figure 4.31.: Exemplary line shapes: Iron shots on Ag with an acceleration potential of 1000 V

4.6. Peak shapes and widths

Besides information about the composition of both, the striking particle and the impact target, spectra recorded with a linear time-of-flight spectrometer also provide insights into the physical state of the impact plasma itself. In particular, the shape of a line is due to the velocity distribution of the corresponding plasma ion, which in turn is due the forming process of the plasma (Mamyrin, 2001). As shown in Section 2.3.4 for the ideal case of a equilibrium plasma, the relation between the line shape and the velocity distribution Eq. 2.75 is governed by only by three parameters: the line's full with at half maximum (FWHM) $\Delta\tau$ expressed in normalised flight time $\tau = t/t_p$, the flight time t_p of the ions started at rest, and the ratio between the ions' thermal speed and the speed of the ion beam, i.e. the Mach number M. Because for $M > 1$ t_p is almost identical with time at peak maximum t_{max}, the line profile of equilibrium plasma ions is completely characterised by $\Delta\tau$ and M, which depends on the acceleration potential U_{acc}. Thus, the dependence of $\Delta\tau$ on U_{acc}, the parameters of the impact process, and of the particles chemical composition allows to determine the thermodynamical properties of plasma produced by an particle or laser impact. It also provides the unique possibility to compare the properties of impact plasmas produced by both processes.

Selection of investigated lines The *TOF* mass spectrometer used in this study was designed investigate the shapes and width of the lines stemming from initial velocity distribution of the ions. The drawback of such a spectrometer is a low mass resolution, as a result neighbouring lines - depending on the impact conditions - may overlap and disturb the shape and widths of on another. Furthermore, due to the small angle of aperture, the ion gain is reduced, lowering the sensitivity of the instrument for weaker lines. Thus, the investigation of peak shapes, widths and their dependency was only for a small selected group of ions, characteristic for each set of experimental parameters.

Table 4.12.: Dependencies of the relative line widths w on the impact velocity v and the energy density D. Listed are the exponents of the relations $w \propto v^a$ and $w \propto D^b$ for particle impacts with iron and Opx particles.

	Velocity v		Energy density D	
	Iron	Opx	Iron	Opx
C	1.09±0.12	1.16±0.11	1.03±0.24	1.21±0.23
O	1.03±0.24		0.9±0.27	
Mg		0.59±0.14		0.69±0.16
Fe	0.67±0.07		0.65±0.07	
Ag	0.19±0.08		0.23±0.07	

4.6.1. Line width dependency on the impact parameters

The dependency of the line widths on the impact velocity, impact energy, and energy density for particle impact and on the laser energy for laser ablation has been evaluated for the following combinations of "impactor" and target materials:

- Shots with iron particles on a Ag target *(C, O, Fe, and alkali contamination)*
- Shots with orthopyroxene dust on Ag *(Mg, C, O, and alkali contamination)*
- Laser shots on iron *(Fig. 4.37 - Fe)*
- Laser shots on gold coated olivine *(Fig. 4.38 - Mg, Al, Si, Fe, Au, and alkali contamination)*

Bulk material lines for impact ionisation For both particle materials the line widths of the bulk materials show a similar behaviour. The values of the relative widths vary between 1 % and 5 %. The difference in range is biased by the slightly different range of impact parameters for both experiments (Table 3.4).
Figures 4.32 to 4.35 show the strong dependency of the line width on the impact velocity and the energy density. On the other hand there is no significant relation between the line width and the kinetic energy of the particles.. For both projectile materials, he ^{12}C and the ^{16}O show also a dependence on the velocity and the energy density. The weaker dependence of target lines may be due to the fact that Ag^+ manifests itself as two isotope lines of similar strength, ^{107}Ag and ^{109}Ag, which overlap in spectra recorded with the linear *TOF* mass spectrometer used for this study. The dependencies of the line widths w on the impact parameters impact velocity v and energy density D can be expressed by the exponents of the relations $w \propto v^a$ and $w \propto D^b$. The values for the exponents obtained in the experiment are listed in Table 4.12.

Alkali contamination for impact ionisation In opposite to the bulk material species, the line widths of alkali metals show neither a dependency on the impact velocity nor on the energy density. Furthermore the lines are narrower, the values reach from of some tenth % to about 2%.

Laser ionisation For the laser experiments all lines including the line of the bulk material ions are narrow with normalised values of some tenth %.

As explained in Section 4.5.1 in, for this investigation only low laser intensities were used, obtaining spectra similar to impact ionisation spectra.

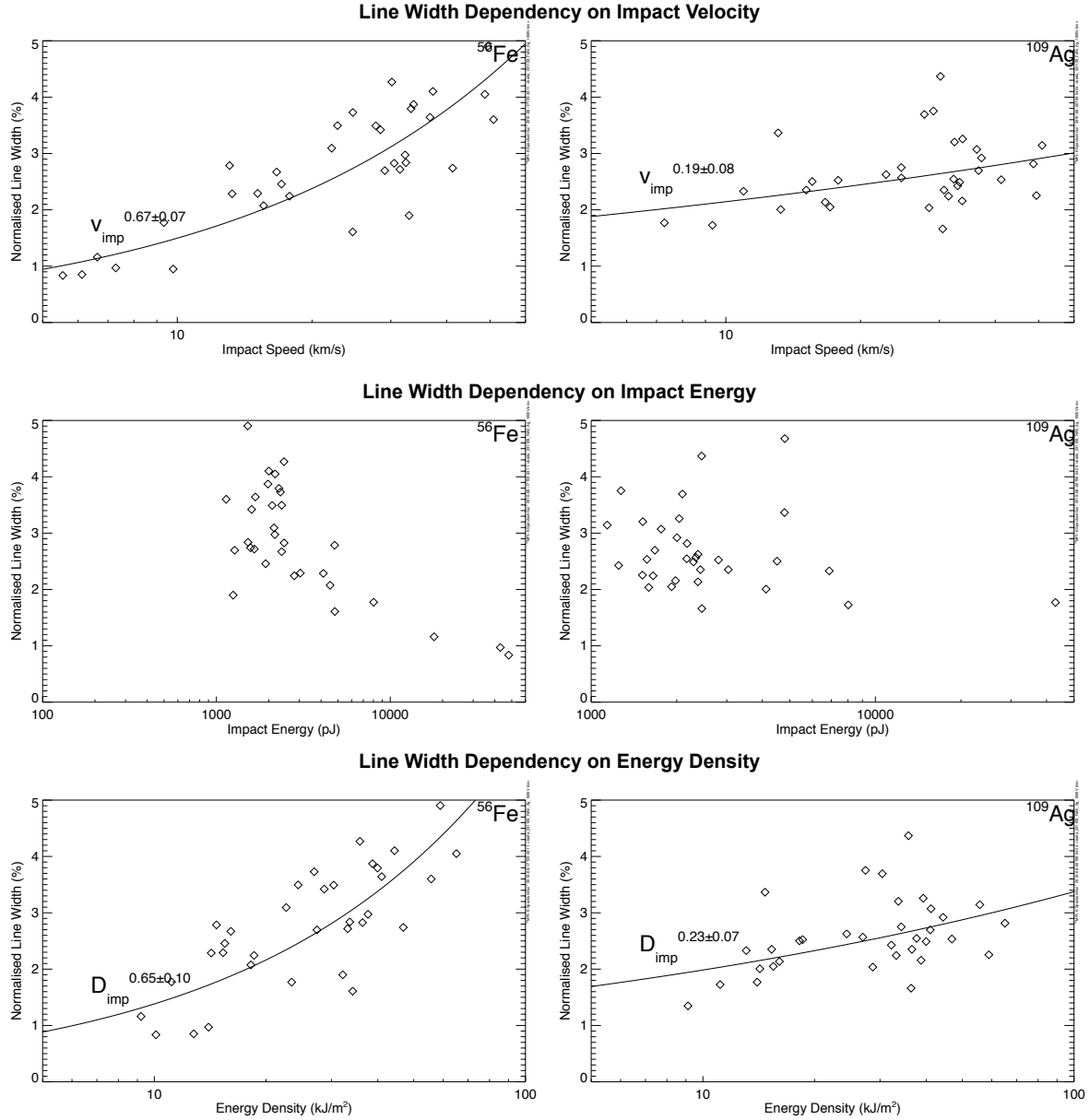

Figure 4.32.: Shots with iron particles on Ag: Widths of the *target* ion lines *(Ag)* and the main constituent of the *particle (Fe)* in dependency with impact velocity, impact energy, and energy density.

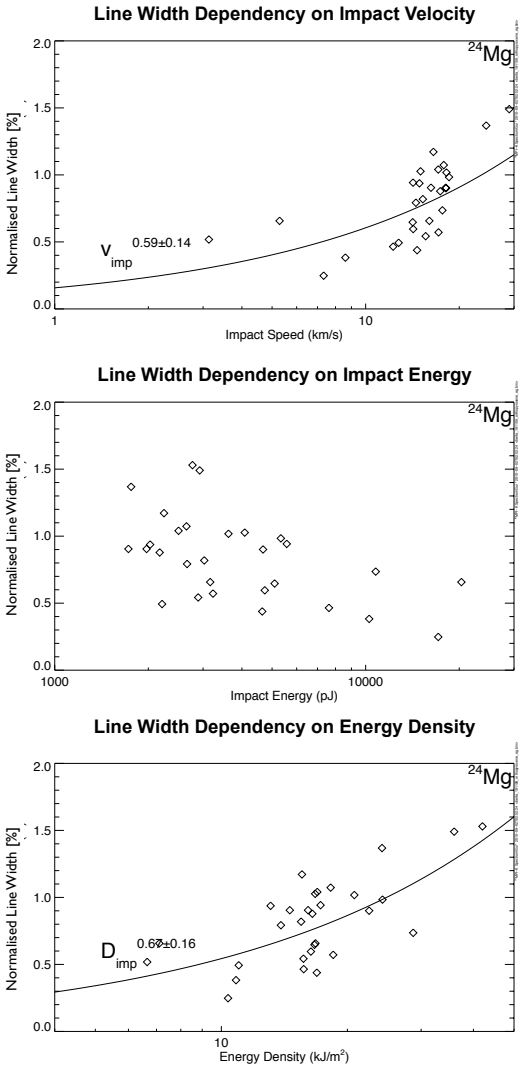

Figure 4.33.: Shots with orthopyroxene particles on Ag: Widths of *magnesium* in dependency with impact velocity, impact energy, and energy density.

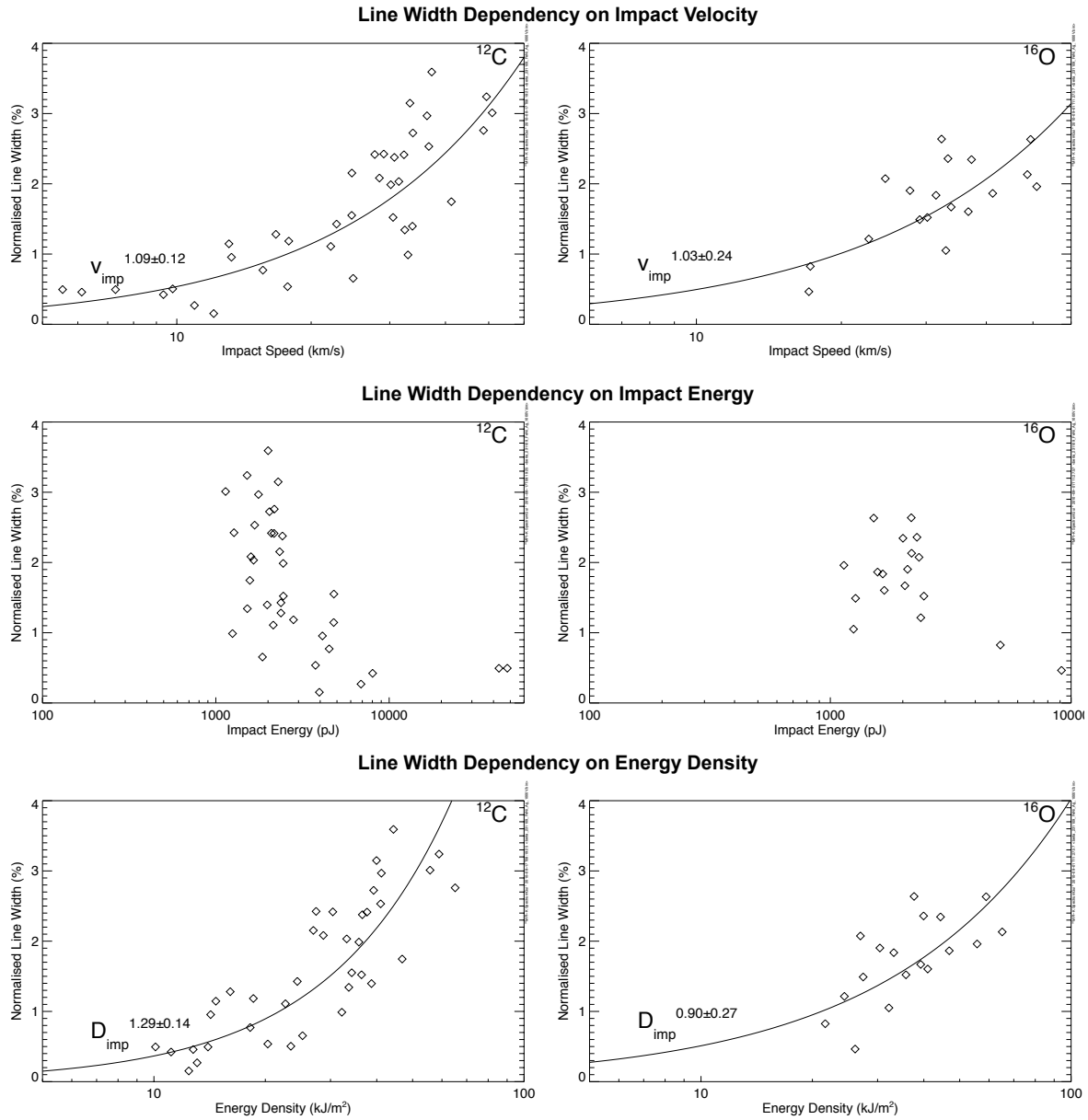

Figure 4.34.: Shots with iron particles on Ag: Widths of carbon and oxygen in dependency with impact velocity, impact energy, and energy density.

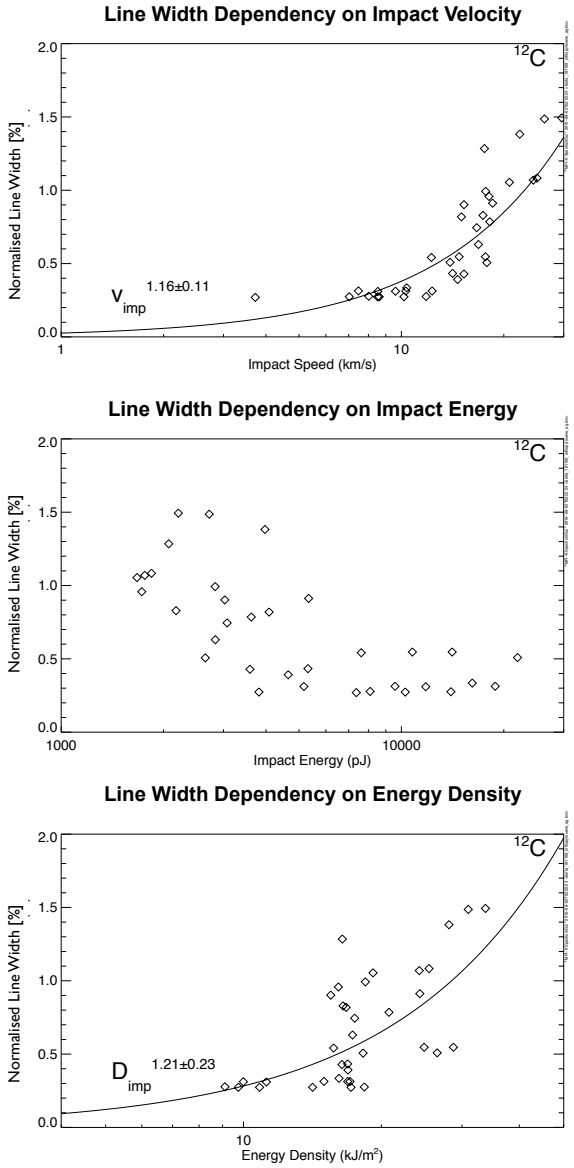

Figure 4.35.: Shots with orthopyroxene particles on Ag: Widths of *carbon* in dependency with impact velocity, impact energy, and energy density.

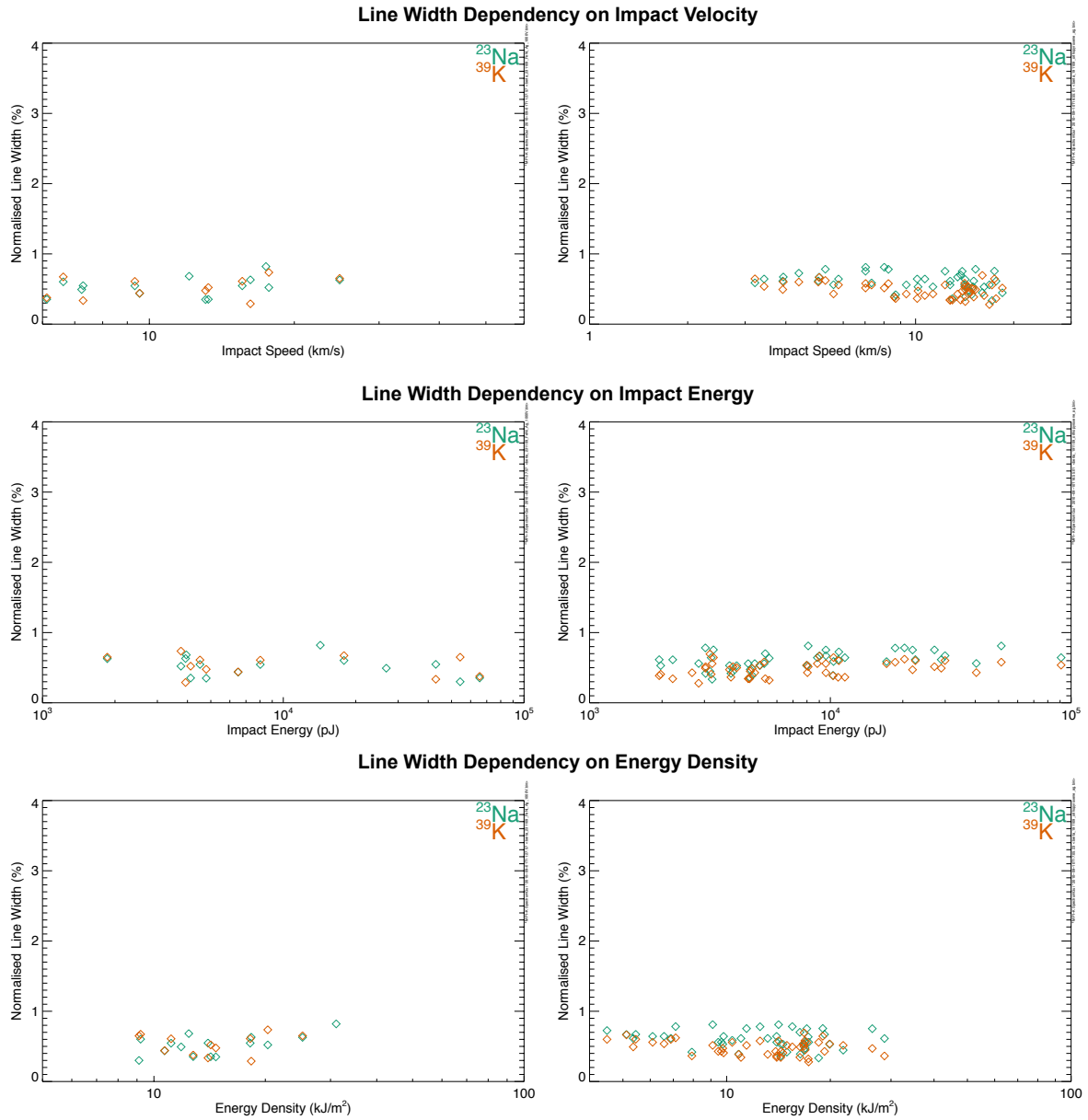

Figure 4.36.: Shots with iron *(left)* and orthopyroxene *(right)* on Ag: Widths of the alkali contamination in dependency with impact velocity, impact energy, and energy density.

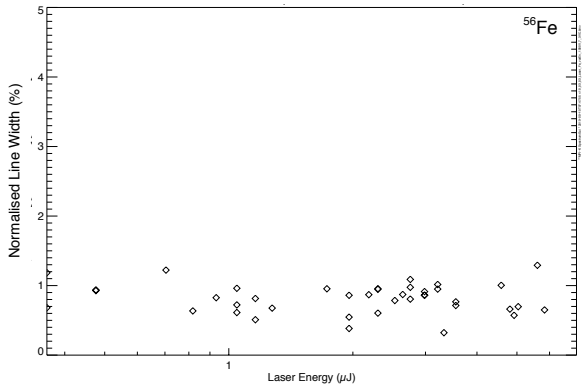

Figure 4.37.: Laser shots on iron: Width of the iron line

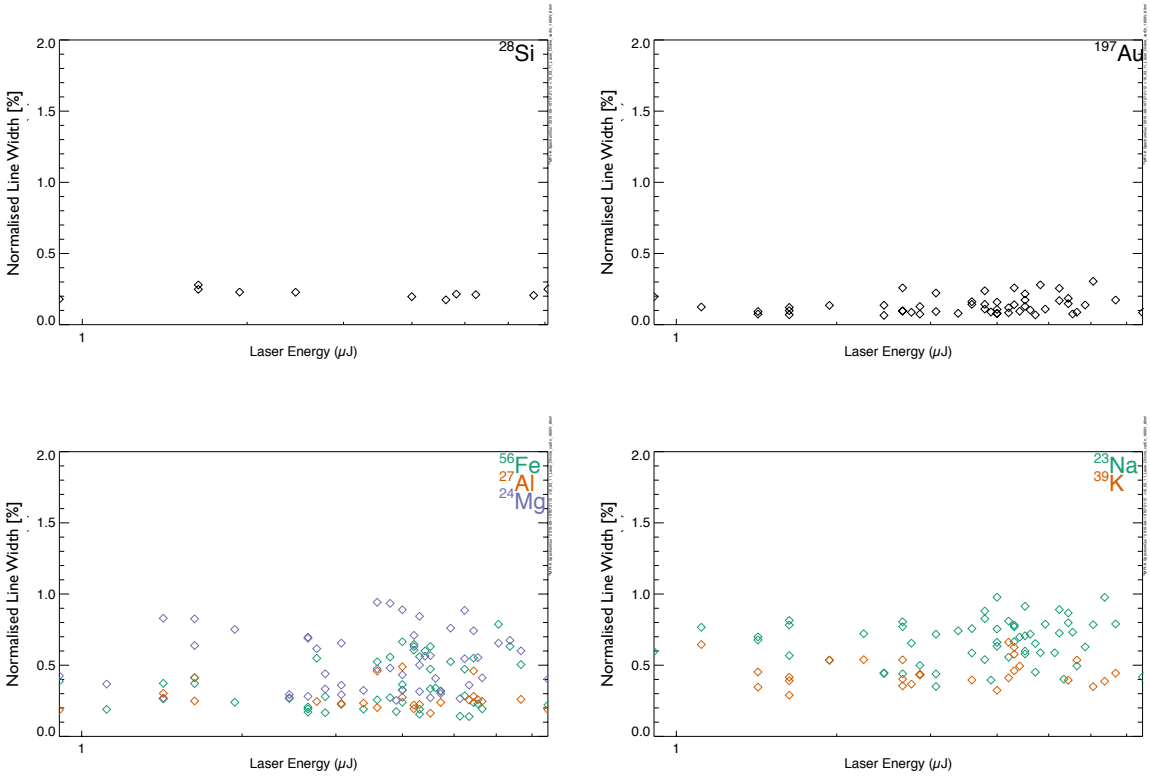

Figure 4.38.: Laser shots on slivine (location2): Line widths of the silicon, metal ion, the gold coating, and the alkali contamination

Table 4.13.: Shots with iron particles on a Ag target: dependence of the relative line widths of sodium and potassium on the acceleration potential applied to the target for impact velocities between $5\,\mathrm{km\,s^{-1}}$ and $10\,\mathrm{km\,s^{-1}}$ *(above)* and of sodium and potassium on the acceleration potential applied to the target for impact velocities between $5\,\mathrm{km\,s^{-1}}$ and $10\,\mathrm{km\,s^{-1}}$ *(bottom)*.

	C	O	Fe
target potential	Line width	Line width	Line width
500 V	5 .30 %±1.95 %	4.89 %±1.58 %	6.63 %±1.65 %
600 V	3 .95 %±1.10 %	1.42 %±1.75 %	5.60 %±0.87 %
700 V	3 .35 %±1.10 %	2.34 %±1.26 %	3.50 %±0.87 %
800 V	3 .37 %±0.90 %	3.26 %±0.63 %	3.83 %±0.40 %
900 V	3 .71 %±0.88 %	2.57 %±0.46 %	3.38 %±0.57 %
1000 V	2 .23 %±0.82 %	1.50 %±0.92 %	2.01 %±1.25 %

	Na	K
target potential	Line width	Line width
700 V	0 .37 %±0.13 %	0.36 %±0.21 %
800 V	0 .67 %±0.17 %	0.45 %±0.13 %
900 V	0 .52 %±0.06 %	0.38 %±0.10 %
1000 V	0 .50 %±0.10 %	0.41 %±0.24 %

4.6.2. Line width dependency on the acceleration potential

The line width was evaluated for iron particle impacts on an Ag target under variation of the accelerating potential applied on the target. Due to the variation of the accelerating filed, the ions reach different velocities passing the grounded grid in front of the target,moving at different speeds towards the detector. Thus, one of the defining parameters for the peak width, the *Mach number* can be changed by the experiment setup and its significance can be evaluated. Table 4.13 lists the width of selected mass lines in Fe on Ag impact spectra as function of the acceleration potential U_{acc} at similar speeds. The line width for the bulk material lines C, O, and Fe decreases for increasing acceleration potential. Whereas no effect is apparent for the lines of the alkali contamination due the variation of the accelerating field.

4.6.3. Line shape and asymmetry

The line shape is characterised by the asymmetry of a line, a quantitative measure will be

$$A = 1 - \frac{1 - \tau_{left}}{\tau_{right}}, \tag{4.5}$$

with τ_{left} and τ_{right} being the times for half of the maximum of the peak normalised due to the flight time of the peak maximum as shown in Figure 4.39.

The lines are highly asymmetric, with a strong preference for fast ions. The line asymmetry depends on the impact velocity and the energy density and is not correlated to the kinetic energy of the impacting particle, exemplified for the iron lines of spectra obtained by particle impact experiments with iron particles and shown in Figure 4.40.

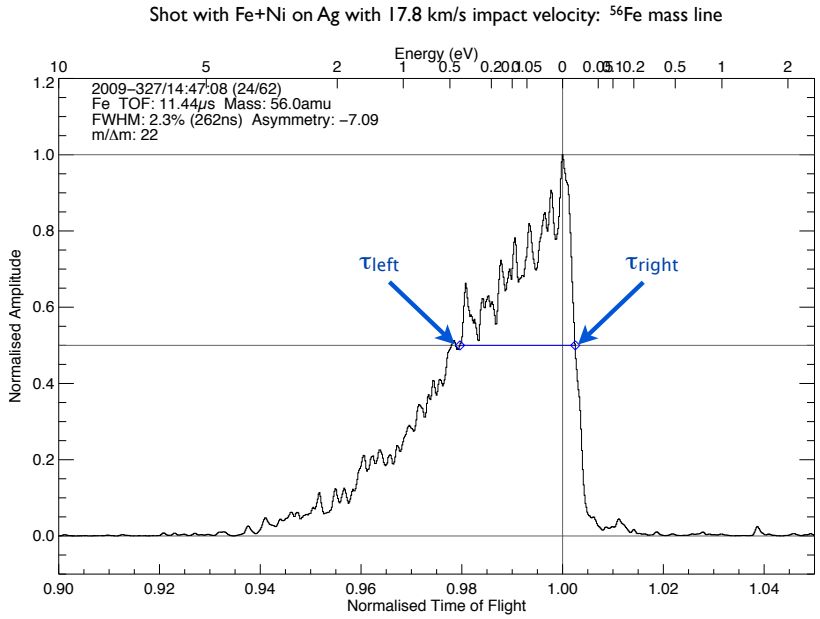

Figure 4.39.: Asymmetry of the iron line for an impact with 17.8 $\mathrm{km\,s^{-1}}$ impact velocity

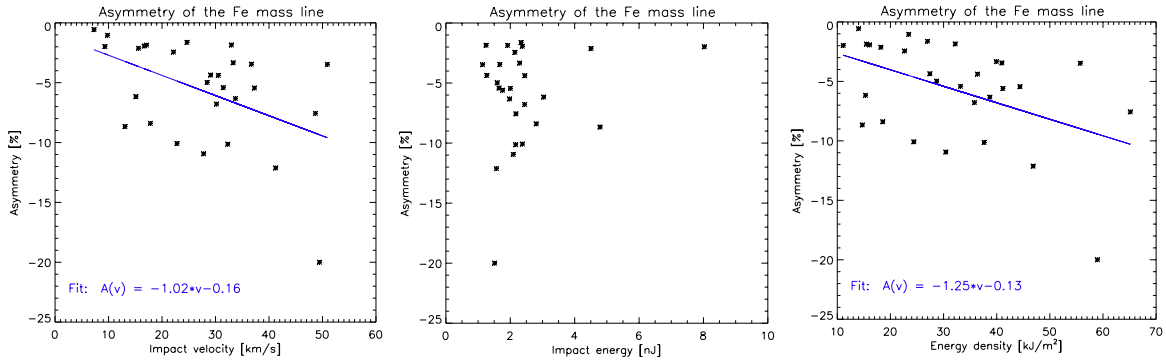

Figure 4.40.: Asymmetry of the iron line in dependence on the impact velocity, the kinetic energy and the energy density of impacting iron particles.

Table 4.14.: Shots with iron particles on a Ag target: dependence of the line asymmetry of carbon, oxygen, and iron on the acceleration potential applied to the target for impact velocities between $30\,\mathrm{km\,s^{-1}}$ and $40\,\mathrm{km\,s^{-1}}$ *(above)* and of sodium and potassium on the acceleration potential U_{acc} applied to the target for impact velocities between $5\,\mathrm{km\,s^{-1}}$ and $10\,\mathrm{km\,s^{-1}}$ *(bottom)*.

U_{acc}	C Asymmetry	O Asymmetry	Fe Asymmetry
500 V	-1 .31±1.47	-3.84±7.63	-12.13±6.80
600 V	-1 .82±1.85	-0.43±0.87	-9.74±5.06
700 V	-1 .71±1.29	-0.78±1.38	-7.76±4.93
800 V	-0 .42±0.46	-0.76±0.73	-7.13±6.46
900 V	-1 .74±0.75	-2.58±4.26	-9.99±3.54
1000 V	-0 .86±1.10	-0.78±1.45	-4.60±2.74

target potential	Na Asymmetry	K Asymmetry
700 V	-0 .09±0.16	0.07±0.13
800 V	-0 .97±0.88	-0.09±0.20
900 V	-0 .19±0.90	-0.02±0.76
1000 V	-0 .16±0.69	0.09±0.24

Table **??** shows evaluated line asymmetries for impact of iron particles on a Ag target within relatively narrow impact velocities and their dependency on the acceleration potential:

- The asymmetry is independent on the acceleration potential.
- The lines of the alkali contamination lines are almost symmetric.
- Iron, the main particle constituent, forms the most asymmetric line .

The selection of the particular lines and the velocity ranges was made based on the same considerations as above.

4.6.4. Comparison and discussion of the line shape for particle impacts and laser ionisation

As shown in Figure 4.31 and discussed in the sections above, the lines have different shapes for impact ionisation and for laser ablation.

- **Fe+Ni on Ag:** For the bulk material lines of target and projectile materials and for the ^{12}C and ^{16}O - lines the lines are highly asymmetric, with a strong preference for fast ions. Assuming that the velocity distribution inferred from the peak shape is directly representative of the energy distribution of the plasma it is clear that the peak form does

not correspond to a Maxwell-Boltzmann distribution. In particular the steep fall towards slower velocities differs from the distribution expected for a plasma in local thermodynamic equilibrium (LTE). This phenomenon can be explained by either an excess of high velocity ions or a depletion in the population of low velocity ions. There is no published research which adequately explains either scenario. For example, there are theoretical models describing the impact plasma as an expanding cloud with an additional bulk velocity leading to directed motion away from the target. This bulk velocity is estimated to be approximately equal to the expansion velocity (Hornung, 2010) and thus, approximately equals 1/3 of the impact velocity (Arnaudeau et al., 1984). This would provide a population of faster ions. However, the reduced field acting on the ions at moment the plasma becomes transparent for field should lead to significantly later ion arrival times.

- **Laser on Fe** The lines for laser ablation are symmetrical and correspond to a Gaussian distribution of the ion velocities. The widths of the lines are narrow and show no significant dependence on the laser intensity in the range used for comparison with impact ionisation (Rohr and Srivastava, 2005). In this range the ion formation is only dependent on the surface properties and the wavelength of the laser light, implying desorption (Krueger, 1983). Thus, the energy of the ions is determined by the photon energy of the laser light and subsequently only varies within a very small range. The rapid change in the characteristics of the lines at higher laser intensity suggests the onset of ablation (see Section 2.2.6). Furthermore, for the laser pulse duration of 5 ns there is an interaction of the laser light with the plasma cloud (Hillier et al., 1967); further ionisation and heating takes place, leading to widening and shifts of the lines (Russo, 1995; Bäuerle, 1996).

- **Alkali contamination lines in particle impacts** The line shapes of alkali contaminants Na and K resemble lines due to laser ablation. This suggests a similar formation process, i.e. desorption. This is consistent with the models of non-equilibrium desorption by Krueger (1982) and Knabe and Krueger (1982). In contrast to this study the authors described the impact ionisation process as in general comparable with laser ablation experiments. In their study the mass spectra of Fe particles impacting on alkali iodide targets were compared with spectra of laser ablation and ion impacts.

4.6.5. Disintegration of weak lines due to decreasing acceleration potential

Figure 4.41 - 4.43 and the following illustrate remarkably a phenomenon occurring during measurements with iron particles impacting on as Ag target with impact velocities above $10\,\mathrm{km\,s^{-1}}$.

Weak lines between about 20 amu and 50 amu disintegrate with decreasing acceleration potential U_{acc}. Instead of forming well shaped peaks with a defined width and, ions produced in this mass range occur in bunches of narrow subsequent spikes, seeming to be amplified signals of single ions.

This suggests that the process originating these species recognised mainly as alkali contamination is far from equilibrium and works due to surface desorption.

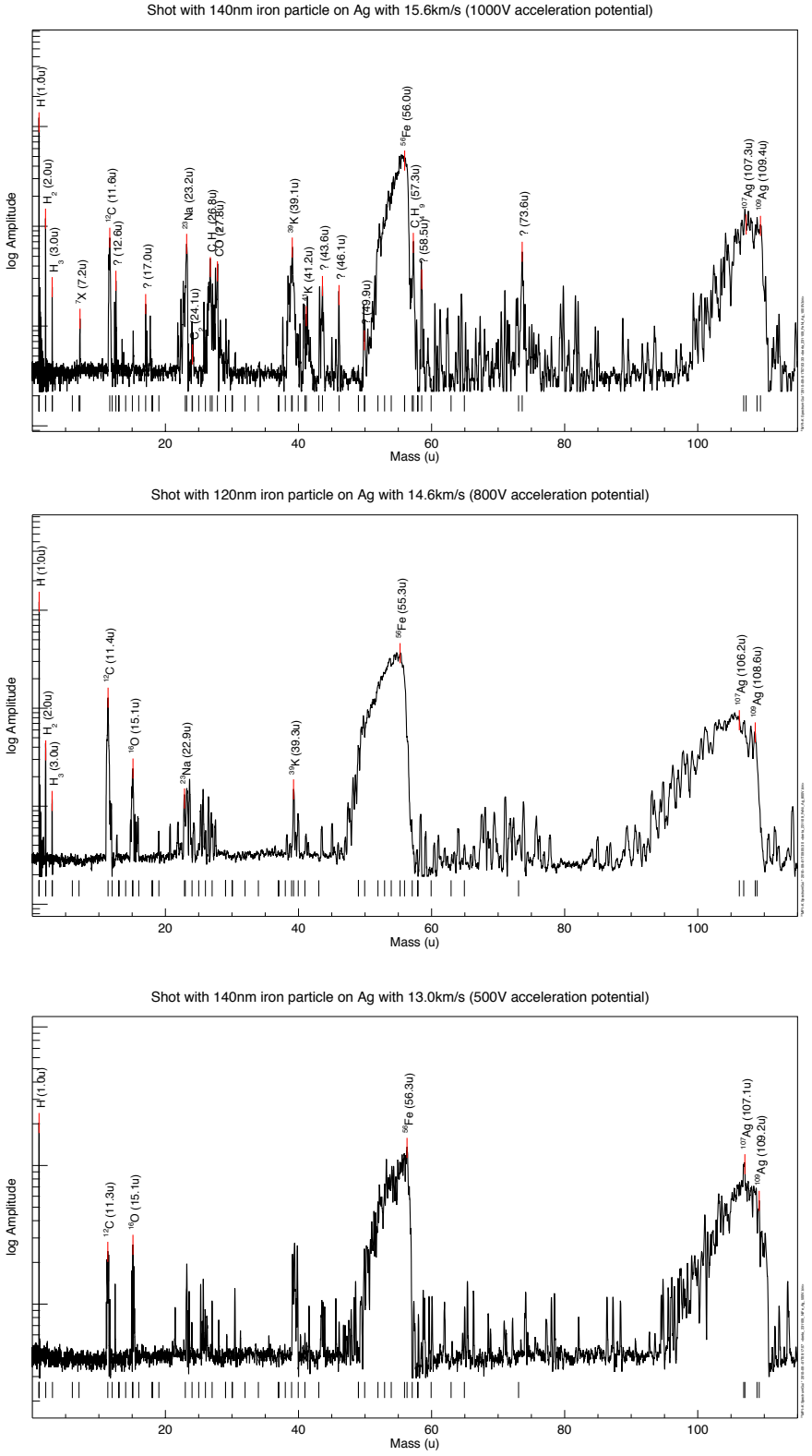

Figure 4.41.: Changing behaviour of the weak lines between 20 amu and 50 amu for decreasing acceleration potential for impact velocities of about 15 $\mathrm{km\,s^{-1}}$

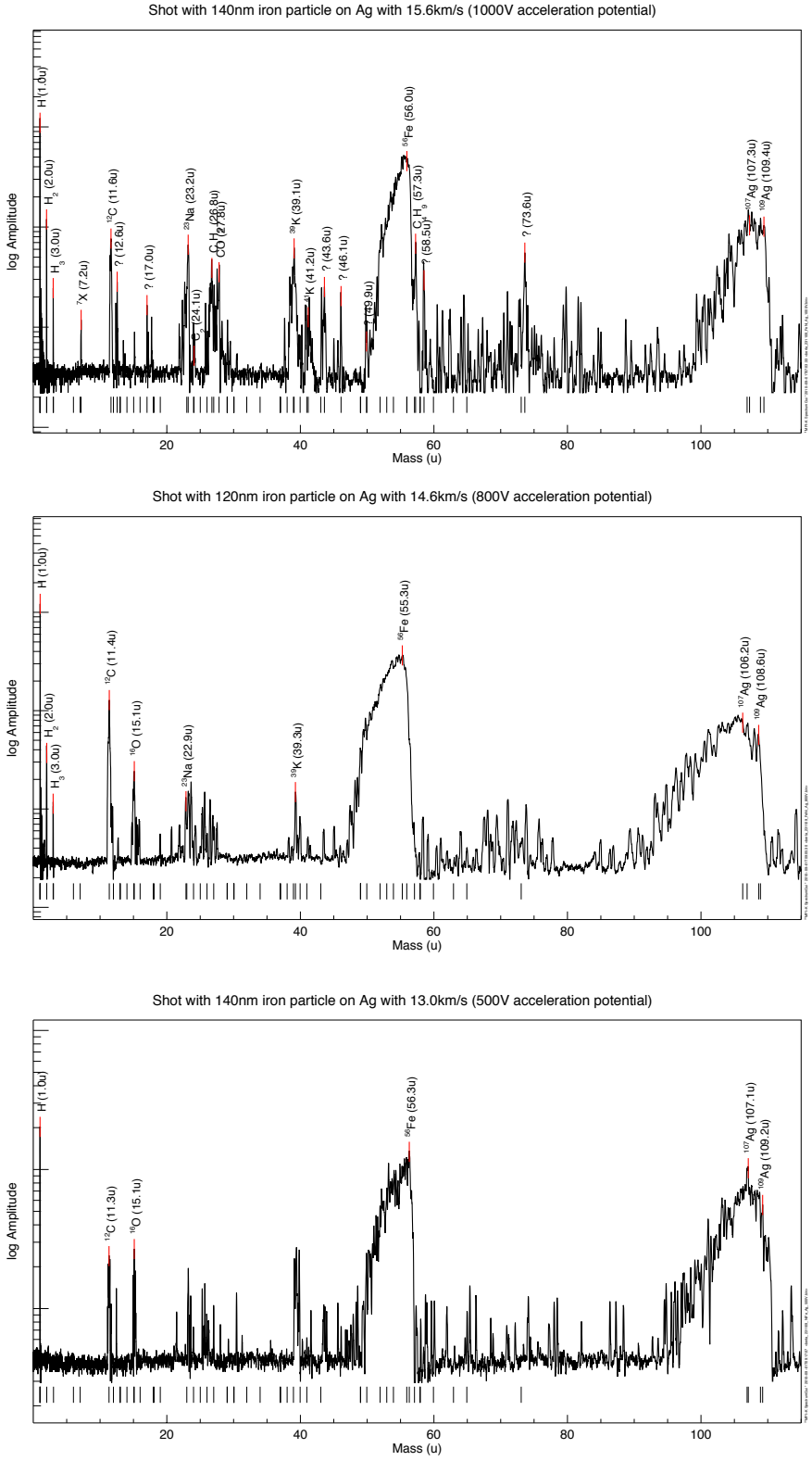

Figure 4.42.: Changing behaviour of the weak lines between 20 amu and 50 amu for decreasing acceleration potential for impact velocities of about 30 km s^{-1}

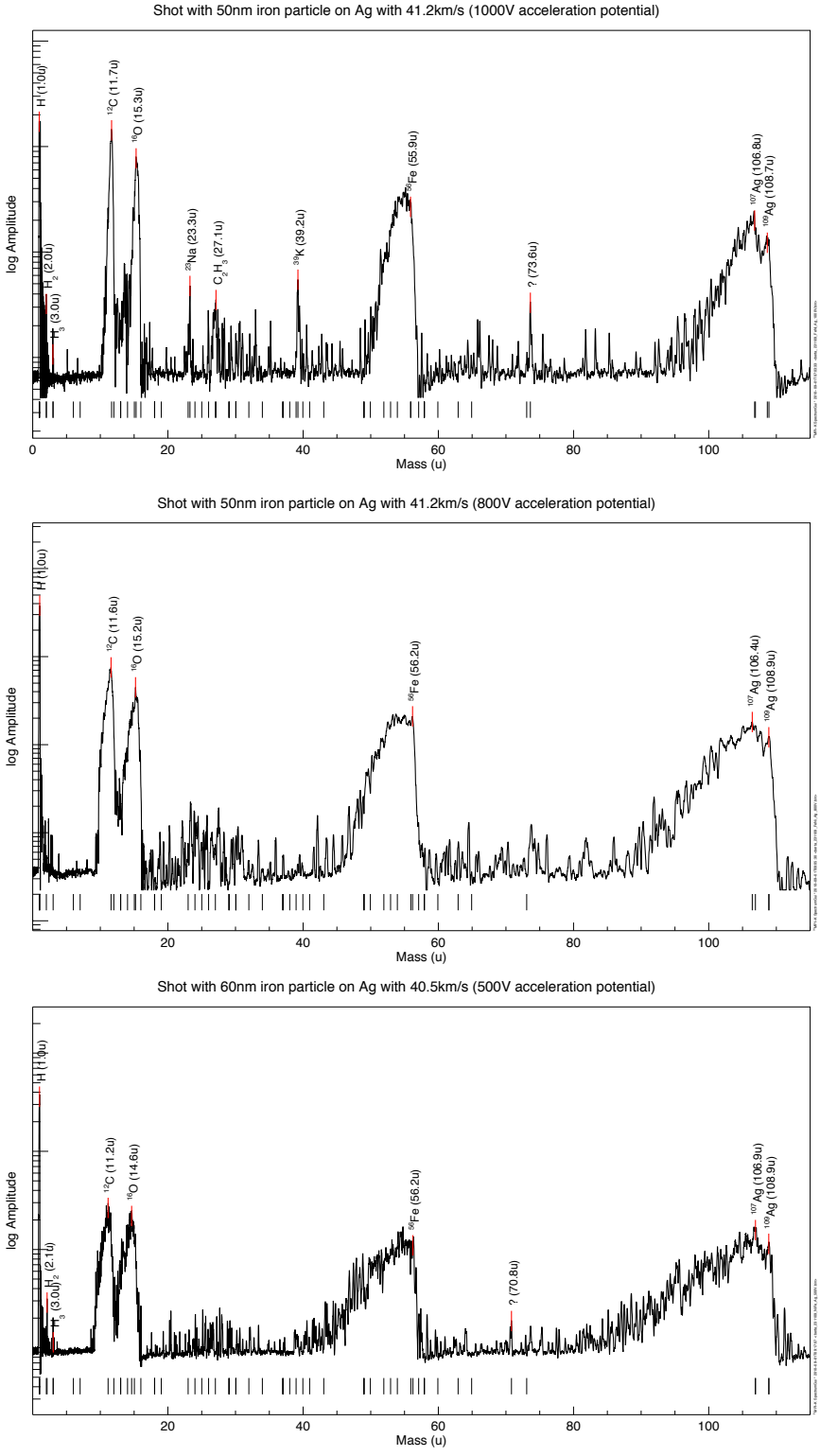

Figure 4.43.: Changing behaviour of the weak lines between 20 amu and 50 amu for decreasing acceleration potential for impact velocities of about 40 km s^{-1}

5. Summary

This summary gives an overview of the results and conclusions of this work, together with any questions which have arisen.

The guiding themes of this work were three questions concerning the processes of impact and laser ionisation:

- How reproducible are mass spectra produced by hypervelocity impacts and by laser ablation under similar physical conditions?
- Is laser ablation a useful analogue for the impact ionisation process?
- How deep is our understanding of the impact ionisation process?

A program of hypervelocity impact and laser induced ionisation experiments was performed to investigate these themes.

These measurements were conducted with a time-of-flight mass spectrometer designed to provide as comparable as possible impact conditions and optimised to obtain direct information about the process, i.e. the velocity distribution of the generated ions. The results provide constraints for the comparability of the processes and for the possibility of simulating particle impacts with laser bombardment of solid surfaces. The laser used in this study is a Nd-YAG solid state laser with a wave length of 355 nm, pulse durations of about 5 ns and a pulse power of up to 200kW. For the laser ionisation measurements the laser beam was focused to a focal spot of about 10μm diameter on metal (iron and a copper/silver alloy) as well as silicate targets (gold coated olivine). These materials were chosen to be comparable to the particle impact experiments shots, which had been performed with iron particles as well as with orthopyroxene and olivine dust on metal targets.

1. Reproducibility
   - **Reproducibility of Laser Processes:**
     The threshold for ionisation, the resulting charge and the characteristics of the generated plasma, as investigated by time-of-flight mass spectroscopy, showed a dependence on the local surface properties, which was as strong as the dependence on the general chemical and physical properties of the target and on the power settings of the laser itself. These local variations can be explained by variations of the surface contamination and to a greater degree by differences in the surface topography.
     For a fixed set up both charge yield and spectra are similar. In this respect laser ablation provides the possibility to produce easily and cheaply many similar ion signals with a high repetition rate.

- **Dependence of Mass Lines on Laser Energy:**
  Line broadening depends non-linearly on the laser energy. At high laser energies mass lines shift to positions consistent with longer flight times, inconsistent with the time-of-flight equation ions with zero initial energy. This implies an acceleration process of unknown nature, probably a plasma process. Furthermore line splitting becomes apparent.
- **Reproducibility of Impact Ionisation:**
  Shots within a small range of impact velocities are very similar, for example the likelihood of the appearance of a mass line and its intensity are the same as well as the shape and widths of the peak. This also is the case - to a slightly lesser degree - for small ranges of impact energy densities. Spectra obtained over small ranges of impact energy on the other hand show far fewer similarities. This implies that the parameter controlling the impact process is either the impact velocity or the impact energy density, the energy is ruled out as a defining parameter.

2. Comparability of both Processes

- **Impact Charge Yield:**
  The charge yields obtained by hypervelocity particle impact ranged between about 5 fC and about 0.75 pC, whereas for the laser processes charge yields were strongly dependent on the specific laser and target configuration and resulted in ranges from 1 fC to about 45 pC.
- **Appearance of lines:**
  Similar time-of-flight mass spectra (i.e. with similar species present) can be achieved for only a narrow range of impact parameters. Over this range of impact parameters the resulting spectra are similar with respect to both the appearance of mass lines of certain species and their intensities. Due to the strong variation of the laser ablation process with local surface conditions and the inherent difficulty to control this, it was not possible to determine a fixed setup of the laser to reliably replicate even this limited set of spectra.
- **Peak Shapes and Line Widths:**
  The shapes of the peaks and the dependence of the line widths on the impact parameters are fundamentally different for impact ionisation and laser processes. Whereas the peak widths of spectra produced in particle impact events have a strong dependence on at least some of the impact parameters, the line width for laser ablation in the comparable energy range (see bullet point above) showed no significant dependence on the laser energy. Peak shapes of impact ionisation events show a much stronger asymmetry with respect to the preference of faster ions as the laser ablation lines. The lines shapes for laser ionisation corresponds with a Gaussian ion velocity distribution.
  Generally laser shots produce narrower, more symmetric lines, implying desorption as the ion formation process.This has major consequences for performance tests and simulations of time-of-flight mass spectrometers with laser set ups. For example, instrument mass resolution measurement derived from laser experiments may tend to overestimate the actual instrument performance under hypervelocity impact conditions.

These findings show that, in general, plasma generated by laser ablation or desorption is not comparable to that created by hypervelocity particle impacts. However, particular aspects of the the laser induce ionisation process can be used as a rough substitute for hypervelocity particle impacts: once found and optimised, a particular laser set up can be used to produce many similar impact events at a high repetition rate, which can then be used for optimising and testing detectors, amplifiers and other electronic components for time-of-flight mass spectrometers developed for the investigation of impact ionisation plasmas.

3. Observations for Hypervelocity Particle Impacts

   - **Impact Charge Yields:**
     Events within a very small range of impact velocities produce charge yields which show a dependence on the particle mass. This dependence also seems to be controlled on the impact velocity. For a statistical evaluation and to investigate other possible relations, i.e. with the densities of the target and particles, the size of the data set was too small.

   - **Impact Plasma Evolution Timescale:**
     The first phase of the plasma evolution has a constant duration of several 100 ns, generated by the electrons produced instantaneously at the moment of impact. The timescales of the latter phases of the plasma evolution depends only on the impact velocity. The rise times decrease with increasing impact speed, implying that this decrease correlates with the higher specific internal energy of the shocked material, leading to higher ion and electron velocities.

   - **Signal Form of Impact Charge:**
     The signal form of the impact charge varies in dependence on the impact velocity. Many charge yield signals for events with impact velocities between $10\,\mathrm{km\,s^{-1}}$ and $15\,\mathrm{km\,s^{-1}}$ showed structures of two or more steps.

   - **Disintegrating mass lines :**
     For decreasing acceleration potentials the weak mass lines between about 20 amu and 40 amu begin to disintegrate from well shaped mass lines to a bunch of clustered needle-shaped peaks. At this time there is no explanation for this phenomenon.

   - **Peak Shapes and Line Widths:**
     The mass lines are highly asymmetric, with a strong preference for fast ions. Due to the unknown spectrometer response function and the unknown distribution ion velocities without further information it impossible to determine whether the observed line shape corresponds to an equilibrium distribution of ion velocities.
     The widths of the lines for most of the investigated species show a dependence on the impact velocity as well as on the impact energy density, whereas no dependence on the impact energy was apparent.
     An exception is the line width of the contamination ions, sodium and potassium, which showed no dependence on any of the impact parameters.

     Again, this implies that the defining parameter of the impact process is either the impact velocity or the impact energy density. Due to the the bias in the accelerated particles' velocities and masses introduced by the functional principle of the dust accelerator, the question, which parameter dominates, could not be answered.

Further investigations over a wider range of kinetic energies of the particles are necessary in the future.

- **Velocity thresholds for the appearance of ion lines:**
  The abundance of particular lines is dependent on the impact velocity of the dust particle. For instance, the ^{16}O-ion starts to show up in mass spectra of Fe+Ni particles impacting an Ag target at velocities above $\sim 12\,\mathrm{km\,s^{-1}}$. The results of this investigation prove that an in-depth investigation of the speed-dependent line appearance is one of the most promising approaches to develop a more accurate method for determining the impact speed than the rise time method.

Bibliography

V. I. Abramov, D. R. Bandura, V. P. Ivanov, and A. A. Sysoev. Energy and angular characteristics of ions emitted as a result of the impact of accelerated particles against a target. *Pis ma Zhurnal Tekhnischeskoi Fiziki*, 17:1–4, March 1991.

N. G. Adams and D. Smith. Studies of microparticle impact phenomena leading to the development of a highly sensitive micrometeoroid detector. *Planet. Space Sci.*, 19:195–+, February 1971. doi: 10.1016/0032-0633(71)90199-1.

N. Altobelli, E. Grün, and M. Landgraf. A new look into the Helios dust experiment data: presence of interstellar dust inside the Earth's orbit. *Astron. Astrophys.*, 448:243–252, March 2006. doi: 10.1051/0004-6361:20053909.

L.V. Al'tshuler. Use of shock waves in high-pressure physics. *Uspekhi Fizicheskii Nauk*, 85 (2):197–258, Feb. 1965.

L.V. Al'tshuler, A.A. Bakanova, I.P. Dudoladov, E.A. Dynin, R.F. Trunin, and B.S. Chekin. Shock adiabatic curves of metals. new data, statistical analysis, and general laws. *Journal of Applied Mechanics and Technical Physics*, 22(2):145–69, March-April 1981. ISSN 0021-8944.

S. Amari and K. Lodders. Pre-solar grains from supernovae and novae. *Highlights of Astronomy*, 14:349–352, August 2007. doi: 10.1017/S1743921307010952.

S. Amoruso, A. Amodeo, V. Berardi, R. Bruzzese, N. Spinelli, and R. Velotta. Laser produced plasmas in high fluence ablation of metallic surfaces probed by time-of-flight mass spectrometry. In *Applied Surface Science*, volume 96-98, pages 175–80, Netherlands, April 1996. Council of Eur.; Comm. Eur. Communities, Elsevier. Laser Ablation. Symposium F: Third International Symposium on Laser Ablation (COLA'95) 1995 E-MRS Spring Conference, 22-26 May 1995, Strasbourg, France.

J. B. Anderson and J. B. Fenn. Velocity distributions in molecular beams from nozzle sources. *Physics of Fluids*, 8(5):780–787, 1965. doi: 10.1063/1.1761320.

S. I. Anisimov, A. V. Bushman, G. I. Kanel', A. B. Konstantinov, R. Z. Sagdeev, S. G. Sugak, and V. E. Fortov. Physics of the damage from high-velocity impact. *Soviet Journal of Experimental and Theoretical Physics Letters*, 39:8–+, January 1984.

F. Arnaudeau, A. de Rouvray, and G. Winkelmuller. Giotto residual ionization. In E. Rolfe, B. Battrick, & R. Reinhard, editor, *ESA Special Publication*, volume 224 of *ESA Special Publication*, pages 21–37, 1984.

S. Auer. *Interplanetary Dust*, chapter Instrumentation, pages 387–438. Springer, 2001.

S. Auer. Circuitry for the power supply of a MCP. Private Communication, 2009.

S. Auer and K. Sitte. Detection technique for micrometeoroids using impact ionization. *Earth and Planetary Science Letters*, 4:178–+, April 1968. doi: 10.1016/0012-821X(68)90013-7.

D. E. Austin, T. J. Ahrens, and J. L. Beauchamp. Dustbuster: a compact impact-ionization time-of-flight mass spectrometer for in situ analysis of cosmic dust. *Review of Scientific Instruments*, 73:185–189, January 2002. doi: 10.1063/1.1427762.

W. J. Baggaley. Interstellar dust in the solar system. *Earth Moon and Planets*, 95:197–209, December 2004. doi: 10.1007/s11038-005-9039-5.

D. R. Bandura and A. A. Makarov. Time-of-flight mass reflection with a large area of ion collection. *International Journal of Mass Spectrometry and Ion Processes*, 127:45–55, August 1993. doi: 10.1016/0168-1176(93)87077-6.

T. H. K. Barron. Grüneisen parameters for the equation of state of solids. *Annals of Physics*, 1:77–90, April 1957. doi: 10.1016/0003-4916(57)90006-4.

D. Bäuerle. *Laser Processing and Chemistry*. Springer-Verlag, 2 edition, 1996.

O. E. Berg and L. H. Meredith. Meteorite Impacts to Altitude of 103 Kilometers. *J. Geophys. Res.*, 61:751–754, December 1956. doi: 10.1029/JZ061i004p00751.

J. Binney and M. Merrifield. *Galactic Astronomy*. Princton Series in Astrophysics, 1998.

D. Bleiner, A. Bogaerts, F. Belloni, and V. Nassisi. Laser-induced plasmas from the ablation of metallic targets: The problem of the onset temperature, and insights on the expansion dynamics. *Journal of Applied Physics*, 101(8):083301–+, April 2007. doi: 10.1063/1.2721410.

N. Bloembergen. Laser-material interactions; fundamentals and applications. In *American Institute of Physics Conference Series*, volume 288 of *American Institute of Physics Conference Series*, pages 3–10, October 1993. doi: 10.1063/1.44887.

D. Brownlee, P. Tsou, J. Aléon, C. M. O. '. Alexander, T. Araki, S. Bajt, G. A. Baratta, R. Bastien, P. Bland, P. Bleuet, J. Borg, J. P. Bradley, A. Brearley, F. Brenker, S. Brennan, J. C. Bridges, N. D. Browning, J. R. Brucato, E. Bullock, M. J. Burchell, H. Busemann, A. Butterworth, M. Chaussidon, A. Cheuvront, M. Chi, M. J. Cintala, B. C. Clark, S. J. Clemett, G. Cody, L. Colangeli, G. Cooper, P. Cordier, C. Daghlian, Z. Dai, L. D'Hendecourt, Z. Djouadi, G. Dominguez, T. Duxbury, J. P. Dworkin, D. S. Ebel, T. E. Economou, S. Fakra, S. A. J. Fairey, S. Fallon, G. Ferrini, T. Ferroir, H. Fleckenstein, C. Floss, G. Flynn, I. A. Franchi, M. Fries, Z. Gainsforth, J.-P. Gallien, M. Genge, M. K. Gilles, P. Gillet, J. Gilmour, D. P. Glavin, M. Gounelle, M. M. Grady, G. A. Graham, P. G. Grant, S. F. Green, F. Grossemy, L. Grossman, J. N. Grossman, Y. Guan, K. Hagiya, R. Harvey, P. Heck, G. F. Herzog, P. Hoppe, F. Hörz, J. Huth, I. D. Hutcheon, K. Ignatyev, H. Ishii, M. Ito, D. Jacob, C. Jacobsen, S. Jacobsen, S. Jones, D. Joswiak, A. Jurewicz, A. T. Kearsley, L. P. Keller, H. Khodja, A. L. D. Kilcoyne, J. Kissel, A. Krot, F. Langenhorst, A. Lanzirotti, L. Le, L. A. Leshin, J. Leitner, L. Lemelle, H. Leroux, M.-C. Liu, K. Luening, I. Lyon,

G. MacPherson, M. A. Marcus, K. Marhas, B. Marty, G. Matrajt, K. McKeegan, A. Meibom, V. Mennella, K. Messenger, S. Messenger, T. Mikouchi, S. Mostefaoui, T. Nakamura, T. Nakano, M. Newville, L. R. Nittler, I. Ohnishi, K. Ohsumi, K. Okudaira, D. A. Papanastassiou, R. Palma, M. E. Palumbo, R. O. Pepin, D. Perkins, M. Perronnet, P. Pianetta, W. Rao, F. J. M. Rietmeijer, F. Robert, D. Rost, A. Rotundi, R. Ryan, S. A. Sandford, C. S. Schwandt, T. H. See, D. Schlutter, J. Sheffield-Parker, A. Simionovici, S. Simon, I. Sitnitsky, C. J. Snead, M. K. Spencer, F. J. Stadermann, A. Steele, T. Stephan, R. Stroud, J. Susini, S. R. Sutton, Y. Suzuki, M. Taheri, S. Taylor, N. Teslich, K. Tomeoka, N. Tomioka, A. Toppani, J. M. Trigo-Rodríguez, D. Troadec, A. Tsuchiyama, A. J. Tuzzolino, T. Tyliszczak, K. Uesugi, M. Velbel, J. Vellenga, E. Vicenzi, L. Vincze, J. Warren, I. Weber, M. Weisberg, A. J. Westphal, S. Wirick, D. Wooden, B. Wopenka, P. Wozniakiewicz, I. Wright, H. Yabuta, H. Yano, E. D. Young, R. N. Zare, T. Zega, K. Ziegler, L. Zimmerman, E. Zinner, and M. Zolensky. Comet 81P/Wild 2 Under a Microscope. *Science*, 314:1711–, December 2006. doi: 10.1126/science.1135840.

M. J. Burchell, M. J. Cole, S. F. Lascelles, M. A. Khan, C. Barthet, S. A. Wilson, D. B. Cairns, and S. P. Armes. Acceleration of conducting polymer-coated latex particles as projectiles in hypervelocity impact experiments. *Journal of Physics D Applied Physics*, 32:1719–1728, July 1999. doi: 10.1088/0022-3727/32/14/325.

A.E. Cameron and Jr. Eggers, D.F. An ion "velocitron". *Review of Scientific Instruments*, 19: 605–607, Sept. 1948.

Robert J. Cotter. *Time-of-Flight Mass Spectrometry: Instrumentation and Applications in Biological Research*. Acs Professional Reference Book, 1997.

B.-K. Dalmann, E. Grün, J. Kissel, and H. Dietzel. The ion-composition of the plasma produced by impacts of fast dust particles. *Planet. Space Sci.*, 25:135–147, February 1977. doi: 10.1016/0032-0633(77)90017-4.

W. Demtröder. *Experimentalphysik 3: Atome, Moleküle und Festkörper*. Springer, 2000a.

W. Demtröder. *Laserspektroskopie: Grundlagen und Techniken*. Springer, 4. edition, 2000b.

H Dietzel, G Eichhorn, H Fechtig, E Grün, H J Hoffmann, and J Kissel. The HEOS 2 and HELIOS micrometeoroid experiments. *Journal of Physics E: Scientific Instruments*, 6(3): 209, instruments and techniques 1973.

Yu P. Dikov, E. N. Evlanov, M. N. Fomenkova, L. M. Mukhin, M. A. Nazarov, O. F. Prilutsky, R. Z. Sagdeev, and B. V. Zubkov. Halley comet dust particle classification according to the data obtained by mass spectrometer PUMA-2. *Advances in Space Research*, 9(3):253–258, 1989. URL www.scopus.com. Cited By (since 1996): 4.

R. Dinger. Energie - und Winkelverteilung lasererzeugter Plasmaionen. Master's thesis, Universität Kaiserslautern, 1980.

J. Dorschner. *Interstellar Dust and Circumstellar Dust Clouds*, pages 727–786. Springer-Verlag, 2001.

J. Dorschner and T. Henning. Dust metamorphosis in the galaxy. *Astronomy and Astrophysics Review*, 6:271–333, 1995. doi: 10.1007/BF00873686.

B. T. Draine. Interstellar Dust Grains. *Annu. Rev. Astrophys.*, 41:241–289, 2003. doi: 10.1146/annurev.astro.41.011802.094840.

S. Drapatz and K.W. Michel. Theorie der Stosswellenionisation von Mikrometeoriten. Vortrag auf der DPG-Frühjahrstagung der Arbeitsgemeinschaft Extraterrestrische Physik vom 15.-17.3.72 in Bonn, 1972.

S. Drapatz and K.W. Michel. Theory of shock-wave ionization upon high-velocity impact of micrometeorites. *Zeitschrift für Naturforschung*, 29 a:870–879, 1974.

E.H. Eberhardt. Gain model for microchannel plates. *Applied Optics*, 18(9):1418–23, 1 May 1979. ISSN 0003-6935.

E.H. Eberhardt. Parameters pertaining to microchannel plates and microchannel plate devices. *ITT Technichal Note*, 127, August 1980.

E.H. Eberhardt. An operational model for microchannel plate devices. In *IEEE Transactions on Nuclear Science*, volume ns-28, pages 712–17, USA, February 1981. IEEE; Power Eng. Soc.; Oak Ridge Nat. Lab.; et al. 1980 Nuclear Science Symposium. 1980. 1980 Symposium on Nuclear Power Systems, 5-7 November 1980, Orlando, FL, USA.

G. Eichhorn. *Untersuchung der Lichtemission bei Hochgeschwindigkeitseinschlägen*. PhD thesis, Universität Heidelberg, 1974.

G. Eichhorn. Measurements of the light flash produced by high velocity particle impact. *Planet. Space Sci.*, 23:1519–1525, November 1975. doi: 10.1016/0032-0633(75)90005-7.

G. Eichhorn. Impact light flash studies - Temperature, ejecta, vaporization. In H. Elsaesser & H. Fechtig, editor, *Interplanetary Dust and Zodiacal Light*, volume 48 of *Lecture Notes in Physics, Berlin Springer Verlag*, pages 243–247, 1976. doi: 10.1007/3-540-07615-8_490.

G. Eichhorn. Heating and vaporization during hypervelocity particle impact. *Planet. Space Sci.*, 26:463–467, May 1978a. doi: 10.1016/0032-0633(78)90067-3.

G. Eichhorn. Primary velocity dependence of impact ejecta parameters. *Planet. Space Sci.*, 26:469–471, May 1978b. doi: 10.1016/0032-0633(78)90068-5.

Günther Eichhorn. Untersuchung der Lichtemission beim Einschlag energiereicher Mikroteilchen. Master's thesis, Max-Planck-Institut für Kernphysik, 1972.

J. Eichler and H.J. Eichler. *Laser: Bauformen, Strahlführung, Anwendungen*. Springer-Verlag, 4. edition, 1998.

I. Esterman. Molecular beam technique. *Reviews of Modern Physics*, 18:300–322, July 1946.

H. Fechtig, E. Grün, and J. Kissel. *Laboratory simulation*, pages 607–669. John Wiley & Sons, 1978.

L.A. Fielding and S.P. Armes. Technical report on coating of olivine particles with polypyrrole. Technical report, University of Sheffield, 2009.

G. J. Flynn. Physical, Chemical, and Mineralogical Properties of Comet 81P/Wild 2 Particles Collected by Stardust. *Earth Moon and Planets*, 102:447–459, June 2008. doi: 10.1007/s11038-007-9214-y.

G. J. Flynn, P. Bleuet, J. Borg, J. P. Bradley, F. E. Brenker, S. Brennan, J. Bridges, D. E. Brownlee, E. S. Bullock, M. Burghammer, B. C. Clark, Z. R. Dai, C. P. Daghlian, Z. Djouadi, S. Fakra, T. Ferroir, C. Floss, I. A. Franchi, Z. Gainsforth, J.-P. Gallien, P. Gillet, P. G. Grant, G. A. Graham, S. F. Green, F. Grossemy, P. R. Heck, G. F. Herzog, P. Hoppe, F. Hörz, J. Huth, K. Ignatyev, H. A. Ishii, K. Janssens, D. Joswiak, A. T. Kearsley, H. Khodja, A. Lanzirotti, J. Leitner, L. Lemelle, H. Leroux, K. Luening, G. J. MacPherson, K. K. Marhas, M. A. Marcus, G. Matrajt, T. Nakamura, K. Nakamura-Messenger, T. Nakano, M. Newville, D. A. Papanastassiou, P. Pianetta, W. Rao, C. Riekel, F. J. M. Rietmeijer, D. Rost, C. S. Schwandt, T. H. See, J. Sheffield-Parker, A. Simionovici, I. Sitnitsky, C. J. Snead, F. J. Stadermann, T. Stephan, R. M. Stroud, J. Susini, Y. Suzuki, S. R. Sutton, S. Taylor, N. Teslich, D. Troadec, P. Tsou, A. Tsuchiyama, K. Uesugi, B. Vekemans, E. P. Vicenzi, L. Vincze, A. J. Westphal, P. Wozniakiewicz, E. Zinner, and M. E. Zolensky. Elemental Compositions of Comet 81P/Wild 2 Samples Collected by Stardust. *Science*, 314:1731–, December 2006. doi: 10.1126/science.1136141.

V. E. Fortov and I. V. Lomonosov. Shock waves and equations of state of matter. *Shock Waves*, 20:53–71, February 2010. doi: 10.1007/s00193-009-0224-8.

R. H. Fowler and L. Nordheim. Electron Emission in Intense Electric Fields. *Royal Society of London Proceedings Series A*, 119:173–181, May 1928.

P. A. Franken, A. E. Hill, C. W. Peters, and G. Weinreich. Generation of optical harmonics. *Phys. Rev. Lett.*, 7(4):118–119, Aug 1961. doi: 10.1103/PhysRevLett.7.118.

J. F. Friichtenicht. Micrometeoroid simulation using nuclear accelerator techniques. *Nuclear Instruments and Methods*, 28:70–+, June 1964. doi: 10.1016/0029-554X(64)90351-9.

J. F. Friichtenicht. Investigation of high-speed impact phenomena (Volume I). Technical Report NASA-CR-70032, NASA, 1965.

J. F. Friichtenicht. Laser-generated pulsed atomic beams. *Review of Scientific Instruments*, 45:51–56, January 1974. doi: 10.1063/1.1686447.

J. F. Friichtenicht and J. C. Slattery. Ionization associated with hypervelocity impact. Technical Report ASA TN D-2091, NASA, 1963.

J. F. Friichtenicht, N.L. Roy, and L. W. Moede. Cosmic Dust Analyzer. Technical Report NASA-CR-140241, NASA, 1971.

N. Fürstenau and F. Hillenkamp. Laser-induced cluster-ions from thin foils of metals and semiconductors. *International Journal of Mass Spectrometry and Ion Physics*, 37(2):135–151, February 1981. ISSN 0020-7381.

G.M. Gandel'man. Quantum mechanical theory of the equation of state for potassium, aluminium and iron. *Zhurnal Eksperimental'noi i Teoreticheskoi Fiziki*, 51(1(7)):147–155, July 1966.

C. W. Gardiner. *Handbook of Stochastic Methods. For Physics, Chemistry and the Natural Sciences*. Springer-Verlag Berlin and Heidelberg GmbH & Co. K, 2nd edition, October 1996. ISBN 3540616349.

D. E. Gault and E. D. Heitowit. The partition of energy for hypervelocity impact craters formed in rock. Technical Report NASA-TM-X-57428, NASA Ames Research Center, 1963.

D. E. Gault, W. L. Quaide, and V. R Oberbeck. Impact cratering mechanics and structures. Technical report, NASA Ames Research Center, 1974.

I.E. Geusic, H.M. Marcos, and L.G. van Uitert. Laser oscillations in nd-doped yttrium aluminum, yttrium gallium and gadolinium garnets. *Applied Physics Letters*, 4(10):182–184, 15 May 1964.

L. Giudicotti, M. Bassan, R. Pasqualotto, and A. Sardella. Simple analytical model of gain saturation in microchannel plate devices. *Review of Scientific Instruments*, 65(1):247–58, January 1994. ISSN 0034-6748.

J.R. Göller. *Kalibrationsmessungen an Mikrometeoritendetektoren für die Missionen ULYSSES, GALILEO und GIOTTO*. PhD thesis, Universität Heidelberg, 1988.

J.R. Göller and E. Grün. Calibration of the galileo/ulysses dust detectors with different projectile materials and at varying impact angles. *Planetary and Space Science*, 37(10):1197–206, October 1989. ISSN 0032-0633.

J. P. Gordon, H. J. Zeiger, and C. H. Townes. The Maser-New Type of Microwave Amplifier, Frequency Standard, and Spectrometer. *Physical Review*, 99:1264–1274, August 1955. doi: 10.1103/PhysRev.99.1264.

A. L. Graps, E. Grün, H. Svedhem, H. Krüger, M. Horányi, A. Heck, and S. Lammers. Io as a source of the jovian dust streams. *Nature*, 405:48–50, May 2000.

E. Grün, H. Fechtig, M. S. Hanner, J. Kissel, B.-A. Lindblad, D. Linkert, D. Maas, G. E. Morfill, and H. A. Zook. The Galileo Dust Detector. *Space Sci. Rev.*, 60:317–340, May 1992a. doi: 10.1007/BF00216860.

E. Grün, H. Fechtig, J. Kissel, D. Linkert, D. Maas, J. A. M. McDonnell, G. E. Morfill, G. Schwehm, H. A. Zook, and R. H. Giese. The ULYSSES dust experiment. *Astronomy and Astrophysics Supplement Series*, 92:411–423, January 1992b.

E. Grün, H. A. Zook, M. Baguhl, A. Balogh, S. J. Bame, H. Fechtig, R. Forsyth, M. S. Hanner, M. Horányi, M., J. Kissel, B.-A. Lindblad, D. Linkert, G. Linkert, I. Mann, J. A. M. McDonnell, G. E. Morfill, J. L. Phillips, C. Polanskey, G. Schwehm, N. Siddique, P. Staubach, J. Svestka, and A. Taylor. Discovery of Jovian dust streams and interstellar grains by the ULYSSES spacecraft. *Nature*, 362:428–430, April 1993. doi: 10.1038/362428a0.

E. Grün, B. Gustafson, I. Mann, M. Baguhl, G.E. Morfill, P. Staubach, A. Taylor, and H.A. Zook. Interstellar dust in the heliosphere. *Astronomy and Astrophysics*, 286:915–924, 1994.

E. Grün, M. Landgraf, M. Horányi, J. Kissel, H. Krüger, R. Srama, H. Svedhem, and P. Withnell. Techniques for galactic dust measurements in the heliosphere. *J. Geophys. Res.*, 105: 10403–10410, May 2000. doi: 10.1029/1999JA900376.

E. Grün, R. Srama, N. Altobelli, K. Altwegg, J. Carpenter, L. Colangeli, K.-H. Glassmeier, S. Helfert, H. Henkel, M. Horányi, A. Jäckel, S. Kempf, M. Landgraf, N. McBride, G. Moragas-Klostermeyer, P. Palumbo, H. Scholten, A. Srowig, Z. Sternovsky, and X. Vo. DuneXpress. *Experimental Astronomy*, 23:981–999, March 2009. doi: 10.1007/s10686-008-9099-4.

E. Grüneisen. Theorie des festen Zustandes einatomiger Elemente. *Annalen der Physik*, 344 (12):257–306, 1912.

B. A. S. Gustafson and N. Y. Misconi. Streaming of interstellar grains in the solar system. *Nature*, 282:276–278, November 1979. doi: 10.1038/282276a0.

D. P. Hamilton and J. A. Burns. Ejection of dust from Jupiter's gossamer ring. *Nature*, 364: 695–699, August 1993. doi: 10.1038/364695a0.

D. O. Hansen. Mass analysis of ions produced by hypervelocity impact. *Applied Physics Letters*, 13(3):89–91, 1968. doi: 10.1063/1.1652528. URL http://link.aip.org/link/?APL/13/89/1.

E.C. Hastings. The explorer xvi micrometeroid satellite. supplement iii, preliminary results for the period may 27, 1963, through july 22, 1963. Technical Report NASA TM X-949, NASA, 1964.

S. Helfert. Geeky stuff. Private Communication, 2010.

J. K. Hillier, S. F. Green, N. McBride, N. Altobelli, F. Postberg, S. Kempf, J. Schwanethal, R. Srama, J. A. M. McDonnell, and E. Grün. Interplanetary dust detected by the Cassini CDA Chemical Analyser. *Icarus*, 190:643–654, October 2007a. doi: 10.1016/j.icarus.2007.03.024.

J. K. Hillier, S. F. Green, N. McBride, J. P. Schwanethal, F. Postberg, R. Srama, S. Kempf, G. Moragas-Klostermeyer, J. A. M. McDonnell, and E. Grün. The composition of Saturn's E ring. *Mon. Not. Roy. Astron. Soc.*, 377:1588–1596, June 2007b. doi: 10.1111/j.1365-2966.2007.11710.x.

J.K. Hillier, S. Sestak, S.F. Green, F. Postberg, R. Srama, and M. Trieloff. The production of platinum-coated silicate nanoparticle aggregates for use in hypervelocity impact experiments. *Planetary and Space Science*, 57(14-15):2081 – 2086, 2009.

Sir J. K. Hillier, A. Mocker, K. Fiege, K. Otto, S. Bugiel, and L. McCoy. Cosmic Goo: Yet some more freaking TOF mass spectra containing even more bloody mass lines nobody cares about. *Zoonoses and Public Health*, 007:666, 2010.

Sir J.K. Hillier, K. Otto, A. Mocker, K. Fiege, and S. Bugiel. The suicidal semikolon; about the extinction of an underappreciated element in scientific publications. *Zprávy o geologických výzkumech*, 3:123–125, 1967.

Sir J.K. Hillier, N. McBride, S.F. Green, S. Kempf, and R. Srama. Modelling CDA mass spectra. *Planetary and Space Science*, 54(9-10):1007–13, August 2006. ISSN 0032-0633.

C Höfer. Präparation und Analyse von Analogmaterial für extraterrestrischen Staub. Bachelor's Thesis, Universität Heidelberg, July 2010.

H.-J. Hoffmann. *Entwicklung eines Detektors zur Massen- und Geschwindigkeitsanalyse von kosmischen Staubteilchen*. PhD thesis, Universität Heidelberg, 1971.

T. E. Holzer. Interaction between the solar wind and the interstellar medium. *Annu. Rev. Astrophys.*, 27:199–234, 1989.

P. Hoppe, K. Lodders, R. Strebel, S. Amari, and R. S. Lewis. Boron in Presolar Silicon Carbide Grains from Supernovae. *Astrophys. J.*, 551:478–485, April 2001. doi: 10.1086/320075.

M. Horányi. Dust streams from Jupiter and Saturn. *Physics of Plasmas*, 7:3847–3850, October 2000. doi: 10.1063/1.1288909.

M. Horányi, G. Morfill, and E. Grün. Mechanism for the acceleration and ejection of dust grains from Jupiter's magnetosphere. *Nature*, 363:144–146, May 1993. doi: 10.1038/363144a0.

M. Horányi, Z. Sternovsky, E. Grün, R. Srama, M. Lankton, and D. Gathright. The Lunar Dust EXperiment (LDEX) on the Lunar Atmosphere and Dust Environment Explorer (LADEE) Mission. In *Lunar and Planetary Institute Science Conference Abstracts*, volume 40 of *Lunar and Planetary Institute Science Conference Abstracts*, pages 1741–+, March 2009.

K. Hornung. Update of the impact ionization problem. In *ESA Special Publication*, volume 187 of *ESA Special Publication*, pages 15–19, 1982.

K. Hornung. Expansion and bulk velocity of the impact ionisation plasma. Private Communication, 2010.

K. Hornung and M. Drapatz. Residual ionization after impact of large dust particles. In *The Comet Hallay Probe Plasma Environment*, pages 23 – 37. European Space Agency, 1979.

K. Hornung and J. Kissel. On shock wave impact ionization of dust particles. *Astronomy and Astrophysics*, 291:324–336, 1994.

K. Hornung and K.W. Michel. Equation-of-state data of solids from shock vaporization. *Journal of Chemical Physics*, 56(5):2072–8, 1 March 1972. ISSN 0021-9606.

K. Hornung, Yu.G. Malama, and K. Thoma. Modeling of the very high velocity impact process with respect to in-situ ionization measurements. *Advanced Space Research*, 17(12):(12)77–(12)86, 1996.

H. Iglseder. *Ladungsemission beim Hochgeschwindigkeitseinschlag*. PhD thesis, Technische Universität München, 1986.

B. Jean and T. L. Rollins. Radiation from hypervelocity impact generated plasma. *AIAA Journal*, 8:1742–1748, October 1970. doi: 10.2514/3.5984.

A. Kantrowitz and J. Grey. A high intensity source for the molecular beam. i. theoretical. *Review of Scientific Instruments*, 22:328–332, May 1951.

W. H. Kegel. *Plasmaphysik*. Springer-Verlag, 1998.

S. Kempf. CDA Spectrum Analyser 4.40. Evaluation Software for *TOF* Mass Spectra, 2010.

S. Kempf, R. Srama, M. Horányi, M. Burton, S. Helfert, G. Moragas-Klostermeyer, M. Roy, and E. Grün. High-velocity streams of dust originating from Saturn. *Nature*, 433:289–291, January 2005a. doi: 10.1038/nature03218.

S. Kempf, R. Srama, F. Postberg, M. Burton, S. F. Green, S. Helfert, J. K. Hillier, N. McBride, J. A. M. McDonnell, G. Moragas-Klostermeyer, M. Roy, and E. Grün. Composition of Saturnian Stream Particles. *Science*, 307:1274–1276, February 2005b. doi: 10.1126/science.1106218.

S. Kempf, R. Srama, V. Schlemmer, E. Grün, A. Mocker, F. Postberg, H. Henkel, J. K. Hillier, M. Horányi, Z. Sternovsky, and R. Thissen. Suda: a dust camera for dust mass spectroscopy of moon surfaces. ?, 2010.

J. Kissel. The Giotto Particulate Impact Analyser. In *ESA Special Publication*, volume 1070 of *ESA Special Publication*, pages 67–83, 1986.

J. Kissel and F.R. Krueger. Ion formation by impact of fast dust particles and comparison with related techniques. *Applied Physics A - Solids and Surfaces*, 42:69–85, 1987.

J. Kissel, A. Glasmachers, E. Grün, H. Henkel, H. Höfner, G. Haerendel, H. von Hoerner, K. Hornung, E. K. Jessberger, F. R. Krueger, D. Möhlmann, J. M. Greenberg, Y. Langevin, J. Silén, D. Brownlee, B. C. Clark, M. S. Hanner, F. Hoerz, S. Sandford, Z. Sekanina, P. Tsou, N. G. Utterback, M. E. Zolensky, and C. Heiss. Cometary and Interstellar Dust Analyzer for comet Wild 2. *Journal of Geophysical Research (Planets)*, 108:8114–+, October 2003. doi: 10.1029/2003JE002091.

J. Kissel, F. R. Krueger, J. Silén, and B. C. Clark. The Cometary and Interstellar Dust Analyzer at Comet 81P/Wild 2. *Science*, 304:1774–1776, June 2004. doi: 10.1126/science.1098836.

W. Knabe. Untersuchungen am Einschlagsionisationsdetektor für die GALILEO- und ISPM-Mission. Master's thesis, Universität Heidelberg, 1980.

W. Knabe. *Massenspektroskopische Untersuchungen der Ionenbildung beim Einschlag schneller Staubteilchen*. PhD thesis, Ruprecht-Karls-Universität Heidelberg, 1983.

W. Knabe and F.R. Krueger. Ion formation from alkali iodide solids by swift dust particle impact. *Zeitschrift für Naturforschung A (Astrophysik, Physik und Physikalische Chemie)*, 37A(12):1335–40, December 1982. ISSN 0340-4811.

W. Koechner. *Solid-State Laser Engineering*. Springer, 1976.

A. V. Krivov, I. Wardinski, F. Spahn, H. Krüger, and E. Grün. Dust on the Outskirts of the Jovian System. *Icarus*, 157:436–455, June 2002. doi: 10.1006/icar.2002.6848.

A. V. Krivov, M. Sremčević, F. Spahn, V. V. Dikarev, and K. V. Kholshevnikov. Impact-generated dust clouds around planetary satellites: spherically symmetric case. *Planet. Space Sci.*, 51:251–269, March 2003. doi: 10.1016/S0032-0633(02)00147-2.

F. R. Krueger. Thermodynamics of Ion Formation by Fast Dissipation of Energy at Solid Surfaces. *Zeitschrift für Naturforschung A (Astrophysik, Physik und Physikalische Chemie)*, 38:385–+, 1983.

F.R. Krueger. Ion formation from solid surfaces due to very rapid energy transfer. In *Applications of Surface Science*, volume 11-12, pages 819–27, Netherlands, July 1982. Proceedings of the Second International Conference on Solid Films and Surfaces, 8-11 June 1981, College Park, MD, USA.

F.R. Krueger. Ion formation by high- and medium-velocities dust impacts from laboratory measurements and halley results. In *Advances in Space Research*, volume 17, June 1996.

H. Krüger, A. V. Krivov, D. P. Hamilton, and E. Grün. Detection of an impact-generated dust cloud around Ganymede. *Nature*, 399:558–560, June 1999. doi: 10.1038/21136.

G. Kurat, H. Palme, A. Embey-Isztin, J. Touret, T. Ntaflos, B. Spettel, F. Brandstätten, C. Palme, G. Dreibus, and M. Prinz. Petrology and geochemistry of peridotites and associated vein rocks of zabargad island, red sea, egypt. *Mineralogy and Petrology*, 48:309–341, 1993. ISSN 0930-0708. URL http://dx.doi.org/10.1007/BF01163106. 10.1007/BF01163106.

N. M. Kuznetsov and Y. P. Raizer. Recombination of electrons in a plasma expanding into a vacuum. *Journal of Applied Mechanics and Technical Physics*, 6:6–12, July 1965. doi: 10.1007/BF01565811.

L.D Landau and E.M. Lifshitz. *Fluid Mechanics*, volume 6 of *Course of Theoretical Physics*. Pergamon Press, 1 edition, 1959.

L. Láska, J. Krása, M. Pfeifer, K. Rohlena, S. Gammino, L. Torrisi, L. Andò, and G. Ciavola. Angular distribution of ions emitted from Nd:YAG laser-produced plasma. *Review of Scientific Instruments*, 73:654–656, February 2002. doi: 10.1063/1.1430037.

P Lavila. Analyzing time-of-flight spectra of cda. Technical report, Max-Planck-Institut für Kernphysik, 2002.

E. H. Levy and J. R. Jokipii. Penetration of interstellar dust into the solar system. *Nature*, 264: 423–+, December 1976. doi: 10.1038/264423a0.

F. Liebau. Die Systematik der Silikate. *Naturwissenschaften*, 49:481–482, January 1962. doi: 10.1007/BF00637032.

F. Liebau. *Structural Chemistry of Silicates. Structure, Bonding and Classification*. Springer, 1985.

W.I. Linlor. Ion energies produced by laser giant pulse. *Applied Physics Letters*, 3(11):210–211, 1 Dec. 1963.

C. M. Lisse, K. E. Kraemer, J. A. Nuth, A. Li, and D. Joswiak. Comparison of the composition of the Tempel 1 ejecta to the dust in Comet C/Hale Bopp 1995 O1 and YSO HD 100546. *Icarus*, 187:69–86, March 2007. doi: 10.1016/j.icarus.2006.11.019.

Stanley M. Livingston and John P. Blewett. *Particle Accelerators*. McGraw-Hill Book Company, Inc., 1962. Add data for field: Note.

C. Loty. Saturation effects in channel electron multipliers. *Acta Electronica*, 14(1):107–19, January 1971. ISSN 0001-558X.

S. G. Love, D. J. Joswiak, and D. E. Brownlee. Densities of stratospheric micrometeorites. *Icarus*, 111:227–236, September 1994. doi: 10.1006/icar.1994.1142.

I.H. Maiman. Stimulated optical radiation in ruby. *Nature*, 187:493–494, 6 Aug. 1960.

B. Makin and J. C. Keck. Variational Theory of Three-Body Electron-Ion Recombination Rates. *Physical Review Letters*, 11:281–283, September 1963. doi: 10.1103/PhysRevLett.11.281.

B. A. Mamyrin. Time-of-flight mass spectrometry (concepts, achievements, and prospects). *International Journal of Mass Spectrometry*, 206(3):251 – 266, 2001. ISSN 1387-3806.

B. A. Mamyrin, V. I. Karataev, D. V. Shmikk, and V. A. Zagulin. The mass-reflectron, a new nonmagnetic time-of-flight mass spectrometer with high resolution. *Soviet Journal of Experimental and Theoretical Physics*, 37:45–+, July 1973.

I. Mann, A. Czechowski, H. Kimura, M. Köhler, T. Minato, and T. Yamamoto. Physical properties of the dust in the Solar System and its interrelation with small bodies. In L. Daniela, M. Sylvio Ferraz, & F. J. Angel, editor, *Asteroids, Comets, Meteors*, volume 229 of *IAU Symposium*, pages 41–65, 2006. doi: 10.1017/S1743921305006678.

G. Markl. *Minerale und Gesteine: Mineralogie - Petrologie - Geochemie*. Spektrum Verlag, 2008.

C. Martin and P. Jelinsky. The size and distribution of electron clouds from a MCP detector. *Internal SSL Report*, August 1980.

T. Mauney and F. Adams. Ion kinetic energy measurements on laser-induced plasmas in laser microprobe mass analysis (LAMMA). Part I. Methodology. *International Journal of Mass Spectrometry and Ion Processes*, 59(1):103 – 119, 1984. doi: DOI:10.1016/0168-1176(84)87073-1.

F. J. McClung and R. W. Hellwarth. Giant Optical Pulsations from Ruby. *Journal of Applied Physics*, 33:828–829, March 1962. doi: 10.1063/1.1777174.

W. K. Meshejian, K. Ramamurti, W. P. Trower, and D. S. Wollan. A Gas Density Detector for Use in Space. *Journal of Spacecraft and Rockets*, 7:1228–+, October 1970. doi: 10.2514/3.30139.

N. Metropolis and Feynman. Equations of state of elements based on the generalized Fermi-Thomas theory. *Physical review*, 75:1561–1573, 1949. ISSN 0031-899X.

N. Metropolis, A. W. Rosenbluth, M. N. Rosenbluth, A. H. Teller, and E. Teller. Equation of State Calculations by Fast Computing Machines. *J. Chem. Phys.*, 21:1087–1092, June 1953. doi: 10.1063/1.1699114.

K.W. Michel and H.G. Wagner. Shock waves and matter. *Die Naturwissenschaften*, 58(2): 65–77, February 1971. ISSN 0028-1042.

A. Mocker. Optimierung der Strahlfokussierung am Heidelberger Staubbeschleuniger. Master's thesis, Ruprecht-Karls-Universität Heidelberg, 2001.

G. E. Morfill and E. Grün. The motion of charged dust particles in interplanetary space. I - The zodiacal dust cloud. II - Interstellar grains. *Planet. Space Sci.*, 27:1269–1292, October 1979. doi: 10.1016/0032-0633(79)90105-3.

E.V. Moskovets. Optimization of the reflecting system parameters in the mass-reflectron. *Applied Physics B (Photophysics and Laser Chemistry)*, B53(4):253–9, October 1991. ISSN 0721-7269.

T. Mothé-Diniz, F. Roig, and J. M. Carvano. Reanalysis of asteroid families structure through visible spectroscopy. *Icarus*, 174:54–80, March 2005. doi: 10.1016/j.icarus.2004.10.002.

F. Müller. Aufbau und erste Messungen zur Simulation von Staubteilchen-Einschlagsionisation durch kurze Laserpulse. Master's thesis, Universität Heidelberg, 2004.

T. Müller, B.K. Sinha, and K.P. Rohr. Direction-selective free expansion of laser-produced plasmas from planar targets. *Physical Review E (Statistical, Nonlinear, and Soft Matter Physics)*, 67(2):26415–1–8, February 2003. ISSN 1063-651X.

P. Mulser, R. Sigel, and S. Witkowski. Plasma production by laser. *Physics Reports*, 6:187–239, January 1973. doi: 10.1016/0370-1573(73)90005-7.

K. Nagel and H. Fechtig. Diameter to depth dependence of impact craters. *Planet. Space Sci.*, 28:567–569, June 1980.

K. Nagel, G. Neukum, G. Eichhorn, H. Fechtig, O. Mueller, and E. Schneider. Dependencies of microcrater formation on impact parameters. In *Lunar and Planetary Science Conference Proceedings*, volume 6 of *Lunar and Planetary Science Conference Proceedings*, pages 3417–3432, 1975.

J.I. Øren. Initial energy and angle distribution of ions generated at hypervelocity impacts. Technical report, ESTEC, 2001.

F. Postberg, S. Kempf, R. Srama, S. F. Green, J. K. Hillier, N. McBride, and E. Grün. Composition of jovian dust stream particles. *Icarus*, 183:122–134, July 2006. doi: 10.1016/j.icarus.2006.02.001.

F. Postberg, S. Kempf, D. Rost, T. Stephan, R. Srama, M. Trieloff, A. Mocker, and M. Goerlich. Discriminating contamination from particle components in spectra of Cassini's dust detector CDA. *Planet. Space Sci.*, 57:1359–1374, October 2009a. doi: 10.1016/j.pss.2009.06.027.

F. Postberg, S. Kempf, J. Schmidt, N. Brilliantov, A. Beinsen, B. Abel, U. Buck, and R. Srama. Sodium salts in E-ring ice grains from an ocean below the surface of Enceladus. *Nature*, 459:1098–1101, June 2009b. doi: 10.1038/nature08046.

G.J. Price and G.W. Fraser. Calculation of the output charge cloud from a microchannel plate. *Nuclear Instruments & Methods in Physics Research, Section A (Accelerators, Spectrometers, Detectors and Associated Equipment)*, 474(2):188–96, 1 December 2001. ISSN 0168-9002.

Yu.P. Raizer. Residual ionization of a gas expanding in vacuum. *Zhurnal Eksperimental'noi i Teoreticheskoi Fiziki*, 37(2(8)):580–582, Aug 1959.

P.R. Ratcliff and F. Allahdadi. Characteristics of the plasma from a 94 km s/sup -1/ microparticle impact. In *Advances in Space Research*, volume 17, pages 87–91, June 1996.

P.R. Ratcliff, M. Reber, M.J. Cole, T.W. Murphy, and K. Tsembelis. Velocity thresholds for impact plasma production. In *Advances in Space Research*, volume 20, pages 1471–6, 1997 1997.

J.F. Ready. Development of plume of material vaporized by giant pulse laser. *Applied Physics Letters*, 3(1):11–13, 1 July 1963.

D. Rogers and R.F. Malina. Optimization of the performance of a tandem microchannel plate detector as a function of interplate spacing and voltage. *Review of Scientific Instruments*, 53 (9):1438–41, September 1982. ISSN 0034-6748.

K. Rohr and S.N. Srivastava. Scaling law of angular emission distributions of laser ablated particle pulses from monoatomic and compound targets. *Nuclear Instruments & Methods in Physics Research, Section B (Beam Interactions with Materials and Atoms)*, 237(3-4): 497–506, August 2005. ISSN 0168-583X.

M. Ross. Matter under extreme conditions of temperature and pressure. *Reports on Progress in Physics*, 48:1–52, January 1985. doi: 10.1088/0034-4885/48/1/001.

V. Rudolph. Massen-Geschwindigkeitsfilter für künstlich beschleunigten Staub. *Zeitschrift für Naturforschung A (Astrophysik, Physik und Physikalische Chemie)*, 21:1993–+, November 1966.

V. Rudolph. Untersuchungen an Kratern von Mikroprojektilen im Geschwindigkeitsbereich von 0,5 bis 10 km/sec. *Zeitschrift für Naturforschung A (Astrophysik, Physik und Physikalische Chemie)*, 24:326–+, March 1969.

Richard E. Russo. Laser ablation. *Appl. Spectrosc.*, 49(9):14A–28A, 1995.

R. Z. Sagdeev, J. Kissel, E. N. Evlanov, M. N. Fomenkova, N. A. Inogamov, V. N. Khromov, G. G. Managadze, O. F. Prilutski, V. D. Shapiro, I. Y. Shutyaev, and B. V. Zubkov. The Dependence of Mass Resolution and Sensitivity of the PUMA Instrument on the Energy Spread of Ions Produced by Hypervelocity Impacts. *Astron. Astrophys.*, 187:179–+, November 1987.

P. Schagen. *Advances in image pick-up and display*, volume 1. Academic Press, New York, 1974.

V. Schlemmer. Design and Fabrication of a Mass Spectrometer for Space-Related Applications. Master's thesis, TU Braunschweig, 2008.

Z. Sekanina. *Cometary Dust*, pages 95–161. Springer-Verlag, 2001.

H. Shelton, C.D. Hendricks, and R.F. Wuerker. Electrostatic acceleration of microparticles to hypervelocities. *Journal of Applied Physics*, 31(1):1243–1246, 1960.

A. E. Siegman. *Lasers*. University Science Books, 1986. ISBN 0935702113.

P.B. Soul. Operational properties of channel-plate electron multipliers. *Nuclear Instruments and Methods*, 97(3):555–65, 15 December 1971. ISSN 0029-554X.

L. Spitzer. *Physics of fully ionized gases*. Dover Publications, 2006.

R. Srama. *Kombination von Messsystemen zur simultanen Messung der Eigenschaften von kosmischen Staub*. PhD thesis, Technische Universität München, Garching, 2000.

R. Srama. Cassini-Huygens and Beyond - Tools for Dust Astronomy. Habilitationsschrift, Universität Stuttgart, 2010.

R. Srama and Auer. S. Low-charge detector for the monitoring of hyper-velocity micron-sized dust particles. *Measurement Science and Technology*, 19(5):055203, 2008.

R. Srama, T. J. Ahrens, N. Altobelli, S. Auer, J. G. Bradley, M. Burton, V. V. Dikarev, T. Economou, H. Fechtig, M. Görlich, M. Grande, A. Graps, E. Grün, O. Havnes, S. Helfert, M. Horányi, E. Igenbergs, E. K. Jessberger, T. V. Johnson, S. Kempf, A. V. Krivov, H. Krüger, A. Mocker, G. Moragas-Klostermeyer, P. Lamy, M. Landgraf, D. Linkert, G. Linkert, F. Lura, J. A. M. McDonnell, D. Möhlmann, G. E. Morfill, M. Müller, M. Roy, G. Schäfer, G. Schlotzhauer, G. H. Schwehm, F. Spahn, M. Stübig, J. Svestka, V. Tschernjawski, A. J. Tuzzolino, R. Wäsch, and H. A. Zook. The Cassini Cosmic Dust Analyzer. *Space Science Reviews*, 114:465–518, September 2004a. doi: 10.1007/s11214-004-1435-z.

R. Srama, A. Srowig, M. Rachev, E. Grün, S. Auer, T. Conlon, A. Glasmachers, D. Harris, S. Helfert, S. Kempf, H. Linnemann, G. Moragas-Klostermeyer, and V. Tschernjawski. Development of an Advanced Dust Telescope. *Earth Moon and Planets*, 95:211–220, December 2004b. doi: 10.1007/s11038-005-9040-z.

R. Srama, M. Rachev, A. Srowig, V. Dikarev, S. Helfert, S. Kempf, D. Linkert, G. Moragas-Klostermeyer, and E. Grün. Performance of an Advanced Dust Telescope. In D. Danesy, editor, *4th European Conference on Space Debris*, volume 587 of *ESA Special Publication*, pages 171–+, August 2005.

M. Sremčević, A. V. Krivov, H. Krüger, and F. Spahn. Impact-generated dust clouds around planetary satellites: model versus Galileo data. *Planet. Space Sci.*, 53:625–641, May 2005. doi: 10.1016/j.pss.2004.10.001.

Z. Sternovsky, K. Amyx, G. Bano, M. Landgraf, M. Horányi, S. Knappmiller, S. Robertson, E. Grün, R. Srama, and S. Auer. Large area mass analyzer instrument for the chemical analysis of interstellar dust particles. *Review of Scientific Instruments*, 78(1):014501–+, January 2007. doi: 10.1063/1.2431089.

B. C. Stuart, M. D. Feit, A. M. Rubenchik, B. W. Shore, and M. D. Perry. Laser-Induced Damage in Dielectrics with Nanosecond to Subpicosecond Pulses. *Physical Review Letters*, 74:2248–2251, March 1995. doi: 10.1103/PhysRevLett.74.2248.

M. Stübig, G. Schäfer, T.-M. Ho, R. Srama, and E. Grün. Laboratory simulation improvements for hypervelocity micrometeorite impacts with a new dust particle source. *Planet. Space Sci.*, 49:853–858, July 2001.

A.A. Sysoev, V.P. Ivanov, T.V. Barinova, Yu.A. Surkov, and V.V. Vysochkin. Mass spectra formation from charged microparticles. *Nuclear Instruments & Methods in Physics Research, Section B (Beam Interactions with Materials and Atoms)*, 122(1):79–83, January 1997. ISSN 0168-583X.

L. H. Thomas. The calculation of atomic fields. In *Proceedings of the Cambridge Philosophical Society*, volume 23 of *Proceedings of the Cambridge Philosophical Society*, pages 542–+, 1927. doi: 10.1017/S0305004100011683.

J.J. Thomson. On the appearance of helium and neon in vacuum tubes. *Nature*, 90(2259):645 – 647, 1913.

R. J. Trumpler. Preliminary results on the distances, dimensions and space distribution of open star clusters. *Lick Observatory Bulletin*, 14:154–188, 1930.

I. Čermák. *Laboruntersuchung elektrischer Aufladung kleiner Staubteilchen*. PhD thesis, Univerität Heidelberg, 1994.

M. von Allmen. *Laser-Beam Interactions with Materials: Physical Principles and Applications*. Springer series in Materials Science 2. Springer-Verlag, 1987.

L. Vočadlo, J.P. Poirer, and G.D. Price. Grüneisen paramters and isothermal equation of state. *American Mineralogist*, 85:390–395, 2000.

S. J. Weidenschilling. Formation of Planetesimals and Accretion of the Terrestrial Planets. *Space Sci. Rev.*, 92:295–310, April 2000. doi: 10.1023/A:1005259615299.

E. C. Whipple. Potentials of surfaces in space. *Reports on Progress in Physics*, 44:1197–1250, November 1981.

D. Whittet. The Composition of Dust in Stellar Ejects. In L. J. Allamandola & A. G. G. M. Tielens, editor, *Interstellar Dust*, volume 135 of *IAU Symposium*, pages 455–+, 1989.

P. R. Willmott and J. R. Huber. Pulsed laser vaporization and deposition. *Reviews of Modern Physics*, 72:315–328, January 2000. doi: 10.1103/RevModPhys.72.315.

M. Witte, H. Rosenbauer, M. Banaszkiewicz, and H. Fahr. The ULYSSES neutral gas experiment - Determination of the velocity and temperature of the interstellar neutral helium. *Advances in Space Research*, 13:121–130, June 1993. doi: 10.1016/0273-1177(93)90401-V.

J.L. Wiza. Microchannel plate detectors. *Nuclear Instruments and Methods*, 162(1-3):587–601, 1-15 June 1979. ISSN 0029-554X.

J.L. Wiza, P.R. Henkel, and R.L. Roy. Improved microchannel plate performance with a resistive anode encoder. *Review of Scientific Instruments*, 48(9):1217–18, September 1977. ISSN 0034-6748.

I. Wojciechowski. Emission of ionic water clusters from water ice films bombarded by energetic projectiles. *Applied Surface Science*, 231:72–77, June 2004. doi: 10.1016/j.apsusc.2004.03.036.

Ya. B. Zel'dovich and Yu. P. Raizer. *Physics of Shock Waves and High-Temperature Hydrodynamic Phenomena*. Dover Publications, mar 2002. ISBN 0486420027.

S. Zhukovska, H.-P. Gail, and M. Trieloff. Evolution of interstellar dust and stardust in the solar neighbourhood. *Astron. Astrophys.*, 479:453–480, February 2008. doi: 10.1051/0004-6361:20077789.

Acknowledgments

I am indebted to so many people for their long-lasting support and encouragement which was invaluable for the successful completion of this work. First and foremost I want to thank the holy trinity, who guided and supervised on this long, windy and interesting road to my PHD:

Prof. Dr. Eberhard Grün for giving me this interesting and challenging task, his patience and his incitements.
Dr. Ralf Srama for believing in me, encouraging me and giving me the opportunity to resume the work on my thesis.
Prof. Dr. Sascha Kempf for his endless help and support. Thank you so much for being such a great mentor - you are an amazing source of inspiration.

I thank Prof. Dr. Mario Trieloff for providing and preparing the silicate samples used as targets.
I am deeply thankful to Dr. Klaus Hornung for all the enlightening discussions about impact ionisation and his encouragement through all this time.

Furthermore, I like to thank those, who helped and supported me with the design and construction of *BERTA*:
Mr. Gerhard Schäfer for his enthusiastic support and for sharing his treasure of experience, my brother-in-law Marko for constructing *BERTA*'s Mercedes-Benz of racks.
Many thanks to the electronic engineers Mr. Matt and Mr. Baust for their help and support, and to Sebastian and Tobi Mellert for helping me to bring *BERTA* to life again. As simple as this instrument was, it had its flaws and quirks. Dr. Siegfried Auer and Zoltán Sternovsky helped me enormously with their experience and their hints and tricks to get the grips with *BERTA*'s MCP.
This work took some time and i want to thank all those who accompanied me through these years:

My colleagues Nico, Jessica, Frank, Sean and Uwe for the great time and for the fun it was to work with you.
I thank my former bosses Anke and Frank, not only for offering me a job but also the opportunity to grow and develop myself in ways I had never imagined.
Very special thanks to Dr. Arno Nützel, my boss at Heidelberger Druckmaschinen AG, for believing in me finishing this work when i had no faith at all and the whole rest of Appl-Spezi-Gang for letting me have great times as the little one in an amazing team.

Thank you, Sir Jon K. Hillier, for the awesome discussions and your companionship in my struggles with the English language (The battle is not yet won). Thank you for being such a great friend and most of all, thank you for showing me your beautiful slippers! It is good to know, that pink and orange are your clan colours.
To my lab crew, Katherina, Sebastian, and Katharina, thank you for being such great friends and colleagues, thank you for being there for me and truly taking me as i am. It is amazing how much our little cosy hole in the ground became my home because of you guys. And of course, Katherina, thank you for introducing me to the pleasures of rock smashing!

The last few months were very challenging and the road was sometimes a little bit bumpy. I thank my friends Katrin, Uwe, Stefan, Christiane, Sanja, Michal, and Jens - for being there for me and and support me in many ways.

Anke and Sascha, thank you for incredibly generous hospitality and support - and Hannah Lotte and Jonas for being the best neighbours one can imagine.

At last I want to thank Brigitte and Rolf, who are always there for me and to whom this work is dedicated.

A. Shock waves in solids

In a gas the pressure is of thermal origin. It is related to the transfer of momentum by its atoms or molecules participating in the thermal motion and the pressure is proportional to the temperature

$$p = nkT. \tag{A.1}$$

The behaviour of condensed matter with respect to a compression is different because the atom or molecules are much closer together and interact strongly. In absence of an external pressure the equilibrium distances of atoms in a sold correspond to the mutual compensation between attractive and repulsive forces in the lattice.
To compress a solid the repulsive forces have to be overcome, these forces will increase rapidly as the atoms are brought together. The compressibility of a solid is defined by

$$\kappa_0 = -\frac{1}{V}\frac{\partial V}{\partial p} \tag{A.2}$$

and will decrease with increasing pressure.
A compression of a condensed medium will generate an internal pressure and increase n internal energy, which have two components (Zel'dovich and Raizer, 2002):

- the elastic component $\mathbf{p_c}$ or $\varepsilon_\mathbf{c}$, which is related to the interaction between the atoms and is independent of the temperature. This elastic, non-thermal component determines the basic features
- the thermal component $\mathbf{p_t}$ or $\varepsilon_\mathbf{t}$ which heats the material very strongly

As the shock strength is increasing, the relative importance of the thermal pressure increases and for extremely strong shock waves the initially solid media behaves like a gas Zel'dovich and Raizer (2002).

A.1. Elastic component - Compression of a cold material

The elastic pressure $\mathbf{p_c}$ and elastic internal energy $\varepsilon_\mathbf{c}$ depend only on the density ρ and the specific Volume$\mathbf{V} = \frac{\mathbf{1}}{\rho}$ and are equal to the total pressure and energy at zero temperature.

As one can see in figure the interaction forces fall of rapidly as the distances between the atoms increases this leads to the fact, that for increasing Volume the potential energy increases asymptotically to a constant value U. This is the binding energy in the body which is approximately equal to the heat of vaporization of the body. Because binding forces weaken at

distances of the order of the dimensions of an atomic cell, the elastic internal energy $\varepsilon_{\mathbf{c}}(\mathbf{V})$ approaches this asymptotic value when the body expands by an order of magnitude. On the other hand repulsive forces dominate when the body is compressed. Then the elastic internal energy increases rapidly.
From the general thermodynamic relation

$$T\,dS = d\varepsilon + p \cdot dV \qquad \text{and for} T = 0 \Rightarrow S = 0 \,(\text{Nernt's Theorem}) \tag{A.3}$$

follows the relation of elastic pressure and potential energy.

$$p_c = -\frac{d\varepsilon_c}{dV} \tag{A.4}$$

This can be regarded as the isotherm and isotrope of cold compression and has the meaning, that the variation of the potential energy is equal to the work of compression.

The slope of the cold compression curve for the internal pressure $\mathbf{p_c}$ determines the speed of elastic waves in the body which is the speed of the sound in the material. Theoretical calculations of cold compression curves are based on quantum mechanical considerations of interatomic interaction. These models are limited for the cases with very strong compression, because there the electronic shells of the atoms lose to some extent their individual structure. The state of the material in this cases can approximately be described by the Thomas-Fermi statistical model or (somewhat more exactly) by the Thomas-Fermi-Dirac model, which is a statistical and semi-classical approach to that problem. The contribution of the nuclei to the thermal state is that of an ideal gas with with translational degrees of freedom. The classical part describes the Z-fold charged nucleus as sourrounded by z electrons which lie in a sphere with $R_0 = \sqrt[3]{\frac{3}{4\pi n}}$, where n is the atomic number density. The non classical part concerns the occupation of the continuous energy states of the electrons by Fermi-Dirac statistics. The accuracy of this model increases with density and temperature and decreases for smaller Z.

A.2. Thermal component

A.2.1. Thermal motions of atoms

There are a definite pressure $\mathbf{p_t}$ and a definite energy $\varepsilon_{\mathbf{t}}$ connected to the thermal morion of the atoms. As a start the electronical contribution will be neglected for the following considerations: only at above 10.000 K thermal excitation of the electrons plays an important role. Also the effect of the melting process will be neglected, because - since the heat of fusion is comparatively small - melting is not important from the energy point of view.

Moderate Temperatures The thermal motion is a harmonic oscillation of the atoms as long the amplitudes of the oscillation are much smaller than the interatomic distances or as long as the vibrational energy $\varepsilon_{\mathbf{vib}} \sim \mathbf{kT}$ is less than the height of the potential barrier which keeps the atoms at their places in the lattice. The harmonic vibration leeds to the specific heat $\mathbf{c_v} = \mathbf{3k}$ for each atom or $\mathbf{c_v} = \mathbf{3Nk}$ for the ensemble of N atoms.

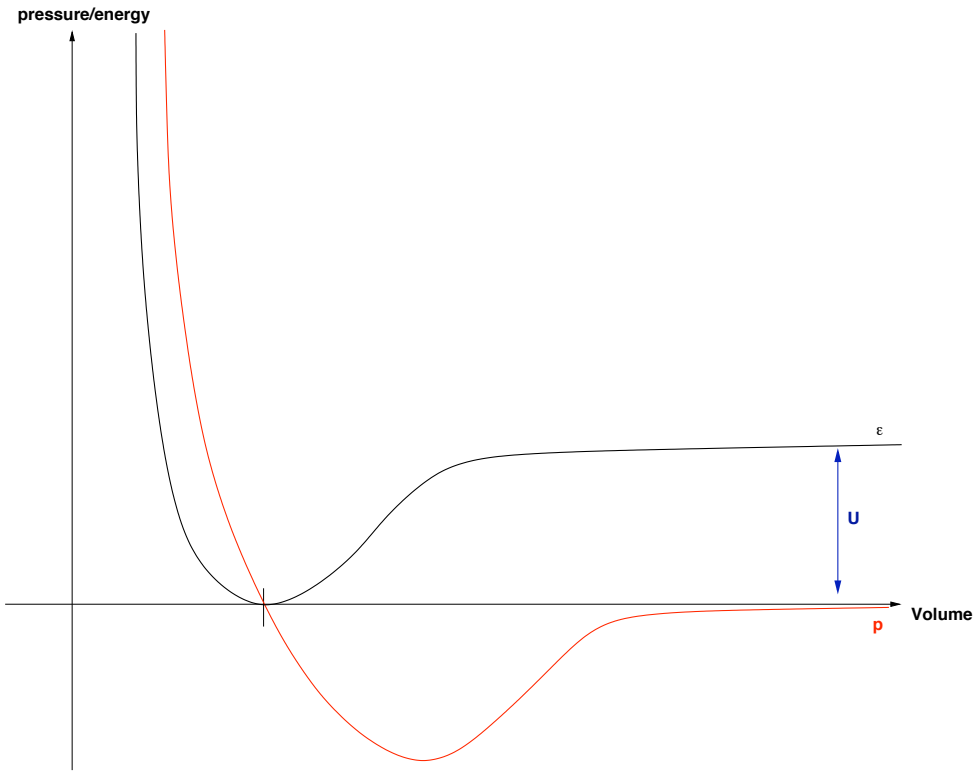

Figure A.1.: Potential energy and elastic curves of a solid body as function of the specific volume

For low temperatures $\mathbf{T} <\sim \mathbf{100K}$ one has to take into account the quantum effects to describe the thermal energy connected with vibrations

$$\begin{aligned} \varepsilon_t &= c_v(T-T_0)+\varepsilon_0 \qquad \text{with}\, c_v = 3Nk \\ \text{where} \quad \varepsilon_0 &= \int_0^{T_0} c_v(T)dT \quad \text{is the thermal energy at room temperature} \end{aligned} \tag{A.5}$$

If $\mathbf{T} \gg \mathbf{T_0}$ the difference between $\boldsymbol{\varepsilon_0}$ and $\mathbf{c_v T}$ becomes negligible and the internal thermal energy simplifies to

$$\varepsilon_t = c_v T \qquad \text{with}\, c_v = 3Nk \tag{A.6}$$

Higher Temperatures For sufficiently high temperatures the atoms are almost completely free to move within the body, so the thermal motion loses its oscillatory character and becomes random and akin to that in a gas. The substance is tranformed into a dense gas of strongly interacting atoms.
In this case the specific heat $\mathbf{c_v} = \frac{\mathbf{3}}{\mathbf{2}}\mathbf{Nk}$ corresponds to the transitional degrees of freedom.
The transition from vibrational to translational motion of the atoms and the corresponding decrease of the the specific heat

$$c_v = 3Nk \qquad \rightarrow \qquad c_v = \frac{3}{2}Nk$$

occurs gradually in range of temperatures for which the kinetic energy of the atoms

$$\varepsilon_k = \frac{3}{2}kT$$

is of the order of the height of the potential barrier against the free motion of the atoms within the body.

$$\frac{3}{2}kT \approx \frac{\Delta U}{N}$$

The boundary between this regions can be defined by the threshhold temperature

$$T_k = \frac{2}{3}\frac{\Delta U}{kN} \tag{A.7}$$

with (A.8)

$$c_v = \begin{cases} 3Nk & \text{for} \quad T < T_k \\ \frac{3}{2}Nk & \text{for} \quad T > T_k \end{cases}$$

Additional Compression If the heated material is additional compressed the potential barrier is sharply increased by the repulsive forces between the atoms. Thus no more free deplacement is possible and the thermal motion becomes again oscillatory. With some rough approximation the thermal motion of the atoms in a compressed material can be regarded as small vibrations even at temperatures of 20.000 to 30.000K.

Equation of State for a material with small vibration of its atoms If the temperature is not to high and the contribution by the excitation of the electrons can be neglected the equation of state can be written as

$$\begin{aligned} p &= p_c(V) + p_t(T,V) \\ \varepsilon &= \varepsilon_c(V) + \varepsilon_t(T,V) \\ \varepsilon &= \varepsilon_c(V) + 3NkT \end{aligned} \tag{A.9}$$

The temperature dependence of the thermal pressure can be derived from the general thermodynamic identity,

$$\left(\frac{\partial \varepsilon}{\partial V}\right)_T = T \cdot \left(\frac{\partial p}{\partial T}\right)_V - p \tag{A.10}$$

the relation of elastic pressure and elastic internal energy $p_c = -\frac{d\varepsilon_v}{dV}$ in combination with the equation of state above (A.9) and the fact that $c_v = 3NkT$ is independent of the volume:

$$\begin{aligned} \left(\frac{\partial}{\partial V}\left(\varepsilon_c(V) + 3NkT\right)\right)_T &= T\left(\frac{\partial}{\partial T}\left(p_c(v) + p_T(T,V)\right)\right)_V - p_c(V) - p_T(T,V) \\ \underbrace{\left(\frac{\partial \varepsilon_c(V)}{\partial V}\right)_T}_{=-p_c} + \underbrace{\left(\frac{\partial (3NkT)}{\partial V}\right)_T}_{=0} &= \underbrace{T\left(\frac{\partial p_c(V)}{\partial T}\right)_V}_{=0} + T\left(\frac{\partial p_t(T,V)}{\partial T}\right)_V - p_c(V) - p_t(T,V) \\ \Rightarrow \quad p_t &= \left(\frac{\partial p_t}{\partial T}\right)_V \cdot T \end{aligned} \tag{A.11}$$

$$\Rightarrow \quad p_t = \varphi(V) \cdot T \tag{A.12}$$

The ratio of thermal pressure and thermal energy is represented by the Grüneisen coefficient $\Gamma(V)$.

$$p_t = \Gamma(V)\frac{c_v T}{V} = \Gamma(V)\frac{\varepsilon_t}{V} \tag{A.13}$$

For a body at the standard volume $V_0(T=0)$ the Grüneisen coefficient $\Gamma_0 = \Gamma(V_0)$ is related to other properties of the material through the thermodynamic relation

$$\left(\frac{\partial p}{\partial T}\right)_V \left(\frac{\partial T}{\partial V}\right)_p \left(\frac{\partial V}{\partial p}\right)_T = -1 \tag{A.14}$$

With the definitions for the isothermal incompressibility κ_0 for standard conditions and for coefficient α of thermal expansion at constant pressure

$$\begin{aligned} \kappa_0 &= -\left(\frac{1}{V_0}\right)\left(\frac{\partial V}{\partial p}\right)_T \\ \alpha &= \frac{1}{V_0}\left(\frac{\partial V}{\partial T}\right)_p \end{aligned}$$

one obtains

$$\Gamma_0 = \frac{\alpha V_0}{c_v \kappa_0} = \frac{\alpha}{\rho_0 c_0 \kappa_0} = \frac{\alpha c_0^2}{c_v} \tag{A.15}$$

The thermal pressure p_t increases on heating. Thus the total pressure can only be constant if the elastic pressure decreases and becomes negative. This leads to the expansion of the body up to that point when the binding forces holding the atoms in the lattice or the negative pressure will no longer counterbalance the repulsive effect of the positive thermal pressure.

A.2.2. Thermal excitation of electrons

n the simplest model of a metal the outer valence electrons of the atoms are removed and form a free electron gas which is governed by Fermi-Dirac-statistics and which is at absolute zero completely degenerated. This means due to the Pauli principle for the absolute zero point that the electrons occupy the lowest energy states and their kinetic energy does not exceed the Fermi limiting energy.

$$E_0 = \frac{h^2}{8\pi^2 m_e}\left(3\pi^2 n_e\right)^{\frac{2}{3}} \tag{A.16}$$

with the corresponding Fermi temperature $T^* = \frac{E_0}{k}$.
If the temperature of the metal increases the electrons partially move to higher energy states which exceed the Fermi limit and this leads to an increasing of the energy of the electron gas. For temperatures $T \ll T^*$ the energy grows in the order of kT and the number of excited electrons is a fraction or the order $\frac{kT}{E_0}$ of the total electron number. The thermal energy of the electrons per mass unit for temperature $T < 30,0000 - 50,000K$ is found to be

$$\varepsilon_e = \frac{1}{2}\beta T^2 \tag{A.17}$$

where the coefficient β depend on the density of the material and is given by

$$\beta = \beta_0\left(\frac{V}{V_0}^{\frac{2}{3}}\right) \quad \text{with} \quad \beta_0 = \frac{4\pi^4}{(3\pi^2)^{\frac{2}{3}}}\frac{k^2 m_e}{h^2} N_e^{\frac{1}{3}} V_0^{\frac{2}{3}} \tag{A.18}$$

where N_e is the number density of free electrons per mass unit and V_0 is the standard volume.

Also one can define an electronic Grüneisen coefficient and then the electronic pressure is

$$p_e = \Gamma_e \frac{\varepsilon_e}{V} = \frac{1}{2}\frac{\varepsilon_e}{V} \tag{A.19}$$

A.3. Three-term equation of state

The total pressure and and the total internal energy are the sum of elastic, thermal and electronical components:

$$\begin{aligned} \varepsilon &= \varepsilon_c(V) + \varepsilon_t + \varepsilon_e \\ p &= p_c(V) + p_t + p_e \end{aligned} \tag{A.20}$$

where

$$\begin{aligned} \varepsilon_c(V) &= \int_V^{V_{0c}} p_c(V)dV \\ \varepsilon_t &= 3Nk(T - T_0) + \varepsilon_0 \\ \varepsilon_e &= \frac{1}{2}\varepsilon_0 \left(\frac{V}{V_0}^{\frac{1}{2}}\right) T^2 \\ p_t &= \Gamma(V)\frac{\varepsilon_t}{V} \\ p_e &= \frac{1}{2}\frac{\varepsilon_e}{V} \end{aligned} \tag{A.21}$$

A.4. Emergence of shock waves from a free solid surface

Weak shock waves

When a shock wave emerges from a free surface the compressed material expands practical to zero pressure and afterwards a rarefraction wave travels backwards into the material with the speed of the sound that corresponds to that state behind the shock front. Because of that the material acquires additional velocity in the direction of the initial motion of the shock.
Weak shock wave means that the dissipated energy is not sufficient to vaporize or even melt the material, which has the effect that the final volume V_1 of the unloaded material differs only little from the standard volume V_0 of the solid. On the other hand for the following the shock should be assumed to be strong enough to neglect effects associated with the strength of the solid and the pressure is isentropic as in a gas or a liquid. This Assumption is valid if the pressure is large in comparison with the ultimate strength of the body. For example a weak plane shock wave of constant strength propagates through a solid with the pressure p, material velocity u and the volume $V \overset{<}{\approx} V_0$. The compression is assumed as small ($V_0 - V \ll V_0$), hence the shock can be described by acoustic equations and the velocity of the shock is equal the speed of sound within the material c_0. The relation between material velocity u and pressure p can be written as

$$p = \rho_0 c_0 u \tag{A.22}$$

.

If the shock wave emerges from the free surface of the solid an unloading, also acoustic wave travels back into the material with the speed $c \approx c_0$. Because the pressure across the wave drops from p to zero the material acquires additional speed

$$u' = \frac{-\Delta p}{\rho c} \qquad \text{with} \qquad \Delta p = -p \qquad \text{and} \qquad \rho \approx \rho_0 \tag{A.23}$$

which leads to the final material velocity u_1

$$u_1 = u + u' \approx 2u \tag{A.24}$$

Strong shock waves

If the shock is very strong and the internal energy ε_1 of the heated material exceeds by many times the binding energy U of the atoms - which is the heat of vaporization at T=0K - the material is completely vaporized, when it expands to a low pressure after the shock wave has emerged from the surface. Then the material behaves like a gas during unloading.

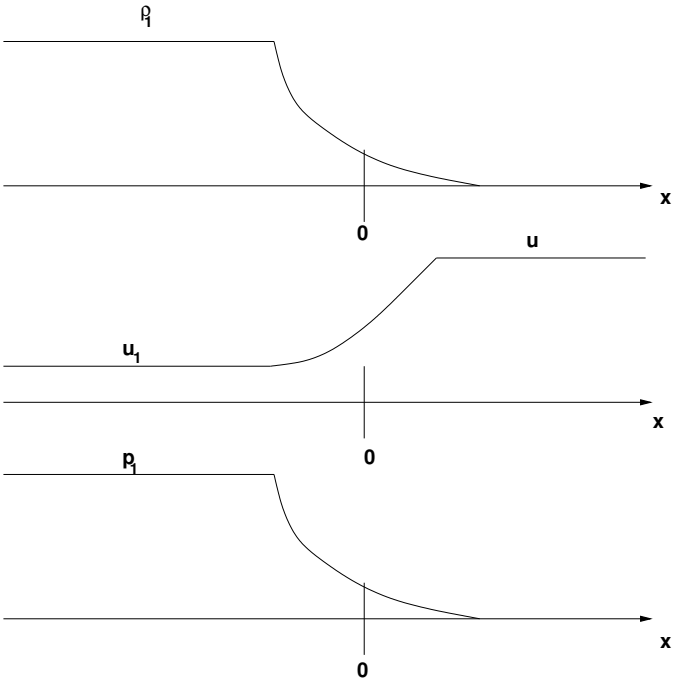

Figure A.2.: Density, velocity and pressure distributions for a strong shock wave emerging on a free surface. In this example the unloading is into a vacuum to strictly zero pressure, so the density and temperature at the leading edge of the material are also equal zero.

B. Micro-channel Plates

A micro-channel plate (*MCP*) is an array of electron multipliers oriented parallel to one another. Each channel can be considered to be a continuous dynode structure.
Typically channels have diameters in the range from 10 to 100 μm and length to diameter ratios (α) between 40 and 100. The channels are typically either normal to the MCP's surface or tilted by an small angle (e.g. 8°).
The matrix consists of lead glass treated in such a way that the characteristics of the secondary electron emission is optimised.The walls are rendered semiconducting to allow charge replenishment from an external voltage source.
Parallel electric contact is provided by the deposition of a metallic costing on front and rear of the MCP, which serves as input and output electrodes. The total resistance between the electrodes is of the order of $10^9\Omega$.

When secondary electrons are emitted from the channel walls by input of particles or radiation, they are accelerated by an electric field generated by a voltage V applied across both sides of the MCP. They travel along parabolic trajectories to strike the opposite wall, thus producing more secondary electrons. This process repeats itself many times along the channel. The result is a large number of electrons released from the output side. Most of the electrical performance characteristics are only a function of the ratio of length to the diameter $L/d = \alpha$ (Wiza, 1979).

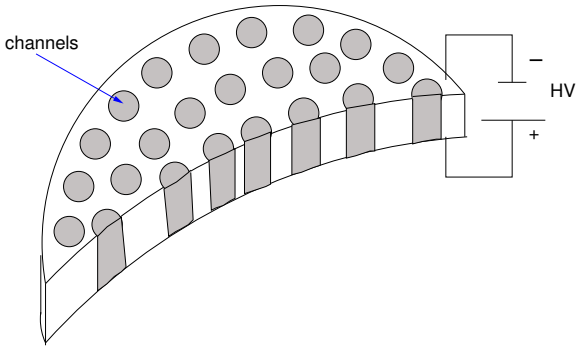

Figure B.1.: Cut-way view through a micro-channel plate

B.1. Theory of operation

B.1.1. The straight channel electron multiplier

Secondary electron emission (SEM)

The performance of a channel multiplier is characterised by the statistical nature of secondary ion emission (Soul, 1971):

- At a fixed incident electron energy E and angle of incident Θ the number of secondary electrons released from a (flat) surface follows an approximate Poisson distribution. Therefore the yield $\delta(E,\Theta)$ is merely the mean value of this distribution.

- At normal incident ($\Theta = 0°$) δ rises with increasing E until a maximum is reached at an impact energy of several hundred eV for most conducting materials, after which the yield decreases again.

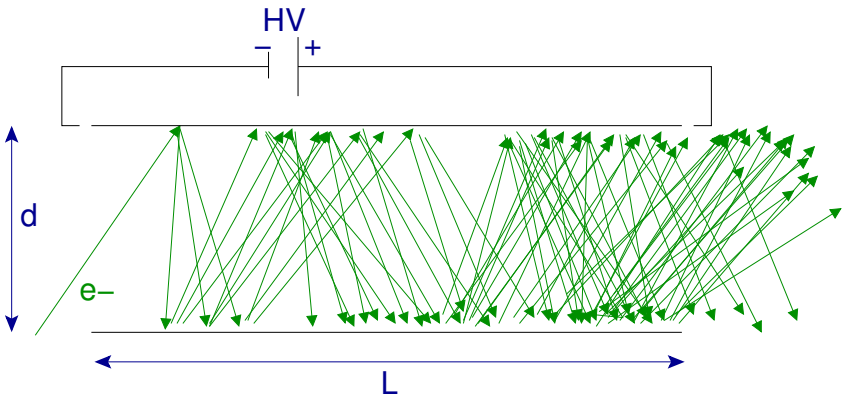

Figure B.2.: Current amplification in a straight channel

Electron trajectories inside the channel

The geometry of an electron trajectory inside a MCP-channel which intersects the channel axis is shown in figure B.3

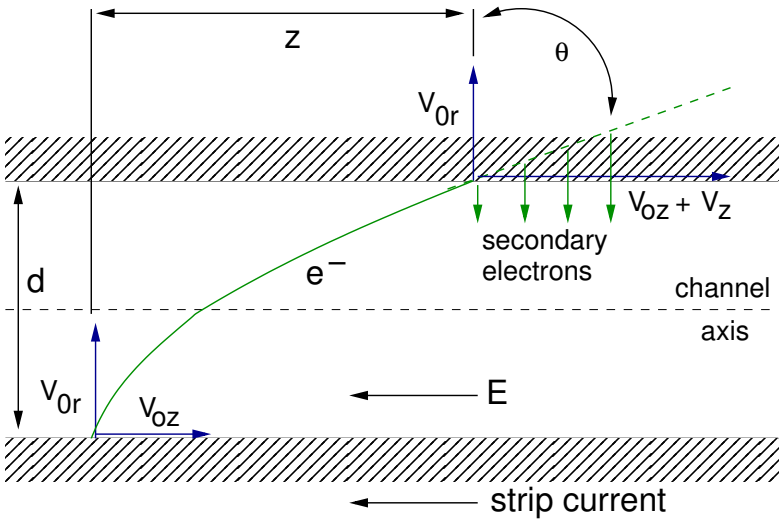

Figure B.3.: Geometry of an electron trajectory in a micro-channel (Eberhardt, 1979)

The axial distance z the electron travels before it hits the opposite wall is given by

$$z = \frac{Ed^2}{4V_{0r}} \cong \frac{Ed^2}{4V_{0r}} \quad \text{for} \quad \sqrt{V_{0r}V_{0z}} \ll V_z \tag{B.1}$$

where e is the electron charge, $e \cdot V_{0z}$ axial emission energy of the electron, $e \cdot V_{0r}$ is the radial emission energy of the electron, $e \cdot V_z$ axial energy gain of the electron during the transit, d the channel diameter, and E is the electric field internal to the channel imposed by the flow of the strip current. Considering a low charge flow the field strength E will as constant and related to V_z and z by

$$E = \frac{V_z}{z} \tag{B.2}$$

Combined with Eq.B.1 this results in

$$z \propto \frac{1}{e \cdot V_{0r}} \tag{B.3}$$

The average displacement $\bar{z}$ for all electrons making up the emission ensemble from a certain point on the channel wall can be described as

$$\bar{z} = \frac{Ed^2}{4\bar{V}_{or}}. \tag{B.4}$$

The sole energy component orthogonal to the channel surface and therefore the sole energy component available for depth penetration is the prior radial emission energy $e \cdot V_{or}$. Therefore no energy is added to the electrons by the applied field E.
The secondary electrons are generated along the penetrating primary electron's path and are traveling from their point of origin to the surface of the channel. On this way there is very little energy-dissipative interaction of the secondary electrons with the channel wall material. Thus the emitted secondary electrons carry a significant fraction of the incident electron: The average radial emission energy $e \cdot \bar{V}_{or}$ is proportional to the bombarding energy $e \cdot \bar{V}_z$

$$\bar{V}_{or} = \frac{\bar{V}_z}{4\beta^2} \tag{B.5}$$

with β being a dimensionless proportionally constant.
With this the average axial displacement $\bar{z}$ between the wall encounters is a constant given by

$$\bar{z} = \frac{1}{2} d \cdot \sqrt{\frac{\bar{V}_z}{\bar{V}_{0r}}} = \beta D, \tag{B.6}$$

Gain calculation

The MCP acts if it were a conventional discrete stage electron multiplier with a fixed number $n = \alpha/\beta = L/(d \cdot \beta)$ of dynodes. Therefore gain of a MCP can be approximated by analogon with the behavior of discrete staged electron multipliers by the power law relationship

$$G = \delta_1 \delta^{n-1} \tag{B.7}$$

where (Eberhardt, 1981)

δ_1 : effective gain per stage for the input electrons
δ^{n-1} : effective gain per stage for the internal cascaded electron multiplication processes

The general shape of $\delta(V_z)$ can usually be approximated by

$$\delta = \left(\frac{V_z}{V_c}^k\right) \qquad \text{and analogously} \tag{B.8}$$

$$\delta_1 = \gamma \cdot \left(\frac{V_{in}+V_z}{V_c}^k\right) \tag{B.9}$$

with V_c being the " first cross-over potential", namely the minimum potential for unity secondary emission ratio is. And $\delta^{n-1}$is the effective gain per stage for the internal cascaded electron multiplication processes.
The secondary emission of electrons is normal to the walls and the gain can be described as (Schagen, 1974):

$$G = \left(\frac{AV}{2\alpha\sqrt{V_0}}\right)^{\frac{2V_0\alpha^2}{V}} \tag{B.10}$$

where

V : total channel voltage
V_0 : initial energy of emitted secondary electrons ($\approx 1eV$)
α : $\frac{L}{d}$
A : proportional constant in the assumed relation $\delta = A\sqrt{V_0}$

Straight channels typically operate at gains of 10^3 - 10^5. The upper limit is set by the onset of **ion feedback**: The probability of producing positive ions by electron collisions with the residual gas and the wall material increases with the electron gain. These ions can drift to the channel input, producing ion pulses. In the case of large single channels ion feedback can be suppressed by bending or twisting the channel.

Response time The average transit time between dynode encounters t_d in a channel multiplier and the total input-output time $n \cdot t_d$ are given by

$$t_d^2 = 2\alpha\beta\frac{md^2}{eV} \tag{B.11}$$

$$(n \cdot t_d)^2 = 2\alpha^3\frac{md^2}{\beta eV} \tag{B.12}$$

Saturation effects in micro-channel plates

There are two types of gain saturation in micro-channels (Giudicotti et al., 1994):

- **Space charge gain saturation** occurs when the accelerating voltage is reduced by the cloud of multiplied electrons moving along the channels.

- **Wall charge gain saturation** occurs when the accelerating axial field along the micro-channel is reduced because the charge extracted from the wall by the previous pulse is not yet completely replenished.

The second type is important in small diameter channels and is the dominant effect in MCPs The current that is flowing through the MCP while excited channels are recharging and that is supplied by the power supply is called **strip current**. If the output current of the MCPS exceeds the strip current not all channels can be recharged effectively until the next projectile will hit the MCP. This causes a **dead time** for the affected channels.

Recharching of the micro-channels

The average axial distance z between wall encounters of electrons is a constant and therefore independent of the applied electric field and the applied voltage between the faces of the MCP. Each incremental length z therefore can be seen as if there were a fixed gap between two bombarded areas. Therefore they can be regarded as dynodes. Each over-all MCP section of the length L with a length-over-diameter ratio $\alpha = L/d$ acts alike a discrete stage electron multiplier with a characteristic number of dynodes:

$$n = \frac{L}{z} = \frac{LD}{Dz} = \frac{\alpha}{\beta} \tag{B.13}$$

The output charge required to supply the output current pulses is stored on the capacitance existing between the channel walls and the external ground potential.

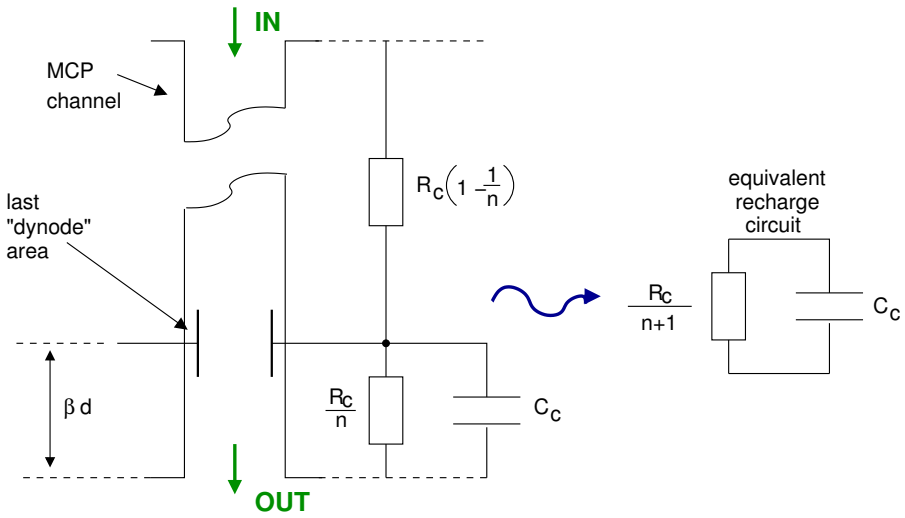

Figure B.4.: Effective Output Configuration (Eberhardt, 1981)

B.1.2. The Chevron

Another more feasible way of suppressing the ion feed back is the so called chevron-MCP. This device consists of of two individual MCPs, which are separated typically by 50 to 150 μm and are individually operated at gains in the 10^4 range. The two plates are oriented to one another in the way that the bias angles (8°/8° or 0°/15°) provide a sufficiently large directional change for preventing positive ions produced on the rear plate to reach the input on the front plate (Wiza et al., 1977).
The plates of the tandem pair can be mounted either in direct contact or separated by an insulator. This allows to apply a potential difference V_d across the gap.

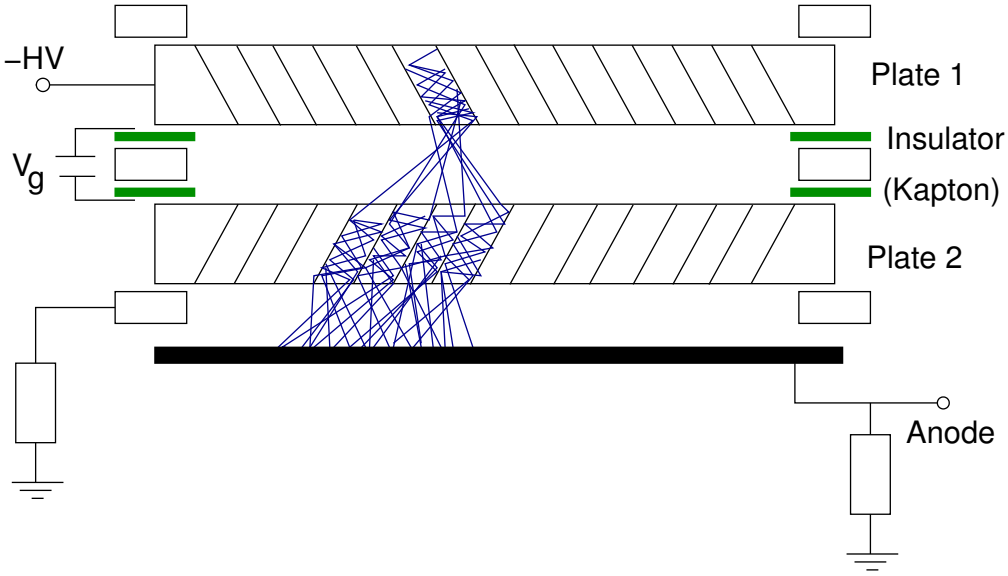

Figure B.5.: Chevron-MCP

The electrons that exit the first plate start a cascade in the next plate by spreading through the gap between the two plates an hitting the second one. The output pulse height distribution over the affected channels show a negative exponential or quasi-gaussian shape.
Important for the optimisation of the performance of a tandem micro-channel plate, such as spatial resolution , the charge gain or the signal-to-noise-ratio is the number of channels of the second stage which are excited by an single channel of the first plate. this number is directly related to the width of the charge cloud impinging the second plate (Rogers and Malina, 1982).
The electron cloud emerging from a single cannel of the first MCP has the size of the average gain of the MCP at the operating voltage . These electrons have an average transverse emission energy of about 0.2 eV for 800 V (Eberhardt, 1980).
Experiments have shown that the cloud distribution is very close to a Gaussian with very narrow wings (Martin and Jelinsky, 1980). If one assumes that the initial energy of the electrons normal to the plate is $E_n = eV_n = 50eV$ (Eberhardt, 1980), the transit time for a electron traveling from one plate to the other will be

$$t = \sqrt{\frac{2m}{e}} \left(\sqrt{V_n + V_g} - \sqrt{V_n} \right) \frac{L}{V_g} \tag{B.14}$$

Because of its transverse energy in this time the average electron will be moved out to a the radius

$$r = v_t \cdot t = t \cdot \frac{2e\sqrt{V_t}}{m} = 2\left(\sqrt{V_n + V_g} - \sqrt{V_n}\right)\frac{L\sqrt{V_t}}{V_g} \tag{B.15}$$

So the width of the electron cloud will be

$$w_c = d + 4 \cdot \left(\sqrt{V_n + V_g} - \sqrt{V_n}\right)\frac{L\sqrt{V_t}}{V_g} \tag{B.16}$$

For low charge densities where space charge effects are neglectable it has been shown that the width of the claud can be described as

So the width of the electron cloud will be

$$w_c = d + \frac{60L}{V_g} \cdot \left(\sqrt{1 + 0.067V_g} - 1\right) \tag{B.17}$$

Thus the result of the inter-plate field is that the available numbers of electrons from emerging from the first stage are concentrated onto fewer channels of the second plate. With increasing input electrons the cascade saturates due to the space charge limit in the channel (Loty, 1971) In order to maintain the maximum gain the inter-plate voltage should be adjusted to permit saturation of the largest possible number of channels. This depends on several factors:

- the gain of the first and of the second plate,
- the size of the gap, and
- the output current, which causes the the second plate to saturate.

The optimized voltage for the maximum gain is given by (Rogers and Malina, 1982):

$$V_{g_{opt}} = \frac{(VL)^2 V_t}{\left(\frac{4g_1g_2}{e\pi\rho S} - d\right)^2} - \frac{8L\sqrt{V_t V_n}}{\sqrt{\frac{4g_1g_2}{e\pi\rho S} - d}} \tag{B.18}$$

where

g_1, g_2	:	unsaturated gains
L	:	gap size
ρ	:	density of channels in the second plate
S	:	maximum number of electrons

(Price and Fraser, 2001)

B.1.3. Optimizing of the MCP adjustments

The MCP used for the *BERTA* instrument is a plate manufactured by Hamamatsu and purchased mounted on a CF100 flange. To operate the device, a power supply circuitry and an amplifier is needed. With the circuitries suggested by the manufacturer, the out put signals showed distinct noise pattern; after sharp, intense pulses like the peak of a hydrogen line, the signal showed oscillations *so-called* ringing. The considerations imply that this damped oscillation may be caused by the recharging of the channels. Thus, the power supply of the potential applied on the plate is of great importance. Figure B.7 shows the optimised wiring, finally achieved after various attempts with a variety of combinations for the resistors and capacitors. This designed reduced the above mentioned ringing significantly(Auer, 2009).

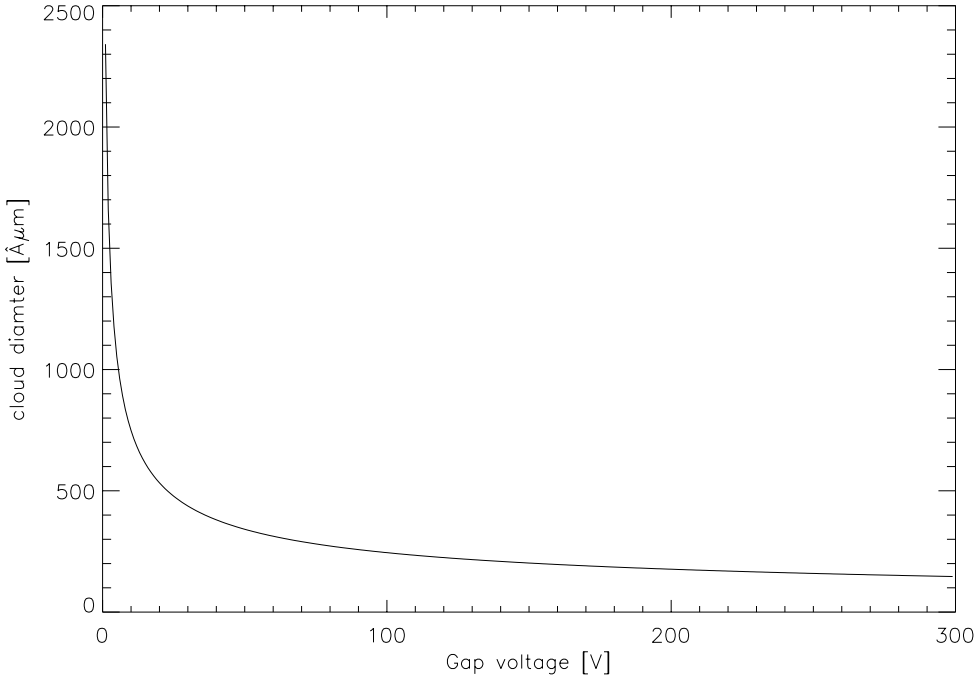

Figure B.6.: Diameter of the charge cloud impinging the second plate

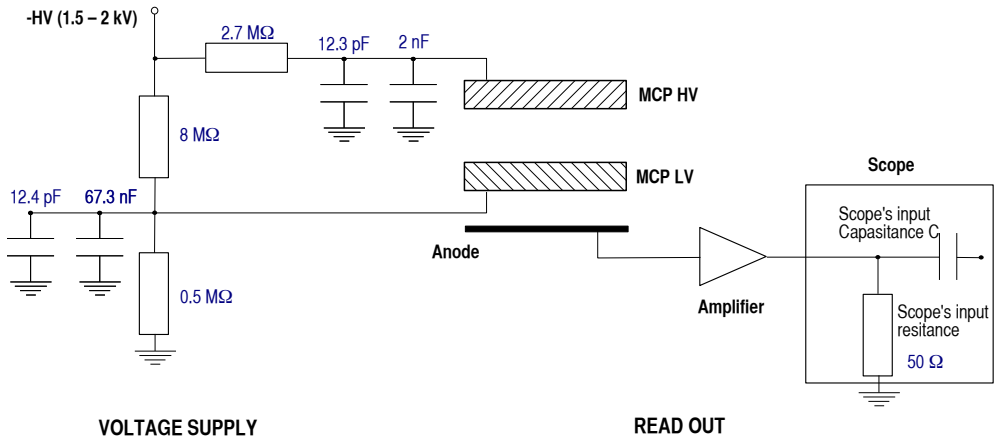

Figure B.7.: Optimised wiring of the MCP

C. Preparation of targets and dust materials

C.1. Cleaning of the targets

The metal targets had been prepared before their mounting in the vacuum chamber as follows:

- 5 min in a ultrasonic bath with acetone for decreasing
- Wiping with a Q-tip drenched in 10% nitric acid
- 3 times of 5 minutes in the ultra-sonic bath with multiple destilled water
- Drying at 80° C

C.2. Overview of the used chemicals

	molecular formula	mass (amu)	boiling point
Cleaning of the metal targets			
Acetone	C_3H_6O	58.08	56°*C* / 330 K
Nitric acid	HNO_3	63.012	83°*C* / 356 K
Destilled water	H_2O	18.02	100°*C* / 212 K

Table C.1.: Used chemicals for the target and dust material preparation

D. Data

D.1. Overview of the particle impact measurements

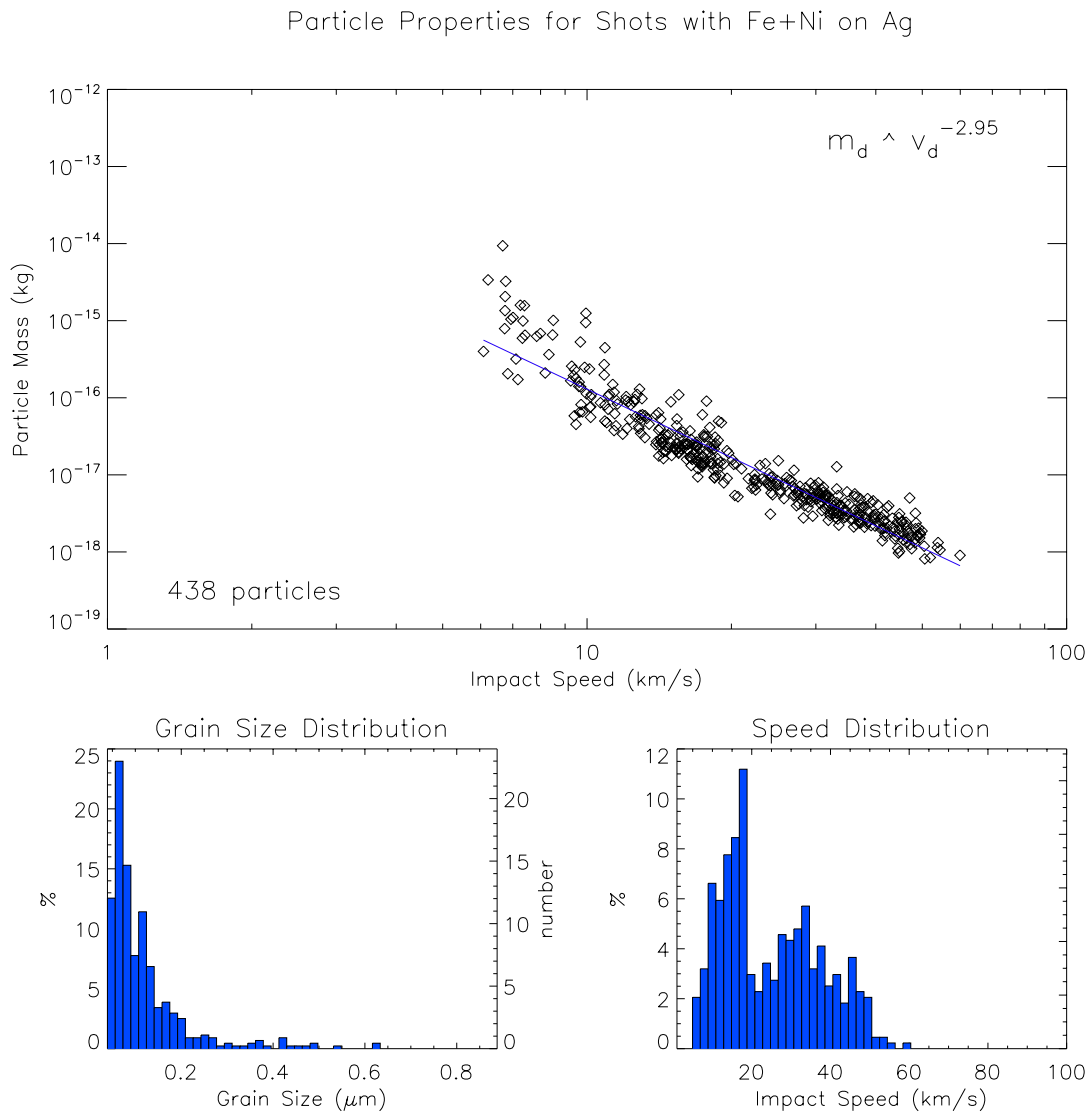

Figure D.1.: Particle properties for shots with Fe+Ni on Ag (*BERTA*).

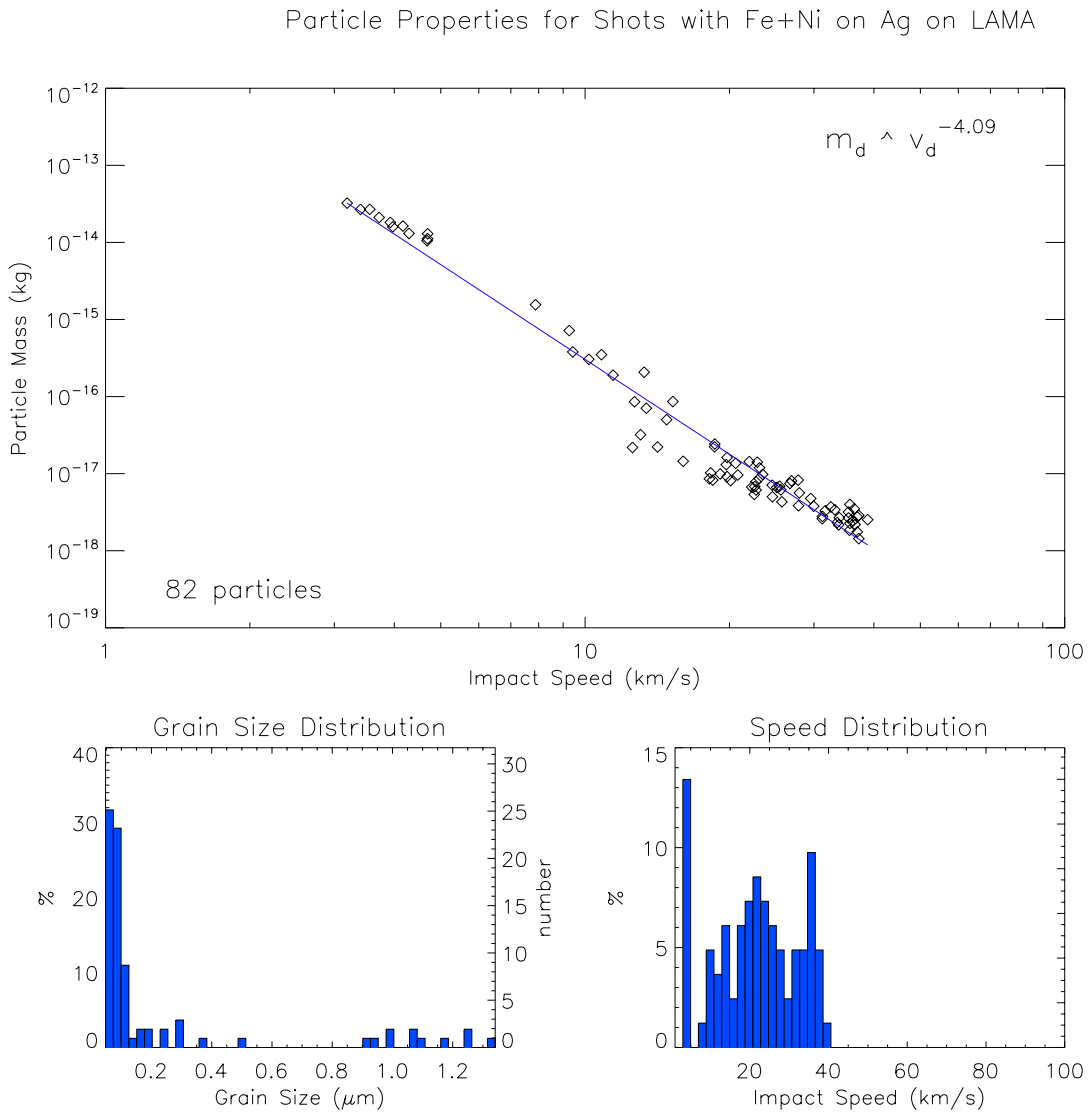

Figure D.2.: Particle properties for shots with Fe+Ni on Ag (*LAMA*).

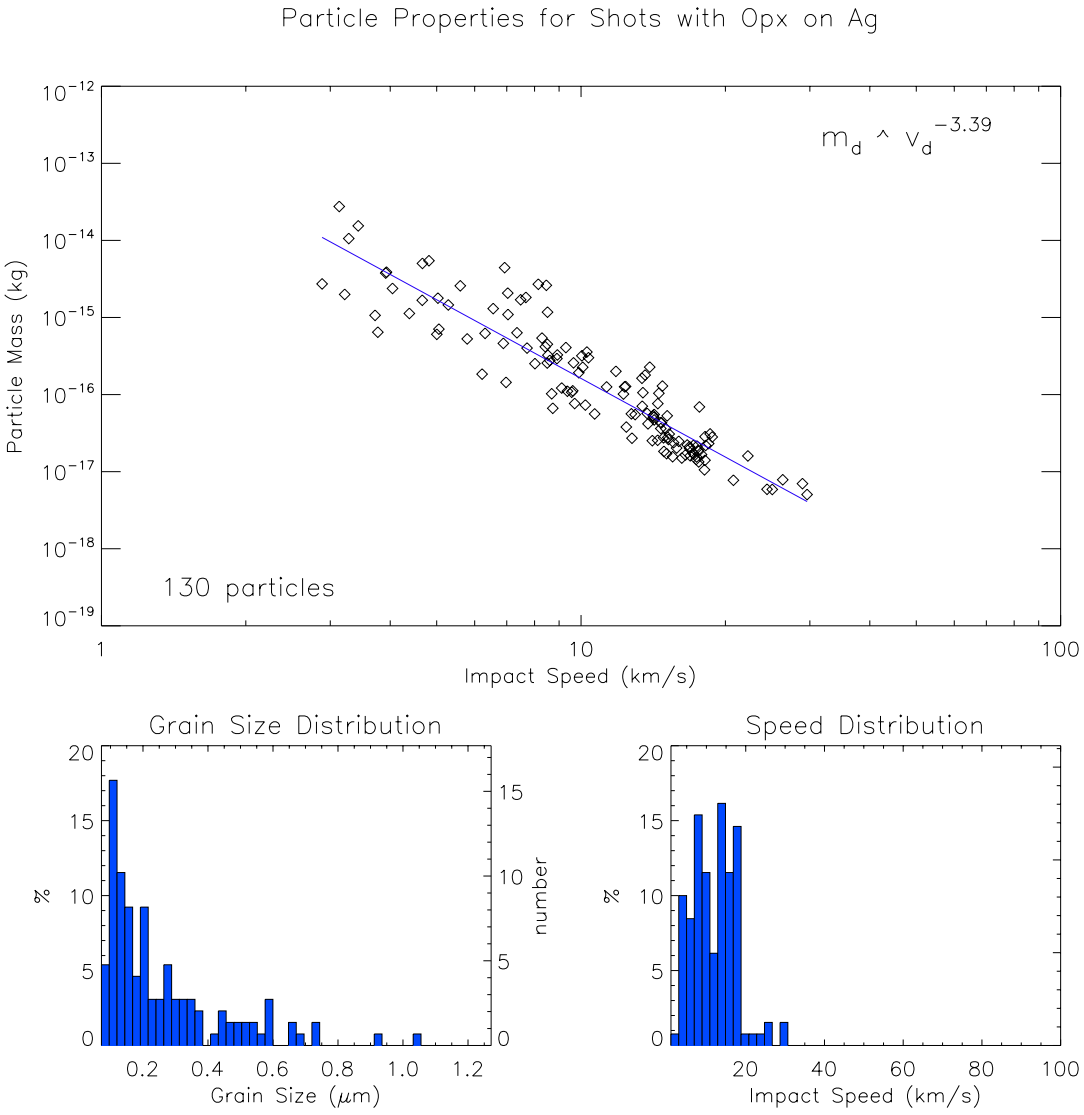

Figure D.3.: Particle properties for shots with platinum-doted Orthopyroxene on Ag (*BERTA*).

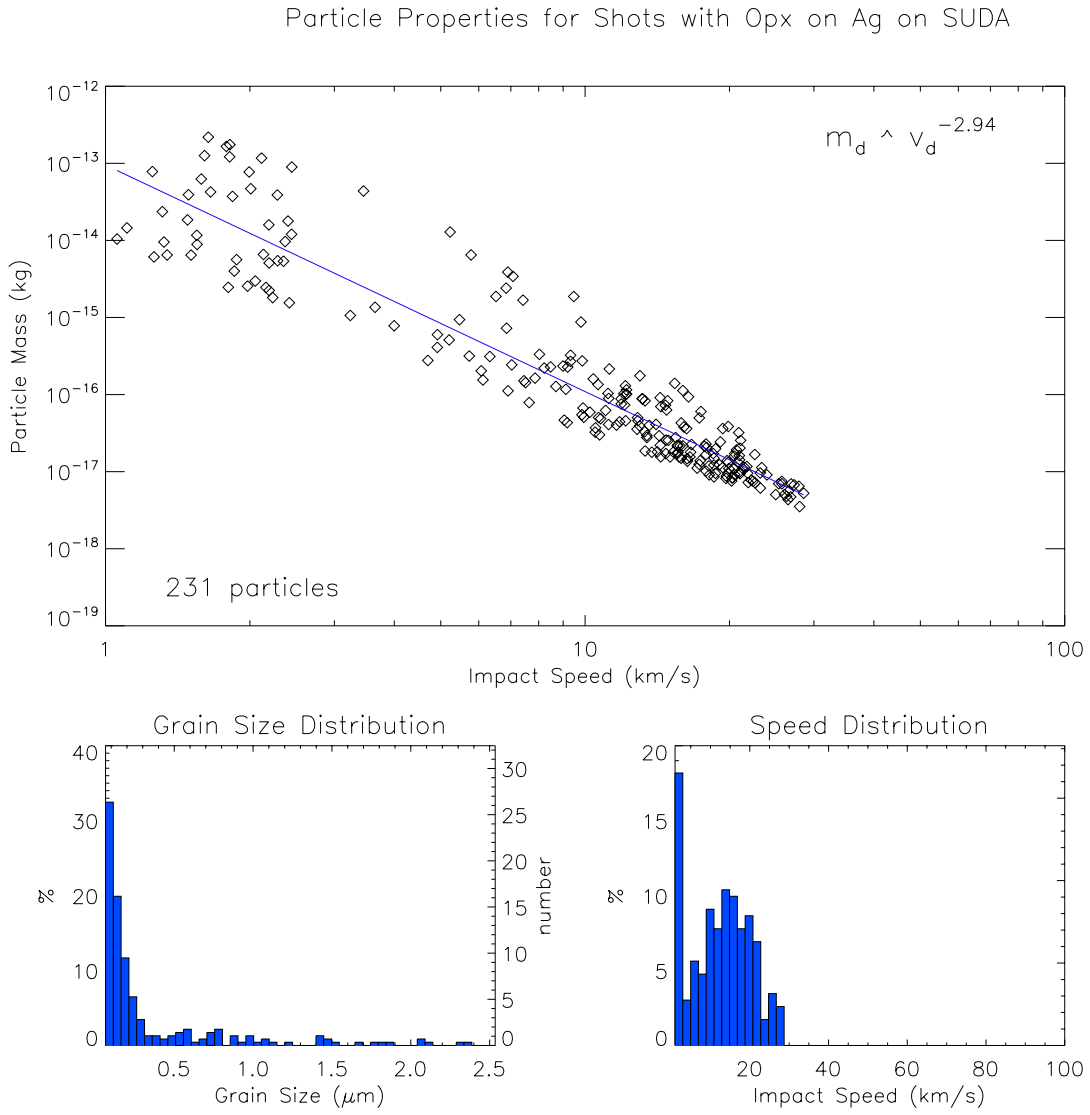

Figure D.4.: Particle properties for shots with platinum-doted Orthopyroxene on Ag (*SUDA*).

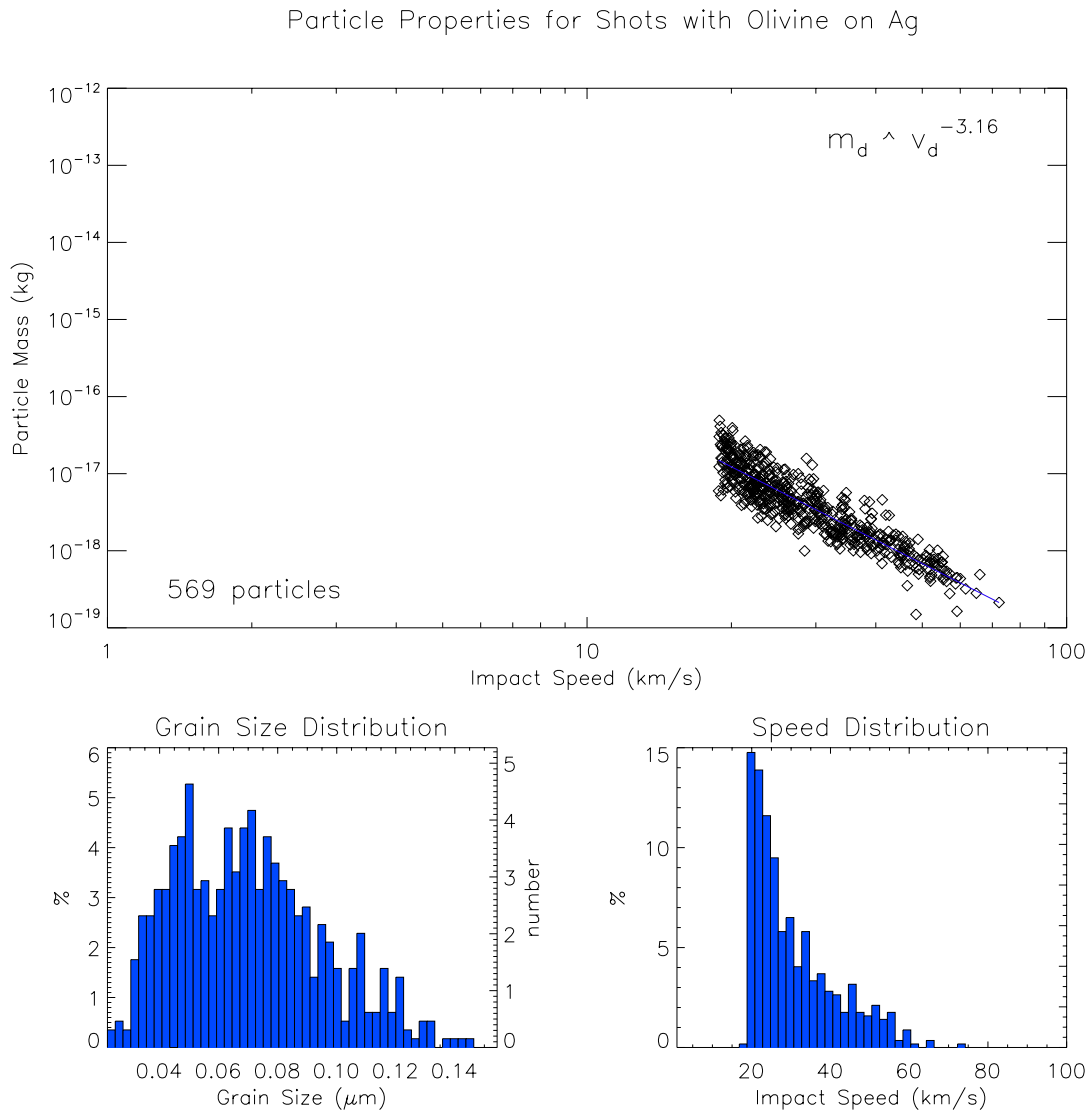

Figure D.5.: Particle properties for shots withPPY-coated Olivine on Ag (*BERTA*).

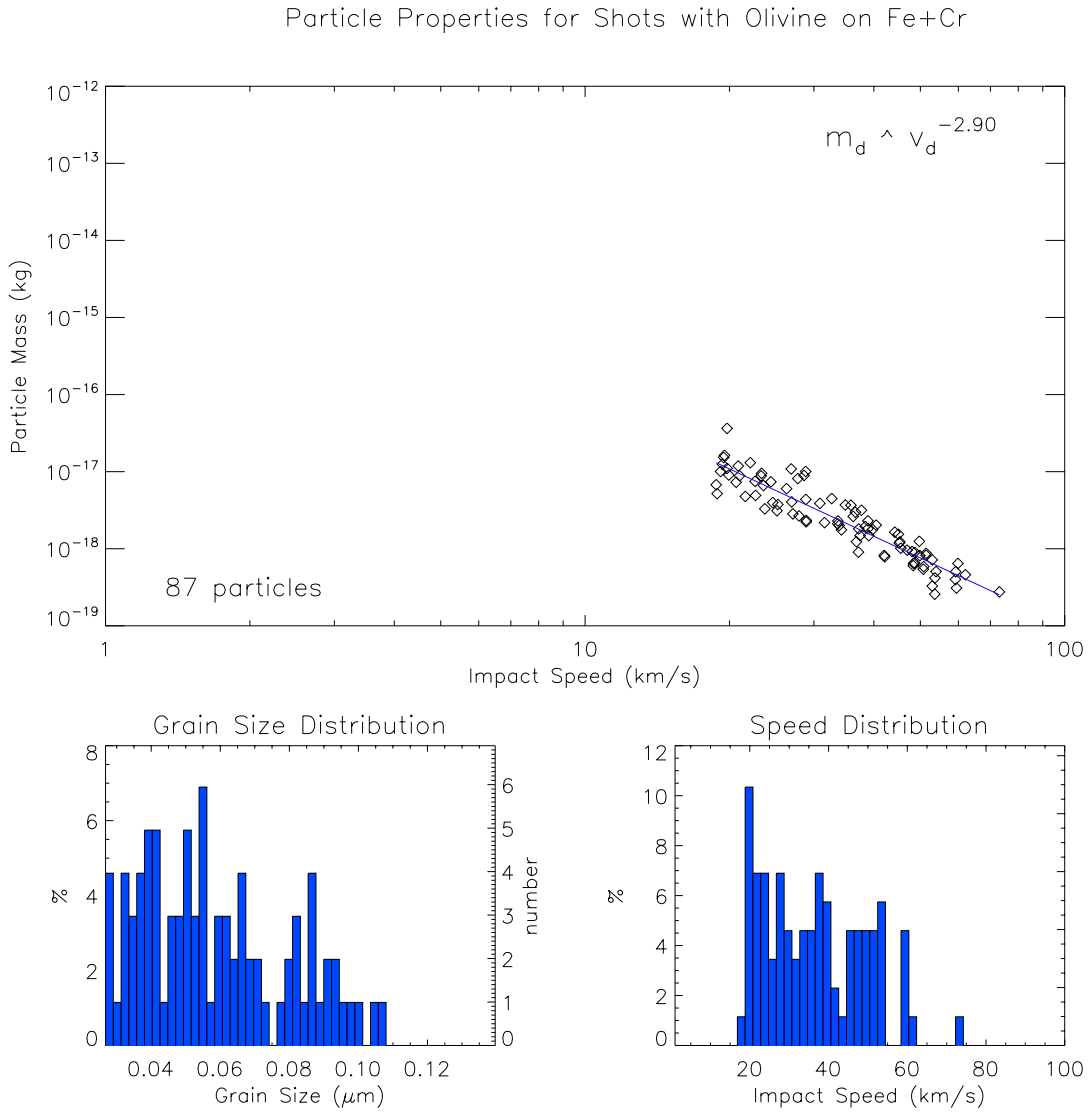

Figure D.6.: Particle properties for shots with Olivine on Fe+Ce (*BERTA*).

D.2. Charge yields

Table D.1.: Mass exponents α and averaged charge yields $\bar{q}$ for shots with iron / nickel particles on a silver target in narrow impact velocity ranges. The dependence of the charge yield on the particle mass within a narrow velocity range is described by $q \propto m^{\alpha}$. *Number* means the total number of particles, Δm the ratio of the maximal and minimal particle mass within a velocity range. σ is the mass exponent describing the dependence of the rise time on the particle mass $t_r \propto m^{\sigma}$ within a narrow velocity range, discussed in Section 4.1.3.

Velocity Range	Number	Δm	α	$\bar{q}$ (fC)	σ
4-5 km s^{-1}	15	14.08	0.66±0.18	54.1± 43.7 (± 80.8%)	-0.04±0.14
5-6 km s^{-1}	21	24.92	0.81±0.17	47.0± 36.3 (± 77.2%)	0.79±0.22
6-7 km s^{-1}	8	45.72	0.63±0.13	58.3± 57.6 (± 98.8%)	0.05±0.19
7-8 km s^{-1}	9	9.21	0.12±0.23	33.2± 16.2 (± 48.8%)	0.23±0.36
8-10 km s^{-1}	19	27.67	0.51±0.13	25.8± 25.0 (± 96.9%)	0.30±0.15
10-12 km s^{-1}	18	13.20	0.55±0.21	19.0± 17.6 (± 92.6%)	0.18±0.15
12-14 km s^{-1}	22	5.27	1.01±0.40	32.7± 33.1 (±101.2%)	0.52±0.19
14-16 km s^{-1}	32	6.72	1.04±0.25	19.6± 27.9 (±142.3%)	0.14±0.21
16-18 km s^{-1}	37	9.61	0.56±0.22	22.4± 23.7 (±105.8%)	-0.04±0.18
18-20 km s^{-1}	23	6.32	0.48±0.30	35.4± 34.4 (± 97.2%)	0.23±0.18
20-25 km s^{-1}	25	5.08	0.03±0.44	48.9± 51.5 (± 70.3%)	0.21±0.24
25-30 km s^{-1}	41	5.52	0.37±0.37	120.1± 83.6 (± 69.6%)	0.12±0.18
35-40 km s^{-1}	36	2.71	1.17±0.28	225.8±125.5 (± 55.6%)	-0.08±0.17
40-45 km s^{-1}	27	4.22	0.91±0.22	228.7±128.2 (± 56.1%)	-0.04±0.12
45-50 km s^{-1}	26	4.55	1.16±0.55	312.6±181.6 (± 58.1%)	-0.32±0.31
		averaged α:	0.67±0.35	averaged σ:	0.15±0.26

Table D.2.: Mass exponents α and averaged charge yields $\bar{q}$ for shots with Olivine particles on a silver target in narrow impact velocity ranges. The dependence of the charge yield on the particle mass within a narrow velocity range is described by $q \propto m^{\alpha}$. *Number* means the total number of particles , Δm the ratio of the maximal and minimal particle mass within a velocity range. σ is the mass exponent describing the dependence of the rise time on the particle mass $t_r \propto m^{\sigma}$ within a narrow velocity range, discussed in Section 4.1.3.

Velocity Range	Number	Δm	α	$\bar{q}$ (fC)	σ
19-20 km s^{-1}	37	6.57	0.79±0.14	108.5± 72.0 (± 66.4%)	0.27±0.14
20-21 km s^{-1}	41	10.13	1.11±0.15	154.4± 150.3 (± 97.3%)	0.08±0.11
21-22 km s^{-1}	33	6.56	1.16±0.15	113.5± 102.3 (± 90.1%)	0.19±0.14
22-23 km s^{-1}	45	7.72	0.98±0.17	155.3± 161.6 (±104.1%)	0.08±0.08
23-24 km s^{-1}	31	7.70	0.77±0.13	135.6± 89.6 (± 66.1%)	0.06±0.08
24-25 km s^{-1}	27	7.52	1.25±0.16	166.7± 116.5 (± 69.9%)	0.09±0.08
25-26 km s^{-1}	22	4.39	0.67±0.26	169.8± 100.5 (± 59.2%)	-0.16±0.09
26-27 km s^{-1}	29	4.38	0.91±0.21	204.0± 184.9 (± 90.6%)	0.02±0.09
27-28 km s^{-1}	17	6.03	0.76±0.31	231.0± 128.6 (± 55.7%)	0.08±0.13
28-29 km s^{-1}	14	15.85	0.99±0.21	257.6± 256.3 (± 99.5%)	-0.24±0.07
29-30 km s^{-1}	19	6.59	1.24±0.48	741.9±1556.9 (±209.8%)	-0.11±0.11
30-35 km s^{-1}	74	5.72	1.02±0.19	589.0±2002.0 (±339.9%)	0.04±0.07
35-40 km s^{-1}	49	4.89	0.69±0.22	495.0± 335.9 (± 67.9%)	0.03±0.10
40-45 km s^{-1}	32	6.82	0.73±0.28	694.4± 595.3 (± 85.7%)	-0.01±0.13
		averaged α:	0.93±0.2	averaged σ:	0.04±0.1

Table D.3.: Mass exponents α and averaged charge yields $\bar{q}$ for shots with platinum coated Opx particles particles on a silver target in narrow impact velocity ranges. Here, the results of measurements with two different *TOF* mass spectrometers, namely the *BERTA* and the *SUDA* instrument, have bee combined to obtain a data set of statistical significance.The dependence of the charge yield on the particle mass within a narrow velocity range is described by $q \propto m^{\alpha}$. *Number* means the total number of particles, Δm the ratio of the maximal and minimal particle mass within a velocity range. σ is the mass exponent describing the dependence of the rise time on the particle mass $t_r \propto m^{\sigma}$ within a narrow velocity range, discussed in Section 4.1.3.

Velocity Range	Number	Δm	α	$\bar{q}$ (fC)	σ
1-2 km s^{-1}	17	88.70	0.58±0.07	6.05±12.24 (±202.31%)	0.04±0.05
3-4 km s^{-1}	8	67.95	0.70±0.10	6.15± 6.75 (±109.76%)	0.03±0.23
5-6 km s^{-1}	10	40.64	0.56±0.15	7.56± 4.32 (± 57.14%)	0.30±0.10
7-8 km s^{-1}	8	43.47	1.15±0.41	11.27±11.29 (±100.18%)	-0.07±0.26
9-10 km s^{-1}	17	43.30	0.93±0.27	8.22± 6.82 (± 82.97%)	-0.07±0.23
12-13 km s^{-1}	18	4.79	0.80±0.49	5.73± 7.22 (±126.00%)	0.09±0.51
15-16 km s^{-1}	20	9.34	1.19±0.31	3.92± 6.52 (±166.33%)	0.18±0.51
19-20 km s^{-1}	11	4.73	0.95±0.40	0.75± 0.22 (± 29.33%)	0.23±0.14
21-23 km s^{-1}	13	3.36	1.00±0.54	1.35± 1.91 (±141.48%)	-0.23±0.62
	averaged α:		0.87±0.23	averaged σ:	0.05±0.17

Table D.4.: Dependence of rise time on the acceleration potential U_{acc}. Measurements for shots with Fe+Ni particles within a velocity range from 4 km s^{-1} to about 60 km s^{-1} and olivine particles within a velocity range from about 20 km s^{-1} up to 60 km s^{-1} have been conducted.Under the assumption that the rise time is dependent only on the particles impact speed, the exponent of the relation $t_r \propto v^{\delta}$ is determined for various acceleration potentials.

	Velocity Exponent δ	
U_{acc}	Fe+Ni on Ag	Olivine on Ag
300 V	-0.75±0.08	–
400 V	–	-0.67±0.06
500 V	-0.85±0.10	–
600 V	-1.13±0.09	-0.77±0.06
700 V	-1.29±0.03	–
800 V	-1.08±0.10	-0.80±0.07
900 V	-1.30±0.09	–
1000 V	-1.15±0.10	-0.81±0.07
1500 V	–	-0.63±0.10
2000 V	–	-0.73±0.05
2500 V	–	-0.97±0.08
3000 V	–	-0.78±0.06

Table D.5.: Dependence of height q and time scale t_r of the individual evolution phases on the particle's mass and impact velocity shown in Figure 4.13 and Figure 4.16. The table lists the velocity exponents β for the charge yield and δ for the rise time defining the dependence of the measure in question on the impact velocity v.

Relation	Step1	Step2	Step3	Step4	Step5	total
$q \propto v^{\beta}$	1.80±0.07	0.35±0.06	0.14±0.06	0.01±0.08	-0.39±0.13	1.08±0.07
$q \propto m^{-0.67} \cdot v^{\beta}$	4.16±0.06	2.71±0.05	2.53±0.05	2.52±0.07	2.35±0.07	3.28±0.05
$q \propto m^{-1} \cdot v^{\beta}$	5.18±0.06	3.72±0.05	3.56±0.05	3.60±0.07	3.51±0.12	4.24±0.05
$t_r \propto v^{\delta}$	-0.06±0.03	-0.49±0.06	-0.59±0.05	-0.81±0.09	-1.15±0.13	-1.11±0.03

Table D.6.: Laser shots on gold coated Olivine: Comparison of the variation of the charge yield for two different locations on the target.

	Location 1		Location 2	
Energy range	Number	Charge yield	Number	Charge yield
6 - 7 μJ	5	10 fC ± 15 fC (±263%)	23	1211 fC ± 1599 fC (±132%)
7 - 8 μJ	14	65 fC ± 66 fC (±199%)	30	882 fC ± 1055 fC (±120%)
8 - 9 μJ	20	113 fC ± 96 fC (±157%)	8	1049 fC ± 1331 fC (±127%)
9 - 10 μJ	13	216 fC ± 228 fC (±164%)	10	1406 fC ± 1056 fC (±75%)
10 - 11 μJ	10	417 fC ± 338 fC (±91%)	12	1066 fC ± 607 fC (±57%)
11 - 12 μJ	7	613 fC ± 263 fC (±58%)	12	1096 fC ± 688 fC (±63%)

D.3. Resulting *TOF* Mass Spectra

D.3.1. Variability of the *TOF* mass spectra

Table D.7.: Theoretical variability of spectra in narrow ranges of the impact velocity. The variabilities have been calculated due to four different models, V_r refers to the variability calculated for 10^6 completely randomised spectra, $V_{2linconst}$ for 10^6 randomised spectra for which the 2 maximum lines were kept constant, $V_{2linvar}$ for 10^6 randomised spectra for which the 2 maximum lines were kept constant, and V_{whiteN} for 10^6 spectra varied with white noise .

Experiment	Instrument	Velocity range	V_r	$V_{2linconst}$	$V_{2linvar}$	V_{whiteN}
Fe on Ag	BERTA	5-10 km s^{-1}	2.68 ±0.40	2.36 ±0.38	0.32 ±0.14	2.02 ±0.47
	BERTA	15-20 km s^{-1}	4.82 ±0.65	4.43 ±0.63	0.39 ±0.17	4.04 ±0.86
	BERTA	30-35 km s^{-1}	4.55 ±0.63	4.14 ±0.61	0.41 ±0.18	3.81 ±0.84
	BERTA	35-50 km s^{-1}	2.77 ±0.40	2.50 ±0.38	0.27 ±0.12	2.19 ±0.48
	LAMA	5-10 km s^{-1}	3.42 ±0.50	3.18 ±0.48	0.24 ±0.11	3.06 ±0.60
	LAMA	15-20 km s^{-1}	5.37 ±0.78	4.81 ±0.74	0.56 ±0.25	4.45 ±1.01
	LAMA	30-35 km s^{-1}	6.46 ±0.87	5.87 ±0.82	0.60 ±0.26	5.49 ±1.17
	LAMA	35-50 km s^{-1}	6.54 ±0.82	6.03 ±0.79	0.51 ±0.23	5.64 ±1.14
Opx on Ag	BERTA	3-4 km s^{-1}	1.60 ±0.40	1.15 ±0.35	0.45 ±0.20	0.99 ±0.39
	BERTA	9-11 km s^{-1}	3.50 ±0.60	3.03 ±0.57	0.47 ±0.20	2.68 ±0.70
	BERTA	18-20 km s^{-1}	5.26 ±0.61	4.95 ±0.60	0.32 ±0.14	4.54 ±0.87
	SUDA	3-4 km s^{-1}	0.99 ±0.27	0.55 ±0.20	0.43 ±0.18	0.48 ±0.22
	SUDA	9-11 km s^{-1}	2.58 ±0.27	2.43 ±0.26	0.15 ±0.07	2.09 ±0.38
	SUDA	18-20 km s^{-1}	1.95 ±0.21	1.83 ±0.21	0.12 ±0.05	1.51 ±0.26

Table D.8.: Empirical variability of spectra in narrow ranges of the impact energy. The variabilities have been calculated due to four different models, V_r refers to the variability calculated for 10^6 completely randomised spectra, $V_{2linconst}$ for 10^6 randomised spectra for which the 2 maximum lines were kept constant, $V_{2linvar}$ for 10^6 randomised spectra for which the 2 maximum lines were kept constant, and V_{whiteN} for 10^6 spectra varied with white noise.

Experiment	Instrument	Energy range	V_r	$V_{2linconst}$	$V_{2linvar}$	V_{whiteN}
Fe on Ag	BERTA	1.5 -2.0 nJ	3.66 ±0.53	3.32 ±0.51	0.34 ±0.15	3.02 ±0.68
	BERTA	2.0 -2.5 nJ	4.09 ±0.57	3.72 ±0.55	0.37 ±0.16	3.41 ±0.75
	LAMA	1.5 -2.0 nJ	6.96 ±0.87	6.43 ±0.83	0.54 ±0.24	6.01 ±1.21
	LAMA	2.0 -2.5 nJ	6.41 ±0.80	5.92 ±0.77	0.49 ±0.22	5.53 ±1.12
	LAMA	3.0 -3.5 nJ	3.46 ±0.50	3.13 ±0.48	0.33 ±0.15	2.86 ±0.65
Opx on Ag	BERTA	2.65-2.85 nJ	3.35 ±0.47	3.07 ±0.45	0.29 ±0.13	2.80 ±0.61
	BERTA	4.0 -4.5 nJ	3.86 ±0.54	3.52 ±0.52	0.34 ±0.14	3.18 ±0.70
	SUDA	2.65-2.85 nJ	1.94 ±0.22	1.82 ±0.21	0.12 ±0.06	1.54 ±0.28
	SUDA	4.0 -4.5 nJ	1.86 ±0.23	1.73 ±0.23	0.14 ±0.06	1.50 ±0.30

Table D.9.: Empirical variability of spectra in narrow ranges of the energy density. The variabilities have been calculated due to four different models, V_r refers to the variability calculated for 10^6 completely randomised spectra, $V_{2linconst}$ for 10^6 randomised spectra for which the 2 maximum lines were kept constant, $V_{2linvar}$ for 10^6 randomised spectra for which the 2 maximum lines were kept constant, and V_{whiteN} for 10^6 spectra varied with white noise.

Experiment	Instrument	Energy density	V_r	$V_{2linconst}$	$V_{2linvar}$	V_{whiteN}
Fe on Ag	BERTA	10-15 kJm^{-2}	2.32 ±0.31	2.08 ±0.30	0.24 ±0.10	1.74 ±0.36
	BERTA	15-20 kJm^{-2}	5.34 ±0.73	4.88 ±0.70	0.45 ±0.20	4.46 ±0.96
	BERTA	20-25 kJm^{-2}	3.67 ±0.63	3.14 ±0.58	0.53 ±0.24	2.92 ±0.76
	LAMA	10-15 kJm^{-2}	6.26 ±0.94	5.75 ±0.91	0.51 ±0.24	6.07 ±1.11
	LAMA	15-20 kJm^{-2}	5.66 ±0.78	5.13 ±0.74	0.53 ±0.24	4.77 ±1.04
	LAMA	20-25 kJm^{-2}	6.28 ±0.80	5.80 ±0.77	0.49 ±0.22	5.39 ±1.10
Opx on Ag	BERTA	5-7 kJm^{-2}	2.64 ±0.53	2.16 ±0.49	0.49 ±0.21	1.90 ±0.58
	BERTA	9-11 kJm^{-2}	3.92 ±0.62	3.48 ±0.59	0.45 ±0.19	3.08 ±0.74
	BERTA	19-21 kJm^{-2}	3.04 ±0.48	2.70 ±0.45	0.34 ±0.15	2.39 ±0.57
	SUDA	5-7 kJm^{-2}	1.98 ±0.42	1.68 ±0.40	0.30 ±0.13	1.74 ±0.42
	SUDA	9-11 kJm^{-2}	3.17 ±0.37	2.99 ±0.36	0.18 ±0.09	2.70 ±0.51
	SUDA	19-21 kJm^{-2}	1.48 ±0.17	1.37 ±0.16	0.10 ±0.04	1.06 ±0.18

Table D.10.: Empirical variability of spectra in narrow ranges of the laser energy. The variabilities have been calculated due to four different models, V_r refers to the variability calculated for 10^6 completely randomised spectra, $V_{2linconst}$ for 10^6 randomised spectra for which the 2 maximum lines were kept constant, $V_{2linvar}$ for 10^6 randomised spectra for which the 2 maximum lines were kept constant, and V_{whiteN} for 10^6 spectra varied with white noise.

Target material	Laser energy	V_r	$V_{2linconst}$	$V_{2linvar}$	V_{whiteN}
Olivine (Spot1)	4.5- 5.0 μJ	3.46 $\pm$0.52	3.10 $\pm$0.50	0.36 $\pm$0.16	2.79 $\pm$0.65
	6.0- 6.5 μJ	3.96 $\pm$0.63	3.51 $\pm$0.60	0.46 $\pm$0.20	3.13 $\pm$0.76
	7.5- 8.0 μJ	3.75 $\pm$0.58	3.34 $\pm$0.55	0.41 $\pm$0.18	2.99 $\pm$0.71
	9.0- 9.5 μJ	1.31 $\pm$0.25	1.06 $\pm$0.22	0.25 $\pm$0.11	0.90 $\pm$0.24
Olivine (Spot2)	4.5- 5.0 μJ	4.04 $\pm$0.70	3.47 $\pm$0.65	0.57 $\pm$0.26	3.14 $\pm$0.82
	6.0- 6.5 μJ	0.71 $\pm$0.13	0.55 $\pm$0.12	0.16 $\pm$0.07	0.46 $\pm$0.11
	7.5- 8.0 μJ	0.86 $\pm$0.16	0.66 $\pm$0.14	0.20 $\pm$0.08	0.53 $\pm$0.13
	9.0- 9.5 μJ	0.72 $\pm$0.15	0.54 $\pm$0.13	0.18 $\pm$0.08	0.46 $\pm$0.12
Iron	1.0- 1.5 μJ	1.47 $\pm$0.46	0.76 $\pm$0.33	0.71 $\pm$0.32	0.77 $\pm$0.46
	2.0- 2.5 μJ	2.71 $\pm$0.59	2.07 $\pm$0.52	0.64 $\pm$0.28	1.92 $\pm$0.64
	3.5- 4.0 μJ	2.85 $\pm$0.65	2.05 $\pm$0.55	0.80 $\pm$0.34	1.91 $\pm$0.68
	8.0- 8.5 μJ	1.07 $\pm$0.39	0.37 $\pm$0.23	0.69 $\pm$0.31	0.49 $\pm$0.42
Ag+Cu	12.0-13.0 μJ	2.65 $\pm$0.52	2.19 $\pm$0.48	0.47 $\pm$0.21	1.99 $\pm$0.59
	14.0-14.5 μJ	2.71 $\pm$0.53	2.25 $\pm$0.49	0.47 $\pm$0.20	2.02 $\pm$0.60
	16.0-16.5 μJ	2.93 $\pm$0.56	2.44 $\pm$0.52	0.49 $\pm$0.21	2.17 $\pm$0.63
	19.0-19.5 μJ	1.09 $\pm$0.31	0.66 $\pm$0.24	0.42 $\pm$0.19	0.59 $\pm$0.26
	21.5-22.0 μJ	2.23 $\pm$0.52	1.61 $\pm$0.45	0.62 $\pm$0.27	1.52 $\pm$0.56
	23.5-24.0 μJ	0.46 $\pm$0.15	0.19 $\pm$0.09	0.27 $\pm$0.12	0.49 $\pm$0.14
	24.5-25.0 μJ	0.83 $\pm$0.20	0.57 $\pm$0.17	0.26 $\pm$0.11	0.48 $\pm$0.16

Table D.11.: Empirical variability of spectra in narrow ranges of the total charge yield. The variability of spectra of impact and laser ablation events producing charge yields within a narrow range is compared. Due to the lack of high resolution mass spectra for laser ablation measurements, a comparison between high and low resolution spectra could not me made.

Experiment	Charge yield	V_r	$V_{2linconst}$	$V_{2linvar}$	V_{whiteN}
Laser on Olivine (Spot1)	10 - 20 fC	2.87 ±0.44	2.56 ±0.42	0.31 ±0.13	2.26 ±0.52
	60 - 70 fC	1.82 ±0.32	1.51 ±0.29	0.32 ±0.13	1.27 ±0.34
	100 - 120 fC	1.12 ±0.20	0.92 ±0.18	0.21 ±0.09	0.73 ±0.18
Olivine on Ag	100 - 120 fC	3.18 ±0.55	2.75 ±0.52	0.43 ±0.19	2.52 ±0.66
Laser on Fe	1 - 10 fC	2.28 ±0.51	1.74 ±0.45	0.54 ±0.23	1.51 ±0.53
	10 - 20 fC	1.87 ±0.55	0.94 ±0.39	0.93 ±0.39	0.92 ±0.53
	20 - 30 fC	1.58 ±0.49	0.79 ±0.34	0.79 ±0.34	0.82 ±0.48
Fe on Ag	1 - 10 fC	1.75 ±0.34	1.40 ±0.31	0.35 ±0.16	1.17 ±0.33
	10 - 20 fC	2.35 ±0.44	1.98 ±0.41	0.38 ±0.16	1.78 ±0.51
	20 - 30 fC	1.63 ±0.29	1.37 ±0.27	0.26 ±0.11	1.11 ±0.27

D.4. Mass line frequencies for impact ionisation

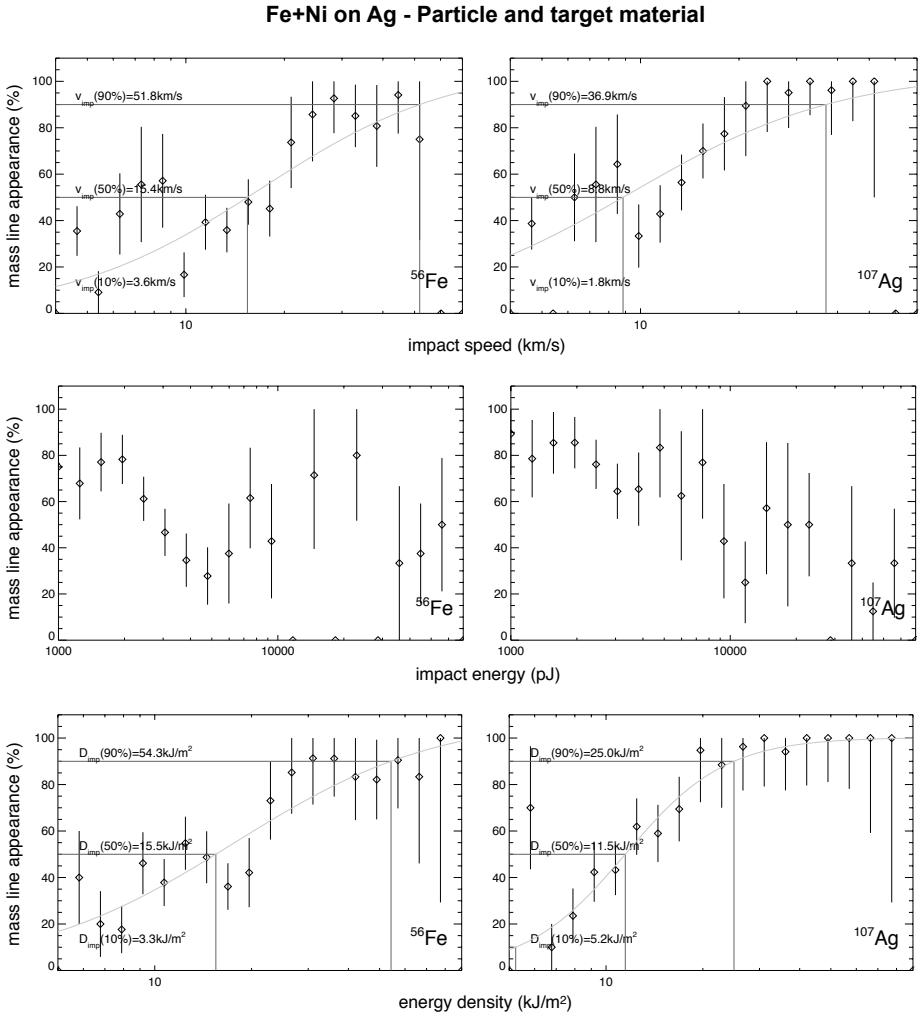

Figure D.7.: Mass line frequencies for the particle material mass line ^{56}Fe and target material mass line ^{107}Ag for *Fe+Ni* particle impacts onto silver in dependence on the impact speed, the kinetic impact energy and the energy density. For the dependency on the impact speed and the energy density the data points could be fitted with a *Fermi* distribution. The result show no significant dependence on the impact energy whatsoever. The error bars represent the *Poisson* distribution of the measurement and depends therefore on the number of data points obtained in a specific range of the impact parameter in question.

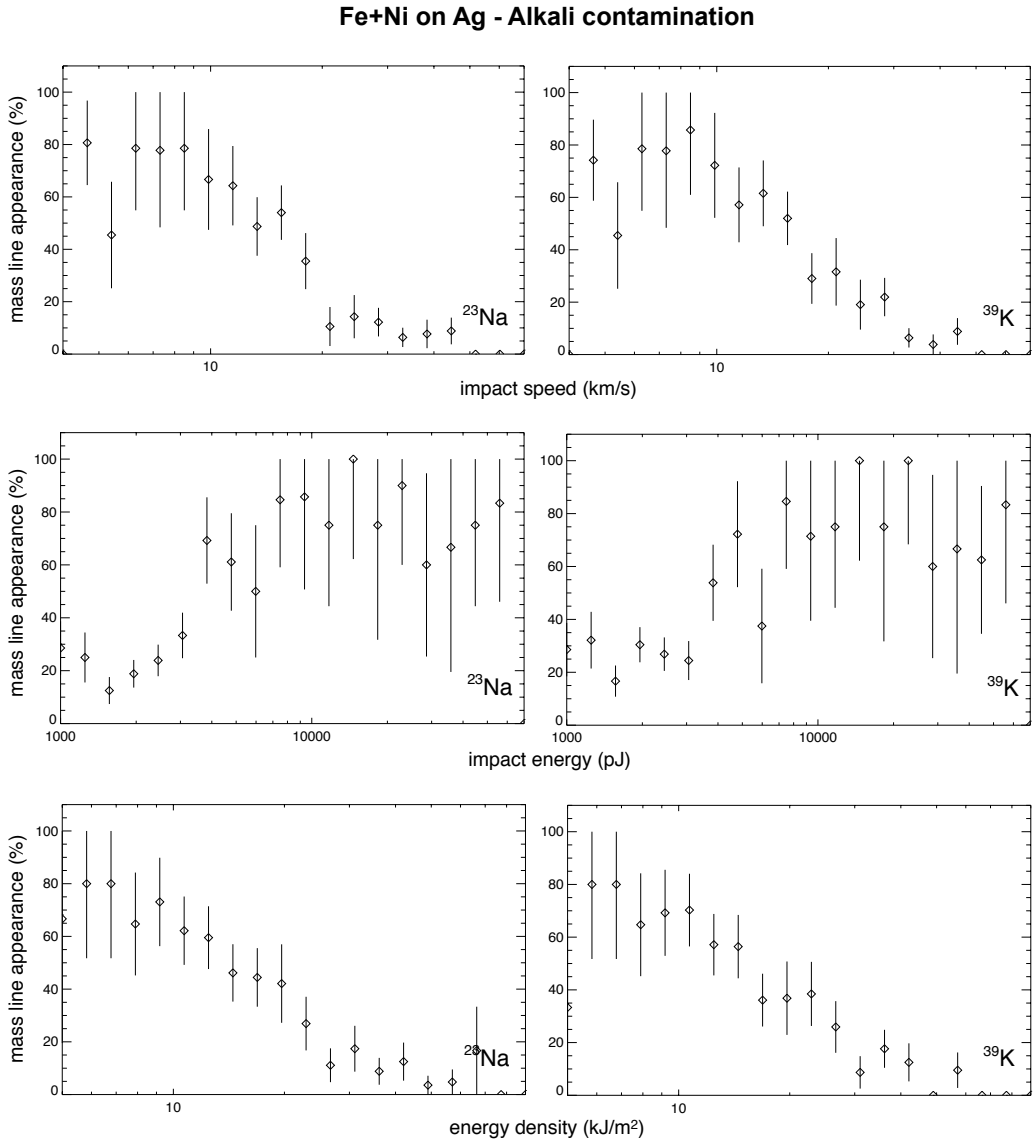

Figure D.8.: Mass line frequencies for the alkali contaminant mass lines ^{23}Na and ^{39}Ag for *Fe+Ni* particle impacts onto silver in dependence on the impact speed, the kinetic impact energy and the energy density. With increasing impact velocites and energy densities the frequency of these lines is decreasing.

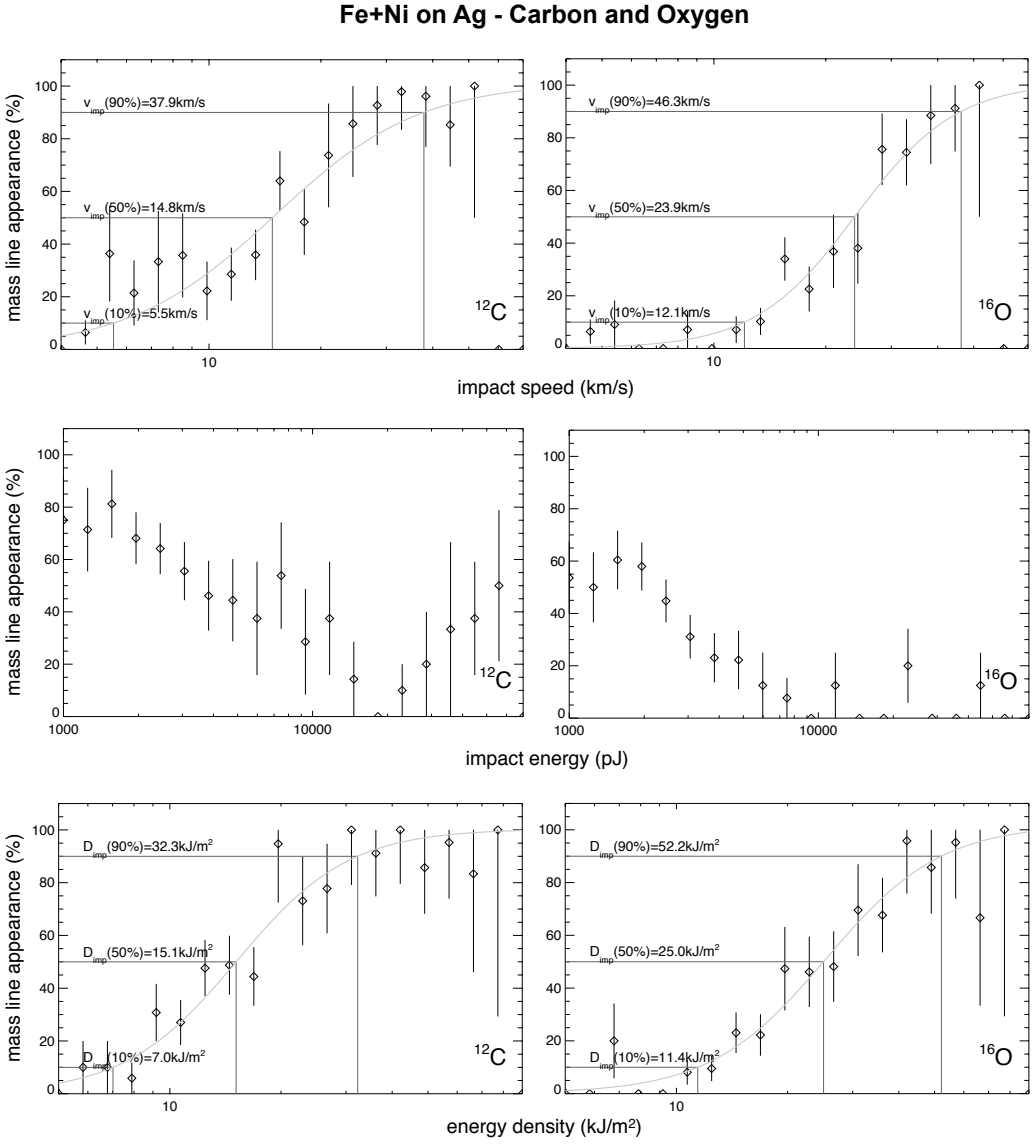

Figure D.9.: Mass line frequencies for the mass lines of ^{12}C and ^{16}O for *Fe+Ni* particle impacts onto silver in dependence on the impact speed, the kinetic impact energy and the energy density. For the dependency on the impact speed and the energy density the data points could be fitted with a *Fermi* distribution. The result show no significant dependence on the impact energy whatsoever. The error bars represent the *Poisson* distribution of the measurement and depends therefore on the number of data points obtained in a specific range of the impact parameter in question.

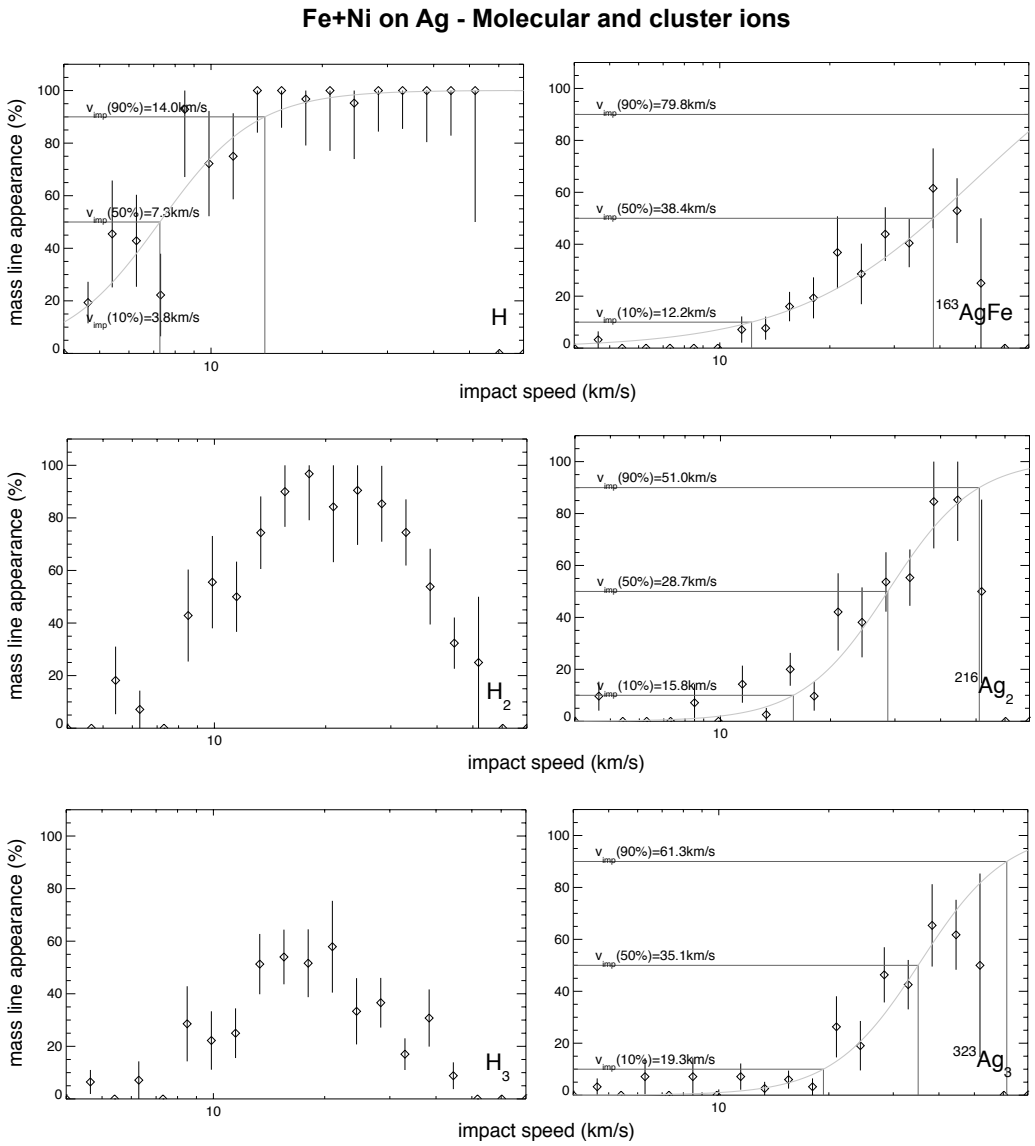

Figure D.10.: Mass line frequencies for atomic and molecular hydrogen, H, H_2 and H_3, and for cluster ion mass lines ^{163}AgFe, $^{216}Ag_2$, and $^{323}Ag_3$ for *Fe+Ni* particle impacts onto silver in dependence on the impact speed. This dependency be fitted with a *Fermi* distribution. The error bars represent the *Poisson* distribution of the measurement and depends therefore on the number of data points obtained in a specific range of the impact parameter in question.

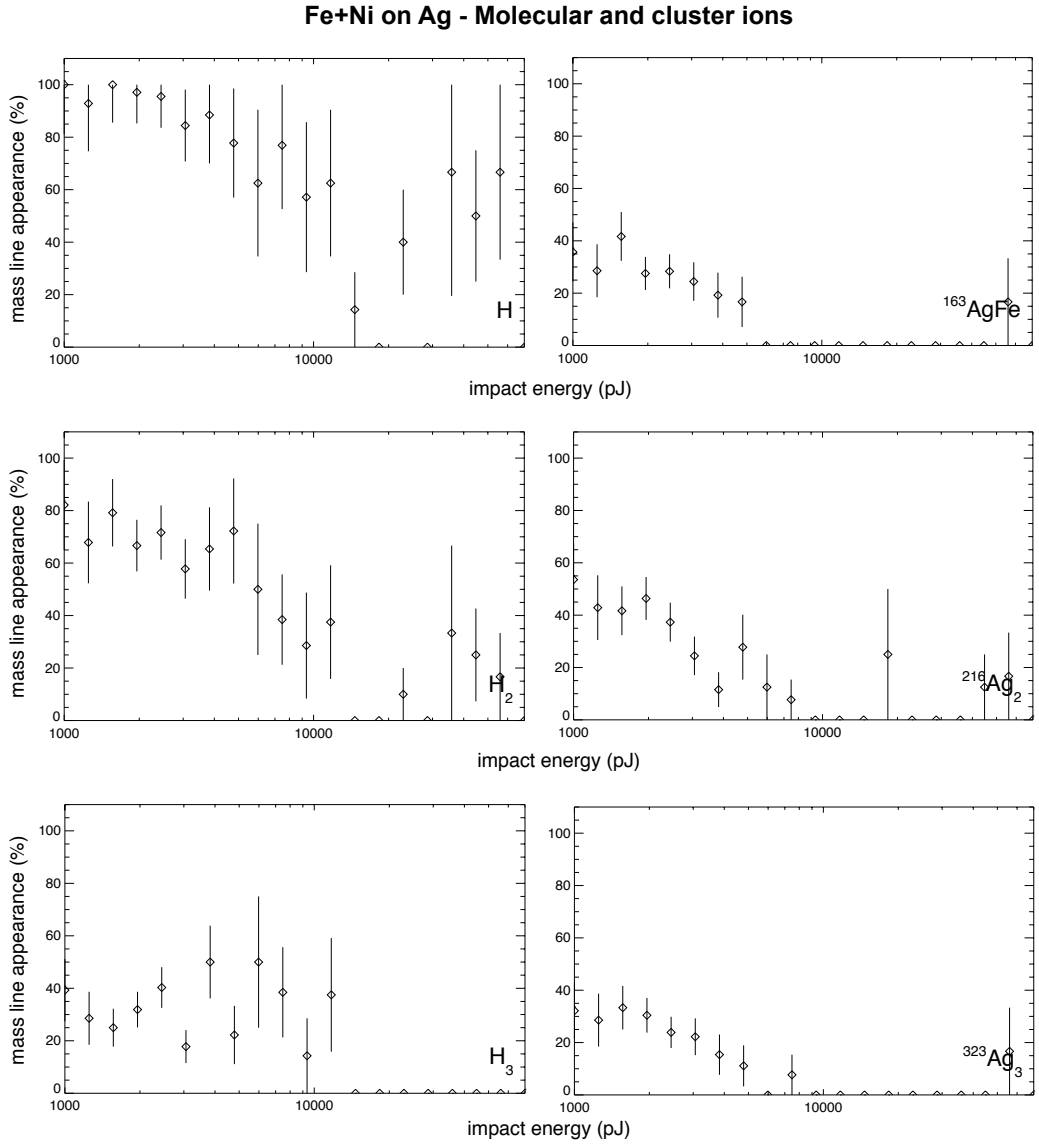

Figure D.11.: Mass line frequencies for atomic and molecular hydrogen, H, H_2 and H_3, and for cluster ion mass lines ^{163}AgFe, $^{216}Ag_2$, and $^{323}Ag_3$ for *Fe+Ni* particle impacts onto silver in dependence on the impact energy. The result show no significant dependence on the impact energy.

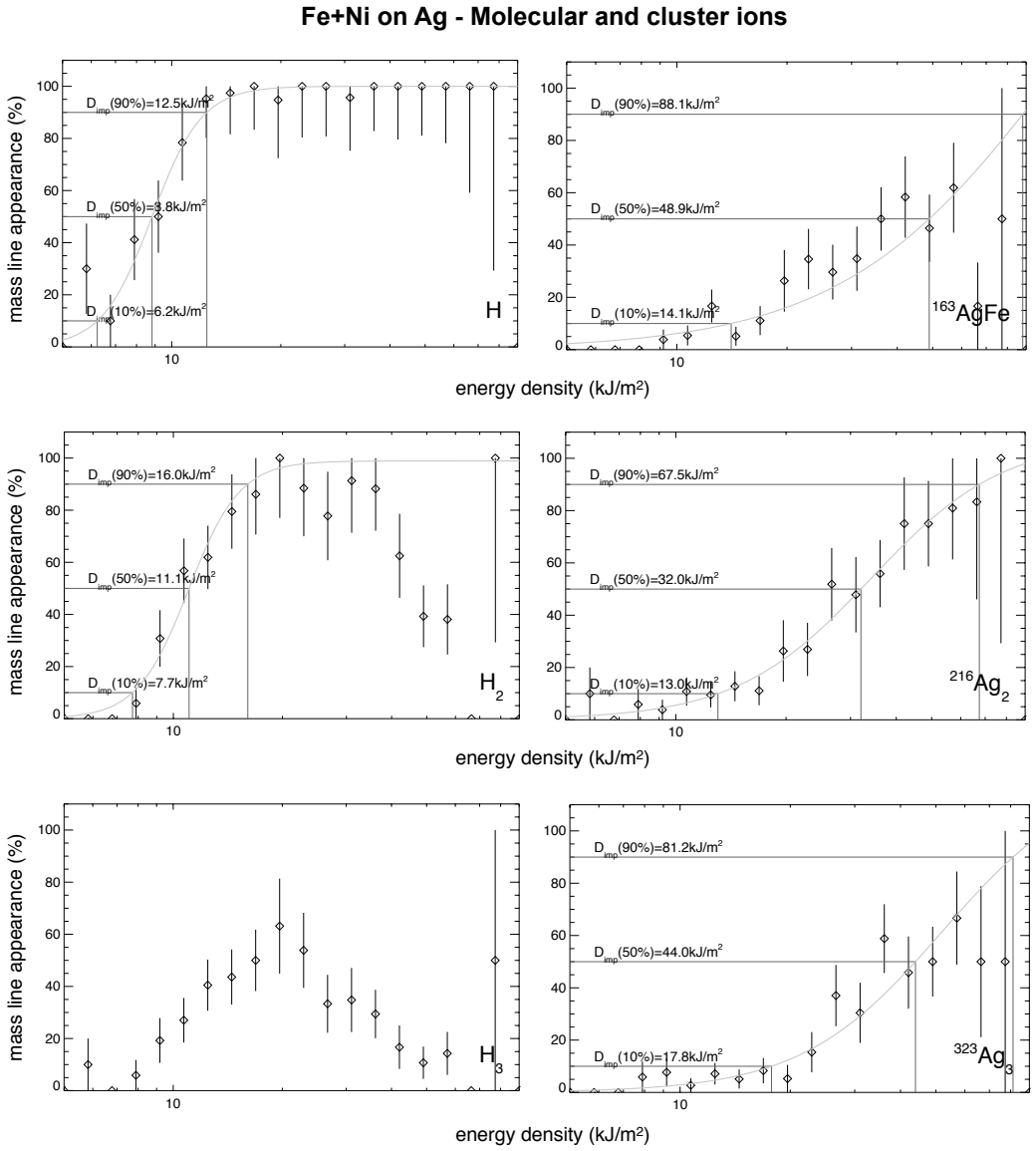

Figure D.12.: Mass line frequencies for atomic and molecular hydrogen, H, H_2 and H_3, and for cluster ion mass lines ^{163}AgFe, $^{216}Ag_2$, and $^{323}Ag_3$ for *Fe+Ni* particle impacts onto silver in dependence on the impact energy. The result show no significant dependence on the impact energy density.This dependency could be fitted with a *Fermi* distribution. The error bars represent the *Poisson* distribution of the measurement and depends therefore on the number of data points obtained in a specific range of the impact parameter in question.

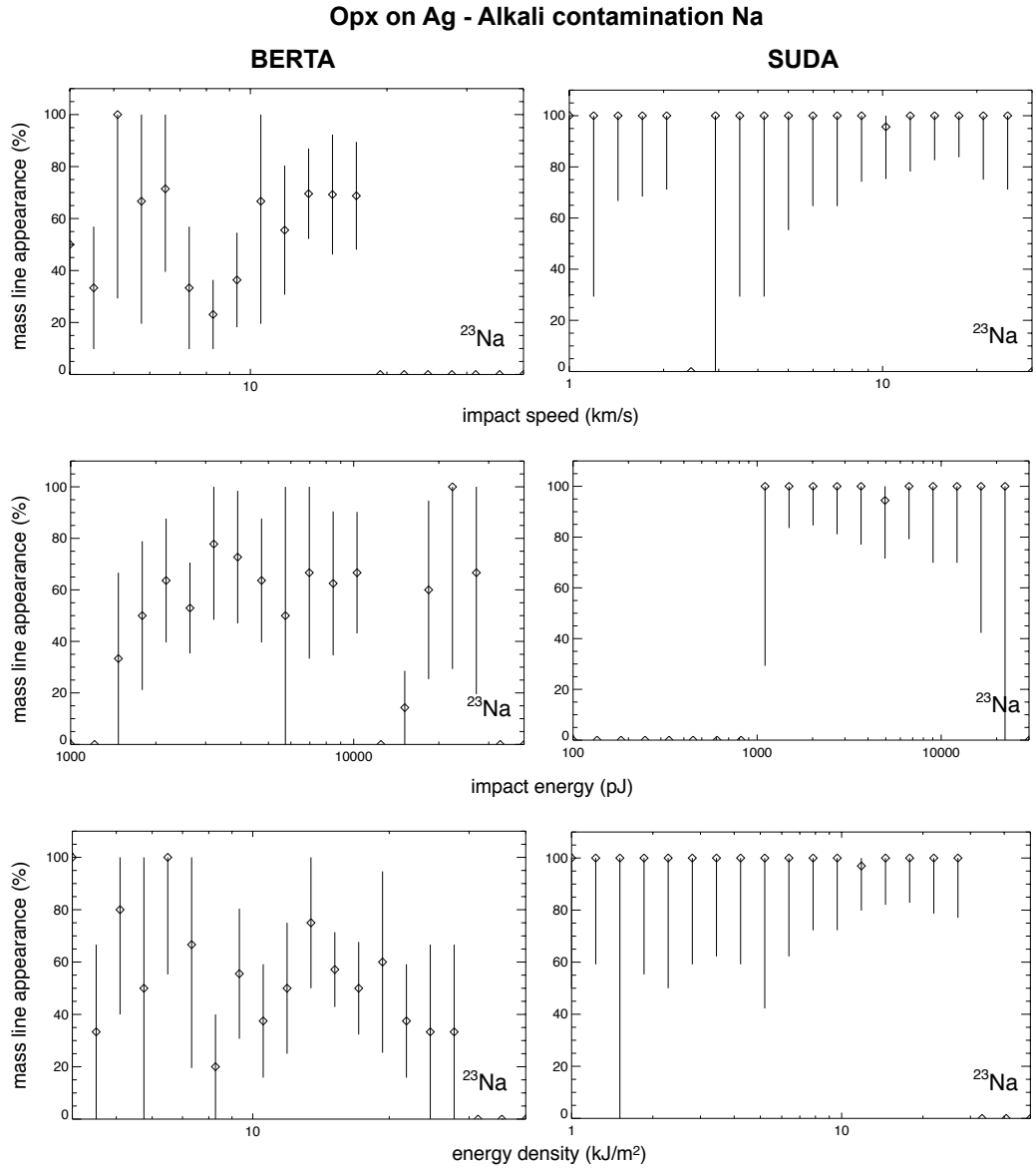

Figure D.13.: Mass line frequencies for the alkali contaminant mass line ^{23}Na for *Opx* particle impacts onto silver in dependence on the impact speed, the kinetic impact energy and the energy density. The results of measurements with the *BERTA* mass spectrometer are compared to those obtained with the *SUDA* instrument. The results show no significant dependence on the impact paramters whatsoever.

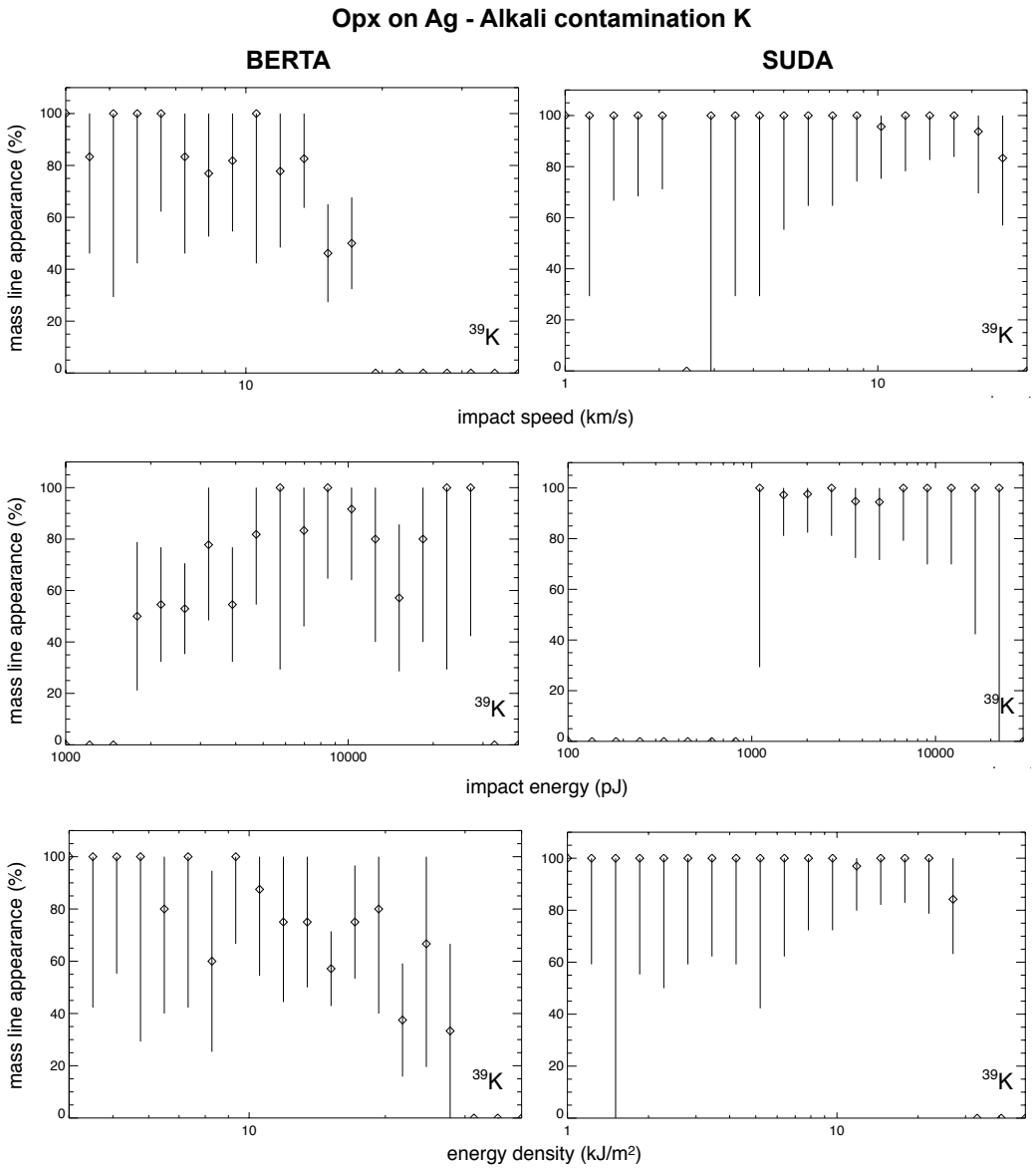

Figure D.14.: Mass line frequencies for the alkali contaminant mass line ^{39}K for *Opx* particle impacts onto silver in dependence on the impact speed, the kinetic impact energy and the energy density. The results of measurements with the *BERTA* mass spectrometer are compared to those obtained with the *SUDA* instrument. The results show no significant dependence on the impact paramters whatsoever.

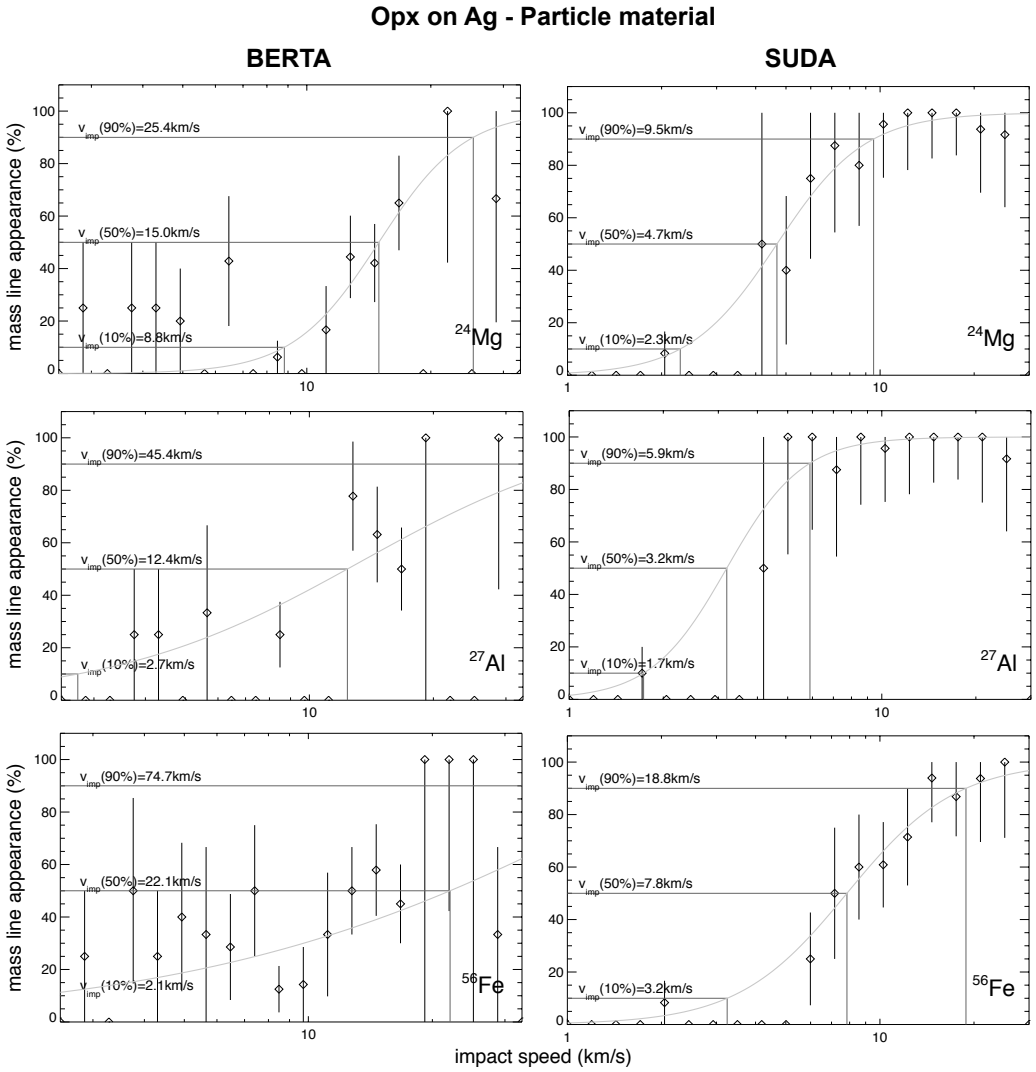

Figure D.15.: Mass line frequencies for the metal particle bulk material mass lines ^{24}Mg, ^{27}Al, and ^{56}Fe for *Opx* particle impacts onto silver in dependence on the impact speed. The results of measurements with the *BERTA* mass spectrometer are compared to those obtained with the *SUDA* instrument. This dependency could be fitted with a *Fermi* distribution. The error bars represent the *Poisson* distribution of the measurement and depends therefore on the number of data points obtained in a specific range of the impact parameter in question.

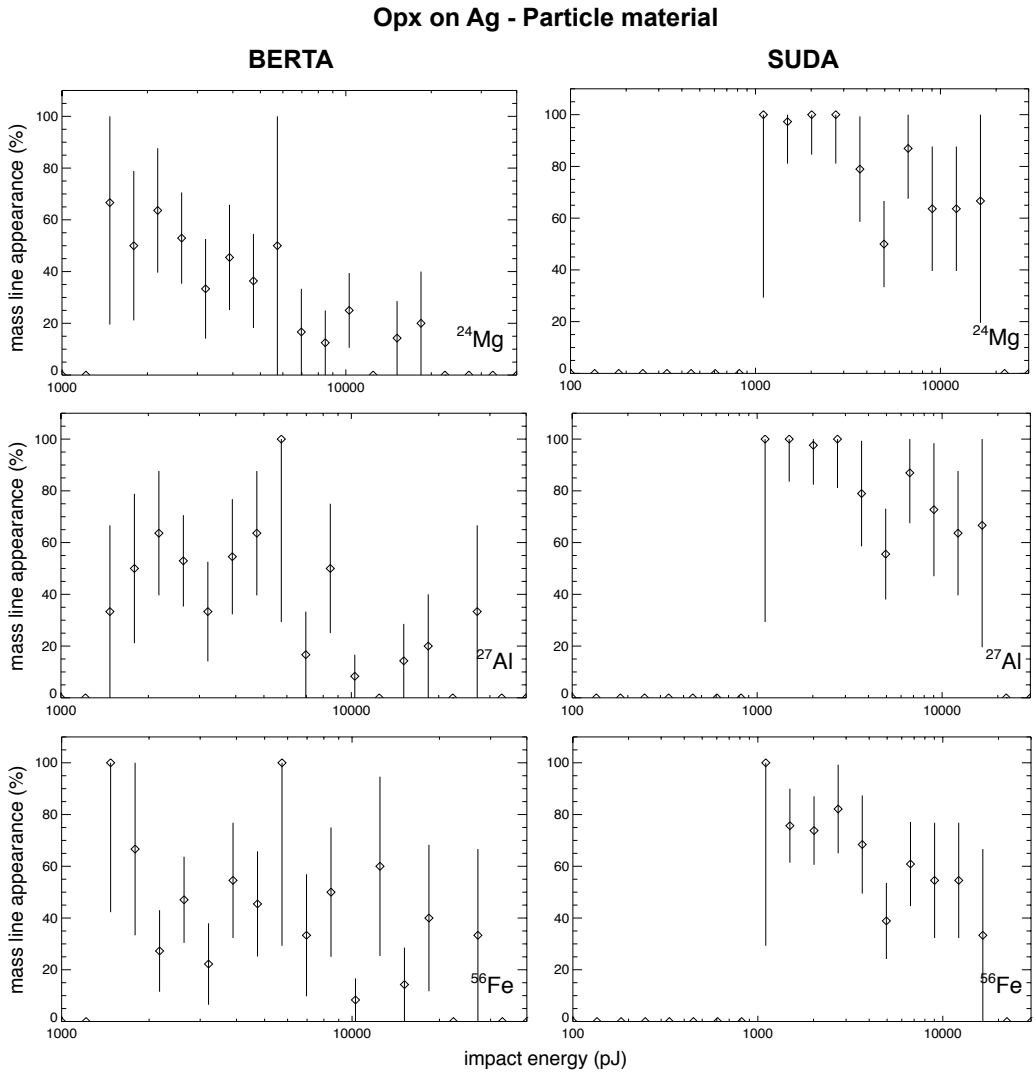

Figure D.16.: Mass line frequencies for the metal particle bulk material mass lines ^{24}Mg, ^{27}Al, and ^{56}Fe for *Opx* particle impacts onto silver in dependence on the impact energy. The results of measurements with the *BERTA* mass spectrometer are compared to those obtained with the *SUDA* instrument. The result shows no significant dependence on the impact energy whatsoever.

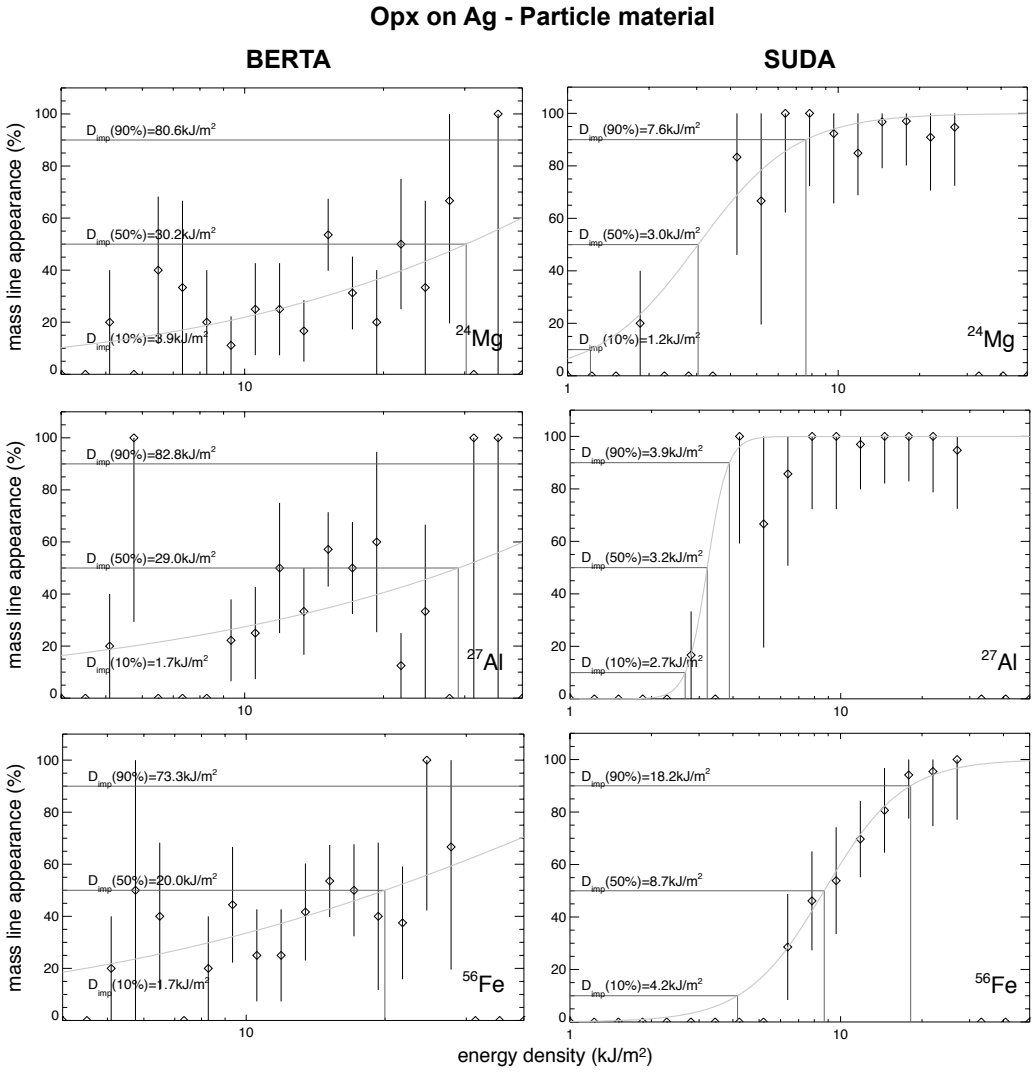

Figure D.17.: Mass line frequencies for the metal particle bulk material mass lines ^{24}Mg, ^{27}Al, and ^{56}Fe for *Opx* particle impacts onto silver in dependence on the impact energy density. The results of measurements with the *BERTA* mass spectrometer are compared to those obtained with the *SUDA* instrument. This dependency could be fitted with a *Fermi* distribution. The error bars represent the *Poisson* distribution of the measurement and depends therefore on the number of data points obtained in a specific range of the impact parameter in question.

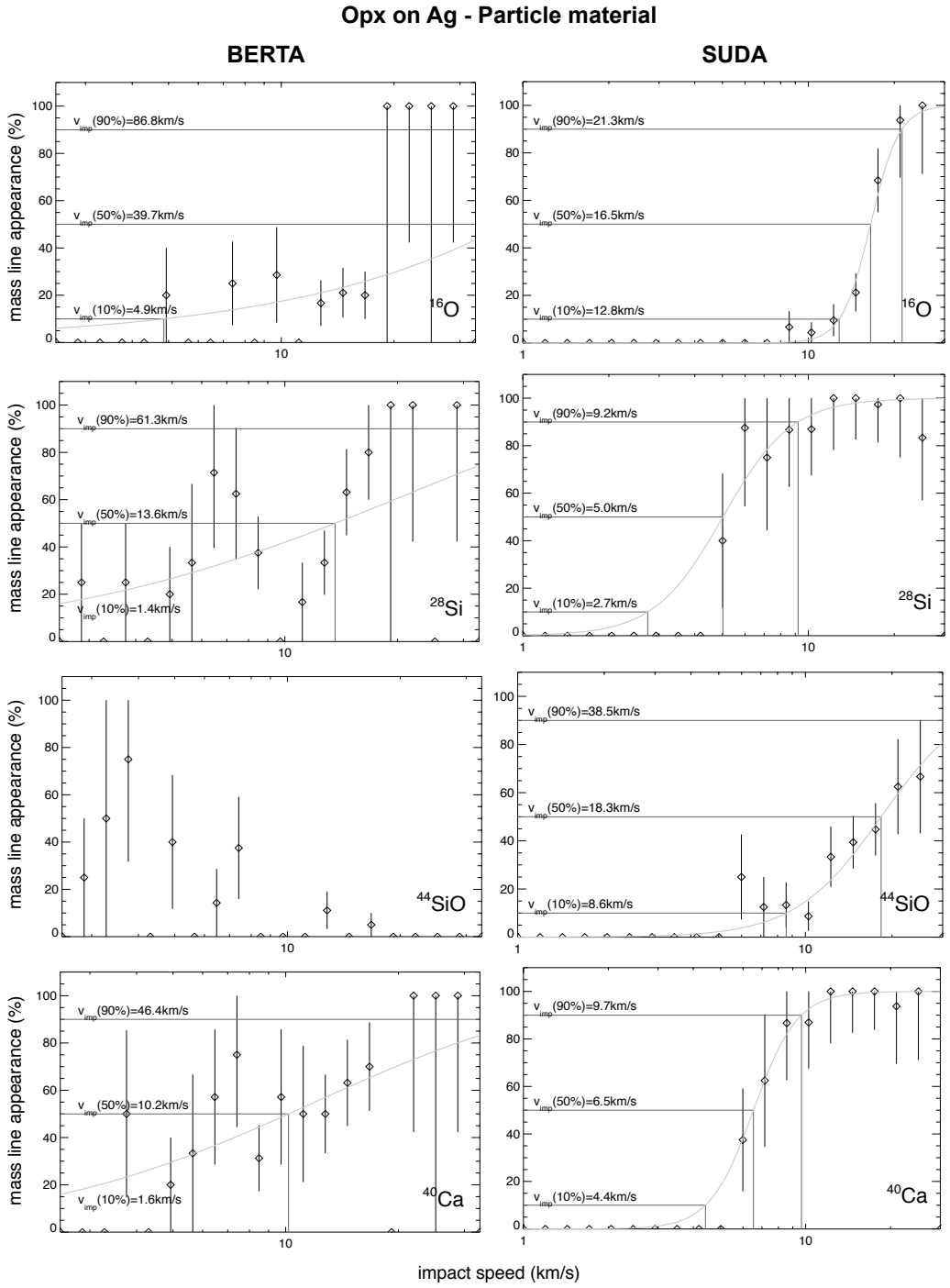

Figure D.18.: Mass line frequencies for the particle bulk material mass lines ^{16}O, ^{28}Si, ^{40}Kand ^{44}SiO for *Opx* particle impacts onto silver in dependence on the impact speed. The results of measurements with the *BERTA* mass spectrometer are compared to those obtained with the *SUDA* instrument. This dependency could be fitted with a *Fermi* distribution. The error bars represent the *Poisson* distribution of the measurement and depends therefore on the number of data points obtained in a specific range of the impact parameter in question.

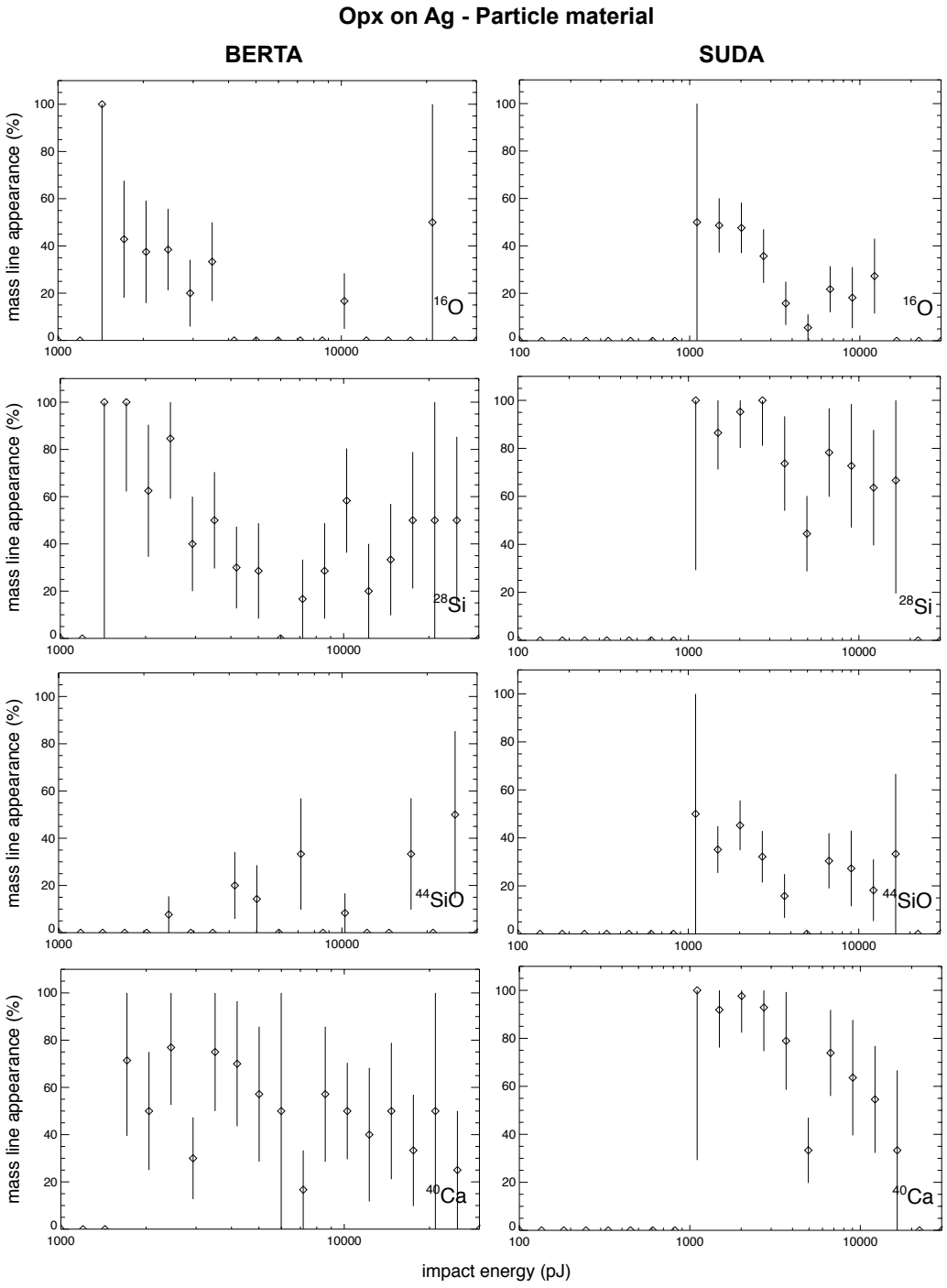

Figure D.19.: Mass line frequencies for the particle bulk material mass lines ^{16}O, ^{28}Si, ^{40}Kand ^{44}SiO for *Opx* particle impacts onto silver in dependence on the impact energy. The results of measurements with the *BERTA* mass spectrometer are compared to those obtained with the *SUDA* instrument. The result shows no significant dependence on the impact energy whatsoever.

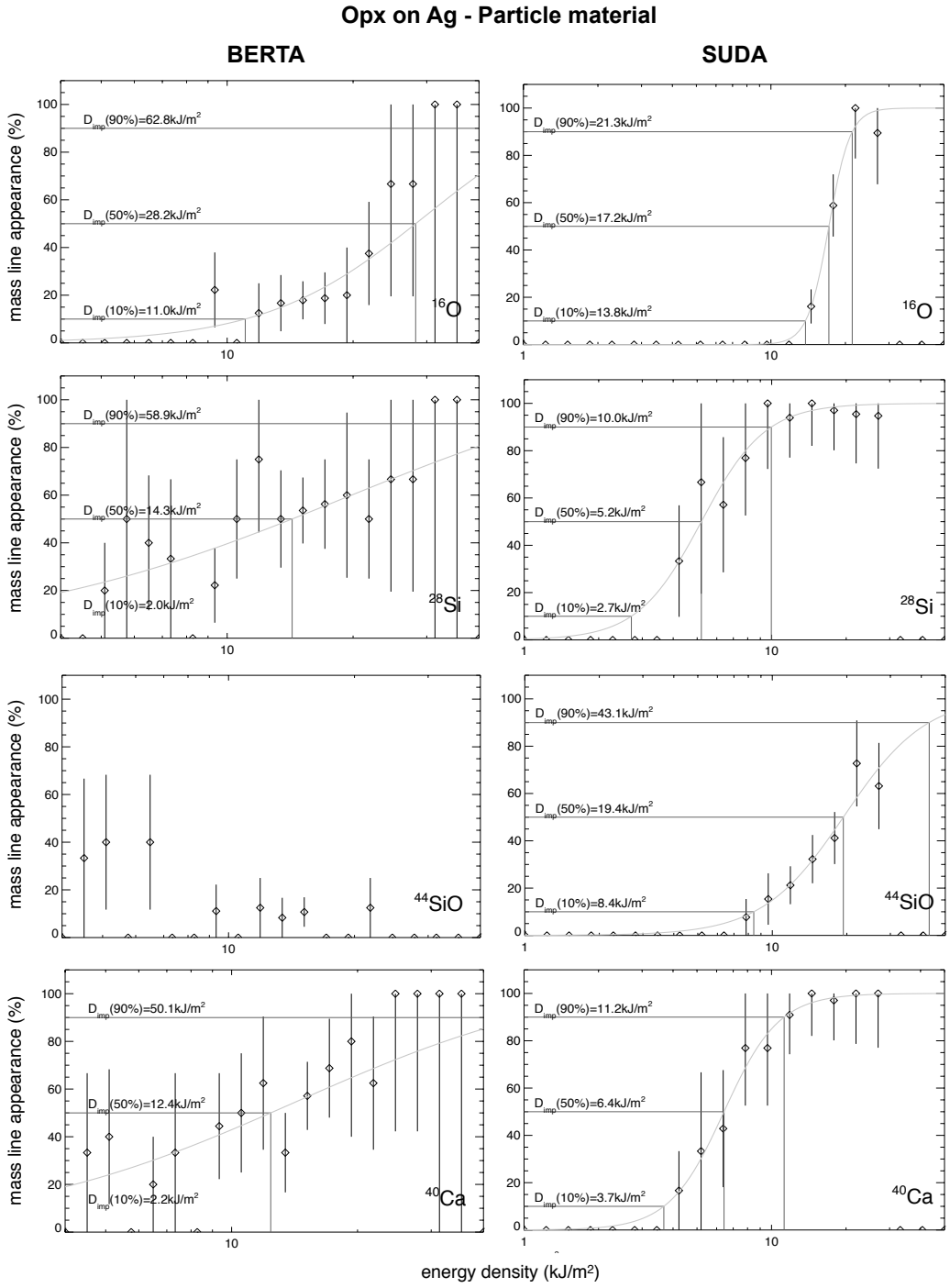

Figure D.20.: Mass line frequencies for the particle bulk material mass lines ^{16}O, ^{28}Si, ^{40}Kand ^{44}SiO for *Opx* particle impacts onto silver in dependence on the impact energy denstiy. The results of measurements with the *BERTA* mass spectrometer are compared to those obtained with the *SUDA* instrument. This dependency could be fitted with a *Fermi* distribution. The error bars represent the *Poisson* distribution of the measurement and depends therefore on the number of data points obtained in a specific range of the impact parameter in question.

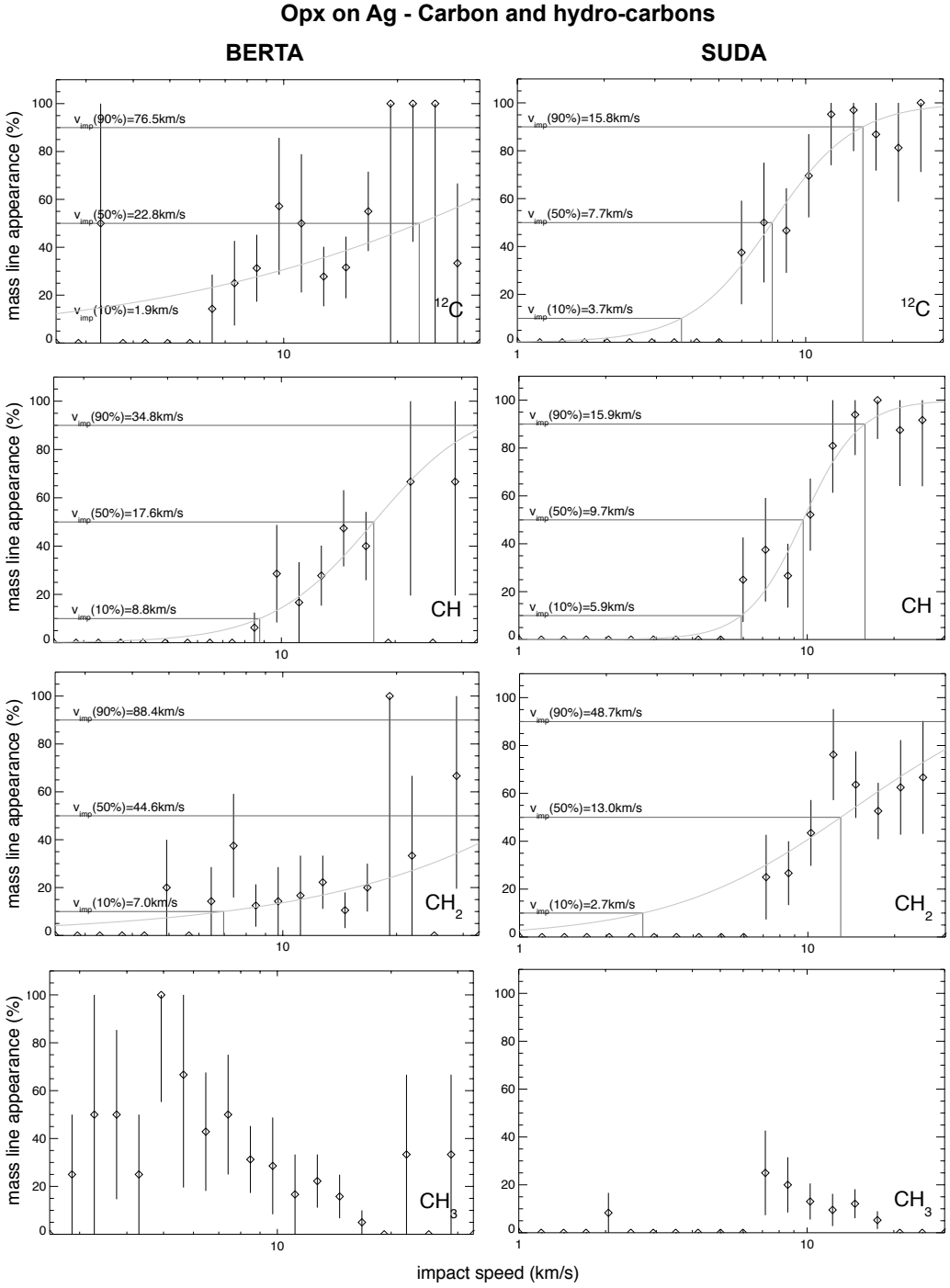

Figure D.21.: Mass line frequencies for the carbon and hydro-carbon mass lines C, CH, $CH_2$and CH_3 for *Opx* particle impacts onto silver in dependence on the impact speed. The results of measurements with the *BERTA* mass spectrometer are compared to those obtained with the *SUDA* instrument. This dependency could be fitted with a *Fermi* distribution. The error bars represent the *Poisson* distribution of the measurement and depends therefore on the number of data points obtained in a specific range of the impact parameter in question.

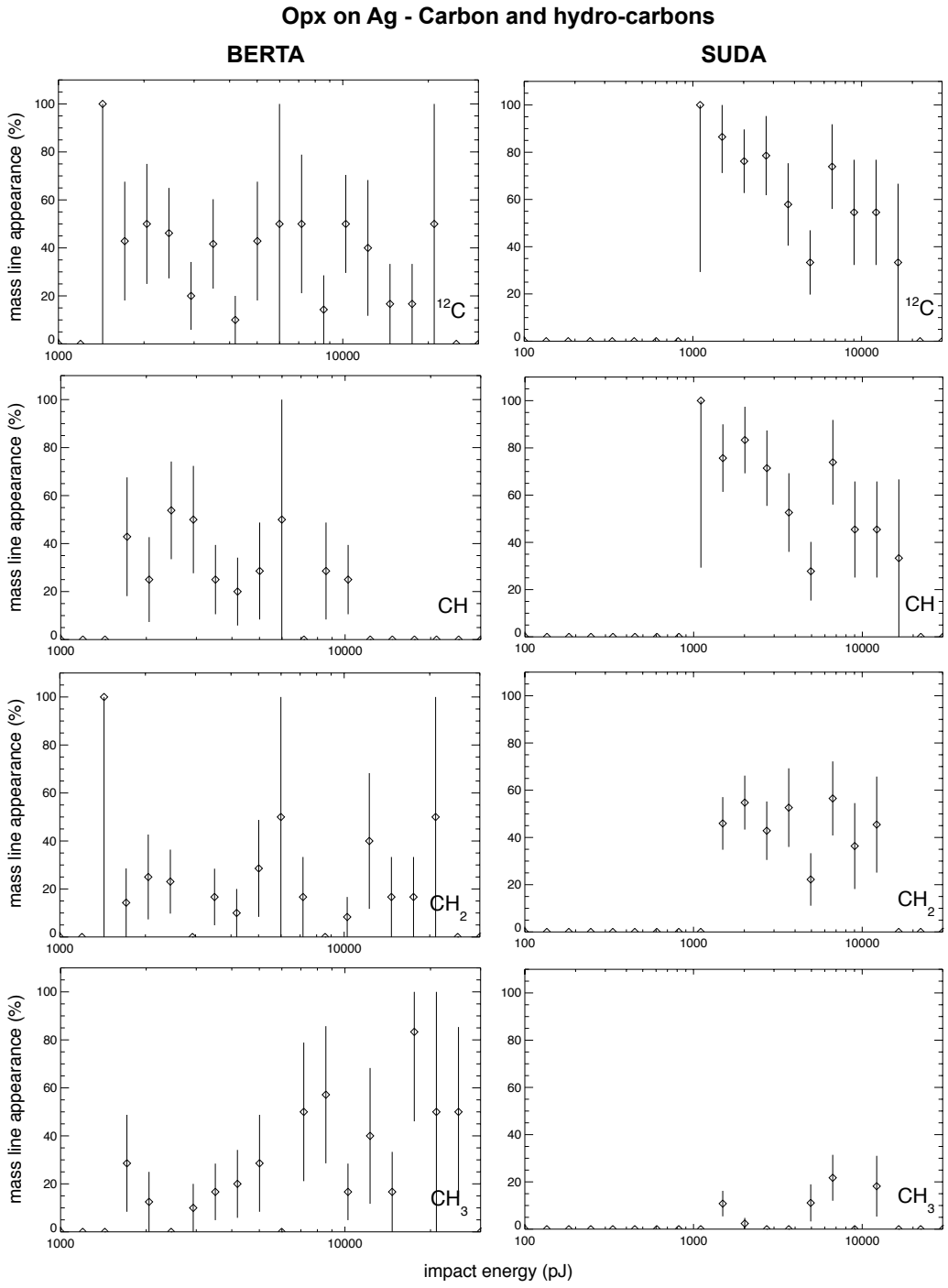

Figure D.22.: Mass line frequencies for the carbon and hydro-carbon mass lines C, CH, $CH_2$and CH_3 for *Opx* particle impacts onto silver in dependence on the impact energy. The results of measurements with the *BERTA* mass spectrometer are compared to those obtained with the *SUDA* instrument. The result shows no significant dependence on the impact energy whatsoever.

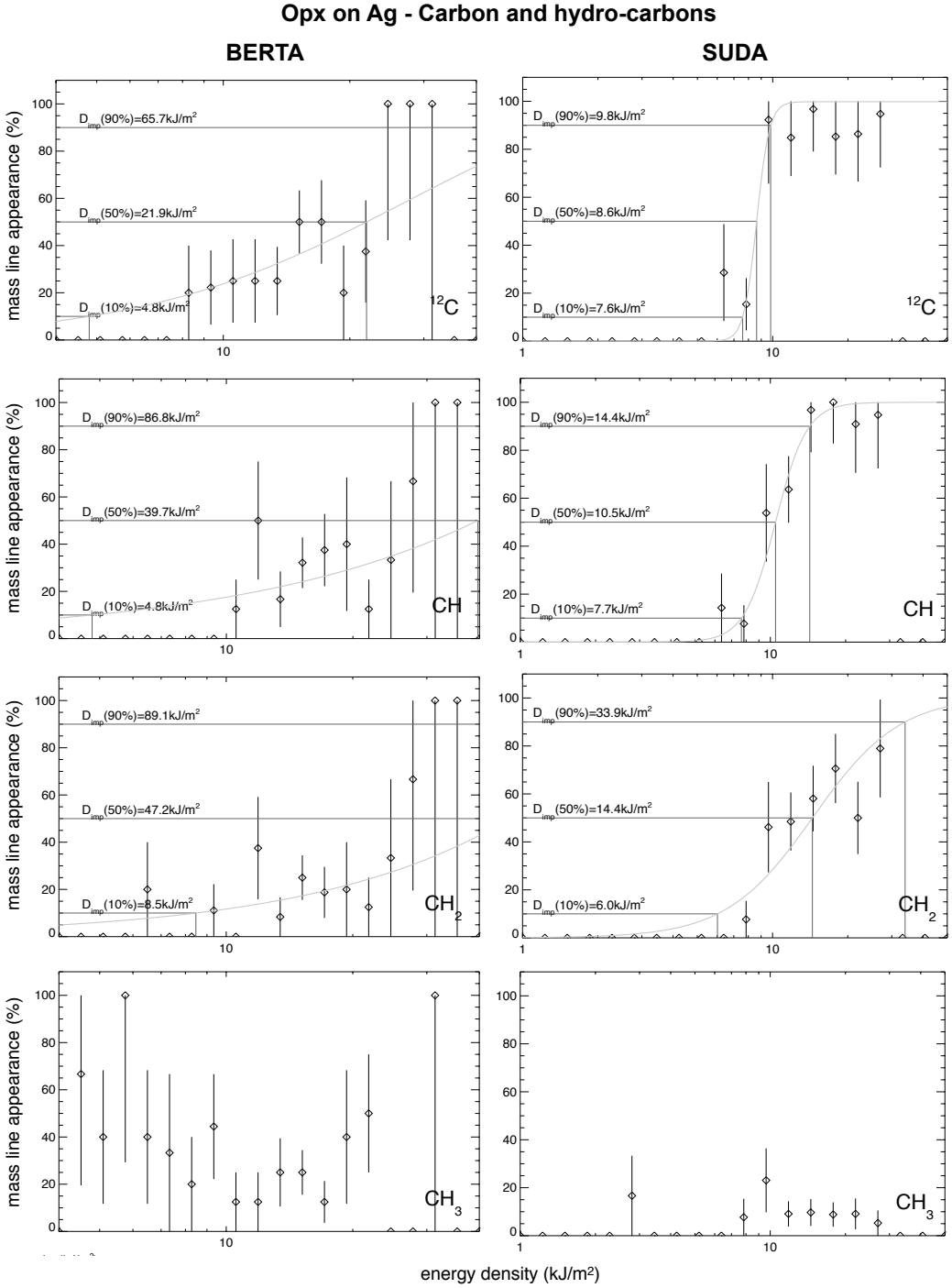

Figure D.23.: Mass line frequencies for the carbon and hydro-carbon mass lines C, CH, $CH_2$and CH_3 for *Opx* particle impacts onto silver in dependence on the impact energy density. The results of measurements with the *BERTA* mass spectrometer are compared to those obtained with the *SUDA* instrument. This dependency could be fitted with a *Fermi* distribution. The error bars represent the *Poisson* distribution of the measurement and depends therefore on the number of data points obtained in a specific range of the impact parameter in question.

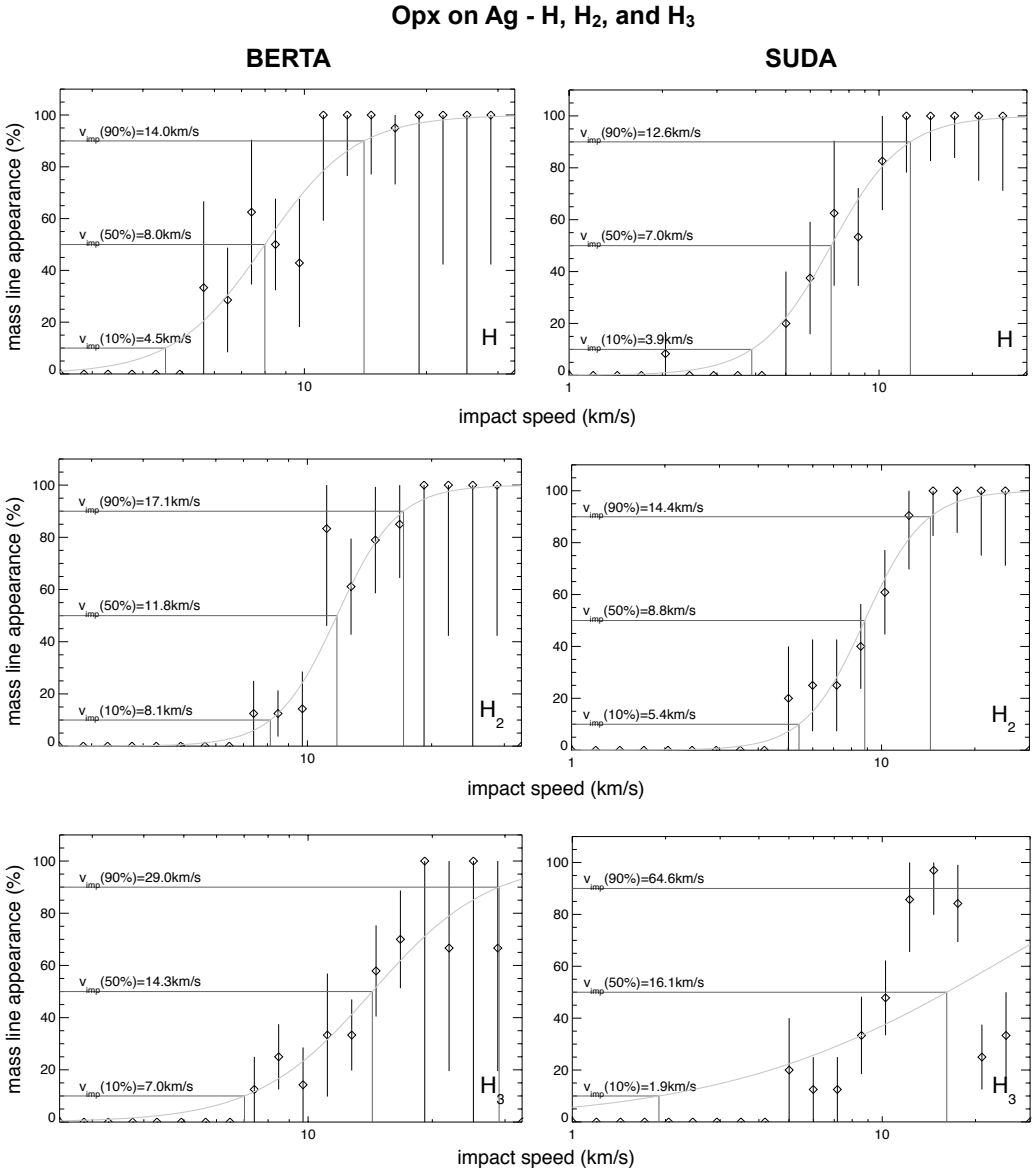

Figure D.24.: Mass line frequencies for atomic and molecular hydrogen, H, H_2 and H_3 for *Opx* particle impacts onto silver in dependence on the impact speed. The results of measurements with the *BERTA* mass spectrometer are compared to those obtained with the *SUDA* instrument. This dependency could be fitted with a *Fermi* distribution. The error bars represent the *Poisson* distribution of the measurement and depends therefore on the number of data points obtained in a specific range of the impact parameter in question.

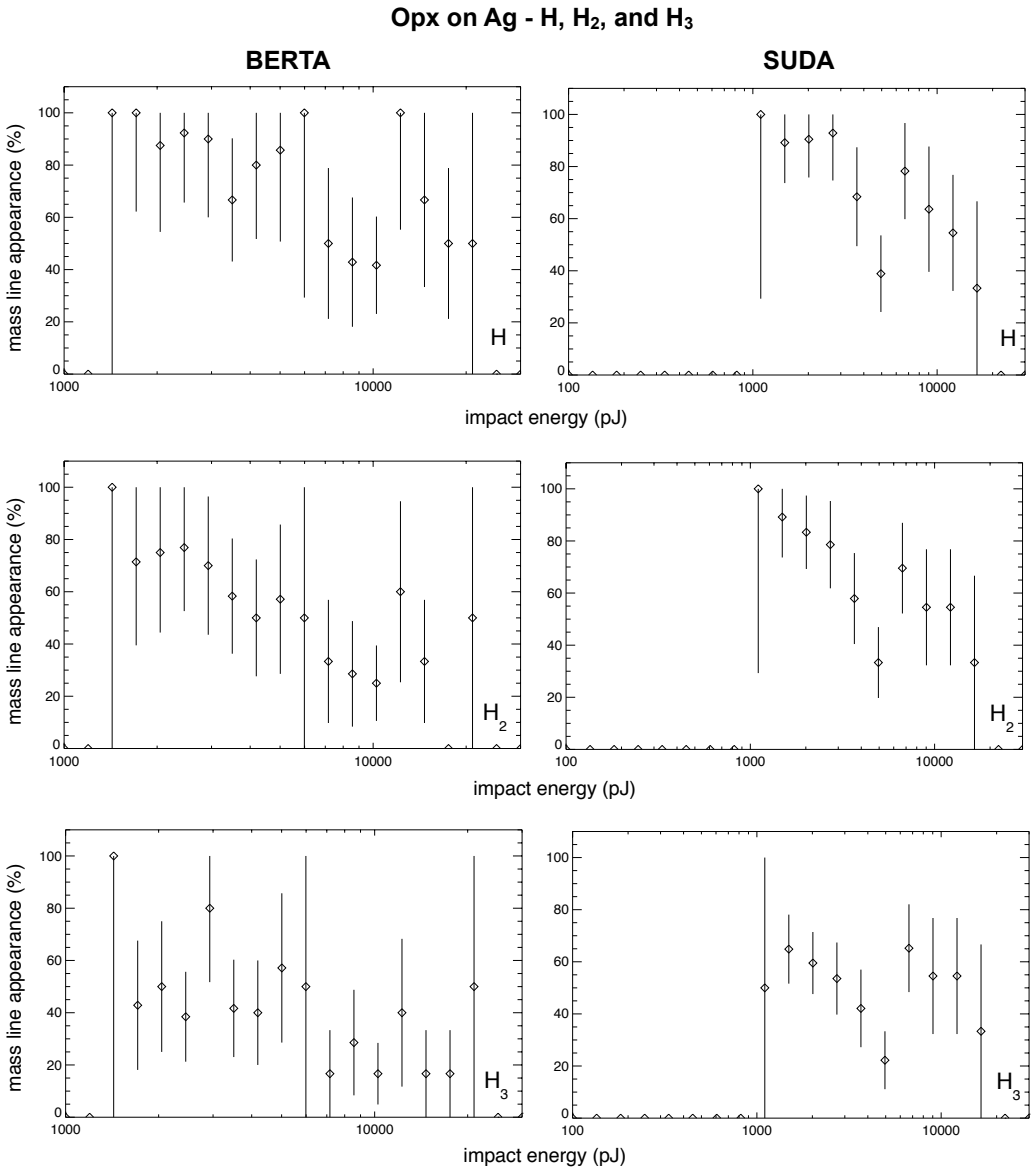

Figure D.25.: Mass line frequencies for atomic and molecular hydrogen, H, H_2 and H_3 for *Opx* particle impacts onto silver in dependence on the impact energy. The results of measurements with the *BERTA* mass spectrometer are compared to those obtained with the *SUDA* instrument. The result shows no significant dependence on the impact energy whatsoever.

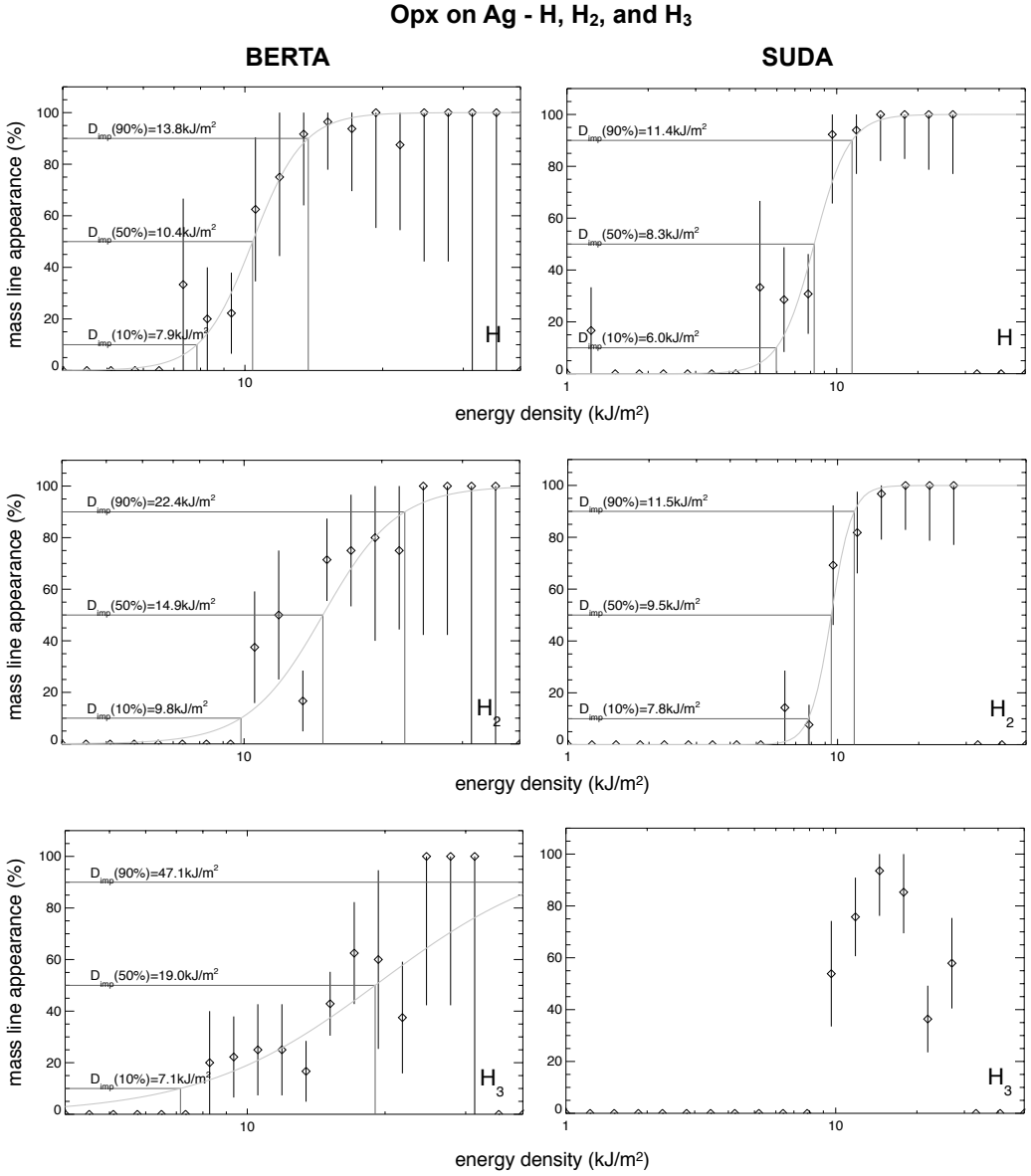

Figure D.26.: Mass line frequencies for atomic and molecular hydrogen, H, H_2 and H_3 for *Opx* particle impacts onto silver in dependence on the impact energy density. The results of measurements with the *BERTA* mass spectrometer are compared to those obtained with the *SUDA* instrument. This dependency could be fitted with a *Fermi* distribution. The error bars represent the *Poisson* distribution of the measurement and depends therefore on the number of data points obtained in a specific range of the impact parameter in question.

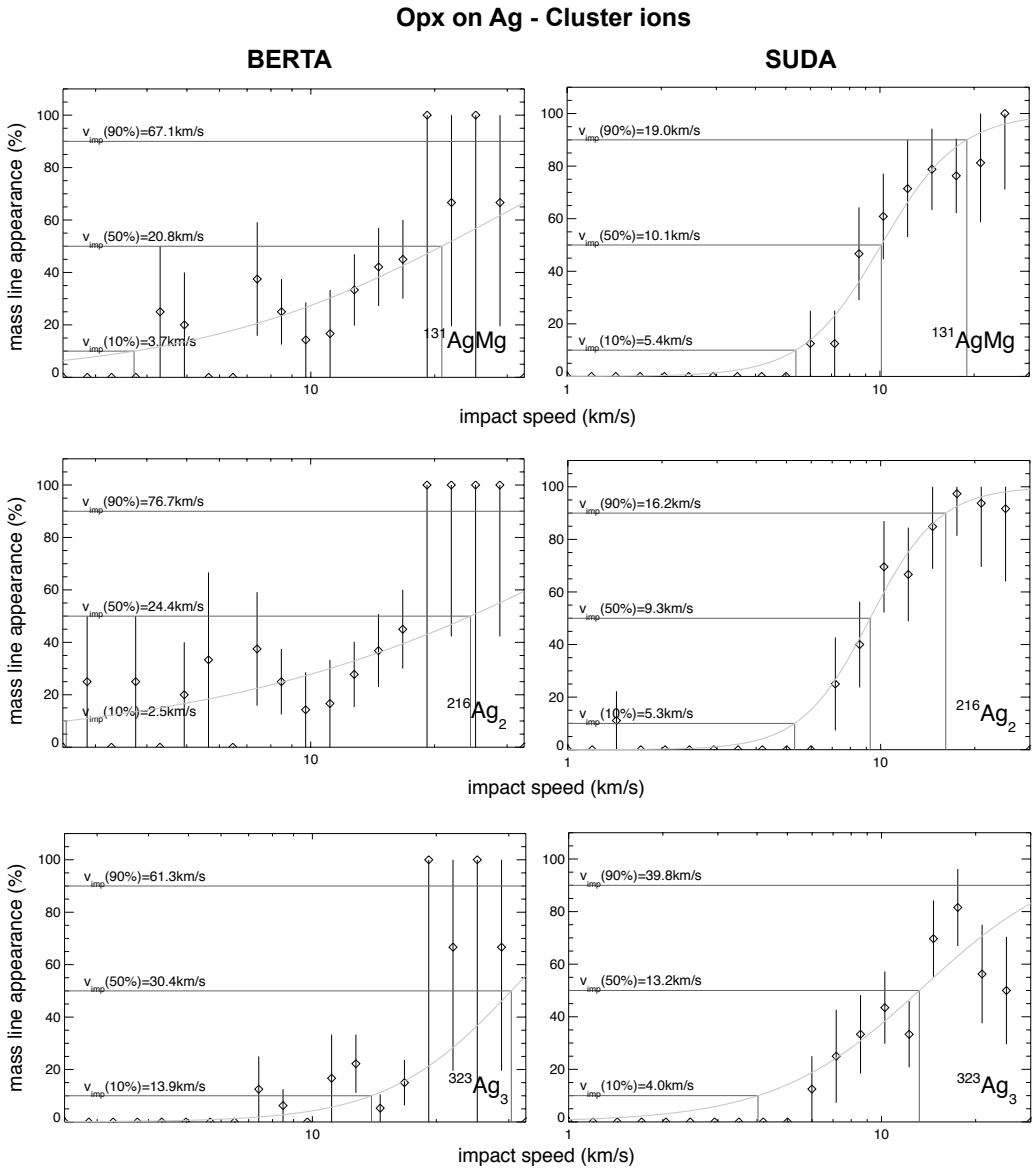

Figure D.27.: Mass line frequencies for cluster ion mass lines ^{163}AgFe, $^{216}Ag_2$, and $^{323}Ag_3$ for *Opx* particle impacts onto silver in dependence on the impact speed. The results of measurements with the *BERTA* mass spectrometer are compared to those obtained with the *SUDA* instrument. This dependency could be fitted with a *Fermi* distribution. The error bars represent the *Poisson* distribution of the measurement and depends therefore on the number of data points obtained in a specific range of the impact parameter in question.

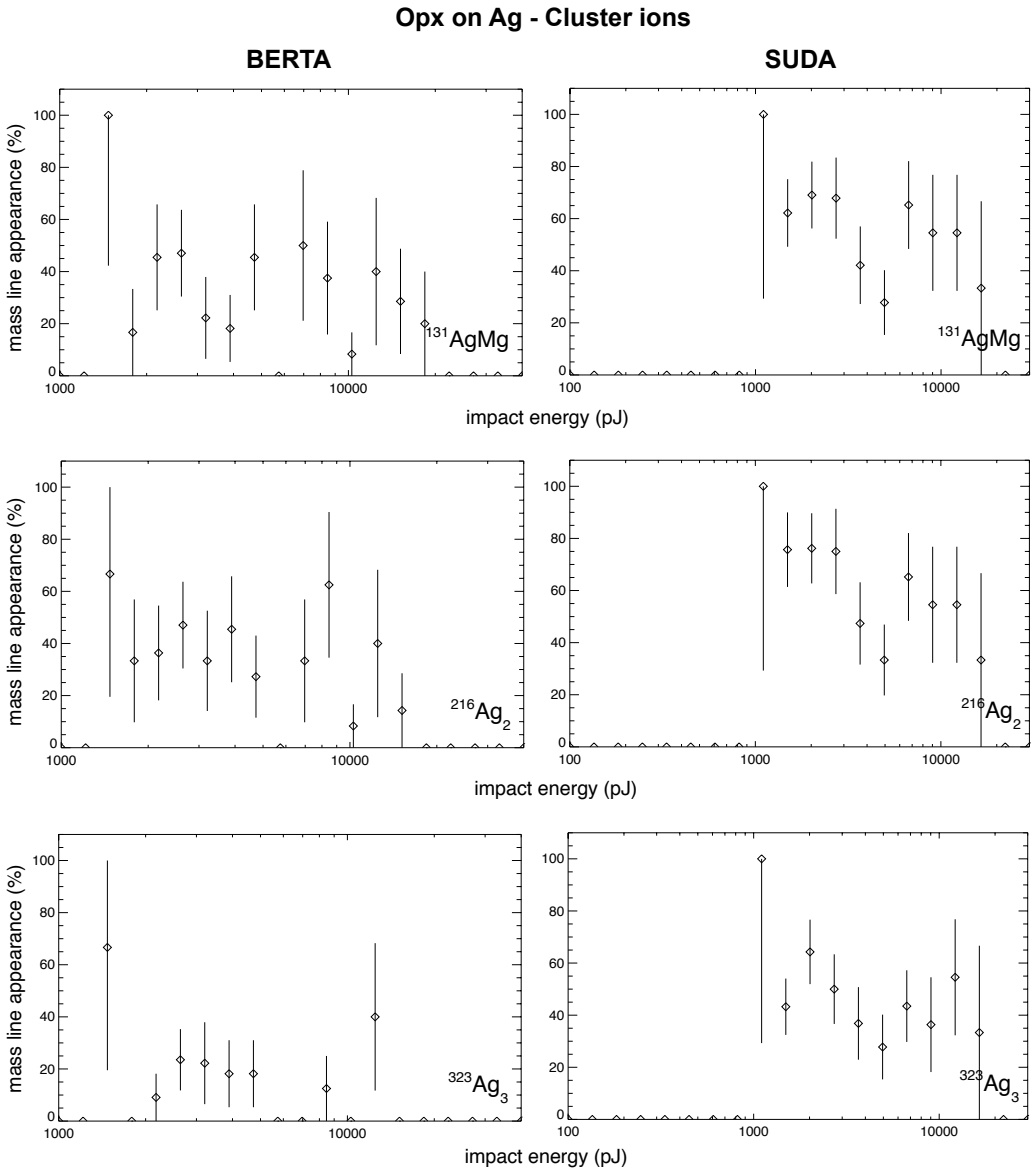

Figure D.28.: Mass line frequencies for cluster ion mass lines ^{163}AgFe, $^{216}Ag_2$, and $^{323}Ag_3$ for *Opx* particle impacts onto silver in dependence on the impact energy. The results of measurements with the *BERTA* mass spectrometer are compared to those obtained with the *SUDA* instrument.The result shows no significant dependence on the impact energy whatsoever.

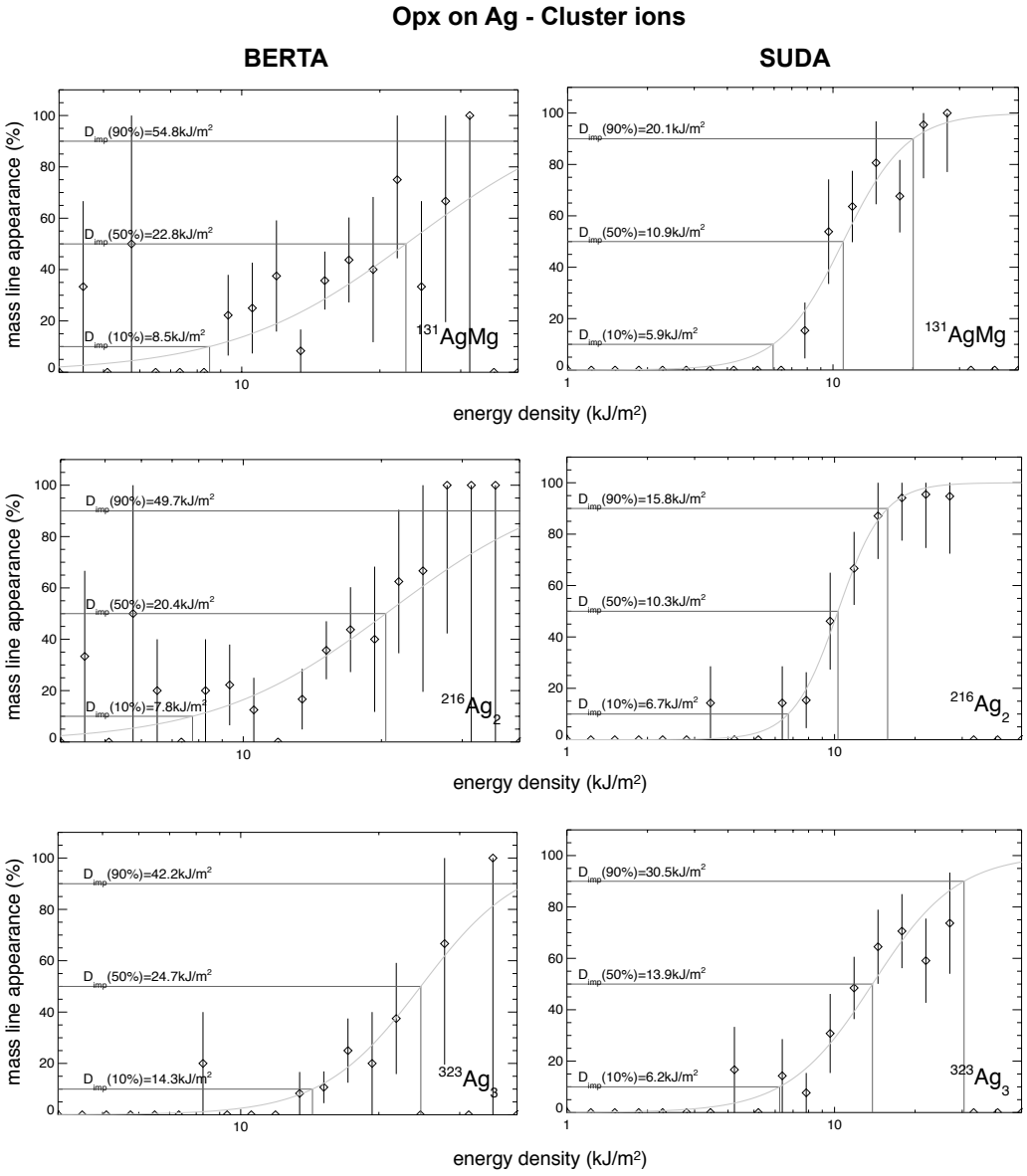

Figure D.29.: Mass line frequencies for cluster ion mass lines ^{163}AgFe, ^{216}Ag$_2$, and ^{323}Ag$_3$ for *Opx* particle impacts onto silver in dependence on the impact energy density. The results of measurements with the *BERTA* mass spectrometer are compared to those obtained with the *SUDA* instrument. This dependency could be fitted with a *Fermi* distribution. The error bars represent the *Poisson* distribution of the measurement and depends therefore on the number of data points obtained in a specific range of the impact parameter in question.

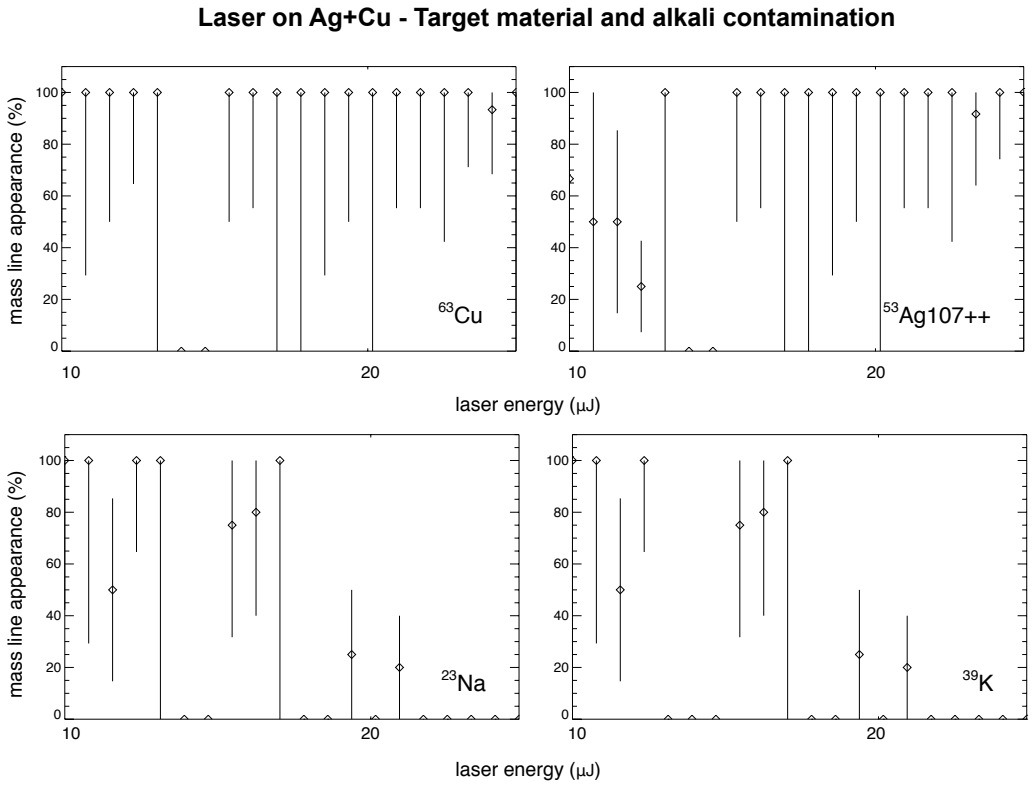

Figure D.30.: Mass line frequencies for the target material mass line ^{63}Cu and ^{107}Ag^{++} and for the alkali contamination mass lines ^{23}Na and ^{39}Kfor laser bombardment of a copper + silver target in dependence on the laser energy. The disappearance of the lines due to the increase of the laser energy is caused by the increasing difficulties of identifying the mass lines due to the broadening and saturation of the peaks.The result show no significant dependence on the laser energy whatsoever.

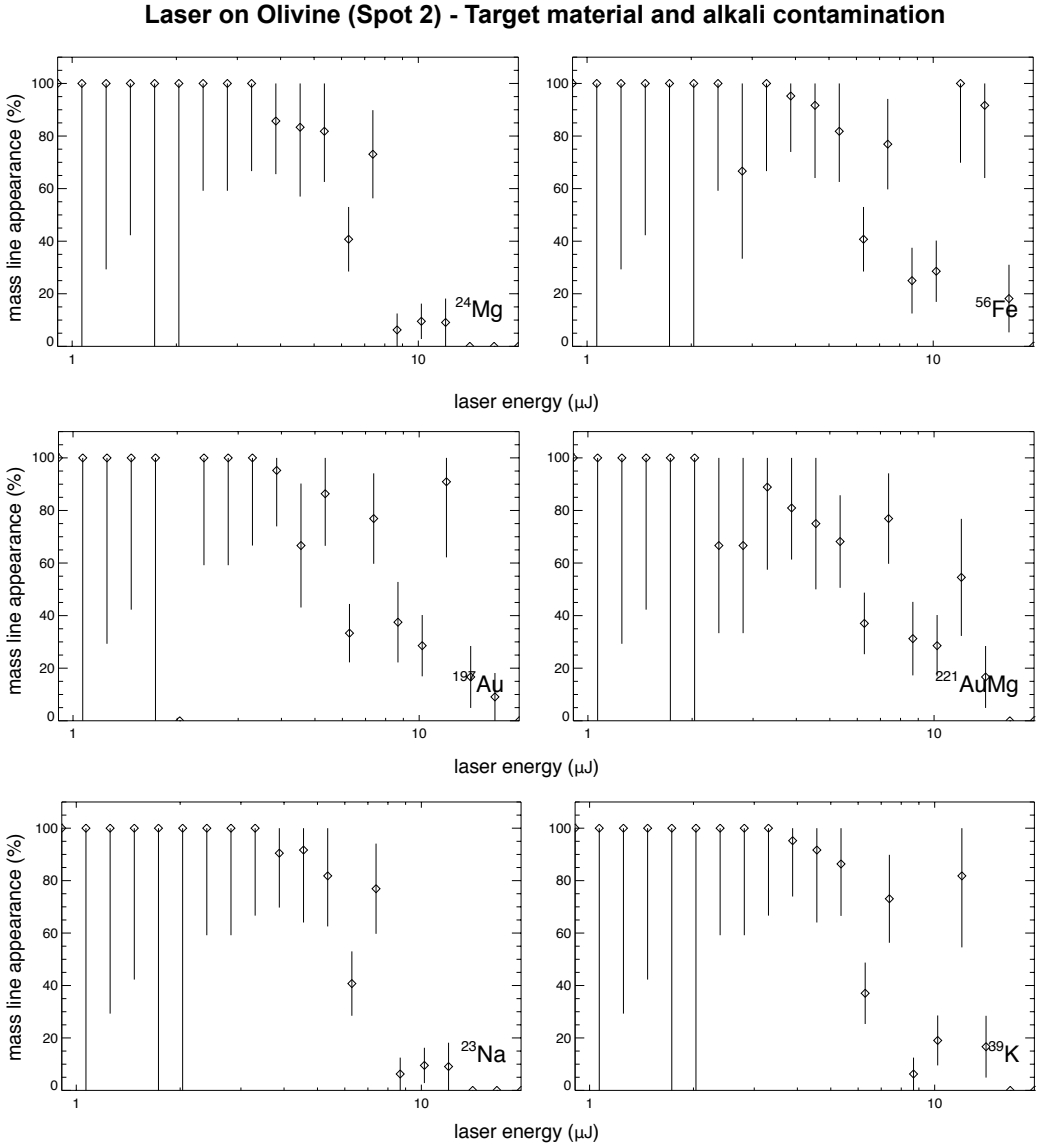

Figure D.31.: Mass line frequencies for the target material mass line ^{24}Mg and ^{56}Fe, the coating material line ^{196}Au, the cluster ion ^{221}AuMg and for the alkali contamination mass lines ^{23}Na and ^{39}Kfor laser bombardment of a gold coated Olivine target in dependence on the laser energy. The disappearance of the lines due to the increase of the laser energy is caused by the increasing difficulties of identifying the mass lines due to the broadening and saturation of the peaks.The result show no significant dependence on the laser energy whatsoever.

Table D.12.: line frequencies in dependence on the impact velocity for Fe+Ni particles impacting a Ag target. The speed or energy density dependence of the relative abundance can be fitted by a Fermi distribution for most of the cases. The curve can be described by the velocity or energy density the relative appearance exceeding 10 %, 50 %, and 90 % of the total spectra number.

	Impact velocity			Energy density		
line	10 %	50 %	90 %	10 %	50 %	90 %
H	$3.8\,\mathrm{km\,s^{-1}}$	$7.5\,\mathrm{km\,s^{-1}}$	$14.0\,\mathrm{km\,s^{-1}}$	$6.2\,\mathrm{kJm^{-2}}$	$8.8\,\mathrm{kJm^{-2}}$	$12.5\,\mathrm{kJm^{-2}}$
H_2	–	–	–	$7.7\,\mathrm{kJm^{-2}}$	$11.1\,\mathrm{kJm^{-2}}$	$16.0\,\mathrm{kJm^{-2}}$
H_3	–	–	–	–	–	–
^{12}C	$5.5\,\mathrm{km\,s^{-1}}$	$14.8\,\mathrm{km\,s^{-1}}$	$37.9\,\mathrm{km\,s^{-1}}$	$7.0\,\mathrm{kJm^{-2}}$	$15.1\,\mathrm{kJm^{-2}}$	$32.3\,\mathrm{kJm^{-2}}$
^{16}O	$12.1\,\mathrm{km\,s^{-1}}$	$23.9\,\mathrm{km\,s^{-1}}$	$46.3\,\mathrm{km\,s^{-1}}$	$11.4\,\mathrm{kJm^{-2}}$	$25.0\,\mathrm{kJm^{-2}}$	$52.2\,\mathrm{kJm^{-2}}$
^{23}Na	–	–	–	–	–	–
^{39}K	–	–	–	–	–	–
^{56}Fe	$3.6\,\mathrm{km\,s^{-1}}$	$15.4\,\mathrm{km\,s^{-1}}$	$51.8\,\mathrm{km\,s^{-1}}$	$3.3\,\mathrm{kJm^{-2}}$	$15.5\,\mathrm{kJm^{-2}}$	$54.3\,\mathrm{kJm^{-2}}$
^{107}Ag	$1.8\,\mathrm{km\,s^{-1}}$	$8.8\,\mathrm{km\,s^{-1}}$	$36.4\,\mathrm{km\,s^{-1}}$	$5.2\,\mathrm{kJm^{-2}}$	$11.5\,\mathrm{kJm^{-2}}$	$25.0\,\mathrm{kJm^{-2}}$
Fe+Ag	$12.2\,\mathrm{km\,s^{-1}}$	$38.4\,\mathrm{km\,s^{-1}}$	$79.8\,\mathrm{km\,s^{-1}}$	$14.1\,\mathrm{kJm^{-2}}$	$48.9\,\mathrm{kJm^{-2}}$	$58.1\,\mathrm{kJm^{-2}}$
Ag_2	$15.8\,\mathrm{km\,s^{-1}}$	$28.7\,\mathrm{km\,s^{-1}}$	$51.0\,\mathrm{km\,s^{-1}}$	$13.0\,\mathrm{kJm^{-2}}$	$32.0\,\mathrm{kJm^{-2}}$	$67.5\,\mathrm{kJm^{-2}}$
Ag_3	$19.3\,\mathrm{km\,s^{-1}}$	$35.1\,\mathrm{km\,s^{-1}}$	$61.3\,\mathrm{km\,s^{-1}}$	$17.6\,\mathrm{kJm^{-2}}$	$44.0\,\mathrm{kJm^{-2}}$	$91.2\,\mathrm{kJm^{-2}}$

Table D.13.: line frequencies in dependence on the impact velocity for Opx particle impacting a Ag target. The speed dependence of the relative abundance can be fitted by a Fermi distribution for most of the cases. The curve can be described by the velocity or energy density the relative appearance exceeding 10 %, 50 %, and 90 % of the total spectra number. To get more reliable results, the *BERTA* measurements are compared with data recorded by the *SUDA* instrument.

	BERTA			SUDA		
line	10 %	50 %	90 %	10 %	50 %	90 %
H	$4.5\,\mathrm{km\,s^{-1}}$	$8.0\,\mathrm{km\,s^{-1}}$	$14.0\,\mathrm{km\,s^{-1}}$	$3.9\,\mathrm{km\,s^{-1}}$	$7.0\,\mathrm{km\,s^{-1}}$	$12.8\,\mathrm{km\,s^{-1}}$
H_2	$8.1\,\mathrm{km\,s^{-1}}$	$11.8\,\mathrm{km\,s^{-1}}$	$17.1\,\mathrm{km\,s^{-1}}$	$5.4\,\mathrm{km\,s^{-1}}$	$8.8\,\mathrm{km\,s^{-1}}$	$14.4\,\mathrm{km\,s^{-1}}$
H_3	$7.0\,\mathrm{km\,s^{-1}}$	$14.3\,\mathrm{km\,s^{-1}}$	$29.0\,\mathrm{km\,s^{-1}}$	$1.9\,\mathrm{km\,s^{-1}}$	$16.1\,\mathrm{km\,s^{-1}}$	$64.4\,\mathrm{km\,s^{-1}}$
^{12}C	$1.9\,\mathrm{km\,s^{-1}}$	$22.8\,\mathrm{km\,s^{-1}}$	$78.5\,\mathrm{km\,s^{-1}}$	$3.7\,\mathrm{km\,s^{-1}}$	$7.7\,\mathrm{km\,s^{-1}}$	$15.8\,\mathrm{km\,s^{-1}}$
CH	$8.8\,\mathrm{km\,s^{-1}}$	$17.6\,\mathrm{km\,s^{-1}}$	$34.8\,\mathrm{km\,s^{-1}}$	$5.9\,\mathrm{km\,s^{-1}}$	$9.7\,\mathrm{km\,s^{-1}}$	$15.9\,\mathrm{km\,s^{-1}}$
CH_2	$7.0\,\mathrm{km\,s^{-1}}$	$44.6\,\mathrm{km\,s^{-1}}$	$88.4\,\mathrm{km\,s^{-1}}$	$2.7\,\mathrm{km\,s^{-1}}$	$13.0\,\mathrm{km\,s^{-1}}$	$48.7\,\mathrm{km\,s^{-1}}$
CH_3	–	–	–	–	–	–
^{16}O	$4.9\,\mathrm{km\,s^{-1}}$	$39.7\,\mathrm{km\,s^{-1}}$	$86.8\,\mathrm{km\,s^{-1}}$	$12.8\,\mathrm{km\,s^{-1}}$	$16.5\,\mathrm{km\,s^{-1}}$	$21.3\,\mathrm{km\,s^{-1}}$
^{23}Na	–	–	–	–	–	–
^{24}Mg	$8.8\,\mathrm{km\,s^{-1}}$	$15.0\,\mathrm{km\,s^{-1}}$	$25.4\,\mathrm{km\,s^{-1}}$	$2.3\,\mathrm{km\,s^{-1}}$	$4.7\,\mathrm{km\,s^{-1}}$	$9.5\,\mathrm{km\,s^{-1}}$
^{27}Al	$2.7\,\mathrm{km\,s^{-1}}$	$12.4\,\mathrm{km\,s^{-1}}$	$45.4\,\mathrm{km\,s^{-1}}$	$1.7\,\mathrm{km\,s^{-1}}$	$3.2\,\mathrm{km\,s^{-1}}$	$5.9\,\mathrm{km\,s^{-1}}$
^{28}Si	$1.4\,\mathrm{km\,s^{-1}}$	$13.6\,\mathrm{km\,s^{-1}}$	$61.3\,\mathrm{km\,s^{-1}}$	$2.7\,\mathrm{km\,s^{-1}}$	$5.0\,\mathrm{km\,s^{-1}}$	$9.2\,\mathrm{km\,s^{-1}}$
^{39}K	–	–	–	–	–	–
^{40}Ca	$1.6\,\mathrm{km\,s^{-1}}$	$10.2\,\mathrm{km\,s^{-1}}$	$46.4\,\mathrm{km\,s^{-1}}$	$4.4\,\mathrm{km\,s^{-1}}$	$6.5\,\mathrm{km\,s^{-1}}$	$9.7\,\mathrm{km\,s^{-1}}$
SiO	–	–	–	$8.6\,\mathrm{km\,s^{-1}}$	$18.3\,\mathrm{km\,s^{-1}}$	$38.5\,\mathrm{km\,s^{-1}}$
^{55}Mn	$2.5\,\mathrm{km\,s^{-1}}$	$31.2\,\mathrm{km\,s^{-1}}$	$84.1\,\mathrm{km\,s^{-1}}$	$13.9\,\mathrm{km\,s^{-1}}$	$46.2\,\mathrm{km\,s^{-1}}$	$56.2\,\mathrm{km\,s^{-1}}$
^{56}Fe	$2.1\,\mathrm{km\,s^{-1}}$	$22.1\,\mathrm{km\,s^{-1}}$	$74.7\,\mathrm{km\,s^{-1}}$	$3.2\,\mathrm{km\,s^{-1}}$	$7.8\,\mathrm{km\,s^{-1}}$	$18.8\,\mathrm{km\,s^{-1}}$
^{107}Ag	$0.9\,\mathrm{km\,s^{-1}}$	$4.2\,\mathrm{km\,s^{-1}}$	$19.1\,\mathrm{km\,s^{-1}}$	$0.8\,\mathrm{km\,s^{-1}}$	$2.1\,\mathrm{km\,s^{-1}}$	$5.5\,\mathrm{km\,s^{-1}}$
AgMg	$3.7\,\mathrm{km\,s^{-1}}$	$20.8\,\mathrm{km\,s^{-1}}$	$67.1\,\mathrm{km\,s^{-1}}$	$5.4\,\mathrm{km\,s^{-1}}$	$10.1\,\mathrm{km\,s^{-1}}$	$19.0\,\mathrm{km\,s^{-1}}$
Ag_2	$2.5\,\mathrm{km\,s^{-1}}$	$24.4\,\mathrm{km\,s^{-1}}$	$76.7\,\mathrm{km\,s^{-1}}$	$5.3\,\mathrm{km\,s^{-1}}$	$9.3\,\mathrm{km\,s^{-1}}$	$16.2\,\mathrm{km\,s^{-1}}$
Ag_3	$13.9\,\mathrm{km\,s^{-1}}$	$30.4\,\mathrm{km\,s^{-1}}$	$61.3\,\mathrm{km\,s^{-1}}$	$4.0\,\mathrm{km\,s^{-1}}$	$13.2\,\mathrm{km\,s^{-1}}$	$39.8\,\mathrm{km\,s^{-1}}$

Table D.14.: line frequencies in dependence on the energy densities for Opx particle impacting a Ag target. line frequencies in dependence on the impact energy density for Opx particle impacting a Ag target. The energy density dependence of the relative abundance can be fitted by a Fermi distribution for most of the cases. The curve can be described by the velocity or energy density the relative appearance exceeding 10 %, 50 %, and 90 % of the total spectra number. To get more reliable results, the *BERTA* measurements are compared with data recorded by the *SUDA* instrument.

	BERTA			SUDA		
line	10 %	50 %	90 %	10 %	50 %	90 %
H	$7.9\,\mathrm{kJm^{-2}}$	$10.4\,\mathrm{kJm^{-2}}$	$13.8\,\mathrm{kJm^{-2}}$	$6.0\,\mathrm{kJm^{-2}}$	$8.5\,\mathrm{kJm^{-2}}$	$11.4\,\mathrm{kJm^{-2}}$
H_2	$9.6\,\mathrm{kJm^{-2}}$	$14.9\,\mathrm{kJm^{-2}}$	$22.4\,\mathrm{kJm^{-2}}$	$7.8\,\mathrm{kJm^{-2}}$	$9.5\,\mathrm{kJm^{-2}}$	$11.5\,\mathrm{kJm^{-2}}$
H_3	$7.1\,\mathrm{kJm^{-2}}$	$19.0\,\mathrm{kJm^{-2}}$	$47.1\,\mathrm{kJm^{-2}}$	–	–	–
^{12}C	$4.6\,\mathrm{kJm^{-2}}$	$21.9\,\mathrm{kJm^{-2}}$	$65.7\,\mathrm{kJm^{-2}}$	$7.6\,\mathrm{kJm^{-2}}$	$8.6\,\mathrm{kJm^{-2}}$	$9.8\,\mathrm{kJm^{-2}}$
CH	$4.8\,\mathrm{kJm^{-2}}$	$39.7\,\mathrm{kJm^{-2}}$	$86.8\,\mathrm{kJm^{-2}}$	$7.7\,\mathrm{kJm^{-2}}$	$10.5\,\mathrm{kJm^{-2}}$	$14.4\,\mathrm{kJm^{-2}}$
CH_2	$8.5\,\mathrm{kJm^{-2}}$	$47.2\,\mathrm{kJm^{-2}}$	$59.1\,\mathrm{kJm^{-2}}$	$6.0\,\mathrm{kJm^{-2}}$	$14.4\,\mathrm{kJm^{-2}}$	$33.9\,\mathrm{kJm^{-2}}$
CH_3	–	–	–	–	–	–
^{16}O	$11.0\,\mathrm{kJm^{-2}}$	$28.2\,\mathrm{kJm^{-2}}$	$62.8\,\mathrm{kJm^{-2}}$	$13.8\,\mathrm{kJm^{-2}}$	$17.2\,\mathrm{kJm^{-2}}$	$21.3\,\mathrm{kJm^{-2}}$
^{23}Na	–	–	–	–	–	–
^{24}Mg	$3.9\,\mathrm{kJm^{-2}}$	$30.2\,\mathrm{kJm^{-2}}$	$80.6\,\mathrm{kJm^{-2}}$	$1.2\,\mathrm{kJm^{-2}}$	$3.0\,\mathrm{kJm^{-2}}$	$7.6\,\mathrm{kJm^{-2}}$
^{27}Al	$1.7\,\mathrm{kJm^{-2}}$	$29.0\,\mathrm{kJm^{-2}}$	$82.8\,\mathrm{kJm^{-2}}$	$2.7\,\mathrm{kJm^{-2}}$	$3.2\,\mathrm{kJm^{-2}}$	$3.9\,\mathrm{kJm^{-2}}$
^{28}Si	$2.0\,\mathrm{kJm^{-2}}$	$14.3\,\mathrm{kJm^{-2}}$	$58.9\,\mathrm{kJm^{-2}}$	$2.7\,\mathrm{kJm^{-2}}$	$5.2\,\mathrm{kJm^{-2}}$	$10.0\,\mathrm{kJm^{-2}}$
^{39}K	–	–	–	–	–	–
^{40}Ca	$2.2\,\mathrm{kJm^{-2}}$	$12.4\,\mathrm{kJm^{-2}}$	$50.1\,\mathrm{kJm^{-2}}$	$3.7\,\mathrm{kJm^{-2}}$	$6.4\,\mathrm{kJm^{-2}}$	$11.2\,\mathrm{kJm^{-2}}$
SiO	–	–	–	$5.4\,\mathrm{kJm^{-2}}$	$19.4\,\mathrm{kJm^{-2}}$	$43.1\,\mathrm{kJm^{-2}}$
^{55}Mn	$6.3\,\mathrm{kJm^{-2}}$	$43.3\,\mathrm{kJm^{-2}}$	$88.0\,\mathrm{kJm^{-2}}$	$16.2\,\mathrm{kJm^{-2}}$	$46.2\,\mathrm{kJm^{-2}}$	$54.9\,\mathrm{kJm^{-2}}$
^{56}Fe	$1.7\,\mathrm{kJm^{-2}}$	$20.0\,\mathrm{kJm^{-2}}$	$73.3\,\mathrm{kJm^{-2}}$	$4.1\,\mathrm{kJm^{-2}}$	$8.7\,\mathrm{kJm^{-2}}$	$18.4\,\mathrm{kJm^{-2}}$
^{107}Ag	$1.6\,\mathrm{kJm^{-2}}$	$6.2\,\mathrm{kJm^{-2}}$	$23.0\,\mathrm{kJm^{-2}}$	$1.1\,\mathrm{kJm^{-2}}$	$2.5\,\mathrm{kJm^{-2}}$	$5.7\,\mathrm{kJm^{-2}}$
AgMg	$8.5\,\mathrm{kJm^{-2}}$	$22.8\,\mathrm{kJm^{-2}}$	$54.8\,\mathrm{kJm^{-2}}$	$5.9\,\mathrm{kJm^{-2}}$	$10.9\,\mathrm{kJm^{-2}}$	$20.1\,\mathrm{kJm^{-2}}$
Ag_2	$7.8\,\mathrm{kJm^{-2}}$	$20.4\,\mathrm{kJm^{-2}}$	$49.7\,\mathrm{kJm^{-2}}$	$6.7\,\mathrm{kJm^{-2}}$	$10.3\,\mathrm{kJm^{-2}}$	$15.8\,\mathrm{kJm^{-2}}$
Ag_3	$14.3\,\mathrm{kJm^{-2}}$	$24.7\,\mathrm{kJm^{-2}}$	$42.2\,\mathrm{kJm^{-2}}$	$6.2\,\mathrm{kJm^{-2}}$	$13.9\,\mathrm{kJm^{-2}}$	$30.5\,\mathrm{kJm^{-2}}$

D.4.1. Mass line widths in dependence on the impact parameters

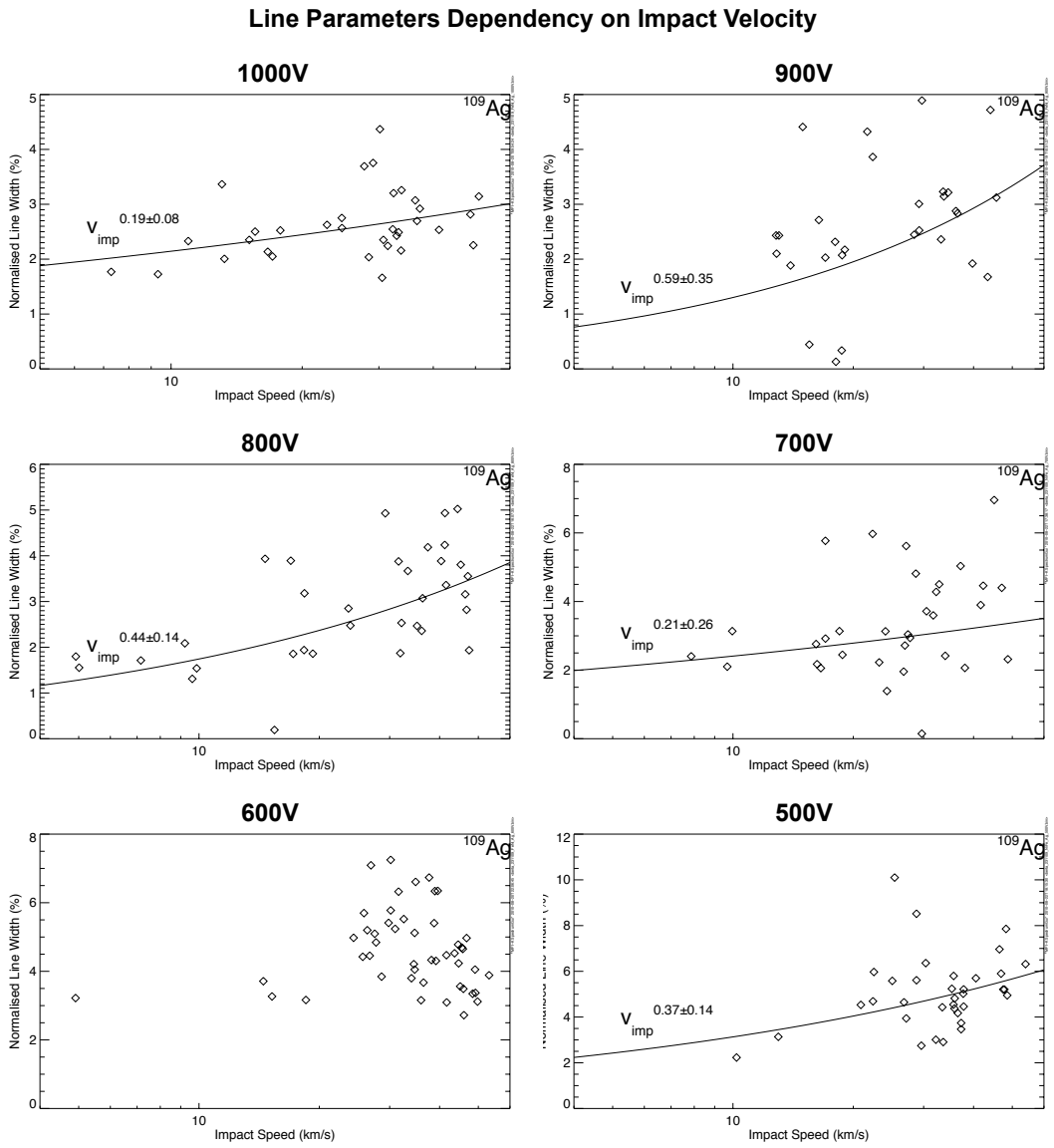

Figure D.32.: Shots with iron particles on silver: line widths of silver ions

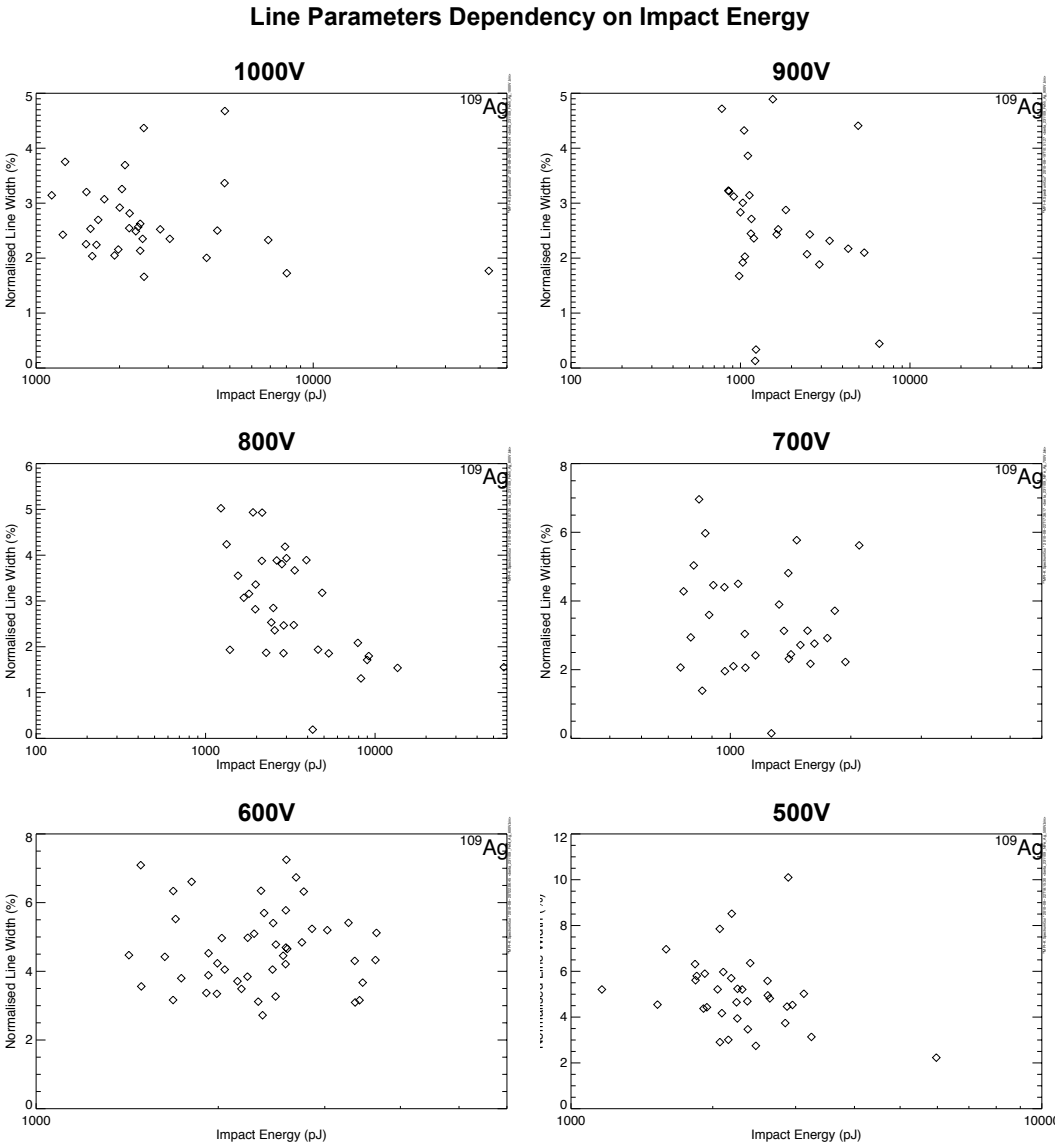

Figure D.33.: Shots with iron particles on silver: line widths of silver ions

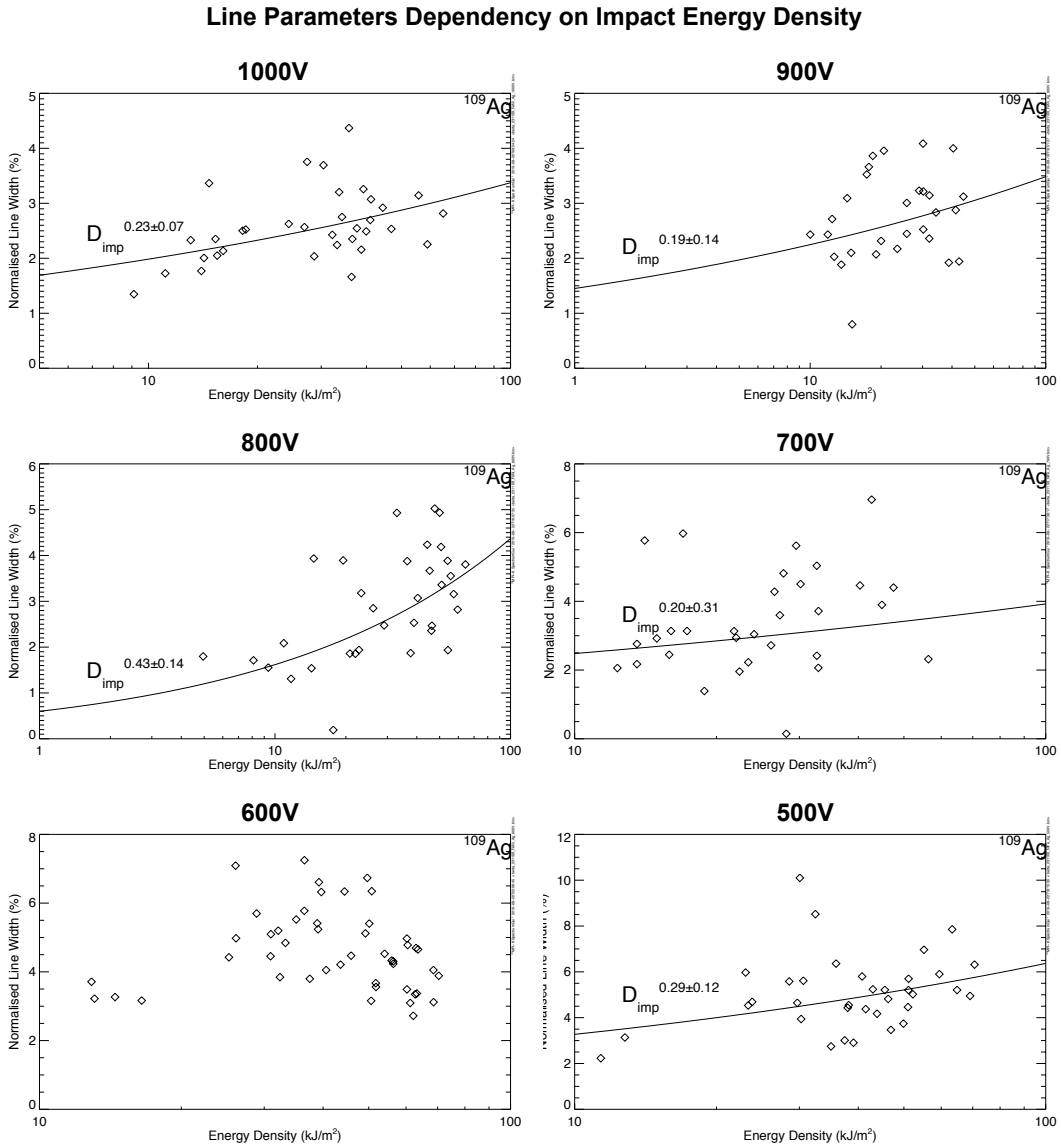

Figure D.34.: Shots with iron particles on silver: line widths of silver ions

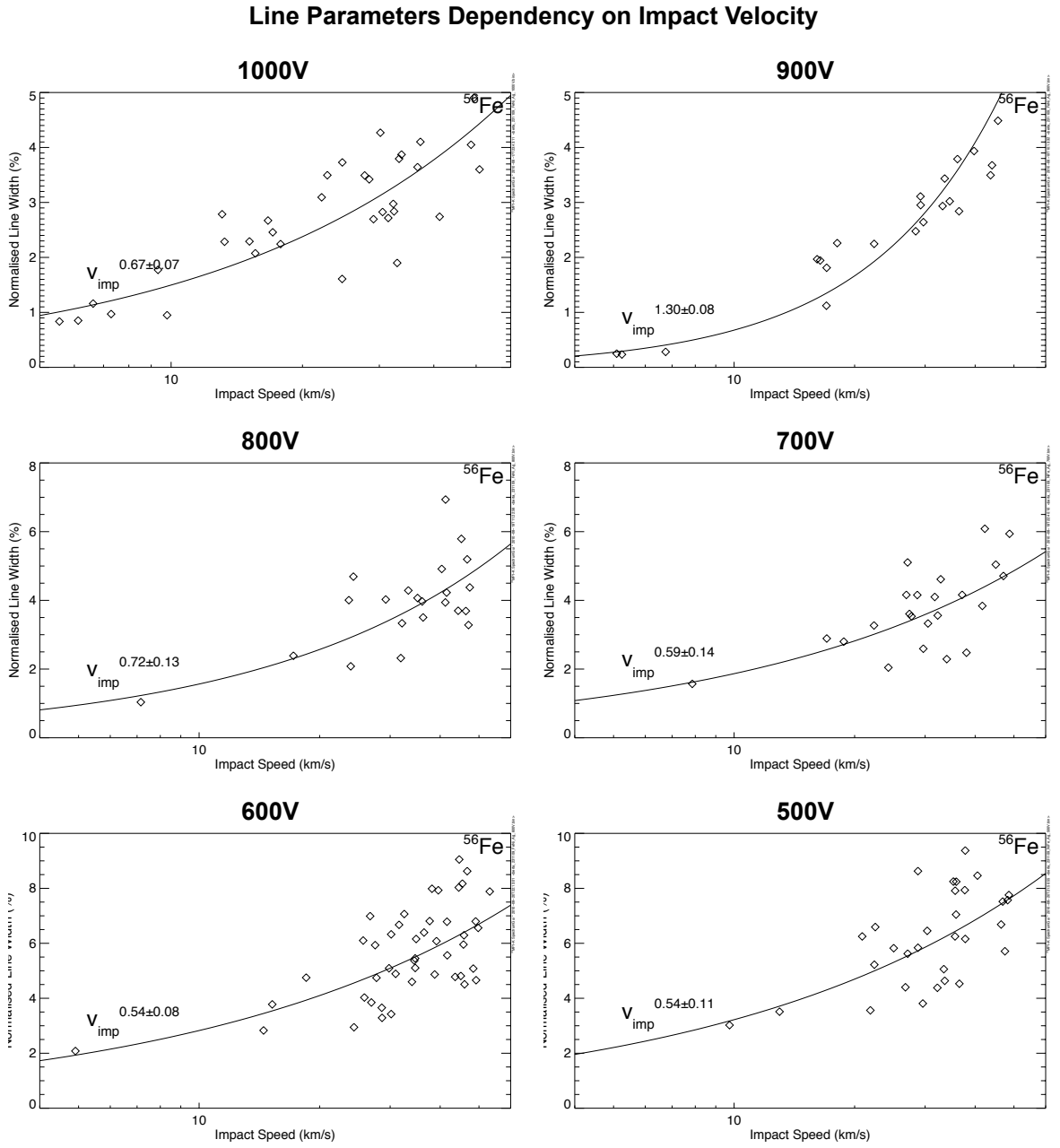

Figure D.35.: Shots with iron particles on silver: line widths of iron ions

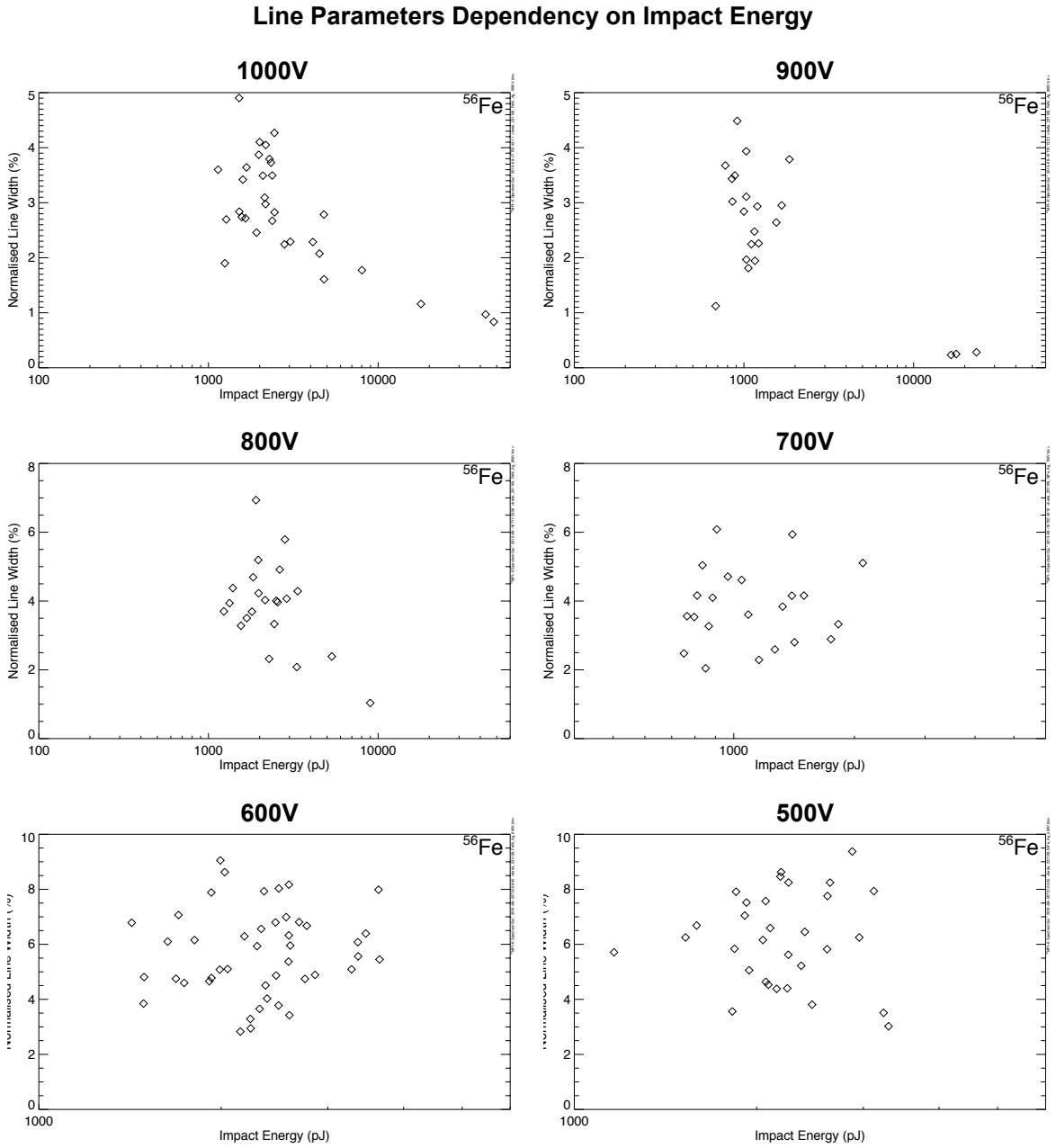

Figure D.36.: Shots with iron particles on silver: line widths of iron ions

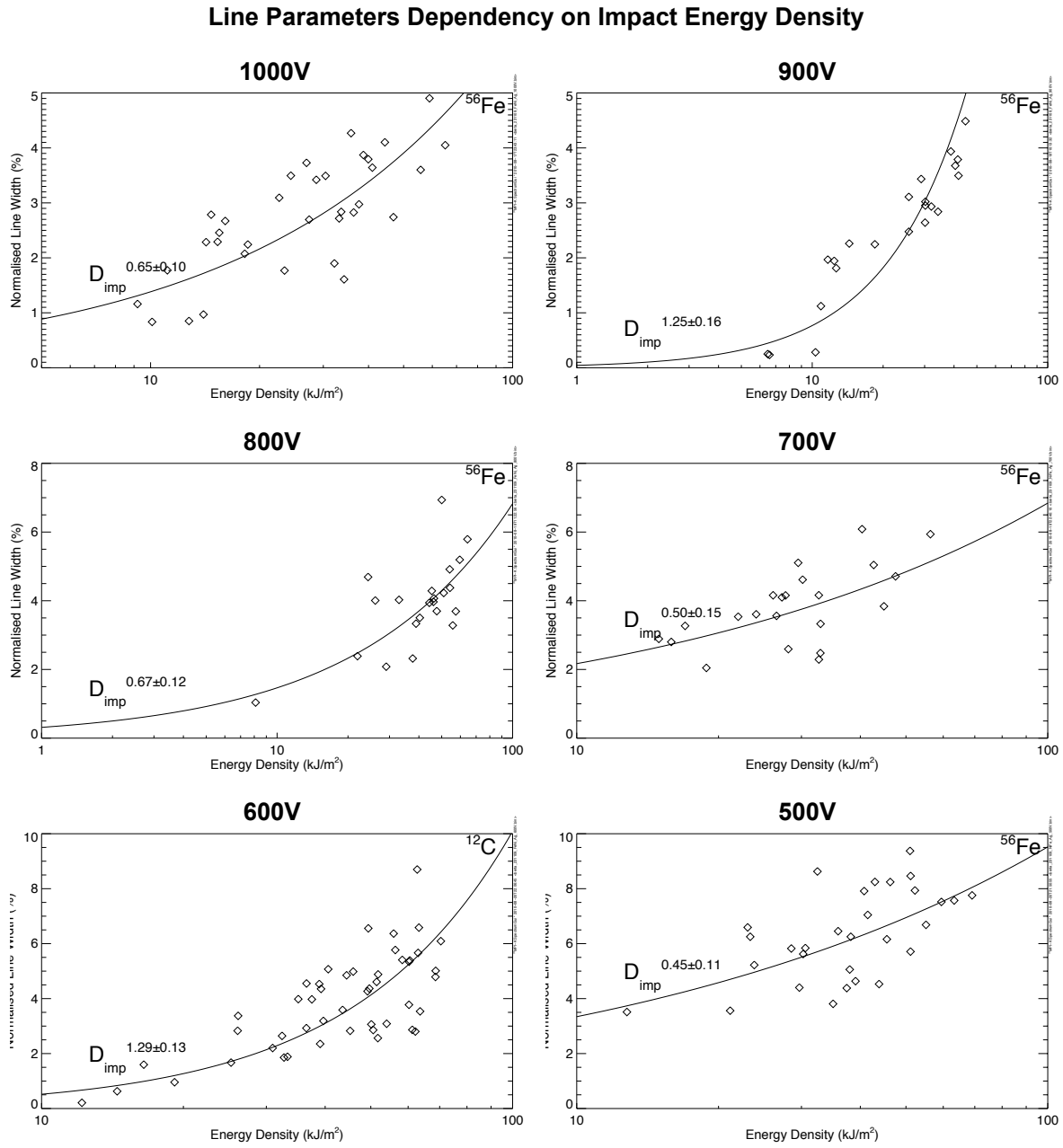

Figure D.37.: Shots with iron particles on silver: line widths of iron ions

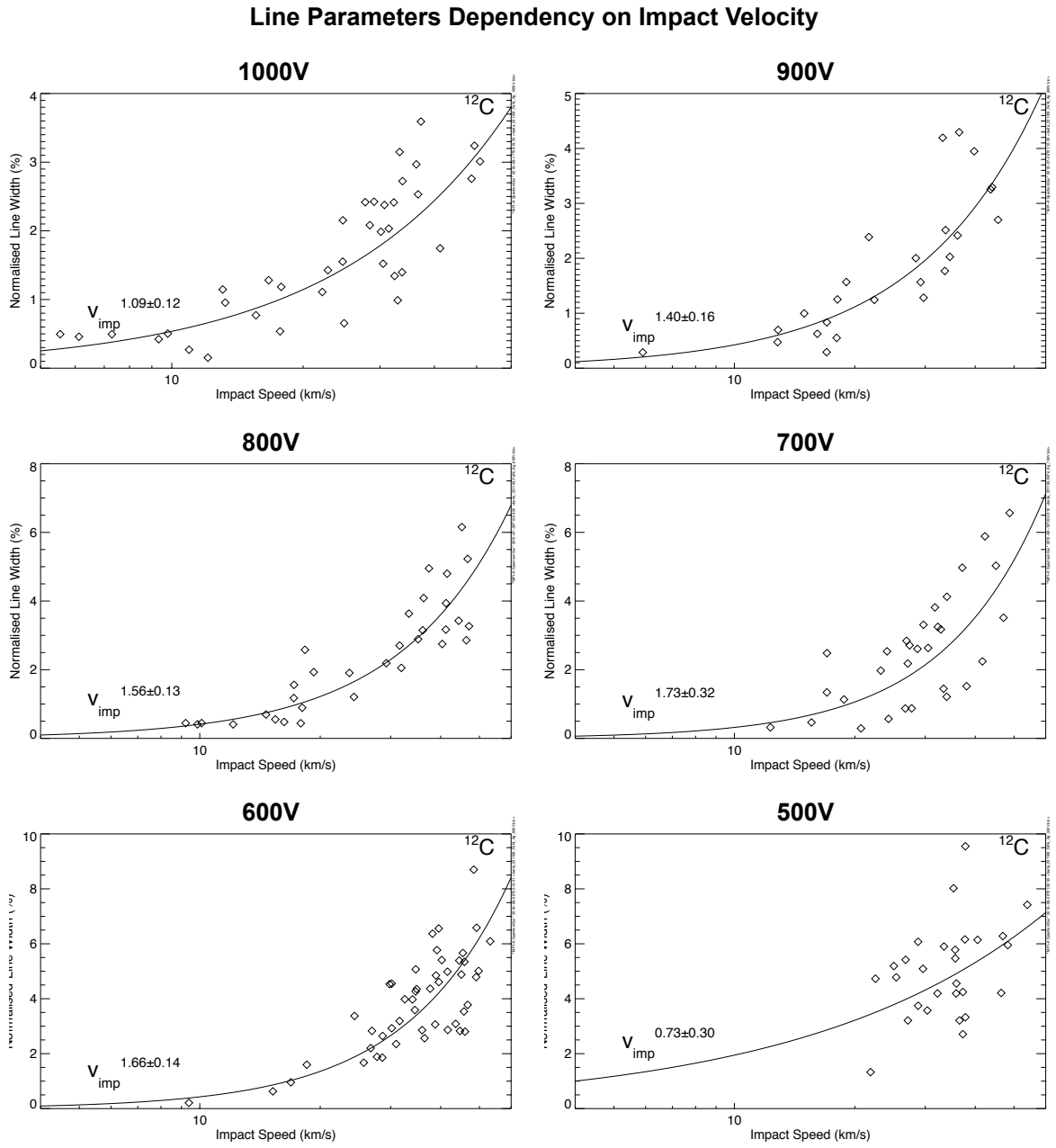

Figure D.38.: Shots with iron particles on silver: line widths of carbon ions

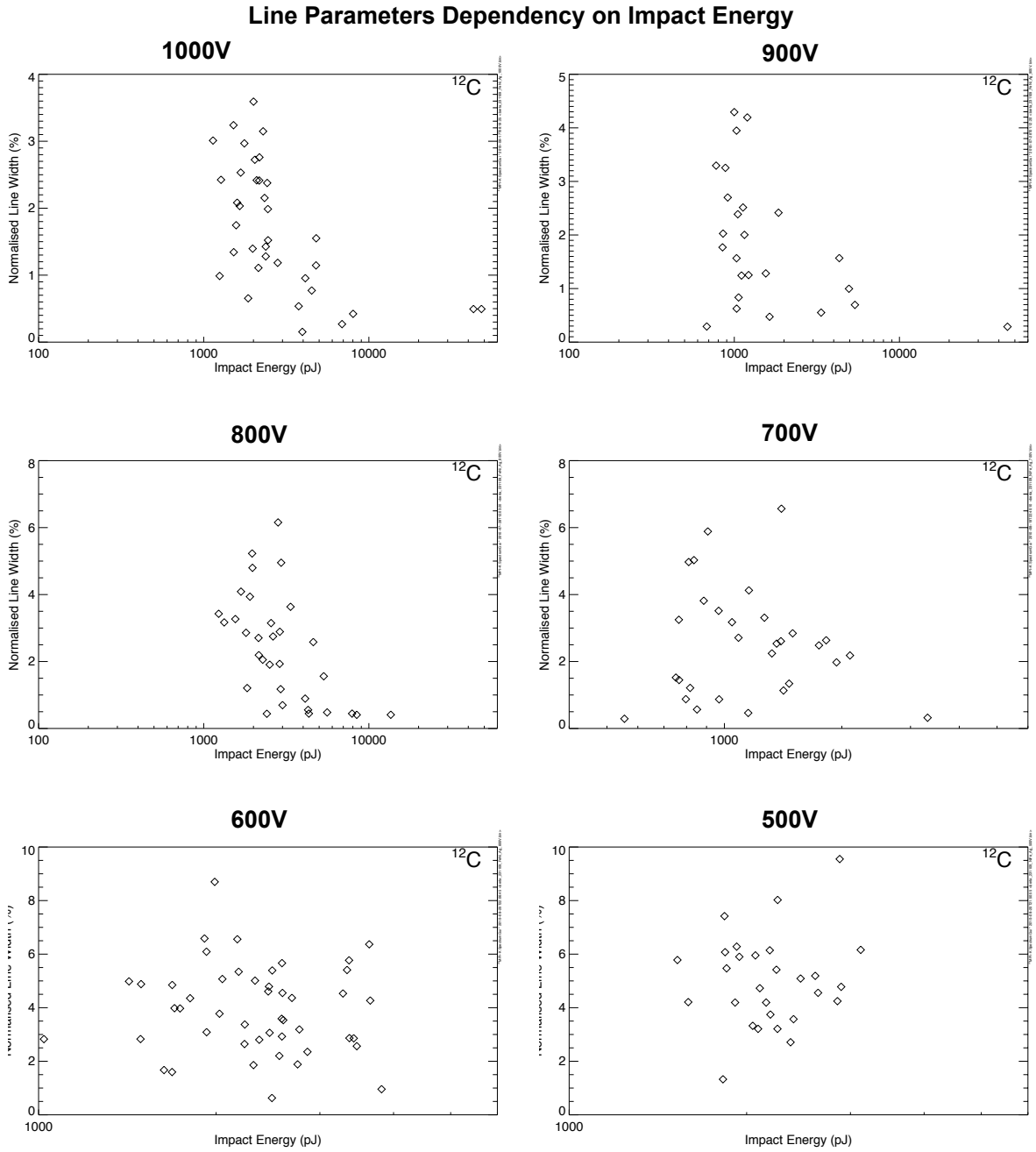

Figure D.39.: Shots with iron particles on silver: line widths of carbon ions

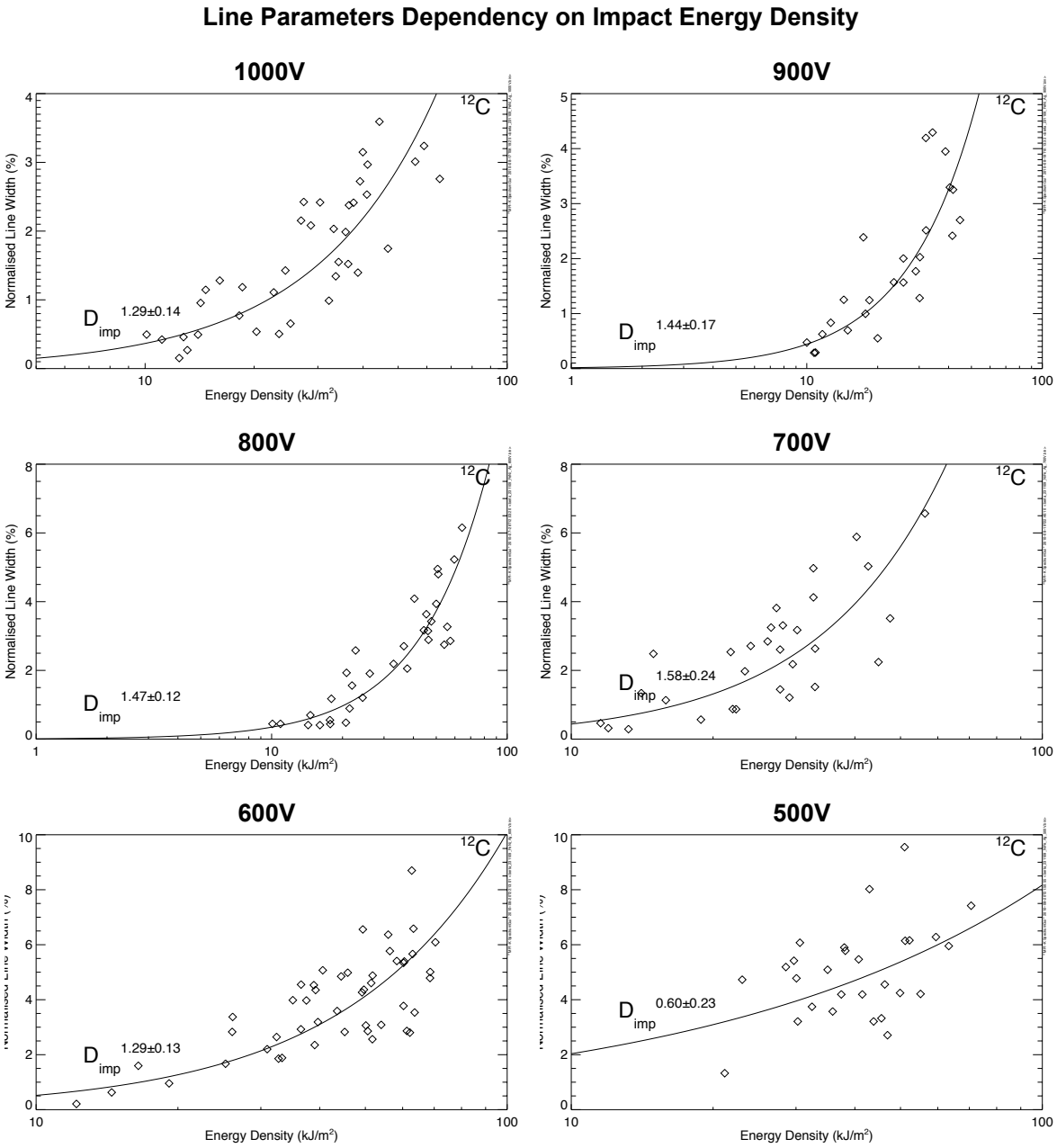

Figure D.40.: Shots with iron particles on silver: line widths of carbon ions

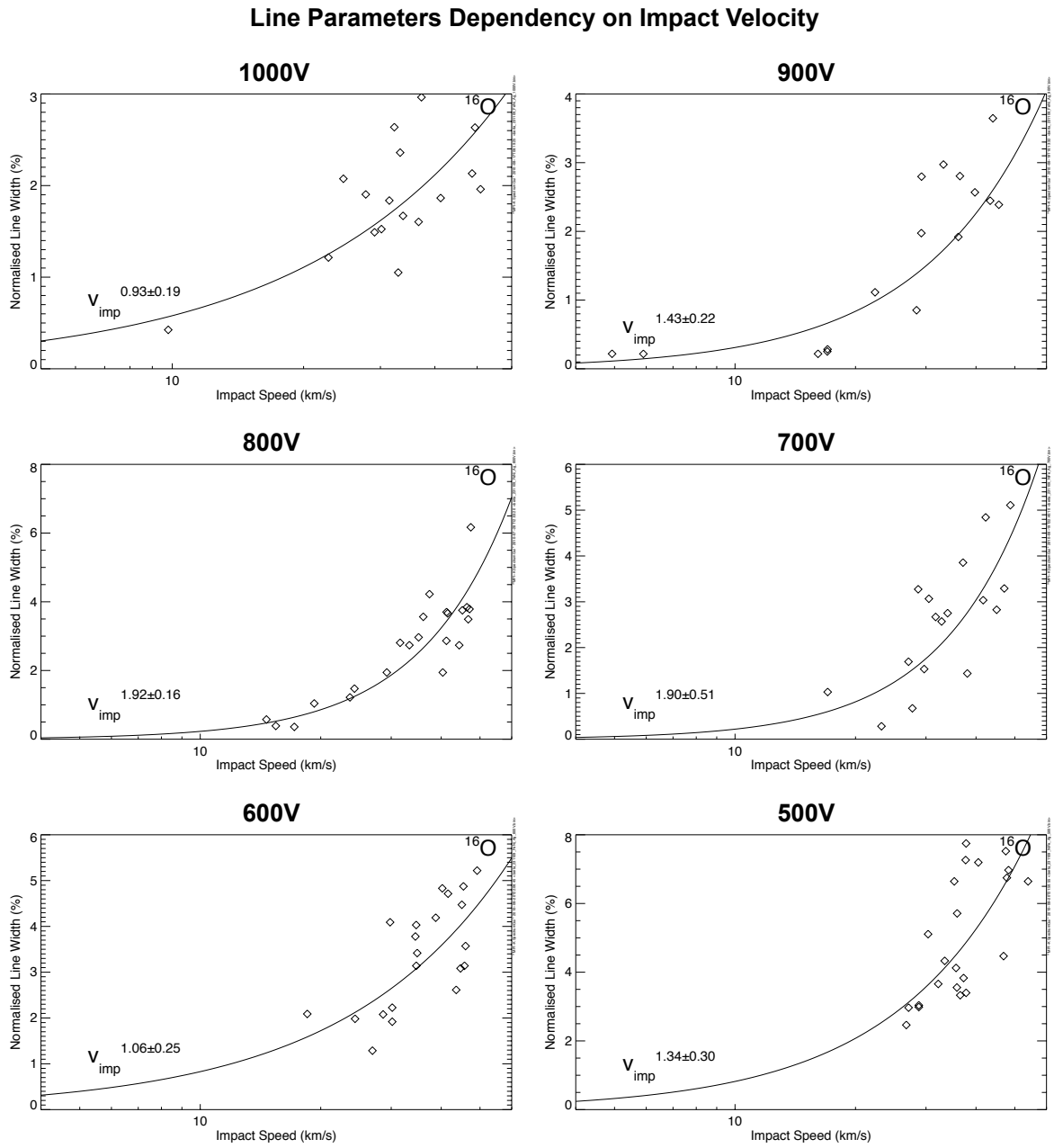

Figure D.41.: Shots with iron particles on silver: line widths of oxygen ions

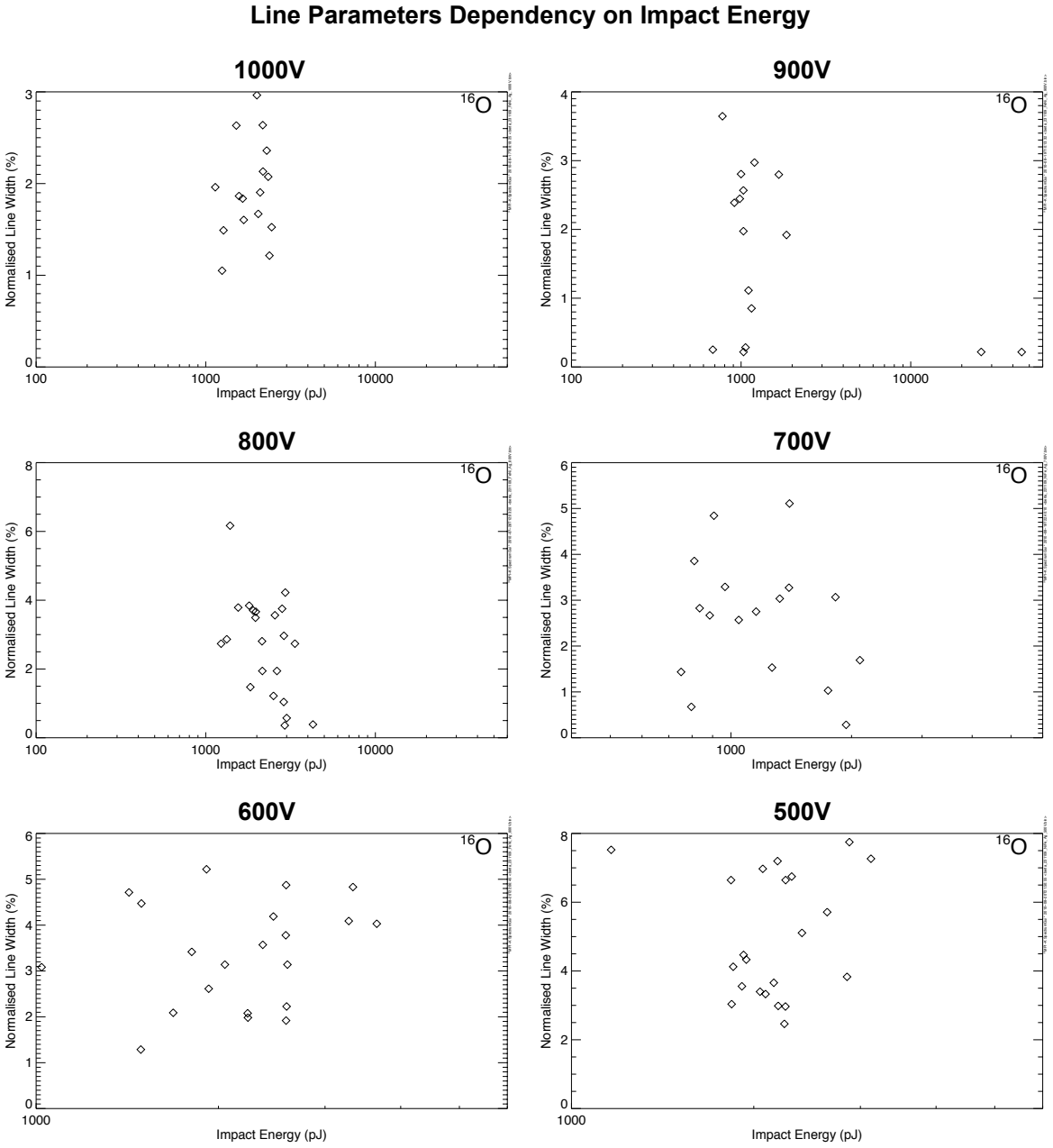

Figure D.42.: Shots with iron particles on silver: line widths of oxygen ions

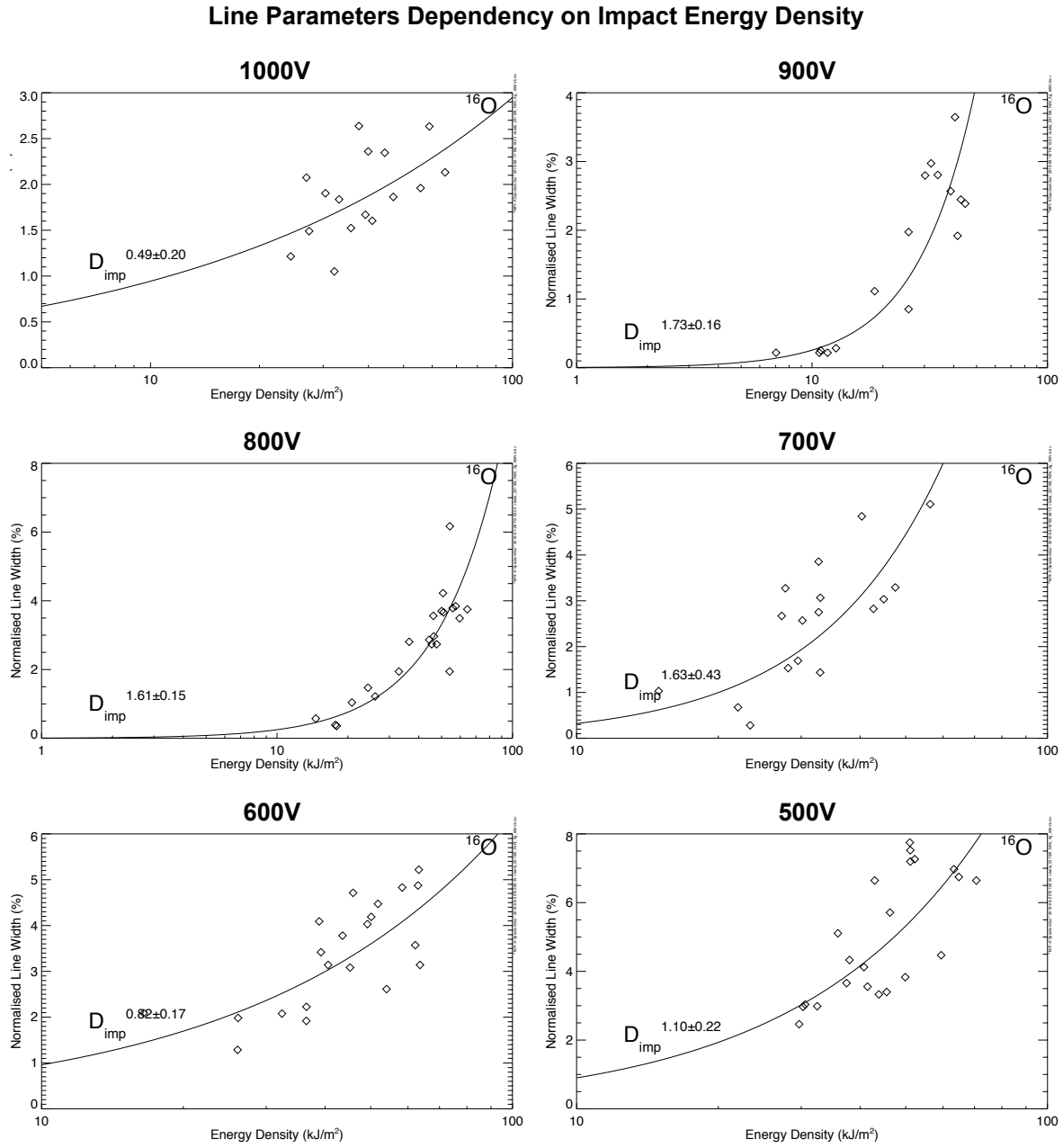

Figure D.43.: Shots with iron particles on silver: line widths of oxygen ions

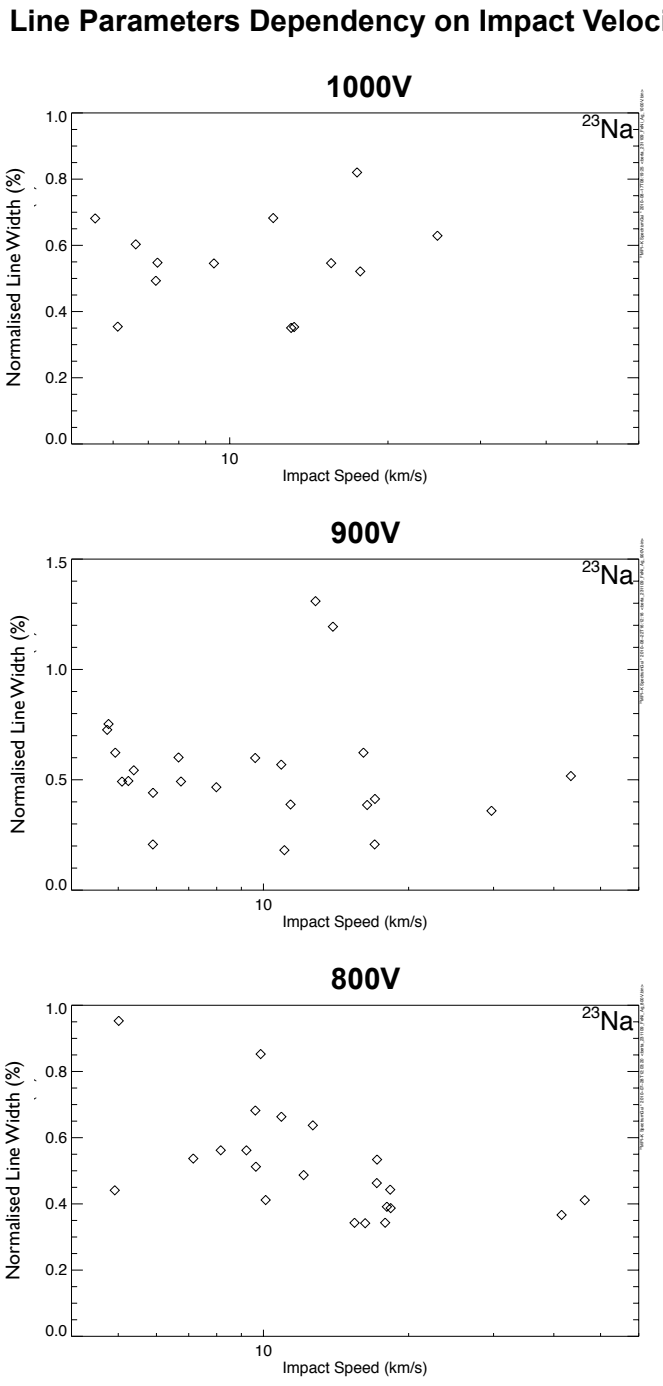

Figure D.44.: Shots with iron particles on silver: line widths of sodium ions

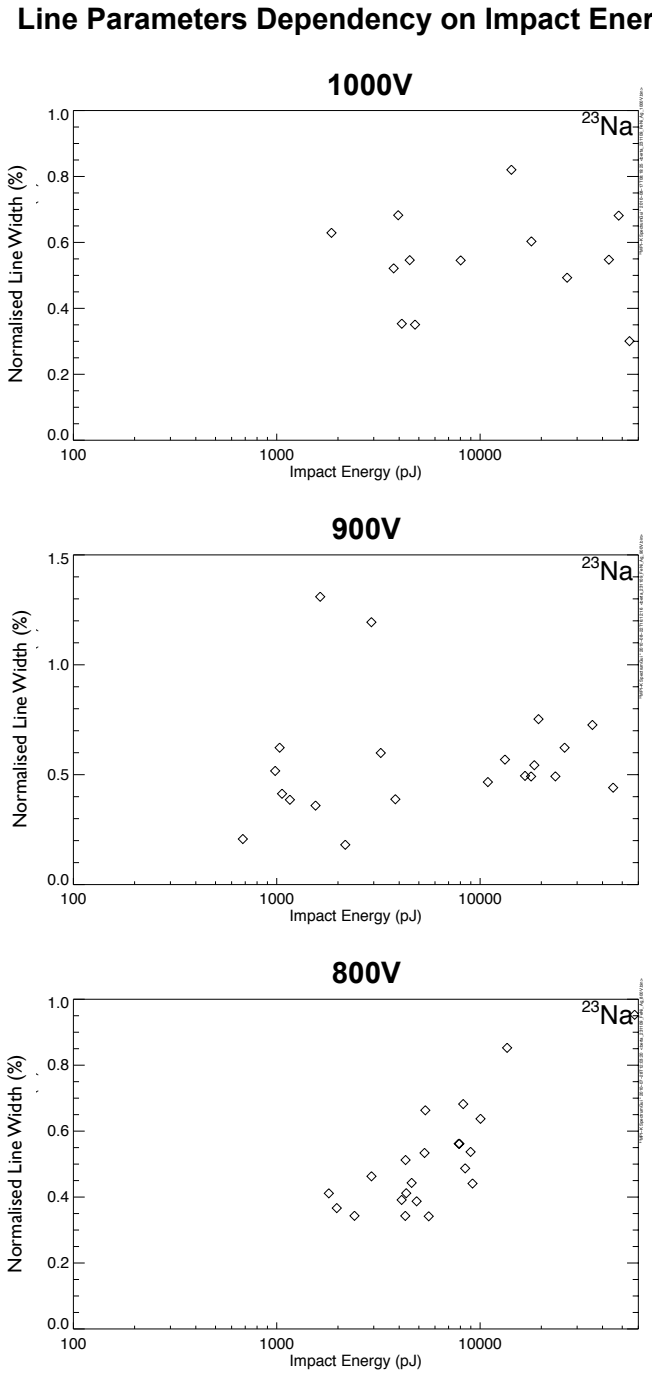

Figure D.45.: Shots with iron particles on silver: line widths of sodium ions

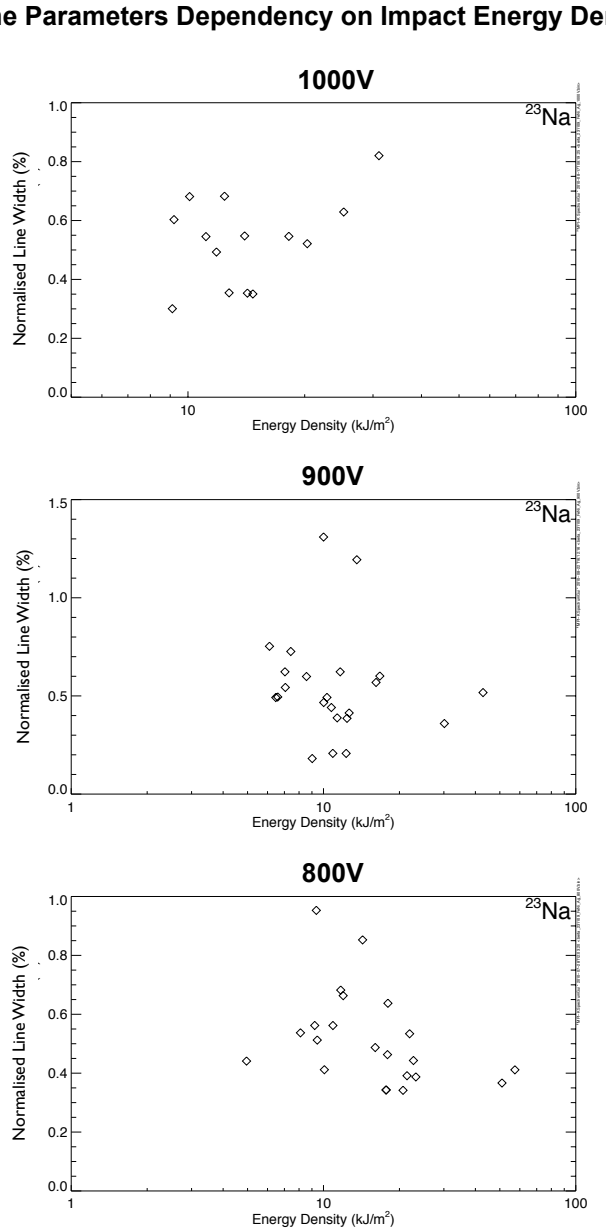

Figure D.46.: Shots with iron particles on silver: line widths of sodium ions

Erklärung

Ich versichere, daß ich diese Arbeit selbständig verfaßt und und keine anderen als die angegebenen Hilfsmittel benutzt habe.

Heidelberg, den 3. Dezeber 2010